Jason W. L. Lee

Novel Developments in Time-of-Flight Particle Imaging

Doctor of Philosophy

Physical & Theoretical Chemistry

Worcester College, University of Oxford

Abstract

Novel Developments in Time-of-Flight Particle Imaging

A thesis submitted in partial fulfilment for the degree of Doctor of Philosophy in Physical & Theoretical Chemistry by:

Jason W. L. Lee

Worcester College
Trinity 2014

In the field of physical chemistry, the relatively recently developed technique of velocity-map imaging has allowed chemical dynamics to be explored with a greater depth than could be previously achieved using other methods. Capturing the scattering image associated with the products resulting from fragmentation of a molecule allows the dissociative pathways and energy landscape to be investigated.

In the study of particle physics, the neutron has become an irreplaceable spectroscopic tool due to the unique nature of the interaction with certain materials. Neutron spectroscopy is a non-destructive imaging technique that allows a number of properties to be discerned, including chemical identification, strain tensor measurements and the identification of beneath the sample surface using radiography and tomography.

In both of these areas, as well as a multitude of other disciplines, a flight tube is used to separate particles, distinguishing them based upon their mass in the former case and their energy in the latter. The experiments can be vastly enhanced by the ability to record both the position and arrival time of the particle of interest. This thesis describes several new developments made in instrumentation for experiments involving time-of-flight particle imaging.

The first development described is the construction of a new velocity-map imaging instrument that utilises electron ionisation to perform both steps of molecular fragmentation and ionisation. Data from CO_2 is presented as an example of the ability of the instrument, and a preliminary analysis of the images is performed.

The second presented project is the design of a time-resolved and position-resolved detector developed for ion imaging experiments. The hardware, software and firmware are described and presented alongside data from a variety of the experiments showcasing the breadth of investigations that are possible using the sensor.

Finally, the modifications made to the detector to allow time-resolved neutron imaging are detailed, with an in-depth description of the various proof-of-concept experiments carried out as part of the development process.

Acknowledgements

Throughout the last three and a half years, I have been fortunate enough to benefit from the guidance of Claire Vallance, who has provided an indefatigable source of inspiration and boundless enthusiasm. Her insight into both the experimental and theoretical aspects of all the work presented here has been incredibly valuable.

Secondly, James Bull who has been a reliable colleague and friend through my time as a DPhil student and whose expertise has allowed all of the work on the electron ionisation experiments to be performed. His interest and discussion in of all of the other projects has been invaluable and is a strong testament to his scientific capabilities.

A big thank you to all members of the PImMS collaboration – a project this large requires the input and skills from a multitude of people in order to make progress in the face of nigh insurmountable hurdles. Thanks are given to the PIs Mark Brouard, Claire Vallance, Andrei Nomerotski, Richard Nickerson and Renato Turchetta for establishing the project; a complete description of the individual contributions to the project is detailed below. In particular, Jaya John John has been an irreplaceable member of the collaboration, having worked on almost all aspects of the sensor, as well as providing a number of extremely helpful discussions over coffee breaks during debugging sessions.

Daniel Pooley at RAL has been a great partner for all the work on the GadMOS project, allowing many exciting and novel measurements to be made on complex systems, and pushing and extending the boundaries of our technology.

Thanks are given to all members of the Vallance group, the Brouard group and other members of the PTCL, who have been a great source of discussion throughout my time as a DPhil student, particularly Simon-John King, Ben Winter, Ed Halford, Lee Harper and Cathy Rushworth. The mechanical and electronics workshops of the PTCL are also gratefully acknowledged for their assistance on all projects, as well as the EPSRC for providing the funding for my DPhil studentship.

Finally, thank you to all the people at Worcester College and the university that I have been lucky enough to become friends with during my time in Oxford, too numerous to name, and to my sister Annabel and brother-in-law Sam for making the last three and half years so enjoyable.

All of the work on electron ionisation, from building the experiments to recording the data, was performed by JWLL and JNB.

The design of the PImMS sensor was carried out by ATC, JPC and IS. The firmware work was performed by JJJ and ATC and all software work has been performed by JWLL. The general characterisation and debugging presented here was performed by JWLL, JJJ, LOH, RP, XC, ESW, ATC and IS.

In the PImMS sensor applications, the laser bench tests were carried out by JWLL, ESW, JJJ, RP and XC, the CS_2 and DMF VMI experiments were performed by JWLL and ESW, and the Br_2 coincidence experiment was set up by CSS and the data was collected by JWLL, CSS, and BW. The measurements of the alpha and beta particles using the PImMS sensor were performed by JWLL and DEP and the comparative measurements using BC400 were performed by DEP and LP.

In the GadMOS project, the initial proof-of-concept experiments were performed by JWLL, DEP, IS, RF and LOH and all the development of the sensor firmware specific for the neutron experiments was carried out by JJJ. All other experiments and data analysis were performed by JWLL and DP and the tomographic reconstruction was carried out by DP.

Initials	Name
JWLL	Jason Lee
JNB	James Bull
ATC	Andrew Clark
JPC	Jamie Crooks
IS	Iain Sedgwick
RT	Renato Turchetta
JJJ	Jaya John John
LOH	Laura Hill
RP	Robert Pisarczyk
XC	Xavier Coubez
ESW	Edward Wilman
EH	Edward Halford
BW	Benjamin Winter
DEP	Daniel Pooley
LP	Luca Pollastri
RF	Richard Farrow

Table of Contents

Part I: Electron Ionisation

Part II: The Pixel Imaging Mass Spectrometry (PImMS) Sensor

Part III: The GadMOS Project

Part I: Electron Ionisation

Publications

- Quantification of ions with identical mass-to-charge (m/z) ratios by velocity-map imaging mass spectrometry
  J. N. Bull, J. W. L. Lee and C. Vallance
  Phys. Chem. Chem. Phys. 15, 13796 (2013).

- Absolute electron impact total ionization cross sections: molecular analogues of DNA and RNA nucleobase and sugar constituents
  J. N. Bull, J. W. L. Lee and C. Vallance
  Phys. Chem. Chem. Phys. 16, 10743 (2014).

- An Introduction to Velocity-Map Imaging Mass Spectrometry (VMImMS)
  J. N. Bull, J. W. L. Lee, S. H. Gardiner and C. Vallance
  EJMS. 20, 117 (2014).

- The dissociative ionization dynamics of N_2 and O_2 molecules by electron impact: Velocity-map imaging
  J. N. Bull, J. W. L. Lee, and C. Vallance
  In preparation

1 Introduction to Electron Ionisation

Electron ionisation (EI) is one of the most fundamental collision processes in particle physics. Developing a detailed understanding of the dynamics is both of fundamental interest, and useful for a range of applications. Since the first mass spectrometry experiments performed by Dempster in 1918, EI has remained one of the major ionisation mechanisms used in analytical and research mass spectrometry for small to medium sized molecules.[1,2] Outside of the laboratory, EI processes are important in a number of naturally occurring and industrial/commercial environments. EI processes are important in the upper atmospheres of planets, particularly through the capture of solar wind particles by planetary magnetospheres. Such processes form a number of atomic ions that are responsible for the transport of energy throughout the atmosphere.[3,4,5] The generation of fusion and other plasmas and their properties can be controlled through EI, and a very topical biological example is the importance of electron interactions with genetic material in living cells inducing significant damage to DNA, causing strand breaks and possible biological apoptosis[6,7].

The majority of detailed studies of EI processes have considered atomic species or simple diatomics, and the fundamental dynamics of certain molecules, such as H_2, have been well studied.[8] However, comprehensive studies of polyatomic systems are relatively scarce. The introduction of more particles into the scattering process when moving to polyatomic molecules can make it exceptionally difficult to reconcile energy and flux balances across all possible contributing energy-transfer and fragmentation pathways either experimentally or theoretically.

This section details the design, construction and application of two electron ionisation instruments to study the dynamical processes involved in molecular electron ionisation. The first instrument is designed to directly and accurately measure *absolute* values of the total ionisation cross section (TICS) of molecules with near unit detection efficiency for all ion species. The second is designed to record ‘quantitative’ nascent ion branching ratios and kinetic energy release distributions through velocity-map imaging (VMI) of the ion fragments following EI. Branching ratios can be converted to partial ionisation cross sections (PICS) through appropriate normalisation of the total ion signal across all fragments. Analysis of the velocity-map images can provide details on the statistical versus non-statistical nature of the fragmentation and, in ideal situations, extract the contributions from various different ionisation channels contributing to the formation of a particular fragment.

1.1 Ion Formation Processes

The impact of a molecule by an electron can result in the formation of an ion by a number of different processes. The majority of EI processes are termed as *inefficient* because the incident electron usually transfers only a fraction of the kinetic energy to the target molecule. As an ionisation mechanism, EI initially produces a nascent parent ion. If the nascent parent ion is unbound in the vertical excitation region, it may rapidly or directly dissociate in a process known as *dissociative ionisation*.

$$e^- + \mathrm{AB} \rightarrow \mathrm{AB}^+ + 2e^- \qquad \text{Single ionisation or } (e,2e) \qquad \text{(i)}$$

$$e^- + \mathrm{AB} \rightarrow \mathrm{AB}^+ + 2e^- \rightarrow \mathrm{A} + \mathrm{B}^+ + 2e^- \qquad \text{Dissociative single ionisation} \qquad \text{(ii)}$$

As the size of the molecule increases, the density of states that the molecule can inhabit and the number of internal conversion pathways also increase. This encourages the efficient redistribution of energy and, promoting statistical dissociation/fragmentation. It is possible to predict the rate of unimolecular decomposition using the quasi-equilibrium theory (QET), an extension of Rice-Ramsperger-Marcus-Kassel (RRKM) theory which accounts for the isolation of molecules in the gas phase.[9,10,11]

EI is described as a "hard" process because a collision-ionisation event generally deposits energy in excess of the ionisation potential, promoting extensive bond cleavage. This type of hard ionisation mechanism is contrasted with "soft" mechanisms such as electrospray which typically exhibits very little fragmentation.

EI is typically assumed to be a rapid process occurring on a timescale faster than nuclear rearrangement and is therefore an example of a *vertical ionisation* process. As a simple numerical example, 70 eV electrons have a speed of 5×10^6 m s^{-1} and would traverse 1.5 Å, a distance similar to a typical bond length, in around 3×10^{-17} s. In comparison, fast C-H stretching vibrations have an IR absorbance around 3000 cm^{-1}, which corresponds to a vibrational period of approximately 1×10^{-14} s, nearly three orders of magnitude slower. In comparison, the formation of ions through infrared multiphoton dissociation (IRMPD) of a parent ion is a relatively slow process as it involves the absorption of dozens or even hundreds of ~0.1 eV photons[12]. This process provides the necessary time for energy to be redistributed throughout the molecule, generally leading to statistical dissociation.

The minimum energy required to remove an electron from the neutral molecule is known as the *adiabatic ionisation energy*, which usually differs from the vertical ionisation energies by 0.1-0.7 eV.[13] Vertical and adiabatic ionisation processes are shown schematically in Figure 1.

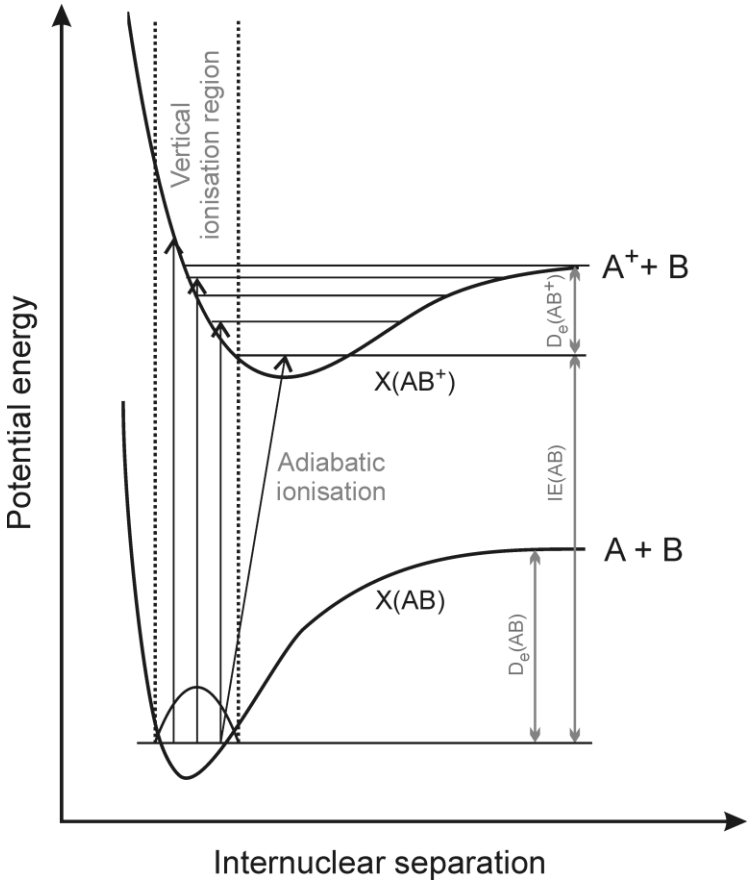

Figure 1 – A schematic demonstration of vertical and adiabatic ionisation for a diatomic AB, also showing the dissociation energy for the neutral AB molecule and parent AB^+ ion from their ground vibrational states, D_e(AB) and $D_e(AB^+)$ respectively, and the lowest ionisation energy, *IE*(AB).

EI may also lead to a multiply-charged ion, for example through Auger processes:

$$e^- + \mathrm{AB} \rightarrow \mathrm{AB}^{n+} + (n+1)e^- \qquad \text{Multiple ionisation } (n > 1) \qquad \text{(iii)}$$

The probability for multiple ionisation processes increases with higher electron energies. For example, the production of N^+ compared to N^{2+} from EI of N_2 as a function of incident electron energy is shown in Figure 2. It can be seen that the lowest electron energy at which N^{2+} is produced, also known as the *appearance energy*, is 70 eV, and that the production is generally two orders of magnitude lower than for the N^+. At electron energies below 100 eV, the production of multiply-charged (parent and fragment) ions is significantly less likely to occur.

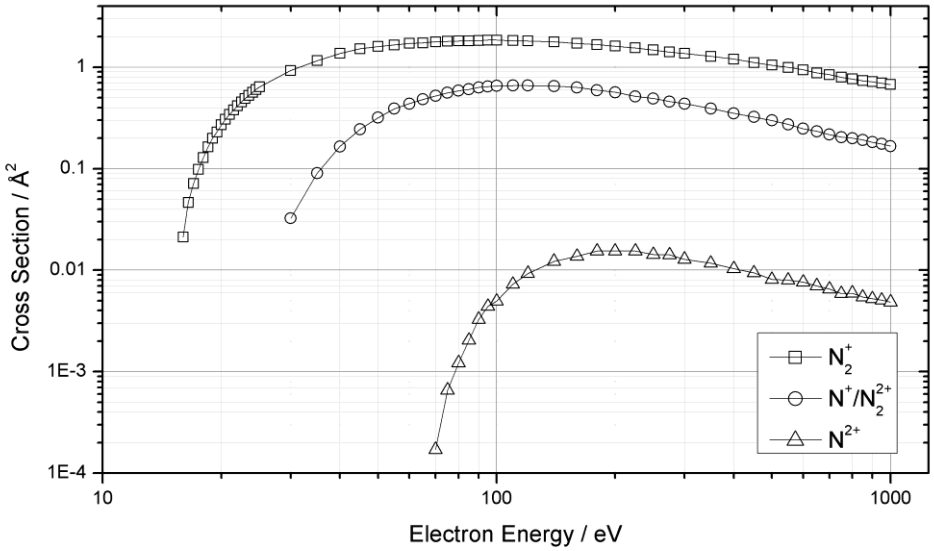

Figure 2 – The production of ions from EI of N_2 as a function of electron energy. Although N^+ is not distinguished from N_2^{2+} in this experiment due to identical *m/z*, N^+ is expected to be the major contribution to the measurement. Values taken from Lindsay and Mangan[14].

A number of other processes may occur when a free electron collides with a molecule. Ion pair formation is the creation of both positive and negative ions from the parent molecule, and typically requires slightly more energy than for single ionisation. Ion pair formation is generally a relatively minor channel compared to single ionisation and dissociative ionisation. For example, production of the ion pair O^-/O^+ from molecular oxygen has a maximum cross section of 0.48 $\times 10^{-2}$ Å^2 at 34 eV, compared to 0.18 Å^2 for O^+ formation from dissociative ionisation and 0.81 Å^2 for O_2^+ formation at the same electron energy.[15,16]

$$e^- + \mathrm{AB} \rightarrow \mathrm{A}^+ + \mathrm{B}^- + e^- \qquad \text{Ion pair formation} \qquad \text{(iv)}$$

At low energies, electron capture (EC) can occur, in which a neutral molecule captures an electron to form a negative ion. This process may be very efficient for electron kinetic energies near zero if the molecule has a large positive vertical electron affinity. At higher energies, collision can induce dissociation in dissociative electron capture:

$$e^- + \mathrm{AB} \rightarrow \mathrm{AB}^- \qquad \text{Electron capture} \qquad \text{(v)}$$

$$e^- + \mathrm{AB} \rightarrow \mathrm{AB}^- \rightarrow \mathrm{A} + \mathrm{B}^- \qquad \text{Dissociative electron capture} \qquad \text{(vi)}$$

In contrast to EI, no electron is produced in EC to carry away the excess energy; consequently EC is a resonant process and generally occurs in collisions involving electrons with energies lower than 10 eV.[17] At the energies considered in the experiments described in this thesis, EC is not expected to contribute to the formation of ions.

1.1.1 Total Ionisation Cross Sections and Partial Ionisation Cross Sections

Classically, the cross section is defined as the effective area that a target species of a given state and velocity presents to an incident colliding partner of a given state and velocity, and is reported in units of area such as m^2 or $Å^2$. Appropriate normalisation of the cross section can then be interpreted as a probability; for example, the probability of the production of an ion *X* from the EI interaction is described by the partial ionisation cross section (PICS), $\sigma_{PICS}(X)$. The total ionisation cross section (TICS), σ_{TICS}, is given by the sum of all the PICS and represents a measure of the overall ion production probability or ionisation efficiency. As the details of the collision process (e.g. electron/ion scattering angle, ion kinetic energy) are averaged out, the cross sections are referred to as integral cross sections, i.e. integrated over all angles. The probability of production of ion *X* in a particular solid angle from the interaction is known as the differential cross section and can be denoted as $\sigma_{PICS}(X, \vartheta, \varphi)$ where ϑ and φ have their usual meaning in spherical polar coordinates as the polar and azimuthal angles. In mass spectrometry, the analytical standard electron kinetic energy is 70 eV, as most organic molecules generally have a maximum TICS near this value. In a classical interpretation, 70 eV roughly corresponds to resonance between the electron de Broglie wavelength and the length of a molecular orbital in an organic molecule (~1.5 Å). When the resonance condition is satisfied, the transfer of energy is maximised, increasing the likeliness of ionisation and fragmentation.[18]

There are two different conventions in reporting TICS, usually defined by the method of ion detection; these are the *counting* TICS and the *gross* TICS. The counting TICS reports the production of an ion independently of the charge state that it possesses, whereas a gross cross section sums over the charge of the ion. For example, $\sigma(X^+)$ would have the same contribution in both conventions; however the gross contribution of $\sigma(X^{2+})$ would be twice that of the counting contribution. Gross cross sections are usually reported in total current measurement experiments, in which there is no way to distinguish the identity of the ion species contributing to a current measurement. Counting cross sections require measurements that allow the charge-state to be determined or experiments that record the number of ions formed directly. At the analytical standard of 70 eV, the production of ions with a charge state greater than one is usually relatively rare, so the gross and counting cross sections are very similar. As illustrated in Figure 2, at electron energies of 100 eV and above, the formation of multiply charged ions can begin to contribute significantly to the TICS. If the PICS of each ion formed, *X*, is known, and *z(X)* represents the charge on ion *X*, conversion between the gross and counting TICS can be performed using the following relationships:

$$\sigma_{\mathrm{TICS,counting}}(E) = \sum_{X} \sigma_{\mathrm{PICS}}(X) \quad (1)$$

$$\sigma_{\mathrm{TICS,gross}}(E) = \sum_{X} z(X) \times \sigma_{\mathrm{PICS}}(X) \quad (2)$$

The experimental methods for measuring the TICS and PICS are described in Section 2 and Section 3 respectively.

1.2 Velocity-Map Imaging

Velocity-map imaging (VMI) is an experimental technique introduced by Eppink and Parker[19] in 1997 that allows the velocities of products formed in a dissociative event to be determined. VMI is a variation on an older method known as *ion imaging*, and overcomes a number of limitations of the previously employed technique. Ion imaging was first demonstrated by Chandler and Houston[20] in 1987, with the first reported application being a study of the methyl fragment resulting from the photodissociation of methyl iodide.

Briefly, their technique involved the interaction of a molecular beam of methyl iodide with two pulsed lasers to cause fragmentation and ionisation. The fragmentation laser interacted with the target molecule to induce photofragmentation. The resulting products expand in a series of concentric spheres, known as *Newton spheres*, with a radius dependent on the time after the fragments are formed and the velocity of the fragments. The second laser pulse photoionises the fragmentation products to produce ions, performed within a few nanoseconds of the first laser, before the products have moved a significant degree or changed their non-equilibrium ensemble.

An electric field is used to extract the ions from the interaction region onto a position sensitive detector, which is usually an MCP/phosphor detector. An ion striking the MCP surface creates a cascade of electrons that is accelerated towards the phosphor screen, inducing phosphor excitation and short flashes of fluorescence that are spatially correlated with the position of the incident ion. The resulting flashes of light can be captured using a two-dimensional imaging detector such as charge-coupled device (CCD) camera, and integrating the images captured over many acquisition cycles produces a two-dimensional image representative of the spatial distribution for that ion being studied. Ions with different values of *m/z* are separated in the experiment by their flight time, allowing the image associated with a particular ion to be recorded by synchronising the exposure window of the CCD camera with the arrival time of the ion at the detector.

One of the drawbacks of conventional ion imaging is that the achievable spatial resolution is limited by the volume of interaction. A molecular beam has a diameter of a few millimetres and the pump and probe laser beams therefore do not create ions from a single well-defined point. When projected

on to a position sensitive detector, the difference in the original position of the ions causes the resulting image to appear blurred. When using an MCP measuring 40 mm in diameter, the error caused by the volume of interaction is approximately 2.5-5%. Ion imaging also employs a gridded mesh in the ion flight path which is an additional source of aberration in the recorded image.

VMI uses the same method to create ions, but the gridded mesh is removed and the ion lenses are set to potentials such that the ion is projected onto a position on the detector that depends only upon the velocity of the ion, independent of where the ion is originally formed. The image is therefore not distorted by the finite interaction volume and the achievable velocity resolution is significantly higher. A schematic of ions being velocity-mapped is shown in Figure 3.

In VMI, the extraction of the ions from the interaction region is typically performed using three electrodes or *ion lenses*, known as the *extractor*, *repeller*, and the *ground*, which are held at constant voltages. These are arranged as shown in Figure 4, with the ion formation region between the extractor and repeller. Extracting the ions compresses the three-dimensional Newton sphere to a two-dimensional projection along the flight axis due to the fact that ions with the same *m/z* value are time-focussed onto the detector and therefore have virtually identical arrival times. In systems possessing cylindrical symmetry, applying an inverse Abel transform allows the reconstruction of the three-dimensional Newton sphere.[21] The objective of reconstructing the Newton sphere is to extract the central two-dimensional slice through the measured velocity distribution parallel to the detector surface, which contains the information of interest from the dissociative process. The measured velocity can be converted to kinetic energy with a suitable calibration factor to yield the *kinetic energy release (KER) distribution*, which can often provide a detailed insight on the partitioning of the energy in the reaction products.

An alternative to employing the inverse Abel transform is to record the central slice of the Newton sphere directly using a technique called *slice imaging*. This involves the use of slightly different ion optics to stretch out the Newton sphere along the flight axis instead of compressing it, first demonstrated by Kitsopoulis *et al*[22]. The voltages applied to the MCP/phosphor detector are then timed so that the detector is only active during the arrival time of ions corresponding to the central slice of the Newton sphere. The technique generally requires an ion flight time distribution of around 250 ns for each ion mass and the ability to activate the detector in pulses of 25 ns.

As a simple example of the capabilities of VMI, in the photodissociation of O_2 to yield two O atoms, conservation of momentum dictates that the atoms must have equal and opposite momenta in the centre-of-mass frame and therefore equal and opposite velocities in the centre-of-mass frame.

Depending on the photon energy, atomic oxygen can be produced in the electronic ground state or in an excited electronic state. Since the energy involved in the fragmentation process is fixed by the photon energy, due to conservation of energy, formation of an excited O* atom reduces the kinetic energy available. In velocity-map ion imaging, the measured velocity distribution of the O products yields the momentum and, with knowledge of the fragmentation energy, allows the electronic state of the O atom produced to be determined.

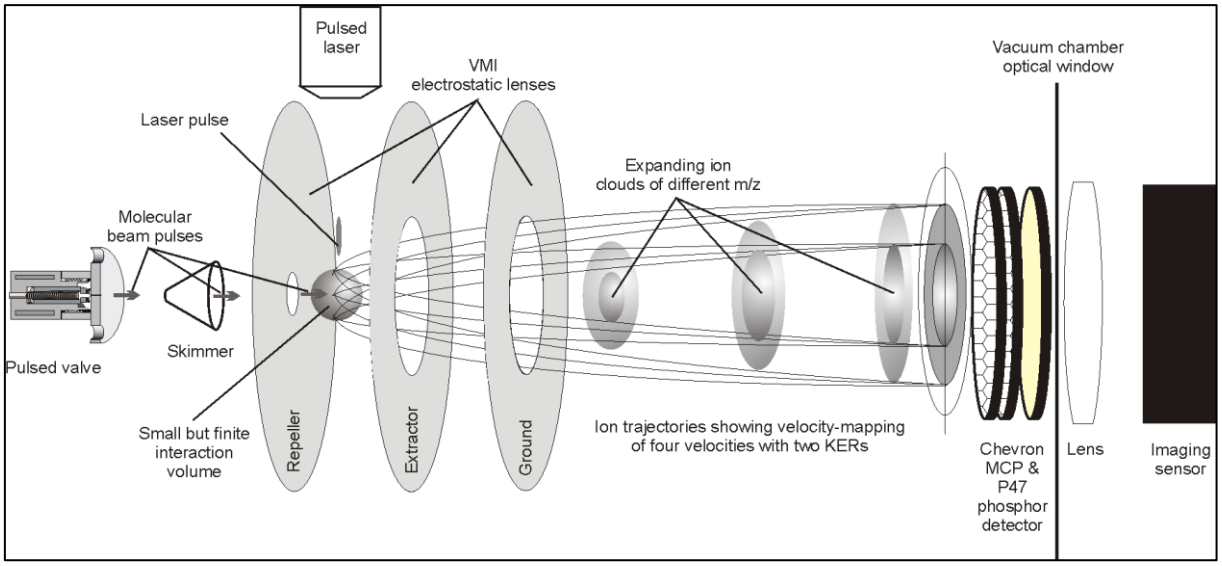

Figure 3 – A schematic of the ions created through crossing the molecular beam and the electron beam being velocity-mapped onto an MCP/phosphor detector. The ion trajectories show ions formed with the same velocity in different parts of the interaction region being mapped onto the same position on the detector.

1.2.1 Velocity-Map Imaging Mass Spectrometry

While VMI provides an excellent approach to studying reaction dynamics, the technique can become restrictively time-consuming for 'large' molecules, i.e. molecules consisting of more than five or so atoms, which often undergo extensive fragmentation. In these cases, the formation of multiple products means that momentum matching is of limited applicability and each ion must be imaged individually. An ideal VMI experiment would record the images associated with all fragments simultaneously, therefore significantly decreasing the experimental time required, and providing the added benefit of reducing any experimental drift that occurs over a long period of time. As ions with different *m/z* values are separated by their arrival at the detector by the flight tube akin to a typical time-of-flight mass spectrometer, such an experiment may be referred to as a velocity-map imaging mass spectrometry (VMImMS) experiment.[23] There are two requirements for a VMImMS experiment: a universal and hard ionisation source; and a detector with the capability to record signal with respect to both position and time. The first of these is elaborated on below, and the second will be discussed in detail in Part II.

1.2.2 Universal Ionisation

Universal ionisation refers to an ionisation source that is capable of ionising any target molecule or molecular fragment. Photoionisation in VMI typically utilises resonance-enhanced multiphoton ionisation (REMPI) to promote the efficiency of ionisation. REMPI is a quantum-state selective ionisation method which provides high ionisation efficiency for the state of interest, but cannot usually ionise multiple quantum states and/or multiple molecules simultaneously. Single-photon ionisation is more suitable, however with the caveat that the photon energy must exceed the ionisation energy of all of the fragments formed. Further, photoionisation cross sections can exhibit sharp features over relative narrow photon energy ranges meaning that direct abundance comparisons between different species may be semi-quantitative at best. Common sources of high energy photons include synchrotron radiation and specialised vacuum ultra-violet lasers. Within a laboratory, photons with energies of 10.51 eV (118 nm) can be readily obtained by tripling the third harmonic of a Nd:YAG laser.[24] Other wavelengths in this region can be generated, with some tenability if desired, by tripling the output of a dye laser. Femtosecond laser sources have been shown to provide a universal ionisation source[25], but are currently prohibitively complex and expensive for many laboratories.

EI is well suited as a universal dissociative ionisation mechanism because the energy is easily tuneable to essentially any desired value, in contrast to the difficulty of achieving photon energies above 10.5 eV. Cross sections can be measured relatively easily and typically show a very smooth and broad energy dependence over many tens of electron volts. However, EI introduces a number of new considerations when employed as the ionisation source.

Firstly, unlike lasers, which can be optically focussed to a very narrow interaction point, the focussing of a beam of electrons is limited due electrostatic, or *space-charge*, repulsion between the electrons. The number of electrons required for appreciable signal levels in a VMI experiment leads to a minimum electron beam diameter of approximately 1 mm and increasing the beam current would cause a significantly larger beam spot. The limitation on beam current, alongside the fact that EI cross sections are typically lower than photoionisation cross section that take advantage of resonant states to improve the yield of ions, means that the EI experiment consequently has a relatively low signal level.

Further, in a typical VMI experiment, the extraction of the ions is performed by holding the ion lenses at static potentials, as neither the neutral molecules/fragments nor the laser pulse is affected by the presence of an electric field. Conversely, the path of an electron is affected significantly by an external electric field due to the low value of *m/z*, requiring the ion lenses to operate in pulsed

mode. Consideration must also be given to creating a suitably short electron beam pulse, ideally with a pulse width of around 10 ns, similar to laser pulses.

However, the biggest consideration is the inefficient nature of the electron collision process in dissociative ionisation. In photofragmentation, the energy of the incident photon is fully absorbed by the molecule. For a molecule in the electronic and vibrational ground state, with knowledge of the photon energy and the states available to the molecule, the resulting state of the molecule can be assigned with a relatively low ambiguity. In EI, the incident electron is likely to deposit only a fraction of the available kinetic energy into the molecule. The inefficient collision means that all states with an excitation energy lower than the incident electron energy can potentially be populated, provided that the transition satisfies the selection rules associated with EI.[26,27] The ion images therefore generally show contributions from a significantly larger number of states than images from analogous photodissociation processes. The analysis of ion images can become far more difficult for even relatively simple diatomic or triatomic molecules.

2 Total Ionisation Cross Section

2.1 Measurement of Total Ionisation Cross Sections

The TICS for a chemical species can be determined experimentally by interacting a known number of molecules with a known number of electrons, and recording the number of ions produced. In passing the electron beam through a volume of the sample gas, the reduction in incident electron current, dI^-, as a result of collisions with the target gas, is proportional to the thickness of a layer or gas sample, dl, the number density of the target gas, *n*, and the incident electron current, I^-, yielding the expression:

$$\mathrm{d}I^- = -\sigma(E) n I^- \,\mathrm{d}l \tag{3}$$

where $\sigma(E)$ is the energy-dependent total ionisation cross section for the molecule. Rearranging the equation and integrating leads to the following:

$$\int_{I_0^-}^{I^-} \frac{\mathrm{d}I^-}{I^-} = -\sigma(E) \int_0^l n \mathrm{d}l \tag{4}$$

$$\ln \frac{I^-}{I_0^-} = -\sigma(E) n l \tag{5}$$

$$\frac{I^-}{I_0^-} = e^{-\sigma(E) n l} \tag{6}$$

Collision with a molecule that results in (e, 2e) ionisation yields a secondary electron and a positive ion. The total positive ion charge can be denoted as I^+. Recognising that charge must be conserved in the system gives $I^- = I_0^- + I^+$, allowing I^- to be substituted, giving:

$$\frac{I_0^- + I^+}{I_0^-} = \frac{I_0^-}{I_0^-} + \frac{I^+}{I_0^-} = 1 + \frac{I^+}{I_0^-} = e^{\sigma(E) n l} \tag{7}$$

The exponential term can be expanded as a Taylor series and truncated to the first term when the quantity $\sigma n l$ is sufficiently small (~1×10^{-3}):

$$1 + \frac{I^+}{I_0^-} = \sum_{k=0}^{\infty} \frac{1}{k!} (\sigma(E) n l)^k \approx 1 + \sigma n l \tag{8}$$

As the number of secondary electrons is relatively small, it is also valid to assume the approximation that $I_0^- \approx I^-$, yielding the following:

$$\frac{I^+}{I^-} = \sigma(E) n l \tag{9}$$

Assuming ideal gas behaviour, $P = nk_BT$, where P is the absolute gas pressure in Pa, k_B is the Boltzmann constant and T is the temperature in Kelvin, yields:

$$\frac{I^+}{I^-} = \frac{Pl\sigma(E)}{k_BT} \tag{10}$$

Measurement of the system temperature, pressure, and ion and electron currents as a function of incident electron energy allows the energy-dependent TICS to be determined. Note that the TICS in this expression is a gross, or total current, cross section, as it accounts for the charge on the ions. This type of measurement is the most common throughout the literature.[16, 28,29]

An ideal experimental determination would ensure that the detection efficiency of both ions and electrons is unity across all required energy and mass ranges. As noted earlier, the measurement of ionisation efficiencies performed using conventional ion sources and mass spectrometers have shown large discrimination effects in the detection efficiency for ions with high kinetic energy[30,31].

2.2 Experimental Considerations

Many EI experiments have different detection efficiencies for ions based upon properties such as the mass, energy or charge of the ion. The differences in detection efficiency, also called *discrimination effects*, can be due to discrepancies in collection efficiency, i.e. ions being excluded from the detector in a non-uniform manner, or due to differences in detection efficiency by the detector in the experiment. In order to produce quantitative and absolute cross section values, any discrimination effect must be minimised and/or thoroughly characterised. These considerations were a crucial element in the instrumentation development and data collection detailed in this thesis, particularly for the velocity-map imaging instrument, described in detail in Section 3, which detects ions using micro-channel plates (MCPs).

The issues of non-uniform collection efficiency have been noted in a number of recent publications and are likely to be responsible for many of the differences seen in experimentally determined PICS measurements throughout the literature.[32,33] For example, sector field mass spectrometers use relatively small extraction slits with weak extraction fields to improve the resolution of *m/z* determination, but may lose ions produced with high KER, i.e. from non-statistical dissociation events or multiple ionisation events, before they are detected. Instruments that use electrostatic optics to focus ions into other small apertures have different focal lengths across different mass ranges and can be another source of collection discrimination.[34,35]

The relative detection efficiency of different ions has also been the subject of considerable discussion in the more recent literature, specifically because most modern scientific instruments use MCPs for

charged particle detection. MCP manufacturers acknowledge various discrimination effects, although often do not provide detailed accounts of such properties. The primary effect is decreasing ion detection efficiency with increasing ion mass and with decreasing energy, which can lead to a significant difference in the signals measured for different ions. Other factors influencing detection efficiency include the incidence angle of the ion and age of the detector.[36,37,38,39]

MCPs detect ions that are accelerated onto the surface of the MCP, and the initiation of primary electron emission resulting from the ions striking the walls of a channel. The channel walls are typically biased at a small angle (<10°) to facilitate the impact. Primary electron emission can be divided into two different contributions; kinetic emission and potential emission. Kinetic emission is due to kinetic energy transfer from the impacting ion to the surface and is dependent on the velocity of the ion. Potential emission is due to the internal energy, charge state or charge density (e.g. X^+ verses X^{2+}) of the ion. Potential emission dominates over kinetic processes at low incident kinetic energies of up to a few hundred electron-volts, whereas in the regime of mass spectrometry in which ion energies are typically well above 1 kV, kinetic processes dominate.[40] The primary electrons begin a cascade of secondary electrons leading to an electron avalanche within the channel, which is ultimately the source of the signal amplification. Using multiple MCPs increases the signal amplification, with achievable amplification factors of 10^4, $10^6 – 10^7$, and $10^8 – 10^9$ for single, double and triple MCP stacks respectively.

Amongst ions extracted using the same potential, discrimination arises from the fact that ions with greater mass are accelerated to a lower velocity and therefore produce fewer primary electrons when interacting with an MCP. The ion detection efficiency can be improved by increasing the extraction potential, and therefore the number of electrons produced, until the efficiency is limited by the sensitive area of the detector, known as the *open area ratio* (OAR). The effect of mass discrimination can therefore be mitigated by operating under high gain experimental conditions, which causes the detection efficiency to be limited by the OAR for all ions of interest. A plot of the detection efficiency as a function of detector bias for He^+, Ar^+ and Xe^+ recorded using a dual chevron-stacked MCP detector by Straub *et al*[38] is shown for different extraction potentials in Figure 4.

As an additional consideration in the use of MCPs, care must be taken to avoid an excessively high ion count rate, particularly if the ions are closely distributed, spatially and temporally. This can result in a saturated gain because charge lost by the channel wall cannot be replenished at a rate exceeding the incident ion flux to that channel, although new materials recently employed in the manufacture of MCPs have a significantly better charge replenishment rate.[41]

For all experiments performed using the velocity-map imaging instrument, described in detail in Section 3, a preliminary image was recorded using a short flight tube and an extraction potential of 7.5 kV to demonstrate that the ions did not exceed the capture radius of the MCP/phosphor detector. This ensured that no high kinetic energy ions were lost due to collection discrimination. The issue of detection discrimination was overcome by the use of ion extraction potentials of 5 – 7.5 kV, in which all of the masses considered have an identical detection efficiency limited by the OAR of the MCPs.

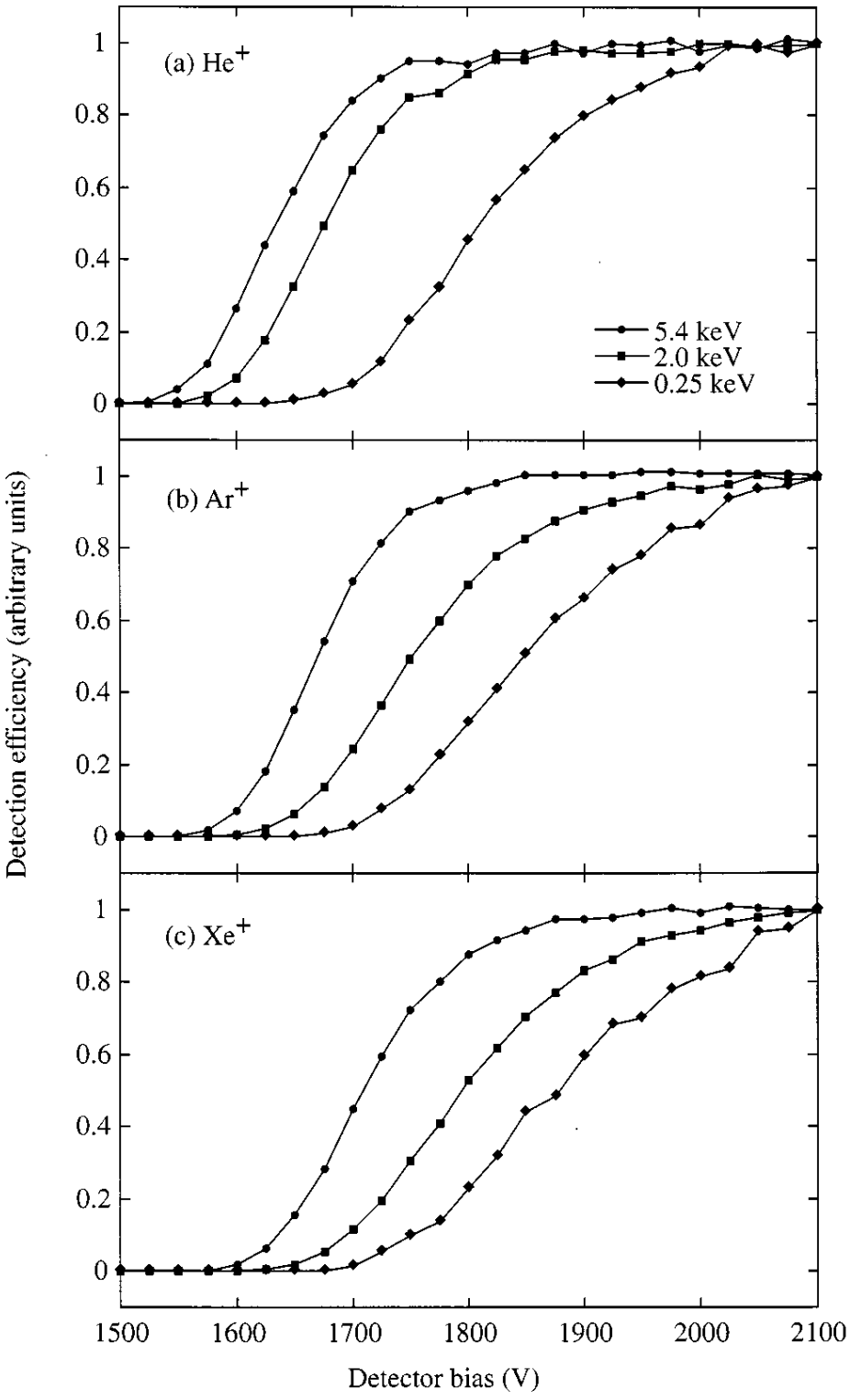

Figure 4 – The detection efficiency as a function of detector bias for He^+, Ar^+ and Xe^+ at various extraction potentials. All curves have been normalised to unity for a detector bias of 2.1 kV. It can be seen that at high extraction potentials and a high detector bias, the detection efficiency of all ions has reached a plateau. Adapted from Straub *et al*[38].

2.3 Experimental Design

The instrument detailed in this section, referred to hereafter as the *TICS instrument*, is a modified rebuilt version of the instrument developed by Peter Harland and co-workers (refs) at the University of Canterbury, New Zealand, which was donated to the Vallance laboratory upon his retirement in 2011. The overall operation of the instrument is illustrated in Figure 5. The ionisation cell, shown in Figure 6, has a length of 35 mm, and is housed inside a square vacuum chamber. The vacuum chamber is evacuated to a background pressure of ~5 × 10^{-8} mbar using a Pfeiffer HiPace 700 turbomolecular pump, which can be isolated from the chamber via a gate valve.

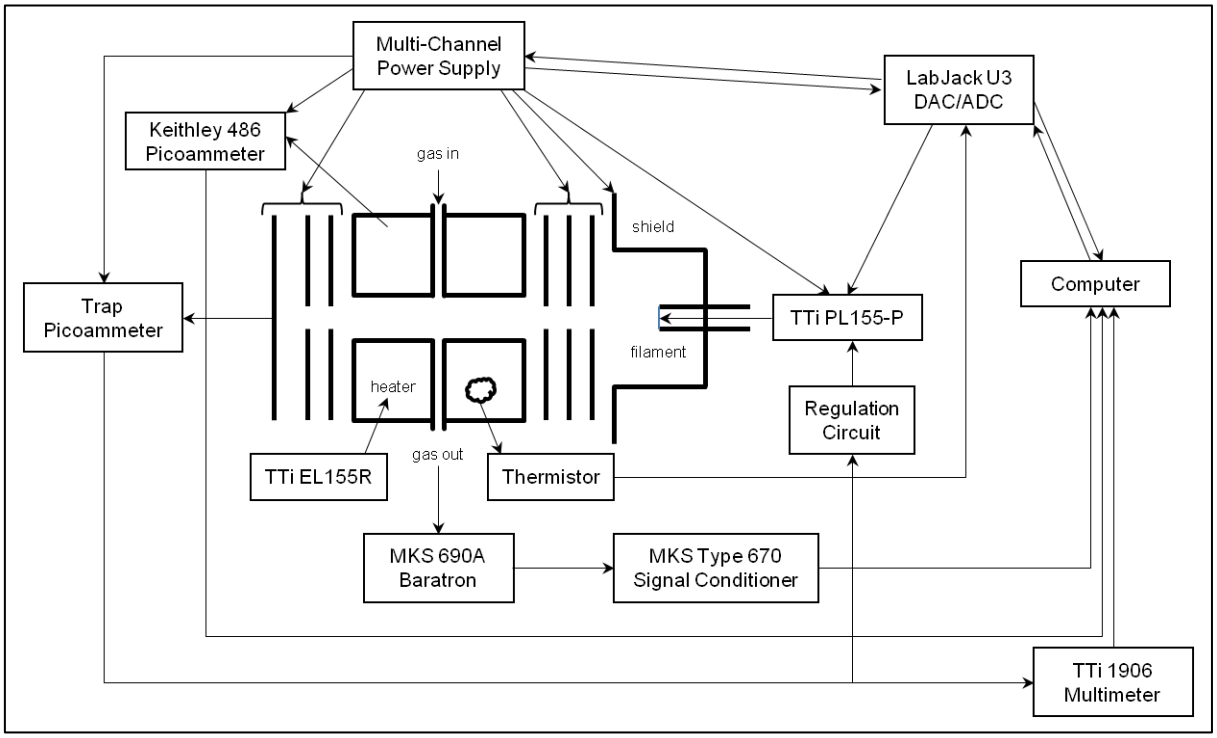

Figure 5 – A representation of the experimental apparatus, showing the connectivity between all components and any computer controlled instruments.

Electrons are generated via thermionic emission from a 50.8 μm diameter rhenium filament biased at the required electron kinetic energy. The filament is coated with $BaZrO_4$ to help reduce the risk of burning out when operated under higher-pressure conditions. The filament is spot welded onto molybdenum pins that are fixed in place by a high-temperature-compatible ceramic block. Electrical current to the filament is supplied by a TTi PL155-P (5 A max) bench power supply, and can be referenced by up to 300 V with a high-current 300 V Spellman module. The emission current density, *J*, can be approximated by Richardson's Law[42]:

$$J = \lambda_{\mathrm{R}} A_0 T^2 e^{-W/k_B T} \tag{11}$$

where k_B is the Boltzmann constant, T and W are the temperature and work function of the metal respectively, λ_R is a material-specific correction factor and A_0 is Richardson's constant, given by:

$$A_0 = \frac{4\pi m {k_B}^2 e}{h^3} = 1.20173 \times 10^6 \text{ A m}^{-2}\text{K}^{-2} \quad (12)$$

where m and e are the mass and charge of an electron and h is Planck's constant. For rhenium, W has a value of 4.85 eV, $\lambda_R \times A_0$ has a value of roughly 100 A cm^{-2} K^{-2} and the operating temperature is 2900-3200 K.[43,44]

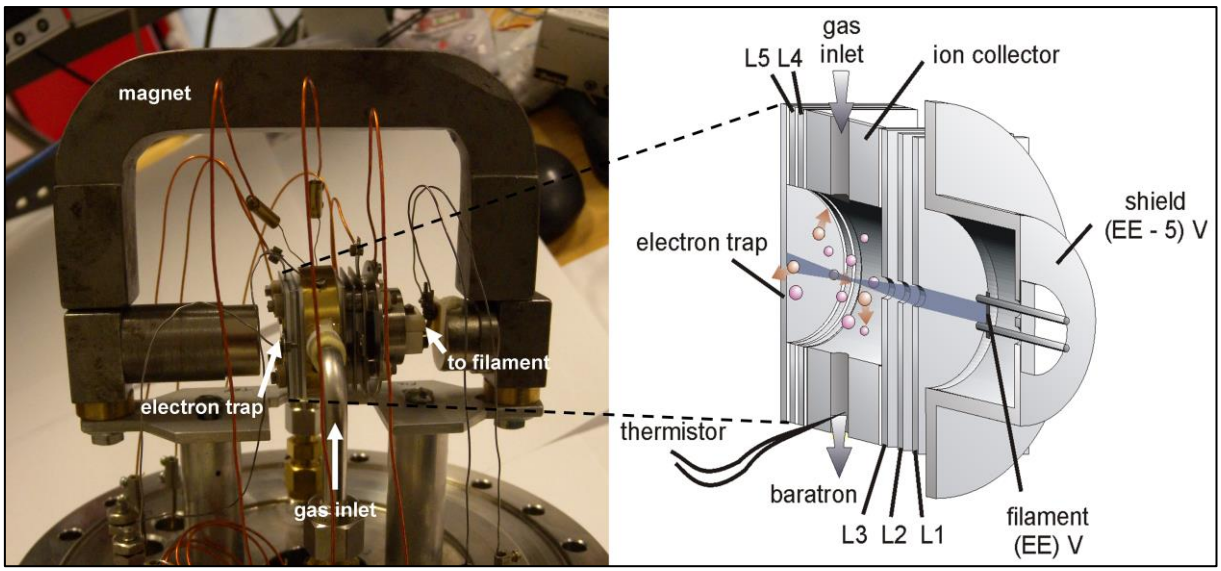

Figure 6 – Left: a photograph of the ionisation cell and rare-earth magnets mounted on a DN160CF flange. Right: a cut-section schematic of the ionisation cell identifying all electrostatic elements. L1-5 refer to electron lenses 1-5, respectively. The length of the cell from the ceramic filament block to the electron trap is 35 mm.

Experiments are typically performed with an electron energy between 15 and 280 V. Below 15 V ionisation cross sections are small, current regulation becomes unstable, and the FWHM energy distribution of the electron beam (around 1 eV) does not permit reliable TICS determinations. Above 300 V, all TICS show typical endoergic decreasing magnitudes due to the fact that, in a classical interpretation, the electron traverses the molecule too quickly to resonantly interact. The FWHM was confirmed to be 1 eV across a range of electron energies by measuring the electron current using a variable retarding potential technique, further detailed in Section 16.1.

Electrons are directed towards the trap using a combination of electric and magnetic fields; electrostatic elements direct and focus the electron beam to the interaction region, and two rare earth magnets of several thousand Gauss field strength assist in magnetically constraining the electron beam to motion along the cell axis. A top-hat shaped "shield" electrode is maintained at a 5 V negative bias with respect to the electron emission energy to assist in electrostatically directing

electrons towards the ionisation cell. Five electrodes, referred to as L1 – L5, of dimensions 25 mm × 25 mm × 1 mm, operate as lenses to focus and direct the electron beam. The first three lenses, L1 – L3, have 1 mm diameter apertures and approximate an Einzel lens configuration, and are typically held at -5 V, -2 V and +1 V with respect to ground, respectively. L3 is held at a slight positive bias to repel ions toward the ion collector. An electron trap at the opposite end of the ionisation cell collects the electron beam. The trap is biased at +10 V and L4 and L5 are held at a slight positive bias to improve the electron collection. The trap is fabricated from 21 carat gold, due to the material properties of high electrical conductivity and the lack of chemical reactivity avoiding oxide layers from forming.

When the potential applied to the filament, i.e. the electron energy, is changed, the electron flux also changes. To maintain a constant electron flux in the experiment at different electron energies, the current impinging on the electron trap is measured and fed to a feedback regulation circuit that adjusts the current applied to the filament appropriately. Typical electron trap currents are regulated to between 30 and 50 nA in order to minimise space-charge effects and also to keep the expression for calculating the TICS valid. This trap current corresponds to filament supply currents of 2.1 to 2.5 A depending on the electron energy.

Ions are created in the “collision region” through the interaction of the electron beam with gas effusively admitted into the ionisation cell perpendicular to the electron beam direction through a variable leak valve (Granville-Phillips Co. Series 203). Vapour from liquid samples is introduced into the apparatus using small sample tubes made of borosilicate glass. The low coefficient of thermal expansion of the glass allows gases and volatile impurities to be removed from liquid samples using freeze-pump-thaw cycles with either acetone/dry ice or liquid nitrogen. The gas pressure of the cell is measured by an MKS 690A Baratron capacitance manometer and is maintained at 10^{-5} - 10^{-4} mbar, depending on the magnitude of the TICS of the species under investigation. The interior of the ion collector is made of brass and is monitored by a computer-interfaced Keithley 486 picoammeter. The high copper content of brass provides very good electrical and thermal conduction properties, although brass begins to outgas by sublimation of zinc under ultra-high vacuum conditions of better than 10^{-8} Torr. The fact that the ion collector surface surrounds the interaction volume promotes near unit detection efficiency. In an experiment, the ion collector is held at a negative bias of 10 V to 15 V, which is sufficient to ensure that all ions are collected, but sufficiently low to prevent the electron energy from being perturbed. This condition was verified through simulations performed using the SIMION 8.0.4 software package.[45] Finally, the ion collector interior surface is coated with a

thin layer of graphite aerosol to prevent incident ions from scattering off and therefore assist in achieving unit charge detection efficiency.

During operation, the rhenium filament emits a significant amount of heat, which is deposited into both the sample gas and the ionisation cell. The temperature of the cell is monitored using a calibrated thermistor embedded in the cell wall. The sample inlet line, valve and connection of the ionisation cell to the Baratron are heated to ~42°C (315 K) using an Omega silicone flexi-variable 240 V heating tape. This matches the average temperature of the ionisation cell and natural operating temperature of the Baratron. The length of tubing connecting the Baratron to the cell is as short as possible to minimise the pressure gradient between the cell and Baratron. Under these conditions the sample gas is assumed to be in thermal equilibrium with the walls of the sample line and ionisation cell during measurements. Two parallel holes drilled along the base of the ion collector allowed thin ceramic rods embedded with nichrome wire to be inserted to act as a heater by passing several hundred milliamps of current using a TTi EL155R power supply.

All wiring connecting the electron trap and ion collector to electrical feedthroughs is made of pure silver wiring chosen for the high electrical conductivity. All other wiring, such as to other lens elements, is solid-core kapton-insulated copper wire.

2.4 Experimental Procedure

The experimental apparatus allows the temperature, electron current, ion current and gas pressure to be measured as a function of electron energy, and therefore the total ionisation cross section can be calculated using the equation given in Section 2.1. Typically, 128 measurements of ion current, electron current, pressure and temperature are recorded and averaged at each electron energy value using the measurement system described in Section 2.5. The full TICS curve for a species is measured at least eight times, and the standard deviation for each series of measurements was always found to be within the 4% instrument calculation error, as shown in the Appendix (Section 16.2).

In studies of non-volatile species, residual sample can accumulate in the sample line causing contamination in subsequent experiments. Therefore, between the measurements of different samples, small quantities of nitrogen are repeatedly admitted and evacuated from the ionisation cell, via the sample line, to remove any remaining non-volatile sample. Residue can also deposit on the surface of the ion collector, which reduces the ion detection efficiency. To monitor these effects, between experiments on different samples, the TICS for nitrogen is recorded. A deviation in the measured values from previously obtained results for nitrogen implies that residual sample is present in the apparatus and that cleaning is required. The ceramic block that holds the filament also

requires regular cleaning to reduce electrical leakage across the surface due to sample build-up and filament boiloff. Additionally, sample deposited on the electrodes can affect the electric fields within the cell, distorting them from their optimum electric field arrangement. As a consequence of these effects, the cell is dismantled, cleaned, and reconstructed approximately every two days when performing measurements on low-volatility species.

2.5 System Measurements and Control

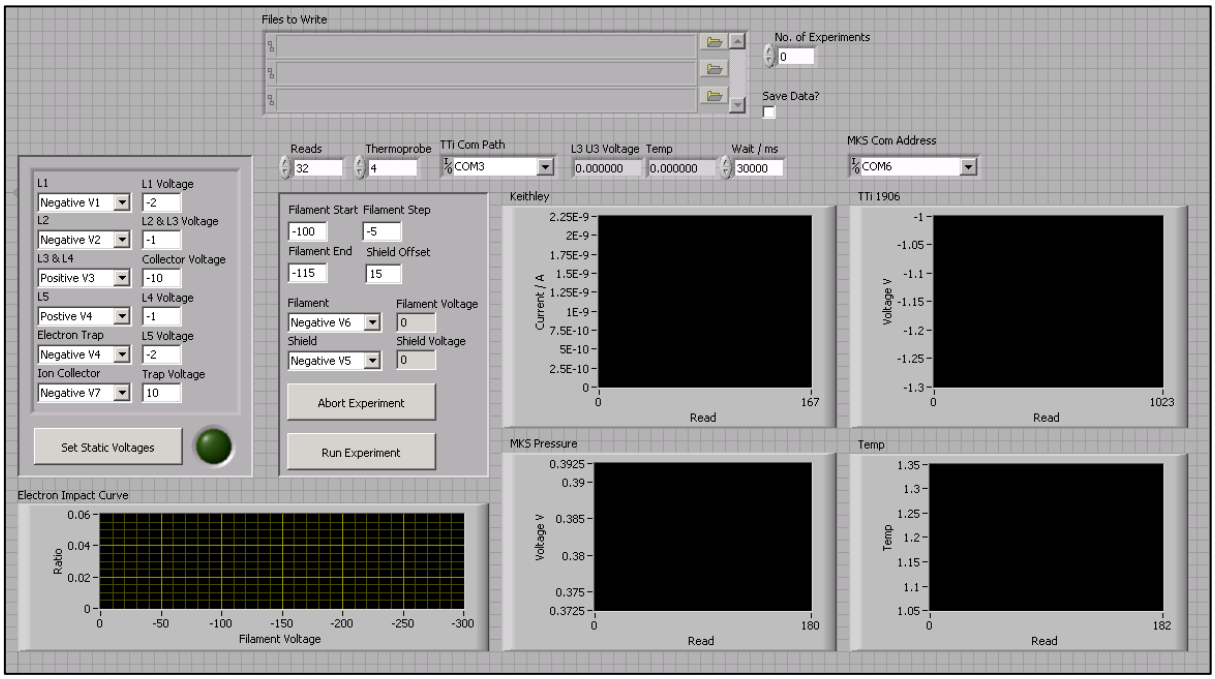

Figure 7 – The front-end of the data acquisition program developed for the TICS instrument. The four plot panels on the right display ion current, electron current, pressure and temperature in real time, and the plot on the bottom left displays the calculated TICS as a function of the energy.

LabVIEW, short for Laboratory Virtual Instrument Engineering Workbench, is a development environment commercially available from National Instruments. The main benefit of the language is the support for accessing hardware instrumentation, combined with automatic memory allocation, parallel processing, code re-use and simplicity of graphical front-end construction. These characteristics mean that developing code to access and control hardware can be performed significantly faster and more easily than with traditional programming languages. A piece of code in LabVIEW is referred to as a Virtual Instrument (VI), and the subroutines that it runs are known as sub Virtual Instruments (sub VIs).

Control of the apparatus and data acquisition was achieved using multiple computer-controlled digital-to-analogue (DAC) and analogue-to-digital (ADC) circuits, as shown in Figure 5. Software was developed to fully automate data acquisition. The software interfaces multiple devices through USB,

RS232, I^2C and GPIB protocols, tied together through a LabVIEW program to create a systematic and comprehensive acquisition routine. The program is controlled through a graphical user interface, or *front-end*, which is shown in Figure 7.

Static voltages (e.g. on the electron lenses) can be set at the beginning of an experiment, and the range and increments of electron energies to be investigated can also be specified. Between each iteration of electron energy, a time delay can be implemented before measurements are taken to allow the system to equilibrate (typically 10 seconds). The program reports the four variables of ion current, electron current, pressure and temperature, plotting the values in real time on four separate graphs. The mean of each of the variables is used to calculate the TICS, which is plotted as a function of the electron energy as the experiment progresses. The electron energy is then changed and the acquisition process is repeated. Experimental results are written to file as the experiment is performed, with the option of repeating the entire experimental run multiple times to improve the statistics and to investigate any experimental variation. This subsection describes the details of some of the systems employed in creating the acquisition system.

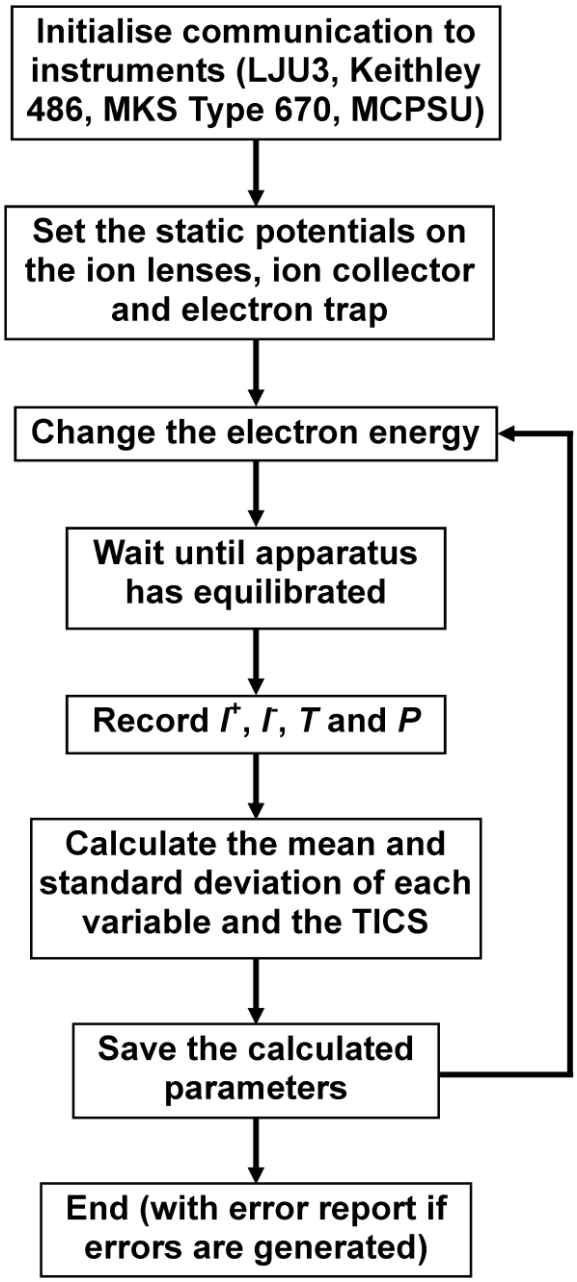

Figure 8 – Summary of the acquisition program under normal operation. If an error is encountered, the program ends and provides an error summary.

2.5.1 LabJack U3

The LabJack U3 is a USB2 interfaced DAC/ADC converter that is responsible for many of the control and acquisition processes within the experiment. The unit is capable of analogue voltage output on two channels, with a range of 0–5 V at 12-bit precision. There are sixteen additional flexible channels that can be used for digital input, digital output or analogue input (0–3.6 V, 10-bit resolution).

One digital output channel and one digital input channel are used to control a custom-built multi-channel power supply (MCPSU) which is used to provide static voltages to many of the internal

components of the TICS instrument. The MCPSU is described in more detail in section 2.5.5. A library of custom LabVIEW drivers was coded to deliver the commands for reading and writing the individual channels of the MCPSU.

One ADC channel is used to monitor the temperature of the cell, as described below. A TTi model 1906 bench multimeter (4 ½ digit) was used to verify the accuracy of the ADC channel. The input voltage to both instruments was incremented from 0.05 to 3.6 V in 0.05 V steps. At each voltage, sixteen measurements were taken by both devices and the mean value and the standard deviation were calculated. The results are shown in Figure 9. Although the LabJack U3 was not able to record lower than 0.25 V accurately, this was below the operating range of the potential divider connected to the thermistor, so was not deemed to be problematic.

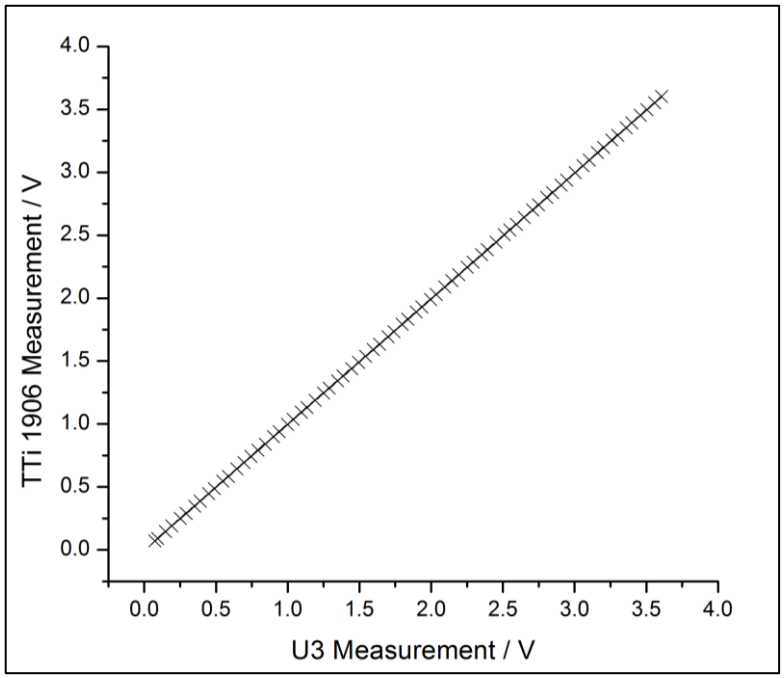

Figure 9 – The LabJack U3 ADC readings and the TTi 1906 multimeter readings for the same output voltage.

2.5.2 Temperature Measurement

As noted earlier, the temperature of the ionisation cell is monitored using a calibrated thermistor embedded into the wall of the brass ion collector. A potential divider circuit was constructed, allowing the potential across one resistor to be measured by an analogue input channel on the LabJack U3. The thermistor was calibrated on the bench by heating and cooling the cell to other temperatures spanning the expected measurement range, and comparing performance with known factory specifications. Conversion of the recorded potential by the acquisition program yields the temperature of the ionisation cell.

2.5.3 Ion and Electron Current Measurement

The ion and electron currents are recorded by a Keithley 486 picoammeter and a second custom-built picoammeter adapted from an electrochemistry potentiostat, respectively. The Keithley 486 is computer-interfaced using a GPIB adapter and controlled using a series of simple read/write commands written in LabVIEW. The custom picoammeter converts current into a potential which is monitored using a RS232-interfaced TTi 1906 high accuracy multimeter with custom LabVIEW drivers. The custom picoammeter was coarsely calibrated using some constant current supplies, and then finely calibrated against the Keithley 486 picoammeter.

2.5.4 Pressure Measurement

The gas pressure is constantly monitored using an MKS 690A Baratron. The signal from the Baratron is read by an MKS Type 670 Signal Conditioner, which is computer-interfaced through an RS232 interface. Custom LabVIEW drivers were developed to facilitate the read out.

2.5.5 Multi-Channel Power Supply Unit (MCPSU)

This power supply was built by the electronics workshop in the PTCL, using a number of recycled Spellman modules. It consists of sixteen independent voltage channels, eight positive and eight negative. The outputs have a 16-bit accuracy and have different ranges; the positive channels consist of four channels with a 0 - 10 V range, three channels with a 0 - 300 V range and one channel with a 0 - 1 kV range. The negative channels have the same range with the opposite polarity. Each output can be manually controlled by an input voltage (0 – 5 V), or computer controlled by an embedded microprocessor that accepts I^2C commands built into the power supply unit. Drivers were developed to deliver commands to the I^2C controller in the MCPSU through two flexible channels, configured for digital input and digital output, on the LabJack U3 (described in Section 2.5.1). The LabJack U3 was controlled via the LabVIEW interface of the acquisition program. The output of each channel can also be sampled to 16-bit accuracy and read out using I^2C commands to the acquisition program. This allows the MCPSU outputs to be constantly monitored, ensuring that the voltages applied within the apparatus remain constant and consistent between experiments. The output and sampling of each channel was tested using the TTi 1906 multimeter in a similar procedure to the method used to test the LabJack U3, and each channel was found to be satisfactorily accurate. The MCPSU is used to apply the following electrical potentials:

- A negative bias on the ion collector walls, through the Keithley picoammeter;
- The positive bias on the trap, through the homebuilt picoammeter;
- The potentials on the electron lenses and shield to direct and focus the electron beam;

- The referencing potential to the TTi PL155-P power supply, which in turn controls the energy of the electrons emitted from the filament.

2.6 TICS Measurements

The TICS instrument has been used to record the TICS for a number of species detailed in the publication by Bull *et al*[46]. The measurements made on molecules that had been previously studied showed excellent agreement with the data in the literature. As an example, the measured TICS for water is compared to the recordings by Straub *et al*[47] in Figure 10. The functional form of the curves recorded is very similar with the main difference in TICS measurement performed at low electron energies where the gradient is steepest. The least squares differences between the curves is minimised by linearly translating the energy axis of one of the curves by 2.9 eV. This matches the combined errors in the electron energy from the two sources, ±1 eV as determined by Straub and approximately 2 eV for the TICS instrument as shown in the Appendix (Section 16.1).

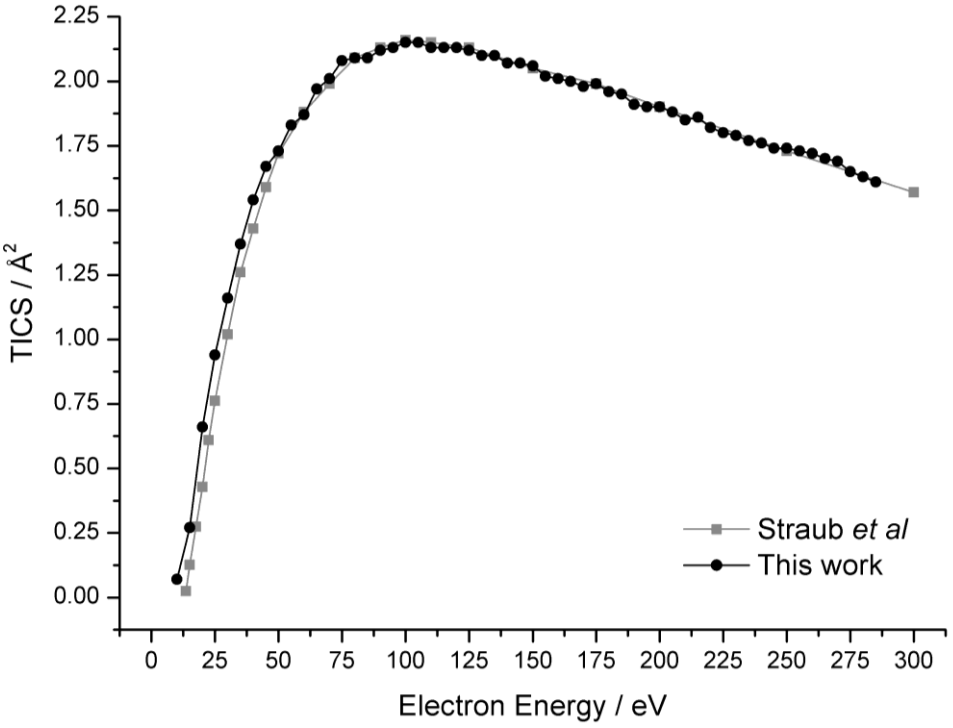

Figure 10 – The TICS recorded for water compared to the measurements performed by Straub *et al*[47].

A subset of the data on newly-studied molecules, namely toluene, benzene, aniline, pyridine and ethylacetamide, is shown in Figure 11. The maximum recorded TICS are compared to values calculated using the semi-classical binary-encounter Bethe (BEB) model[48,49] employing the procedure described by Bull *et al*[50] and the polarizability correlation mode[51,52]. The experimental results are generally in good agreement with the theoretical results, as shown in Table 1, and provide

confidence for using the obtained data for further studies such as the experiment described in Section 4.

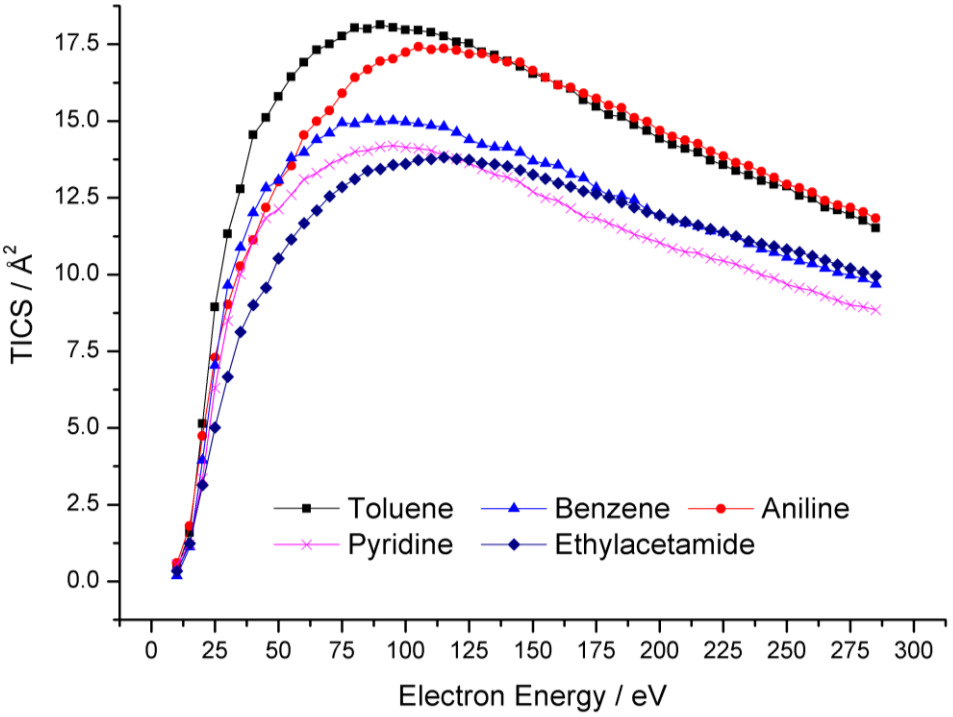

Figure 11 – The TICS recorded as a function of incident electron energy for a series of organic species.

Table 1 – The experimentally determined maximum TICS for the species under consideration, compared to the theoretical maximum TICS calculated using the BEB model and polarizability correlation model.

Species	$\sigma_{\mathrm{expt}}^{\mathrm{max}}$ / Å^2	$\sigma_{\mathrm{BEB}}^{\mathrm{max}}$ / Å^2	$\sigma_{\mathrm{COL}}^{\mathrm{max}}$ / Å^2
Toluene	18.13	17.58	18.14
Aniline	17.42	16.77	17.33
Benzene	15.05	14.61	15.14
Pyridine	14.20	13.43	13.92
Water	2.15	2.29	2.14
Ethylacetamide	13.83	13.94	14.10

3 The Electron Ionisation Velocity-Map Imaging Mass Spectrometer

The electron ionisation velocity-map imaging mass spectrometer (EIVMIMS) is shown schematically in Figure 12. The vacuum system consists of two vacuum chambers: a four-way ISO LF-160 source chamber; and a six-way ISO LF-160 imaging chamber that can be fitted with a flight tube extension. A double layered mu-metal shield can be installed along the length of both chambers to provide magnetic shielding for electron imaging experiments.

The four faces of the source chamber consist of: a source flange with a pulsed molecular beam course (Hannifin-Parker Series 9 general valve) and VMI optics mounted on four parallel alignment rods; a connection to a turbomolecular pump (Pfeiffer Vacuum HiPace 1800), separated by a manual gate valve (VAT Series 140); a dual hot cathode ionisation and Pirani gauge (Pfeiffer Vacuum PBR 260); and the connection to the imaging chamber. The HiPace 1800 turbo pump was intially backed with a Pfeiffer Vacuum Duo 20 M dual-stage rotary vane pump, and later backed using an Edwards EDM18 rotary pump. A Pfeiffer Vacuum TPR 280 Pirani gauge was used to monitor the foreline pressure. The typical base pressure of the source chamber is $\sim 5 \times 10^{-8}$ mbar.

The six faces of the imaging chamber consist of: the connection to the source chamber; an outlet to a second turbomolecular pump (Pfeiffer Vacuum HiPace 700); a second dual cathode gauge (Pfeiffer Vacuum PBR 260); LF-160 to 2¾" CF flange with an attached electron beam source (PSP Vacuum Technology ELS 100); and the MCP-phosphor detector assembly via a LF-160 to 6" CF adapter. The HiPace 700 turbo pump is backed with a Pfeiffer Vacuum Duo 5 M dual-stage rotary vane pump, monitored by a second Pfeiffer Vacuum TPR 280 Pirani gauge. The typical base pressure is $\sim 2 \times 10^{-8}$ mbar. Two opposing faces have windows to permit entry and exit of a laser beam orthogonal to both the molecular beam gas pulse and the electron beam. This allows for future laser or combined laser-pump electron-ionisation-probe experiments.

A gas source system was constructed using Swagelok fittings with a sample reservoir used to contain the molecule under investigation. The pressure of the reservoir is monitored using a Pfeiffer piezo-gauge. Manually controlled heating tape (Omegalux HTWC Series) runs from the sample entry and around the chamber containing the sample reservoir. The reservoir is connected to the pulsed valve mounted on the source flange, where the molecular beam is generated. The valve is operated by a custom-built valve pulsing unit.

All five pressure gauges are monitored through a computer-interfaced Pfeiffer Vacuum MaxiGauge TPG 256 A vacuum gauge controller. Programmable set points with relay outputs were connected into an interlock system to provide vacuum protection for the imaging detector and electron gun. At pressures greater than 5×10^{-7} mbar, the vacuum interlock on the power unit is broken, turning off all sensitive electronics and requiring manual reset.

The beam source, skimmer (2 mm diameter aperture) and ion optics are mounted on four stainless steel alignment rods. A translator (MDC BLM 275-2) allows the molecular beam valve to be translated forwards and backwards by up to two inches in order to optimise the nozzle-skimmer separation. The ion optics are arranged in a typical velocity-map imaging (VMI) arrangement (extractor, repeller and ground), within which the ionisation interaction region lies equidistant between the extractor and repeller. A home-made Faraday plate (coated with graphite spray) with a slight positive bias terminates the electron beam, and the incident current is monitored using a Keithley model 486 picoammeter. The electron beam has a diameter of approximately 1 mm at the interaction region and pulses of 30 ns are achievable. The electron gun and the electron beam pulsing units are described in detail in Section 3.1 and Section 3.2.4 respectively.

Ions that are created in the interaction between the molecular beam and the electron beam are extracted by pulsing the VMI optics immediately after the electron beam pulse has fully traversed the interaction region. The extractor and repeller lenses are pulsed from ground to high voltage, accelerating ions toward the detector, as illustrated in Figure 3, using a pair of Behlke model HTS-101 fast transistor switches with a factory specified rise-time of 8 ns. The ion flight distance from the beam crossing region to the detector is 240 mm in the configuration shown in Figure 12, with the possibility of adding a flight extension tube between the VMI optics and the imaging detector to increase the total flight length to 420 mm.

The ion detector consists of a matched pair of micro-channel plates (MCPs), a phosphor screen and a camera. The two 40 mm diameter MCPs are mounted in a chevron arrangement giving an amplification factor of $10^5 – 10^7$ depending on the voltage applied to each plate. An ion striking the MCPs creates a cascade of electrons, which is detected by a 40 mm diameter P47 phosphor screen. The subsequent luminescence has a 95% decay time of 120 ns (exponential decay time of 70 ns) and can be detected by an ordinary CCD camera to record the image associated with a particular arrival time. A photomultiplier tube (PMT) with a 50 Ω impedance coupled to an oscilloscope (Tektronix TDS 2024B) allows the one-dimensional TOF spectrum to be recorded.

The camera used for the majority of the experiments performed to date is an intensified charge-coupled device (CCD) camera (Photonic Science Mini FDI) with a resolution of 1391 x 1040 pixels. The repetition rate of the camera is between 10-20 Hz depending on the image size recorded, which sets the limit on the overall experiment acquisition rate. Each mass-to-charge ratio in principal can be imaged individually by setting the appropriate camera aperture window. Although the minimum exposure time per frame is 1 ms, the intensifier can be time gated down to a minimum width of 70 ns, resulting in a suitably narrow time interval when the camera is sensitive. In some cases, different ions will have arrival times within 120 ns, i.e. within the phosphor decay time. Each ion with a different mass-to-charge ratio can be individually imaged through pulsing the electrical potential supplied to the MCPs, effectively changing them from an insensitive state to a sensitive state. MCP pulsing was achieved by applying a 500 V pulse to the second MCP with a baseline voltage sitting just below the ion signal detection threshold using a Photek GM-MCP-2 MCP pulsing unit, capable of providing 9 ns duration pulses at 1 KHz repetition rates.

The technique of gating over the arrival times allows high-resolution images to be obtained for a selected ion mass using a CCD camera. However, for large molecules with extensive fragmentation and multiple ion arrival times, the experiments are inefficient as only one ion image can be recorded per experimental cycle. The throughput can be significantly increased using an appropriate multi-mass imaging detector, such as the PImMS sensor, which is described in detail in Part II.

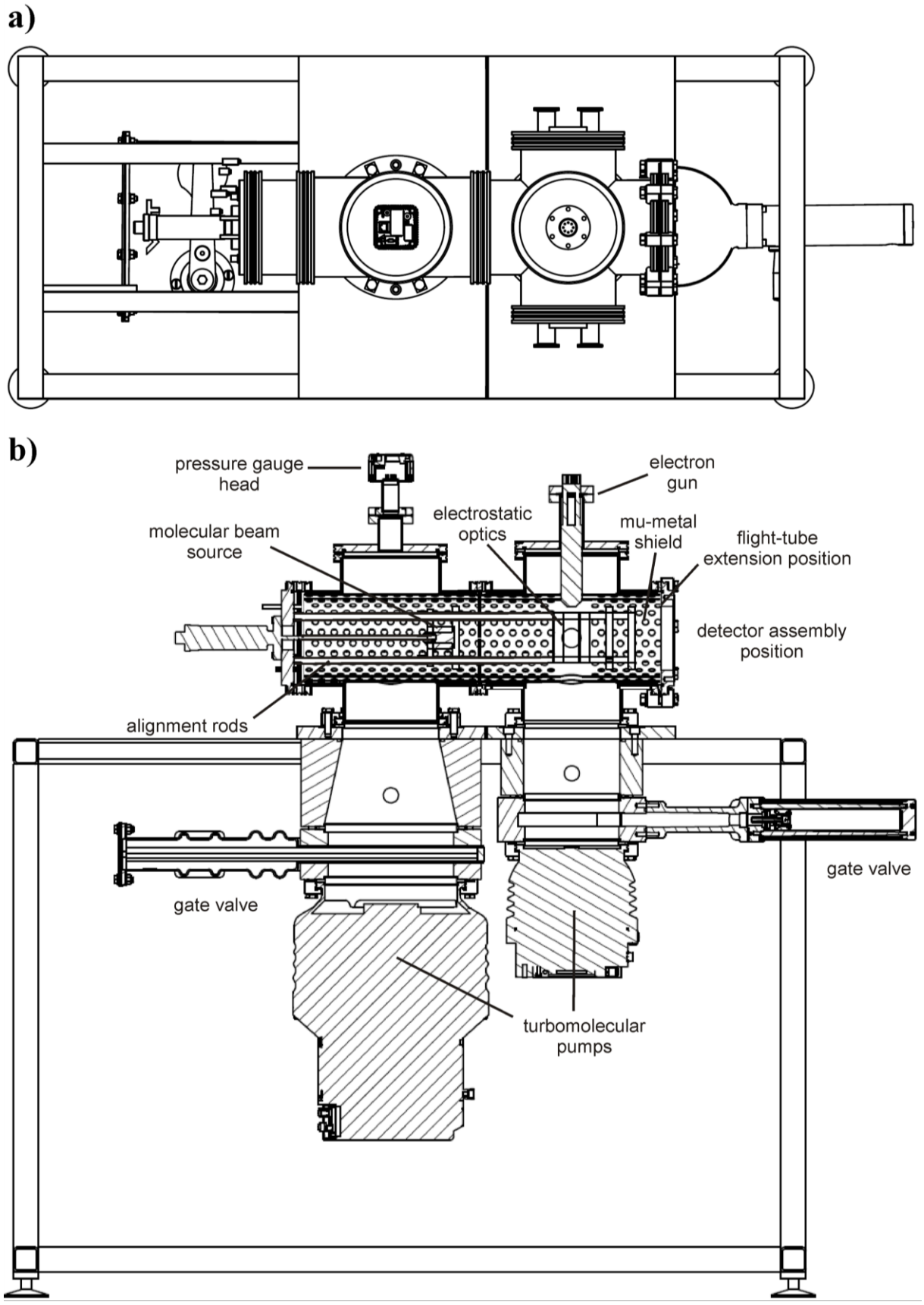

Figure 12 – a) and b) The top view and side section view, respectively, of the EIVMIMS.

3.1 The Electron Ionisation Source

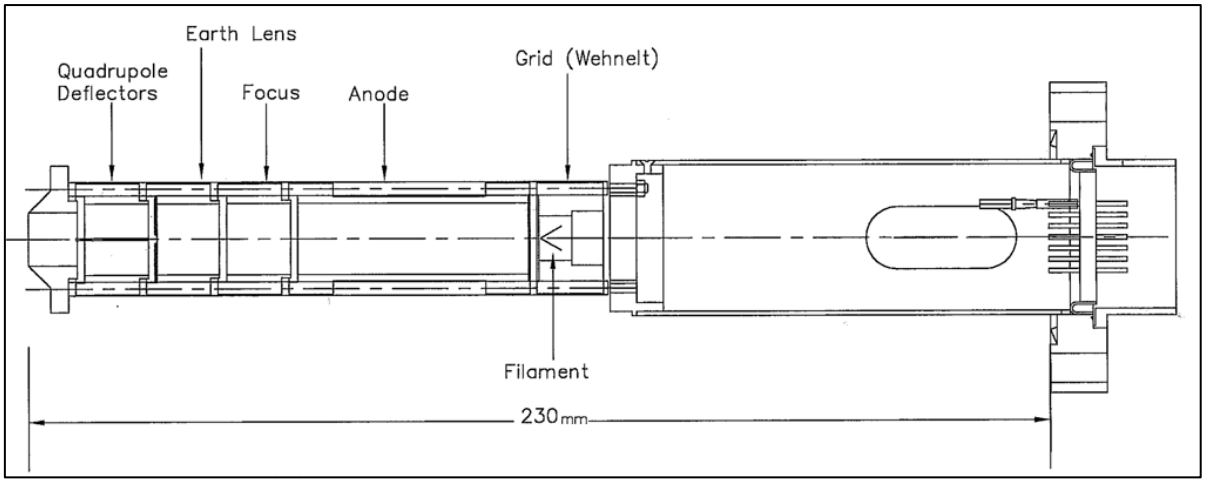

Figure 13 – A schematic illustration of the electron gun, from the ELS 100 user manual.

The ELS 100 is a commercial electron gun manufactured by PSP Vacuum Technology, which provides an electron beam with a continuously tunable energy from 5 – 100 eV. The electron energy can be controlled either manually or via an external reference (0 – 10 V). The external reference was computer interfaced using a LabJack U6 Pro DAC unit (described in Section 3.2.1) and an optically-isolated operational amplifier. The electron energy resolution is specified to be 250 meV (FWHM), and is primarily defined by the properties of the filament source. Electrons are produced by thermionic emission from a LaB_6 single-crystal surface (Applied Physics Technologies, part number 12630). LaB_6 has a work function of 2.36 eV and an operating temperature of approximately 1800 K. $\lambda_R \times A_0$, the constants for Richardson's Law introduced in Section 2.3, has a value of roughly 120 A cm^{-2} K^{-2} so the rate of electron emission should be comparable to that for the rhenium filament.[53]

The crystal in the electron gun has a 16 µm flat diameter and a 90° cone angle, as shown in Figure 14. The shape of the crystal emission point affects the beam current, spot size, and brightness. In general, a small cone angle (60°) results in higher brightness, but a larger angle (90°) provides longer life and easier alignment. The 90° cone angle and a 16 µm flat tip of the crystal in this electron gun provides high brightness, a moderate source size, and a very good lifetime under operating pressures of 1×10^{-6} Torr or lower. Heating of the crystal is performed through "shunts", as labelled in Figure 14, as opposed to heating through the mount itself. This allows the crystal to respond more rapidly to the applied voltage, as the mount does not need to equilibrate in temperature.

The applied current is manually controlled and normally operates between 1.0 – 1.3 A. Space charge effects become apparent in DC beams with currents greater than approximately 1.2 A. The electron gun has a number of internal components (Wehnelt shield, anode, focus, earth) that can be held at a

static current to focus the electron beam, controlling the focal distance and spot size. Additionally, a series of four (quadrupolar) deflector plates, immediately before an earthed exit aperture, allow the beam to be directed.

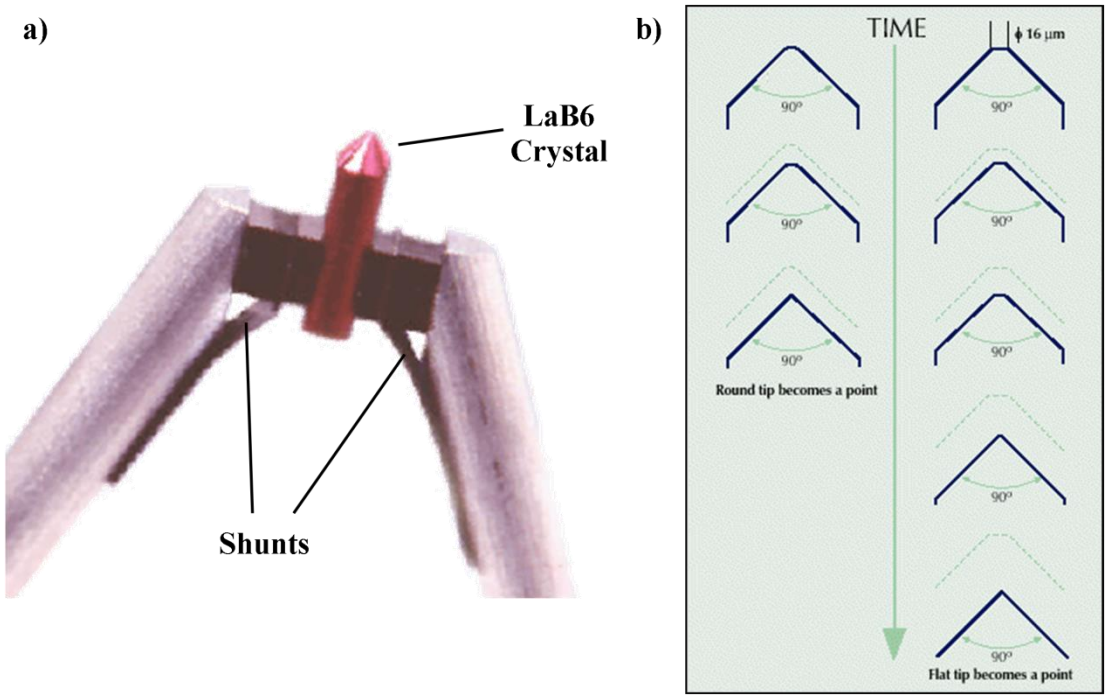

Figure 14 – a) A photograph of the LaB_6 crystal, showing the shunts. b) The crystal tip shape and the degradation of the shape over time. The flattened tip significantly extends the crystal lifetime.

A narrow pulse of electrons is desirable in order to create the smallest possible interaction region with the molecular beam, for reasons discussed in Section 1.2. A model of the electron gun was created in SIMION 8.0.4 to simulate different pulsing methods.[45] Two possible methods were simulated; in the first, the voltage on one of the deflector plates was held constant whilst the voltage on the opposite plate was varied with a triangular wave, deflecting the beam through an aperture, as shown in Figure 15. However, it was found that this was not a feasible approach as the voltages required to cause a deflection would cause a full repulsion of the electron beam toward the source crystal. The second simulation created a pulsing sequence by applying a square wave potential to the earth element shown in Figure 13, where the high voltage was ground and the low voltage was a greater magnitude than the initial potential of the electrons. This causes a complete repulsion of the electron beam when low and allows the beam to pass through the aperture when at ground. This is shown schematically in Figure 16. The pulsing of the aperture assembly required a power supply that could create a square wave with a duration on the order of tens of nanoseconds, able to pulse up to ground from a potential of -100 V or lower. This power supply is described and characterised in section 3.2.4.

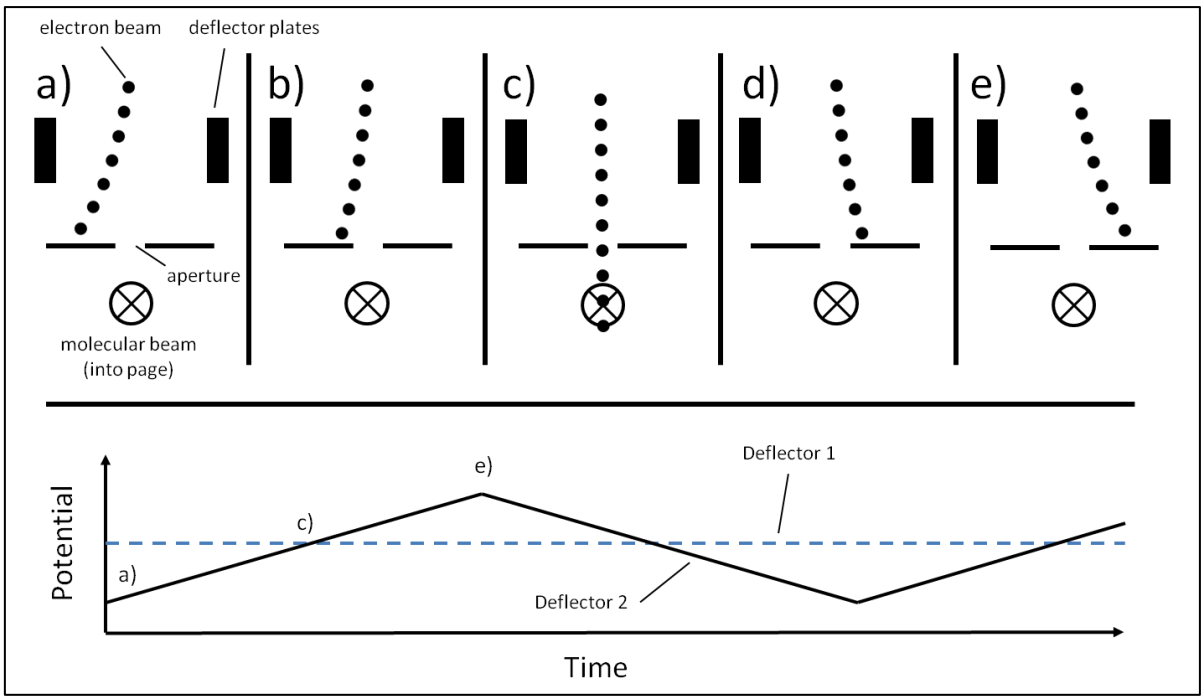

Figure 15 – a)-e) The proposed deflection of the electron beam with a triangular wave applied to one of the deflector plates. The other is held at a constant voltage (represented by the dashed blue line). When the voltages are equal, the beam should pass through the aperture as shown in c).

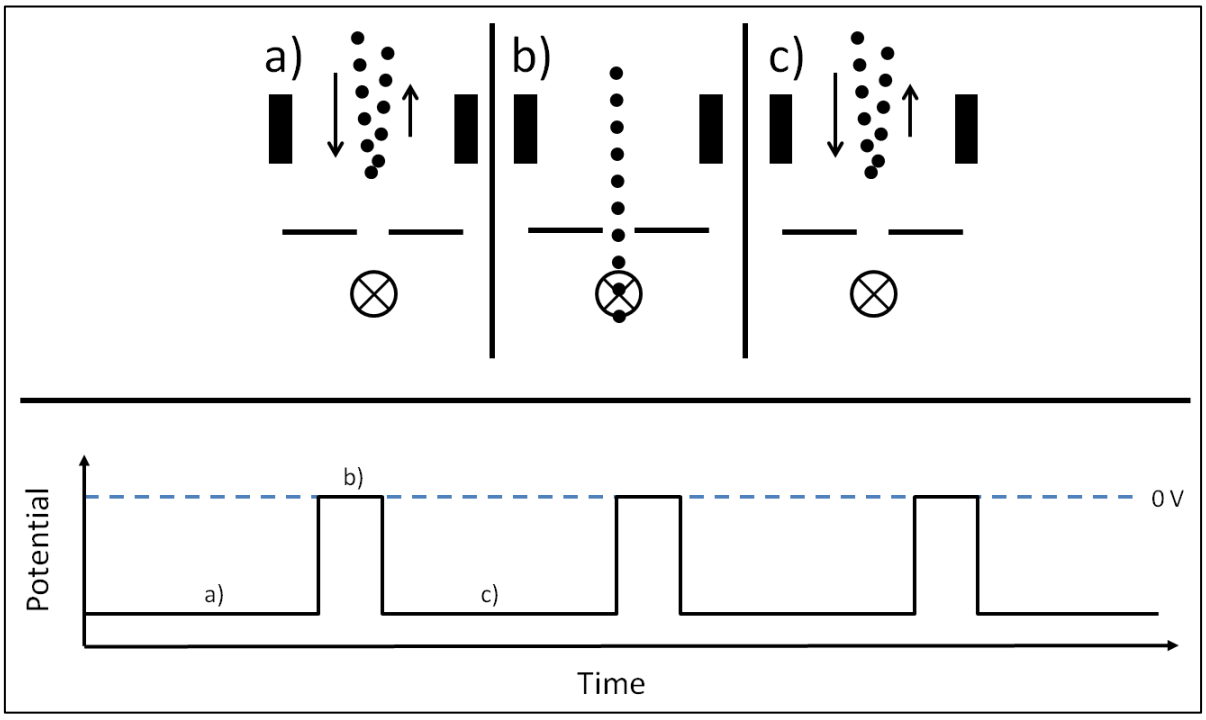

Figure 16 – The proposed deflection of the electron beam with a square wave applied to the earth lens labelled in Figure 13. The voltage is pulsed from a sufficiently negative voltage to repel the electron up to ground to allow the beam to pass through the aperture at the original electron energy.

3.2 Electronic Equipment

3.2.1 LabJack U6 Pro

The LabJack U6 Pro is a USB-interfaced ADC/DAC device similar to the LabJack U3 (Section 2.5.1). The U6 Pro was chosen to control the electron gun energy due to the higher resolution achievable in the ADC/DAC channels. The U6 Pro has two DAC channels (0 – 5 V, 12-bit resolution) and fourteen ADC channels (up to ±10, 18-bit resolution).

The accuracy of the U6 Pro ADC channels was tested using the same method as described for the LabJack U3 and was found to perform satisfactorily. An additional test was performed to determine the accuracy of the DAC channels, which was used to control the electron energy in the VMI experiments. The voltage held on a DAC channel was monitored by both the input ADC channel and the TTi 1906 multimeter. Ten readings of the voltage were taken in the range 0 - 5 V at 0.024 V increments. The results, displayed in Figure 17, showed that the maximum output of the DAC channel was limited to 4.9 V, as opposed to the 5 V that should have been possible.

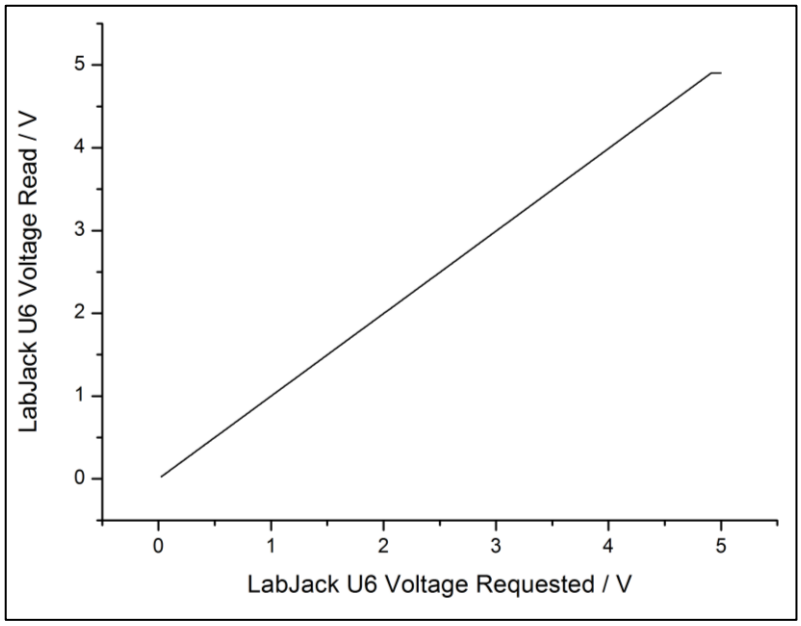

Figure 17 – The LabJack U6 Pro ADC channel measurements as a function of different potentials on a LabJack U6 Pro DAC channel. Note that the full 0 – 5 V output could not be accessed, as evidenced by the plateau at DAC voltages above 4.9 V.

The range 0 – 4.5 V was used as the input for a LM741 tunable operational amplifier, which linearly scaled the potential to 0 – 10 eV. This was then used as the input for the electron gun power supply. The final applied electron energy resolution when controlling the energy with the L6 Pro and operational amplifier was determined to be 25 meV, compared to the specified energy resolution of the electron beam of 250 meV.

3.2.2 Positive & Negative Ion Optics Power Supplies

The acceleration of charged particles toward the detector requires potentials to be applied to the electrostatic optics that constitute the velocity-map imaging lenses. Positive particles require a positive charge on the lens elements, whereas negative particles require a negative charge. To facilitate this, two power supplies, high voltage positive (HVP) and high voltage negative (HVN), were manufactured, with outputs ranging from 0 to +10 kV and 0 to -10 kV, respectively. The pulsing of the ion optics is controlled through another custom trigger unit controlled by a BNC 575 pulse generator.

3.2.3 MCP & Phosphor High Voltage Power Supply

A two-channel power supply based on high voltage Spellman modules was constructed to supply electrical potentials to the MCP/phosphor detector. The channel was capped at maximum values of +2 kV and +5 kV for the MCP and phosphor line respectively. As mentioned in Section 3, the power supply had an interlock system that was controlled by the pressure gauge controller (described in Section 3), allowing power to be supplied to the detector only if the pressure in the detection region was below 5×10^{-7} mbar.

3.2.4 Negative Plate Pulser

The negative plate pulser (NPP) was used to provide a stopping potential to the front of the electron gun. By pulsing the potential to a ground voltage, electrons were emitted from the electron gun, creating a pulsed electron beam, as previously described in Section 3.1. An input voltage on the pulser unit determines the magnitude of the stopping voltage, scaled up by a factor of 100 and was supplied by the LabJack U6 Pro, described above in Section 3.2.1. An input trigger determines when the pulse to ground is applied and the width of the pulse is controlled manually, with a minimum width of approximately 30 ns. The internals of the NPP consist of three metal-oxide-semiconductor field-effect transistors (MOSFETs), one for the overall pulse, one to ‘pull’ the pulse on, and one to ’drag’ the pulse down to the baseline value. Pulsing the electron beam had the effect of slightly changing the beam focus point compared to a DC beam.

3.3 Computer Interfacing

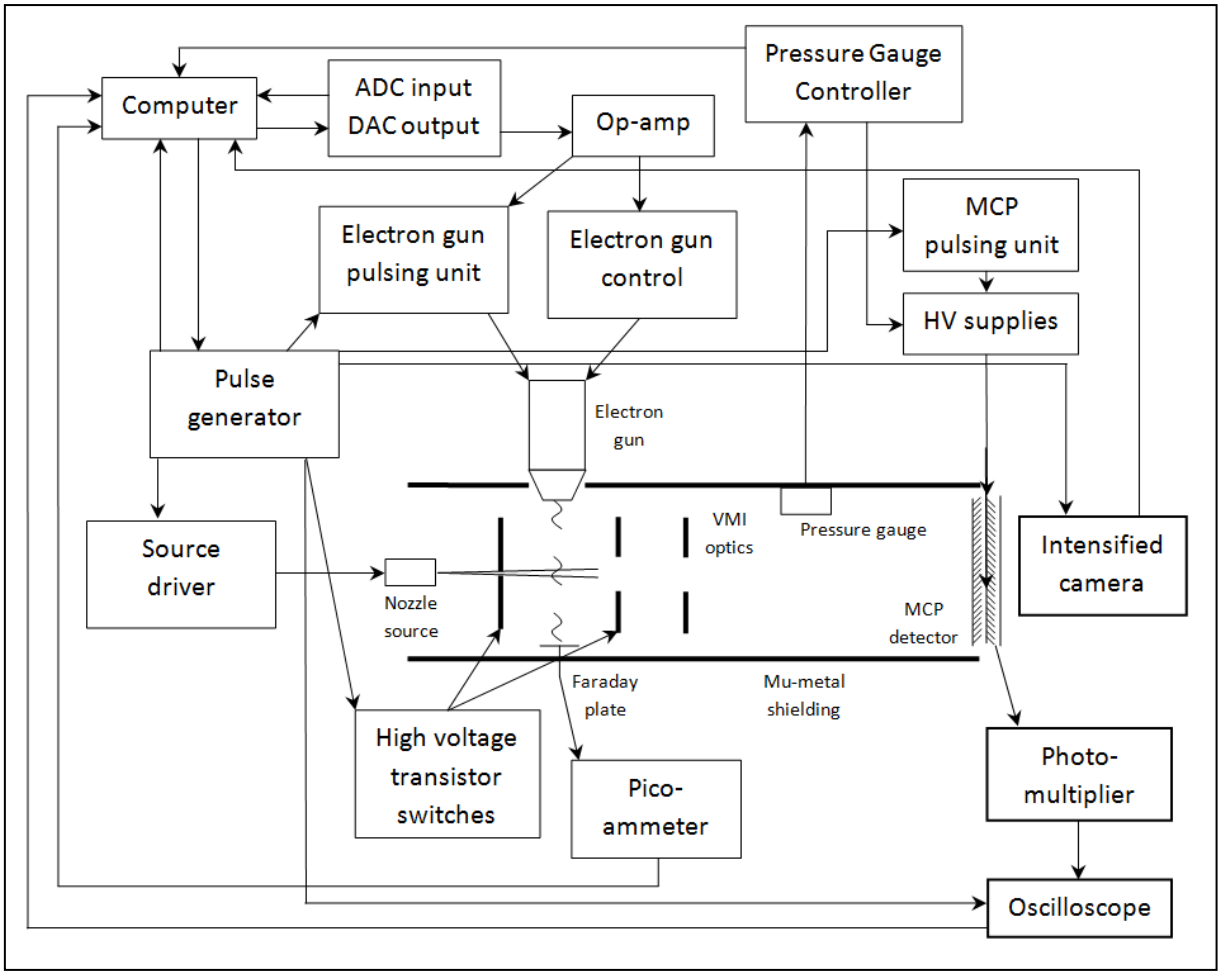

Figure 18 – A schematic representation of the experimental apparatus, showing the connections between all components and any computer controlled instruments.

Many of the electronic components were computer interfaced in order to increase the rate of data acquisition, to allow "on-the-fly" analysis to achieve high quality data through signal averaging. These devices are entirely controlled in a LabView environment, providing a full user interface and online visualisation. Each device has a library of low-level drivers, primarily developed over the last three years, allowing custom programs to be created very quickly.

The intensified CCD camera was interfaced through a Camera Link connection to a frame grabber (PC2 CamLink manufactured by DALSA). The Model 575 pulse generator from Berkeley Nucleonics Corporation and Maxi Gauge TPG 256A pressure gauge were both interfaced via RS232. The LabJack U6 Pro (described in Section 3.2.1) and the TDS 2024B oscilloscope from Tektronix were controlled via USB2 interface. The custom drivers for all devices were written in LabVIEW.

3.4 Image Acquisition Program

Computer interfacing of all the apparatus associated with the EIVMIMS instrument allowed automated acquisition of ion images to be performed 24 hours a day, seven days a week. The acquisition program was developed in LabVIEW utilising all driver libraries noted above. E-mail capabilities allowed the program to inform the users immediately in the event of a vacuum failure. A screenshot of the front-end is shown in Figure 20 and the typical procedure performed is shown schematically in Figure 21. Once a species of interest has been loaded into the sample line, the program is able to record images of all the produced ions at a range of electron energies, adjusting the parameters for the flight times of different ions. For each ion, the user can specify the number of frames to be recorded, the electron energy, the electron stopping voltage, the width and delay of the CCD image intensifier, and the timing of the electron beam pulses, which can be changed appropriately to measure the background image. An ion image is acquired and summed over a number of experimental cycles, typically 100,000 to 500,000 CCD camera frames to achieve an acceptable signal-to-noise ratio. An intensity threshold is applied to each image acquired by the CCD camera to subtract background noise from the CCD sensor. The resulting image is then centroided and event-counted as described below to improve the spatial resolution of the composite image. This process is necessary as the burst of light resulting from an ion impacting the MCP/phosphor detector typically illuminates a number of pixels on the CCD camera. The large spot recorded for each ion causes the recorded ion image to appear blurred.

Centroiding and event-counting are used to improve the spatial resolution of the recorded image. Two methods are employed by the program, both of which are described by Chang *et al*[54] Li *et al*[55]*.* In the first method, the image is scanned for local maxima, each pixel corresponding to a local maximum is assigned a value of 1, and every other pixel is assigned a value of 0. The second method assigns a value of 1 to each pixel with an intensity greater than the specified threshold and assigns a value of 0 to pixels with an intensity below the threshold. The threshold is chosen appropriately to be below the signal level recorded for an impacting ion, but above the general background noise of the CCD sensor. In the resulting binary image, the centre-of-mass of each ion spot is then calculated and assigned a value of 1 and all other contributing pixels are assigned a value of 0.

Both centroiding algorithms are performed in real-time as the images are acquired. The rate of acquisition is not decreased by this relatively computationally demanding task due to the implementation of a queued buffer system for the process to take place, which is displayed pictorially in Figure 19. It should be recognised that this method of image analysis yields the counting

cross section as defined in Section 1.1.1, provided that count rates are sufficiently low that ion signals do not overlap spatially on the detector.

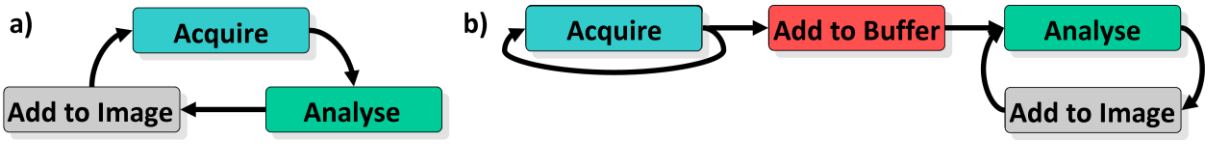

Figure 19 – The schematic difference between performing the centroiding analysis: a) consecutively after image acquisition; b) in parallel.

Once the ion image has been collected, the data is immediately saved locally and is also sent via e-mail to a back-up server and to the users. The program then loads the parameters for the next experiment and repeats the procedure after a specified delay period until the list of experiments is completed. Due to the relative stability of the experiment and the fact that minimal user supervision is required (in contrast to a laser-based experiment), the automated program can be used to record different ion images continuously for several days. Continuous measurement on the instrument vastly increases the experimental throughput, helping to overcome the issue of low signal associated with EI that is discussed in Section 1.2.2.

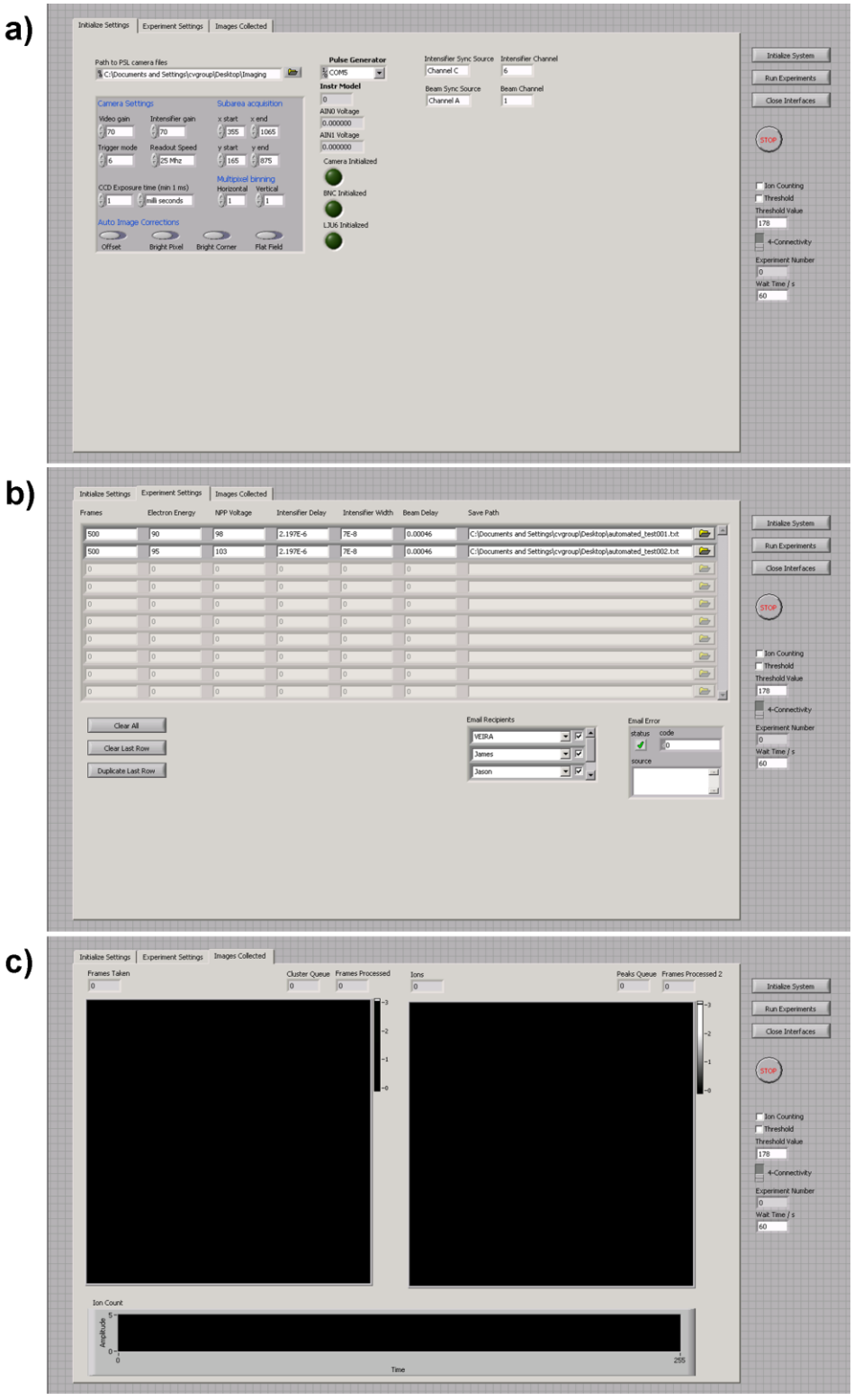

Figure 20 – Screenshots of the automated VMI Acquisition program in the three main states. a) Initialisation of the communication channels to the various pieces of hardware controlled in an experiment. Green lights indicate that the interface has been established successfully. b) Experimental parameters are entered by the user, allowing multiple experiments to be performed automatically. c) Real time display of the image currently being acquired. The two displays show the composite images that have been processed via the two different centroiding techniques described in the text. The graph at the bottom shows the ion count acquired per experimental cycle in real time.

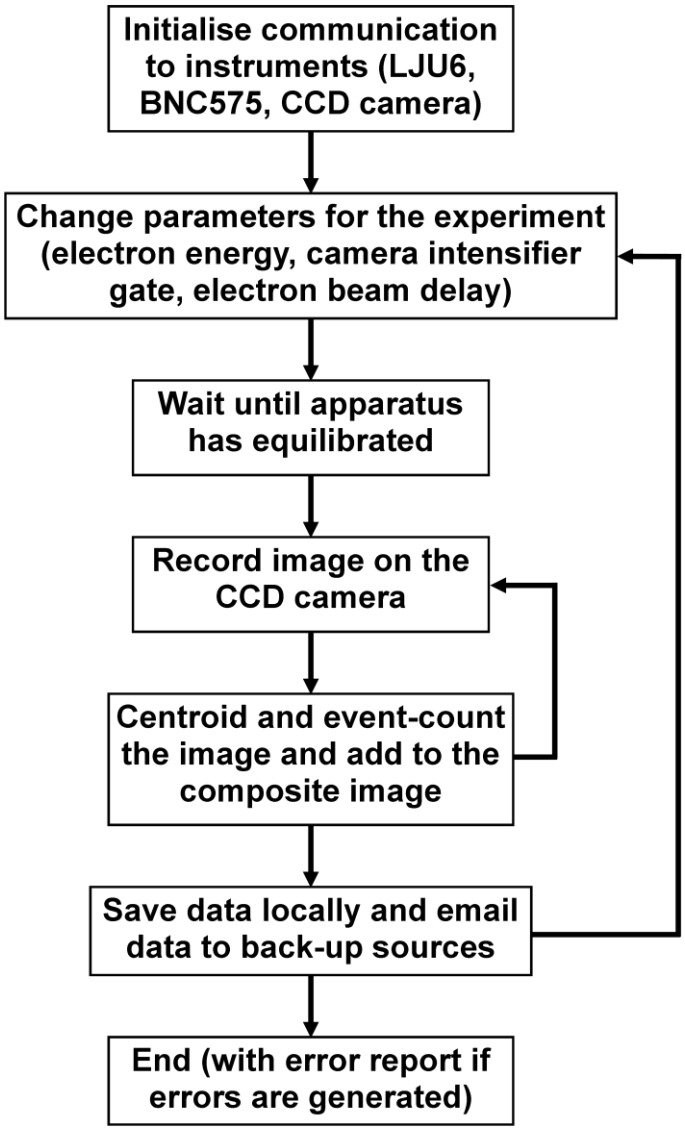

Figure 21 – The procedure performed by the acquisition program under normal operation. The program will end if an error occurs at any point, generating an error report if so.

3.5 Image Analysis

The recorded ion images are usually processed using the polar onion-peeling (POP) algorithm developed in the laboratory of Verlet[56]. The algorithm reconstructs the full three-dimensional fragment distribution from the two-dimensional image of the compressed Newton sphere and is applicable in systems exhibiting cylindrical symmetry around an axis parallel to the projection plane. The image is first converted from Cartesian to polar coordinates by overlapping the image with a polar grid with pixels that are a similar size to the original Cartesian pixels. The intensity of the pixels in polar coordinates is calculated from the original image taking into consideration the contribution of Cartesian pixels based on the degree of overlap. This conversion process means that the level of noise is increased near the centre of the image. Integrating the polar image with respect to the radial

coordinates yields the convoluted radial spectrum, i.e. the intensity distribution as a function of pixel number from the centre of the image. The convoluted radial spectrum shows the velocity distribution of the three-dimensional Newton sphere that has been projected onto the two-dimension detector.

The central slice of the Newton sphere, as described in Section 1.2, contains the information of interest. To extract the central slice, the outermost pixels in the image, which correspond to the outside of the Newton sphere, are fitted to the following function:

$$I(\theta) = N(r) \sum_{n} \beta_n(r) P_n[\cos(\theta)] \tag{13}$$

where $I(\theta)$ is the intensity as a function of angle, and $P_n[\cos(\theta)]$ is the n^{th} order Legendre polynomial. The fitting yields $N(r)$, which is an intensity factor, and $\beta_n(r)$, which are the (velocity-dependent) anisotropy parameters. The fitted contribution of the outer shell of the Newton sphere to all the inner pixels constituting the crushed image is then subtracted from the complete image. Next, the set of pixels that is next furthest from the centre of the image is fitted to the same function and the contribution is subtracted for all pixels contained within the radius. Repeating this procedure until the centre of the image is reached produces the desired two-dimensional slice of the Newton sphere. Performing a radial integration yields the velocity distribution of the ion, which can be converted to kinetic energy distribution using a known calibration factor. In order for the POP algorithm to work, the entire Newton sphere must be recorded by the detector, i.e. no ions can exceed the dimensions of the MCP, otherwise the contribution from the highest KER ions cannot be subtracted from the signal nearer the centre of the detector.

3.6 Electron Ionisation Images

Images of N^+ and O^+ from the dissociation of N_2 and O_2, respectively, were recorded using the EIVMIMS over an electron energy range of 35 – 100 eV. In both cases, the gas was supplied by BOC with a >99.9% purity. Images were recorded under the same velocity-mapping conditions for the two gases with both the 240 mm and 480 mm flight paths. Using a short flight path allowed the complete KER distribution to be recorded and using a longer flight path increased the spatial resolution of the region associated with low KER, which was useful as the images contained many features. A full interpretation is currently in preparation for publication; presented here are the ion images recorded at 100 eV for N^+ and O^+ in Figure 22 and Figure 24 respectively. The radial integration representing the convoluted KER distribution are shown for N^+ and O^+ in Figure 23 and Figure 25 respectively.

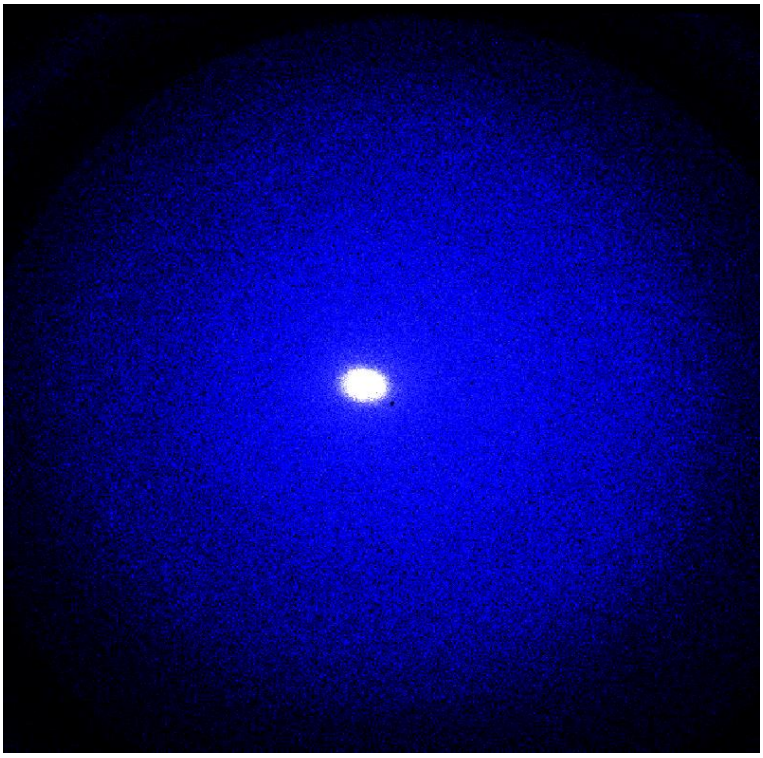

Figure 22 – The ion image recorded for N^+ and N_2^{2+} from EI of N_2 at an electron energy of 100 eV. N_2^{2+} has an identical value of *m/z* as N^+, and is responsible for the bright area in the centre of the image.

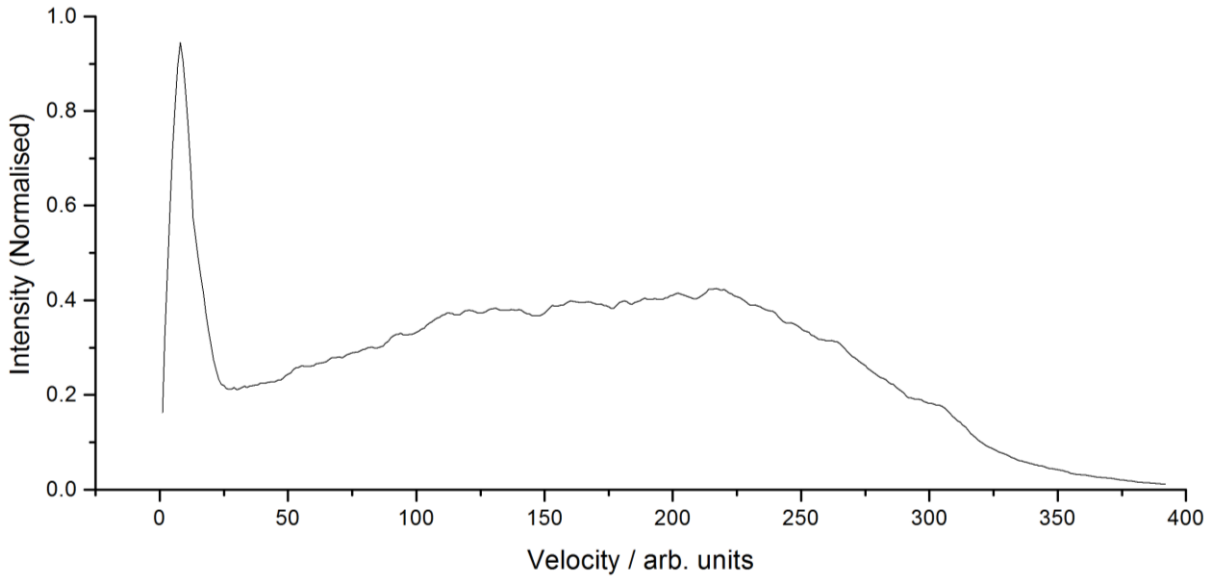

Figure 23 – The normalised convoluted velocity profile extracted from the ion image shown in Figure 22.

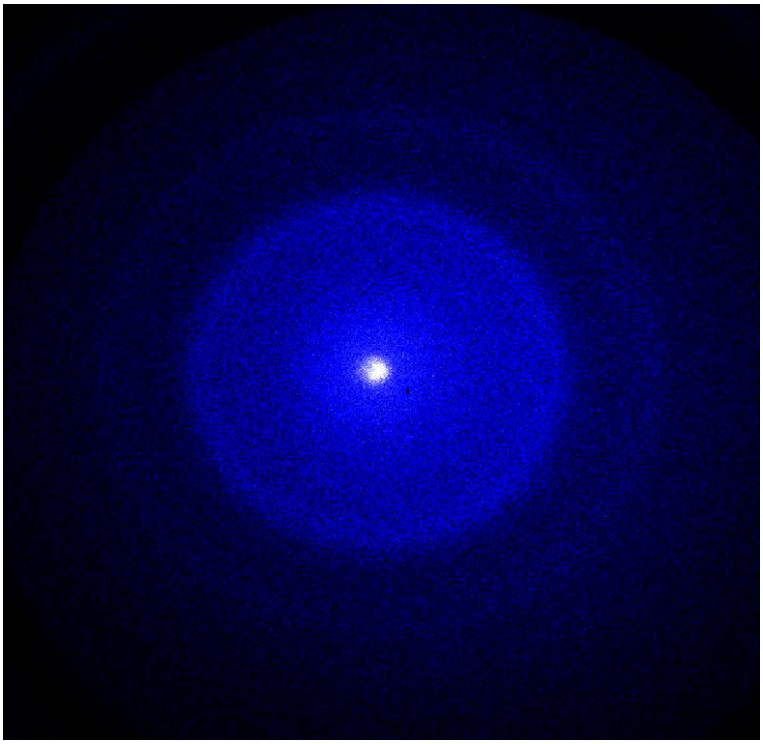

Figure 24 – The ion image recorded for O^+ and O_2^{2+} from EI of O_2 with an electron energy of 100 eV. O_2^{2+} has an identical value of *m/z* as O^+, and is responsible for the bright area in the centre of the image.

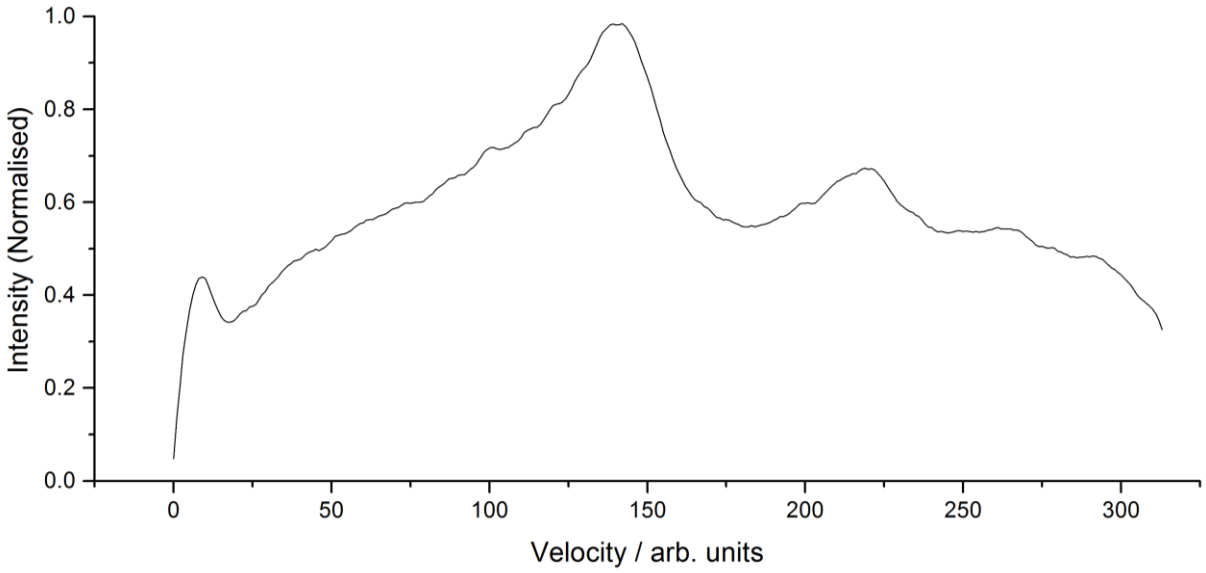

Figure 25 – The normalised convoluted velocity profile extracted from the ion image shown in Figure 24.

4 The Electron Ionisation of CO_2

Carbon dioxide (CO_2) constitutes 0.04% of the Earth's atmosphere and is the most abundant molecule in the atmospheres of Venus and Mars, accounting for over 95% by volume on both planets.[57,58] The molecular properties and dynamics of the CO_2 molecule have become increasingly topical and the subject of many studies in recent years due to the vast evidence linking the level of CO_2 to the global warming and climate change processes.[59] Study of CO_2 is also of interest from the viewpoint of chemical physics as it is one of the simplest polyatomic molecules, composed of three atoms in a linear and symmetric arrangement. The aim of the present study was to use data from the instruments described in Section 2 and Section 3 to provide an insight into the ionisation dynamics using a combination of the TICS, PICS, and KER distributions.

A number of ionisation cross section measurements have been previously reported for CO_2, many of which have been summarised in the reviews of Itikawa[60], Lindsay and Mangan[14], and Raju[61]. Recommended in these reviews are the TICS and PICS measurements of Straub *et al*[62]. Their experimental apparatus, shown in Figure 26, is now briefly detailed.

The experiment is housed inside an open-architecture chamber, which is effusively filled with the sample gas of interest to a pressure of around 3×10^{-6} Torr. An electron beam is pulsed into the interaction region with 20 ns electron bursts. Ions are formed along the length of the electron flight path and approximately 200 ns after each electron pulse, a 3 kV pulse with a 55 ns rise time is applied to the top plate, accelerating positive ions to the grounded bottom plate. The ions that pass through the grid-covered aperture in the bottom plate are accelerated to 5.4 keV by applying a potential to the grid. A 25 mm diameter dual MCP detector is used to detect the ions. The detector samples a proportion of the ions that is assumed to be representative of the ions formed in the electron beam path. The total number of ions formed along the electron beam path is found by scaling the number detected on the MCP by the ratio d/l, where l is the total path length of the electrons through the sample gas and d is the diameter of the MCP detector.

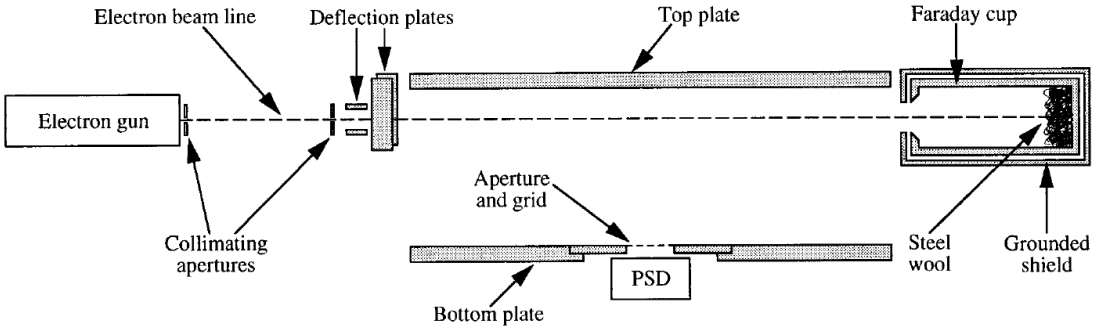

Figure 26 – Schematic illustration of the instrument used to record the EI TICS and PICS for CO_2 by Straub *et al*[62]. PSD refers to the *position-sensitive detector*, which was a 25 mm diameter dual MCP detector.

Utilising the position-sensitive aspect of the MCP detector ensures that no high KER ions exceed the dimensions of the detector in the direction perpendicular to the electron flight, as it can be demonstrated that no ions are recorded at the edge of the detector. An example of the signal collected for O^+ ions produced by EI of CO_2 at 1000 eV electron energy is shown in Figure 27. Additionally, the signal was remeasured using a 40 mm diameter MCP detector and was shown to reproduce the cross sections within error. Absolute values for the cross sections are obtained by calibrating the detection efficiency of the grid and MCPs by repeatedly directing an ion beam alternatively onto the detector and into a second Faraday cup. The efficiency was found to be 37.8%, from a grid transparency of 65% and an MCP efficiency of 58%.

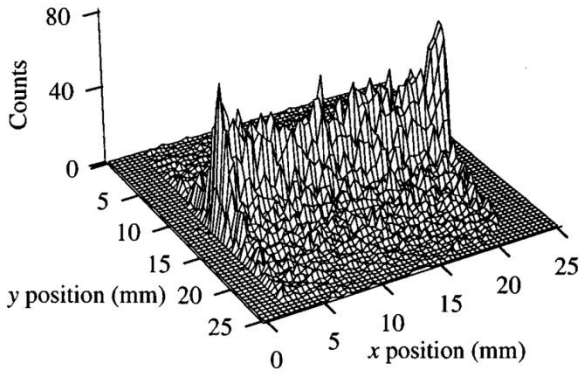

Figure 27 – The position distributions recorded for O^+ ions produced by 1000 eV EI of CO_2, showing complete collection efficiency. The electron beam is parallel to the *x* direction. Figure adapted from Straub *et al*[62].

The EI TICS for CO_2 was recorded previously on the original version of the instrument described in Section 2 by Hudson *et al*[63]. The electron beam current was regulated to approximately 75 nA and measurements were made from 15 eV to 250 eV. The experiment had a background pressure of 5×10^{-7} Torr and a cell pressure of 3×10^{-4} Torr during sample measurement. The TICS curve is shown in

Figure 28, with a maximum value of the cross section found to be 3.74 Å^2 at 125 eV. The curve is compared with measurements made by Straub *et al* showing a maximum TICS of 3.66 Å^2 at 100-120 eV with a 7% error for energies below 25 eV and 5% error above 25 eV.

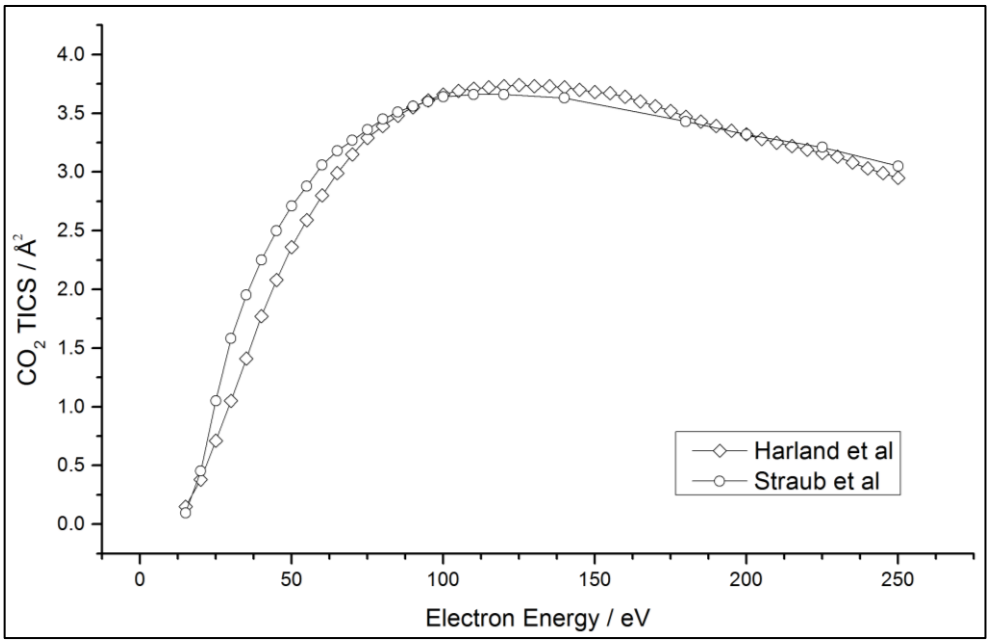

Figure 28 – The TICS for CO_2 recorded by Hudson *et al*[63] and Straub *et al*[62].

The KER distributions for CO^+, O^+ and C^+ have been previously recorded by Velotta *et al*[64] and Locht and Davister[65]. The experimental apparatus of Velotta is shown in Figure 29. An Ar-CO_2 mixture at 9×10^{-5} Torr was interacted with a pulsed electron beam of 50 ns width. The extraction voltage was switched on 2 μs after the electron beam had cleared the interaction region and ions were admitted to the drift tube through a 1 mm aperture. The drift tube was maintained at a negative potential of 546 V to bias ions toward the detector, which consisted of an electron multiplier read by a time-to-amplitude converter and multi-channel analyser (TACMCA) described by Esposito *et al*[66]. The electronics were capable of recording the ion flight time with a time resolution of 1.1 ns. The KER distribution was inferred through the deconvolution in the recorded TOF distribution, assuming that any deviation from a completely uniform flight time was the result of kinetic energy released along the flight axis.

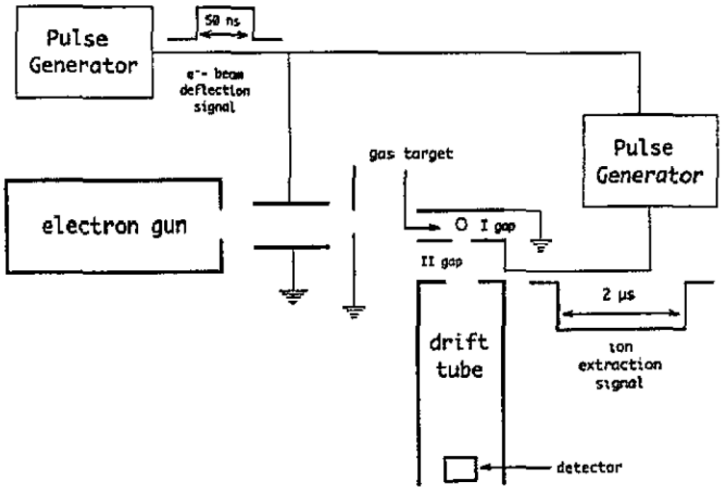

Figure 29 – A schematic representation of the experimental apparatus used by Velotta *et al*, adapted from their publication[64].

The apparatus used by Locht *et al* is described in detail in a previous publication by Locht and Schopman[67]. Ions produced in a Nier-type ion source by the electron ionisation drift out of the ion chamber and are focussed on the ion source exit slit. Ions that possess sufficient energy to pass through a retarding lens are accelerated into a quadrupole mass spectrometer and the ion current is collected on a 17-stage Cu-Be electron multiplier. The ion current is measured as a function of retarding potential at fixed electron energies between 20 and 99 eV with a pressure of approximately 2×10^{-6} Torr of CO_2 in the ion chamber.

4.1 Experimental

The experimental data shown in the rest of this chapter was recorded using the previously described EIVMIMS instrument. The molecular beam consisted of pure CO_2 with a stagnation pressure of 2.5 bar, admitted to the apparatus through the general valve at a repetition rate of 15 Hz. Measurements were made for electron energies between 35 eV and 100 eV; below 35 eV, the combination of the reduced electron current from the electron gun and the low cross-section of CO_2 led to a very weak signal for the daughter ions.

The ion TOF spectrum was recorded at electron energies between 35 eV and 100 eV in 5 eV increments using the photomultiplier measurement of light from the phosphor screen, and visualised on an oscilloscope. TOF spectra were recorded with repeller potentials of 5.000 kV and 7.000 kV, and extractor potentials optimised to achieve velocity-mapping conditions. In both instances, the TOF spectrum was averaged over 1024 recordings at each electron energy. Discrimination effects on the detection efficiency at different masses at these extraction potentials are not expected. Background spectra were recorded at the same electron energy for the same number of experimental cycles,

immediately after the TOF spectra were recorded in order to minimise the effect of experimental variation (e.g. from a change in the stagnation pressure). The background measurements were performed under the same experimental conditions, although with the electron and VMI extraction pulses synchronised so that the electron pulse cleared the interaction region before the molecular beam pulse was present.

The ion images were recorded using the Photonic Science Mini FDI CCD camera at electron energies of 35 eV and between 40 eV and 100 eV in 10 eV increments. The repeller and extractor lens voltages were set at 5.000 kV and 3.550 kV respectively for all images and the centroiding algorithm described in Section 3.4 was applied to all frames recorded by the CCD camera. The ion flight length was 23 cm. Ions of a selected *m/z* were isolated using the MCP pulsing unit set to a gate of width 70 ns centred at the ion arrival time of interest. The ion images for CO^+, C^+ and O^+ were accumulated over 500,000 experimental cycles at electron energies between 50 and 100 eV and 1,000,000 experimental cycles at 40 eV and 35 eV. The image of the parent ion, CO_2^+, was only recorded at 100 eV; the velocity distribution does not change at different electron energies and the image recorded should be representative of the velocity distribution within the molecular beam. The strong signal levels allowed an image to be collected over 10,000 experimental cycles. The image of CO^{2+} was recorded only at 100 eV over 2,500,000 experimental cycles. All background measurements were accumulated over half of the number of experimental cycles as the signal measurements, i.e. 250,000 experimental cycles if 500,000 experimental cycles were recorded for the ion image, and scaled appropriately prior to background subtraction.

4.2 CO_2 TICS and PICS Measurements

The ion TOF spectra recorded at different electron energies with a repeller voltage of 7.5 kV are shown in Figure 30a). The spectrum recorded at 100 eV with a repeller voltage of 7.5 kV is shown in Figure 30b) with the ion flight time converted to *m/z* to allow ions to be more easily identified. It can be seen that a small amount of Ar is present as a background gas, providing a contribution of Ar^+ to the spectra due to the relatively large cross section (2.49 $Å^2$ at 70 eV).[68]

It is assumed that the arrival time distribution for a given ion mass is determined primarily by the focusing properties of the extraction field, and therefore that ions have a similar arrival time distribution at different electron energies. In the present work these are modelled as Gaussian functions. In the experimental data, each mass peak also has an exponentially decaying 'tail' resulting from the finite emission time of the phosphor screen in the imaging detector. The recorded ion peaks were therefore fitted to Gaussian functions convoluted with an exponential decay using the function:

$$y = y_0 + \sum_n \frac{A_n}{t} \exp\left[0.5 \times (w_n/t)^2 - (x - x_{c,n})/t)\right] \times \frac{\mathrm{erf}\left(z_n/\sqrt[2]{2}\right) + 1}{2} \quad (14)$$

$$z_n = \frac{x - x_{c,n}}{w_n} - \frac{w_n}{t} \quad (15)$$

where y_0 is a linear offset, t represents the exponential decay constant, erf is the Gauss error function, which determines when the exponential decay begins, and w_n, A_n, and $x_{c,n}$ represent the width, amplitude, and x-axis offset of the n-th Gaussian respectively. Six main features were seen in the TOF spectra, i.e. CO_2^+, Ar^+, CO^+, CO_2^{2+}, O^+, C^+, so n took a value of six.

With the above assumptions, the centre and width of a Gaussian representing an ion should remain constant (within a small margin) for spectra recorded using different electron energies. Similarly, the exponential decay of each peak is due to the decay of the luminescence of the phosphor screen, which should remain constant across all ion peaks at all electron energies.

To calculate the relative contribution of each ion to the spectra, the fit was first performed on the spectrum recorded at an electron energy of 100 eV to give approximate values for the position and width of each peak and the exponential decay constant. The spectrum at 100 eV was chosen as it had the most prominent features. The resulting fit is shown in Figure 30c). The values of the widths, positions and decay constant were then used as starting values in a fitting procedure across all spectra recorded at different electron energies with the appropriate parameters shared across all 14 spectra, i.e. the width of a Gaussian for a particular ion was allowed to vary, but had the same value in all 14 fits.

The exponential decay constant of each peak was found to be 71.4 ns, compared to the literature value of 70 ns for P47 phosphor.[69] Scaling the sum of the areas of the Gaussians for a given electron energy to the TICS values shown in Figure 28 yields the PICS for each ion formed by EI of CO_2. The results are shown in Figure 31 and compared to the PICS recorded by Straub *et al*[62], showing excellent agreement for the fragment ions. A deviation is seen in the PICS curve for CO_2^+ which becomes pronounced at lower electron energies. This deviation can be explained by the difference in TICS recorded by Hudson *et al*[63] and Straub *et al*[62]. The TICS and the percentage difference between the data sets, shown in Table 2, demonstrate a difference in TICS values that reaches 38% at the electron energies considered in this study, which fully accounts for the difference in the measured CO_2^+ TICS.

The ion TOF spectra and the calculated TICS using a 5 keV extraction potential are shown in the Appendix (Section 16.3) with virtually identical results.

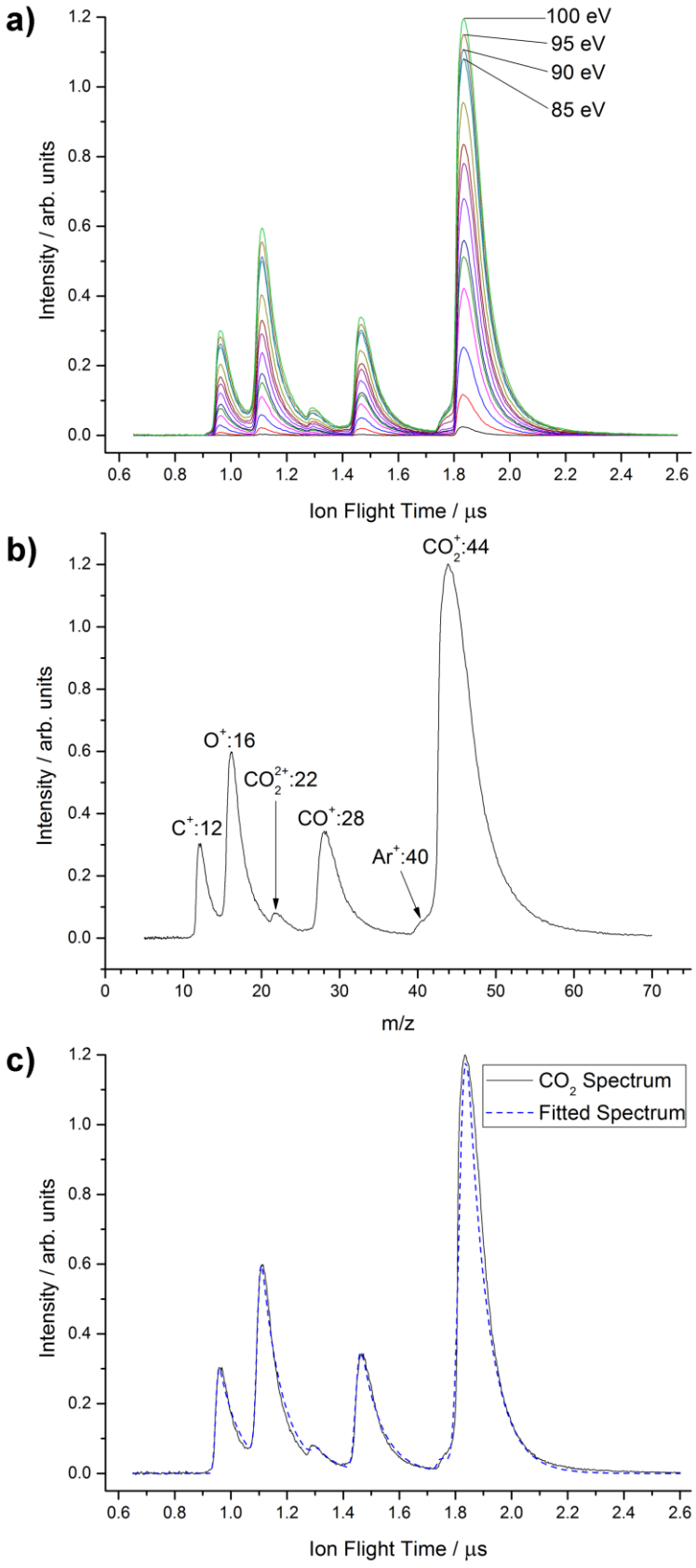

Figure 30 – a) The CO_2 TOF spectra recorded with a repeller voltage of 7.5 kV. b) The mass spectrum of CO_2 recorded at 100 eV with a 7.5 kV extraction potential. c) The CO_2 TOF spectrum recorded at 100 eV, fitted to six Gaussian peaks convoluted with an exponential decay with a shared decay constant.

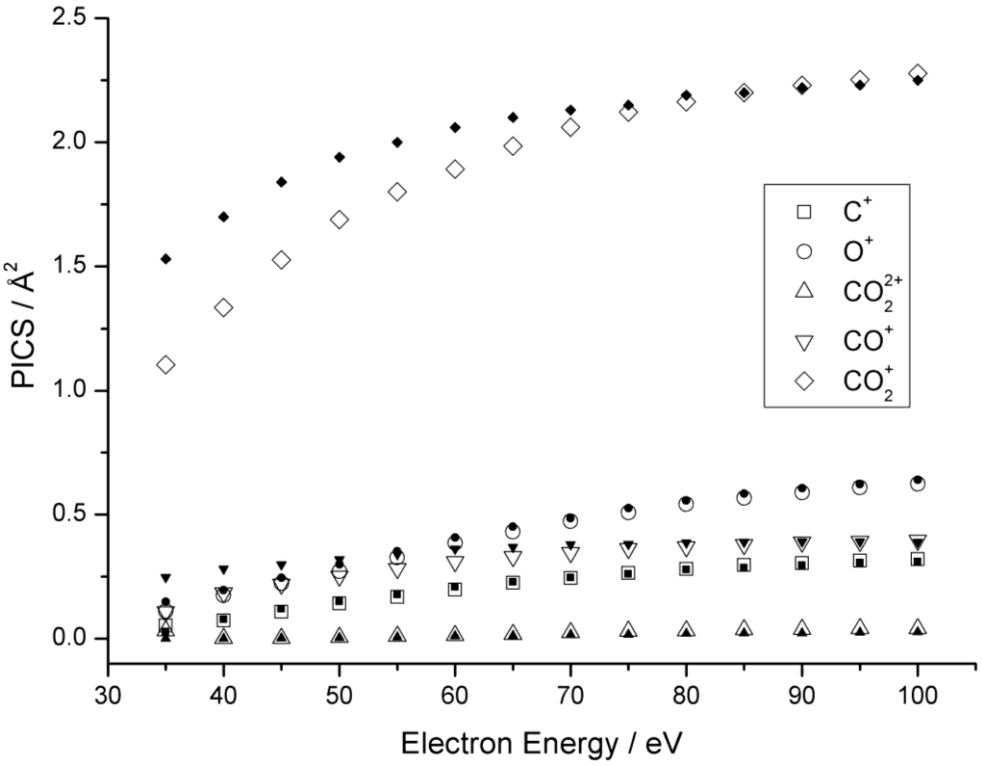

Figure 31 – PICS of ions formed in EI of CO_2, with a 7.5 kV extraction potential. Data from this work is shown with hollow symbols ○, measurements performed by Straub *et al*[62] are shown with smaller filled symbols ●.

Table 2 – The TICS recorded by Hudson *et al*[63] and Straub *et al*[62] at low electron energies and the percentage difference between the data sets.

Electron Energy / eV	Hudson *et al* TICS / Å^2	Straub *et al* TICS / Å^2	Difference / %
30	1.05	1.60	52.6
35	1.41	1.95	38.4
40	1.77	2.23	25.7
45	2.08	2.67	28.5
50	2.36	2.88	22.1
55	2.59	3.06	18.2
60	2.80	3.24	15.7
65	2.99	3.36	12.3
70	3.15	3.45	9.6

4.3 CO_2 Ion Images

For each fragment ion image, the scaled background image was subtracted and the resulting background-corrected image was analysed using the POP program[56] described in Section 3.5. For all ions, the first 25 data points from the KER distribution have been excluded due to the accumulation of error by the POP program at low KER values arising from the conversation from Cartesian to polar coordinates. The ion velocity distributions resulting from this analysis were converted to KER distributions, which are shown and discussed in the following sections.

4.3.1 CO_2^+ Ion Image

As expected, the image for the parent ion, CO_2^+, showed a distribution consisting of a spot centred in the middle of the detector, as depicted in Figure 32b). The velocity and KER distributions are shown in Figure 32a) and reflect the velocity distribution of neutral CO_2 in the molecular beam. The change in momentum of the CO_2 nuclear framework in the ionising collision is negligible.

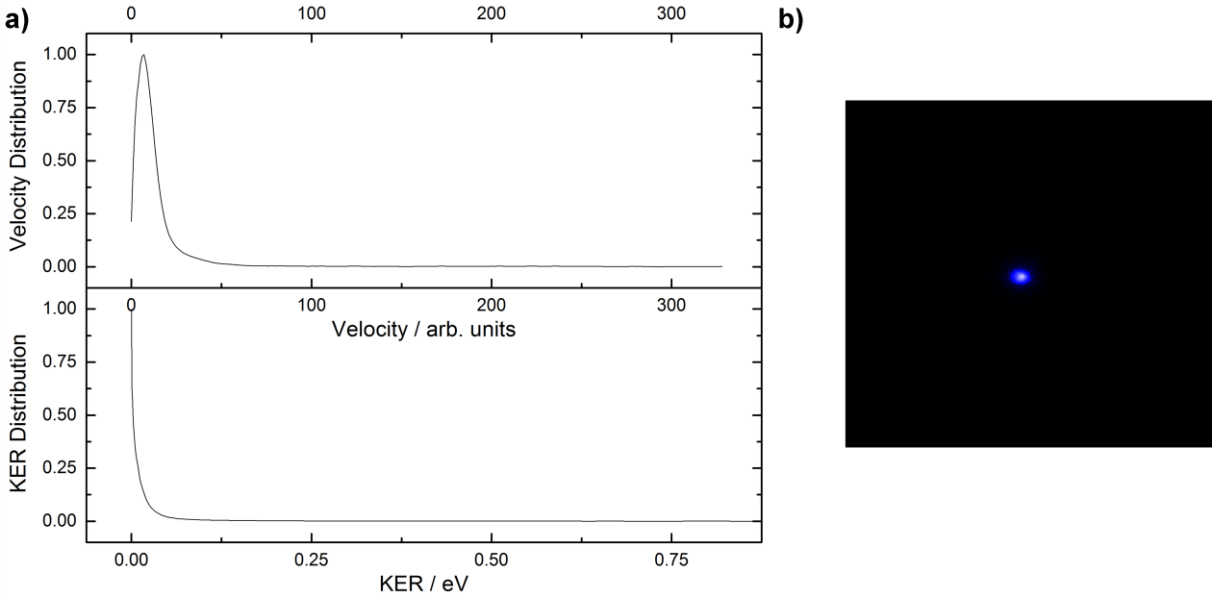

Figure 32 – a) The velocity distribution and the KER distribution recorded for CO_2^+. b) The ion image recorded for CO_2^+ at 100 eV.

4.3.2 CO^{2+} Ion Image

The ion image recorded CO^{2+} from 2,500,000 experimental cycles is shown in Figure 33. The signal level was exceptionally low, implying either that formation of CO^{2+} is a relatively minor fragmentation pathway at these energies, and/or that the ion is unstable and rapidly undergoes further fragmentation before detection. In the latter case, it might be expected that either the ion flight time distributions for C^+ and O^+ would be broadened or that C^{2+} and O^{2+} would be visible in the TOF spectra, neither of which is seen in the measurements performed. C^{2+} and O^{2+} were seen in the experiments performed by King and Price[70], with appearance energies of around 75 eV for both ions. At an electron energy of 100 eV, the intensity of the signal recorded for C^{2+} and O^{2+} are 0.03% and 0.01% of the intensity for CO_2, respectively.

The velocity distribution, shown in Figure 33, is very noisy and the only notable feature is the broad feature extending out to near the edge of the detector. The KER distribution reveals that the majority of CO^{2+} ions are formed with less than 0.5 eV of kinetic energy.

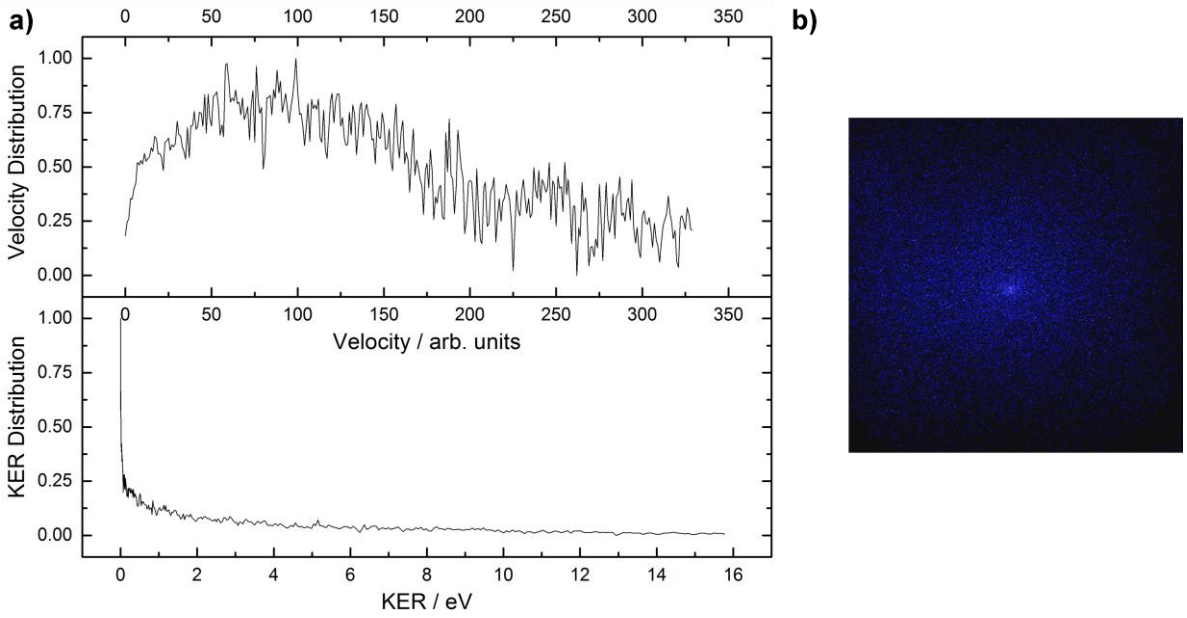

Figure 33 – a) The velocity distribution and the KER distribution recorded for CO^{2+}. b) The ion image recorded for CO^{2+} at 100 eV.

4.3.3 O^+, CO^+, and C^+ Ion Images

The KER distributions recorded for CO^+, O^+ and C^+ are shown in Figure 35a), Figure 36a), and Figure 37a) respectively and the distributions recorded by Velotta *et al*[64] and Locht *et al*[65] for the relevant ions are also shown in the same figures as parts b) and c), respectively. The experimental setups of Velotta *et al* and Locht *et al* were described earlier in Section 4. The ion images recorded at an electron energy of 100 eV are also shown in Figure 35e), Figure 36e), and Figure 37e).

Features in the KER distribution are seen to have a dependence on the incident electron energy that could be fitted well by a series of Gaussian peaks. These fits took the form:

$$y = y_0 + \sum_n \frac{A_n}{w_n \times \sqrt[2]{\pi/2}} \exp\left[-2\left(\frac{x - x_{c,n}}{w_n}\right)^2\right] \quad (16)$$

where y_0 represents a linear offset and A_n, w_n and $w_{c,n}$ are the amplitude, width and x-axis offset of the n-th Gaussian respectively. For each ion, the number of Gaussians chosen for the fit was the minimum required to fit the data satisfactorily, namely four for O^+ and CO^+ and three for C^+.

The contribution from each Gaussian may be interpreted as representing the contribution from a particular pathway leading to the formation of the ion. In a diatomic, such distributions can often be understood as a result of the *reflection approximation*. The reflection approximation, described by Hagstrum and Tate[71], is exemplified in Figure 34 showing the kinetic energy distribution of O^+ ions from dissociative ionisation of NO from a particular ionisation pathway. Curve 1 represents the potential energy curve of the initial electronic state of the molecule, curve 2 is the square of the molecular wavefunction, ψ_i^2, and curve 3 represents the upper electronic potential energy curve to which the molecule is excited. For EI processes involving electron energies well above the energy of the transition, it is assumed that the probability of the transition is mainly dependent on wavefunction overlap of the upper state and the lower state. The probability of a molecule having a particular energy in the excited state is therefore proportional to the molecular distribution in the lower state, which in the context of these experiment, can be assumed to be both the ground electronic and ground vibrational state. For a diatomic, and neglecting processes such as curve crossing, if the vertical ionisation region allows access to states above the dissociation limit of the upper curve, the excess energy after dissociation will be partitioned into kinetic energy in the products. Hence, the measured ion KER distribution should be representative of the initial state of the molecule and the shape of the upper curve, yielding curve 4 in the example. The assignment of a Gaussian to represent the outgoing wavepacket is most valid when the lower wavefunction is strongly bound and harmonic, and the upper state leading to dissociative ionisation is close to linear over the Frank-Condon region and strongly repulsive, leading to highly impulsive dissociation.

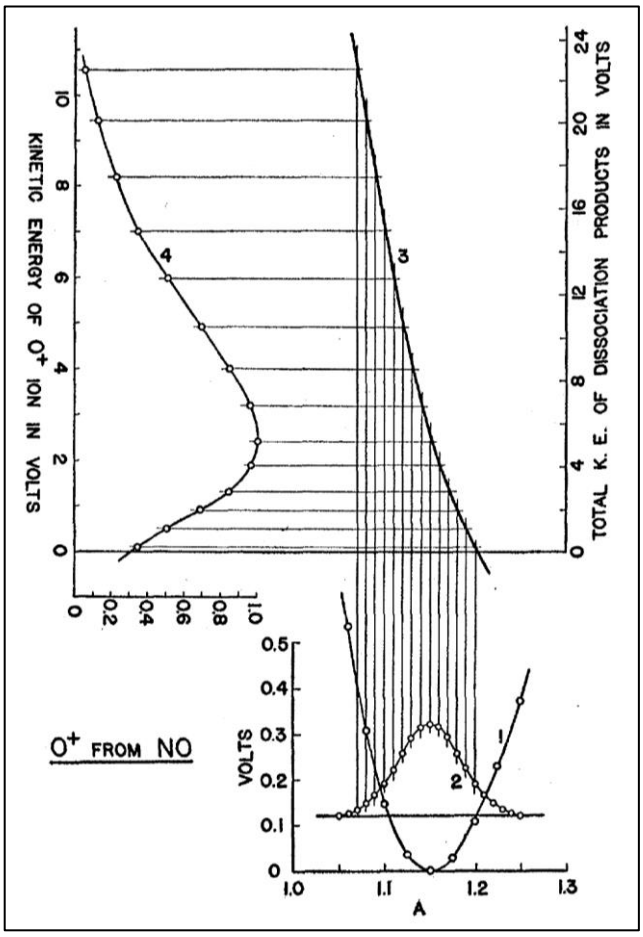

Figure 34 – An example of the reflection approximation for O^+ ions from the dissociative ionisation of NO. See the text for a full explanation. Adapted from Hagstrum and Tate[71].

The situation is not quite as simple for molecules consisting of more than two atoms. For example, a triatomic forming an atom and a two-atom fragment, the energy in excess of the dissociation limit may be partitioned between the kinetic energy of the products and vibrational excitation of the diatomic. For molecules with a large number of internal energy conversion pathways, the redistribution of energy may be fast compared to the dissociation, and the energy distribution of the fragments will be similar to a Maxwell-Boltzmann distribution rather than representative of the dissociative dynamics. Such processes are referred to as *statistical dissociation*. Further, the potential energy curves are no longer described by a single internuclear separation and whilst some work has been performed on a multidimensional reflection approximation for polyatomics[72], the ideal analysis would require a theoretical study of the energy landscape of CO_2, which is beyond the scope of this work. Electronic structure calculations on the various accessible potential energy surfaces would ideally be performed in order to assign the features seen in the KER distribution to particular dissociation pathways. The fragmentation products specific to CO_2 are discussed in Section 4.3.3.

Within this analysis, it was assumed that each Gaussian, representing a component of the ion KER, retained the same position and width at different incident electron energies, with the amplitude representing the relative contribution from the pathway of interest to the ion PICS. For each ion, the fit was first performed on the KER distribution measured at 100 eV to determine reasonable starting values for the widths and positions of each Gaussian. The fit was then performed globally over the KER distributions measured at different electron energies, with the Gaussian position and width parameters allowed to vary but taking the same value across the different spectra. The data was fitted well by sharing these values, implying that the assumption that the position and width of the Gaussians did not vary significantly with electron energy is valid. The fitting procedure produced values for the amplitude for the Gaussians at each electron energy, which, with values for the position and width, allowed the area contributing toward the KER distribution for each Gaussian to be calculated. For each spectrum, the sum of the areas of the Gaussians was then scaled so that their sum was equal to the PICS for the ion recorded in Section 4.2 at the same electron energy, yielding a semi-quantitative measure of the energy dependence of the feature.

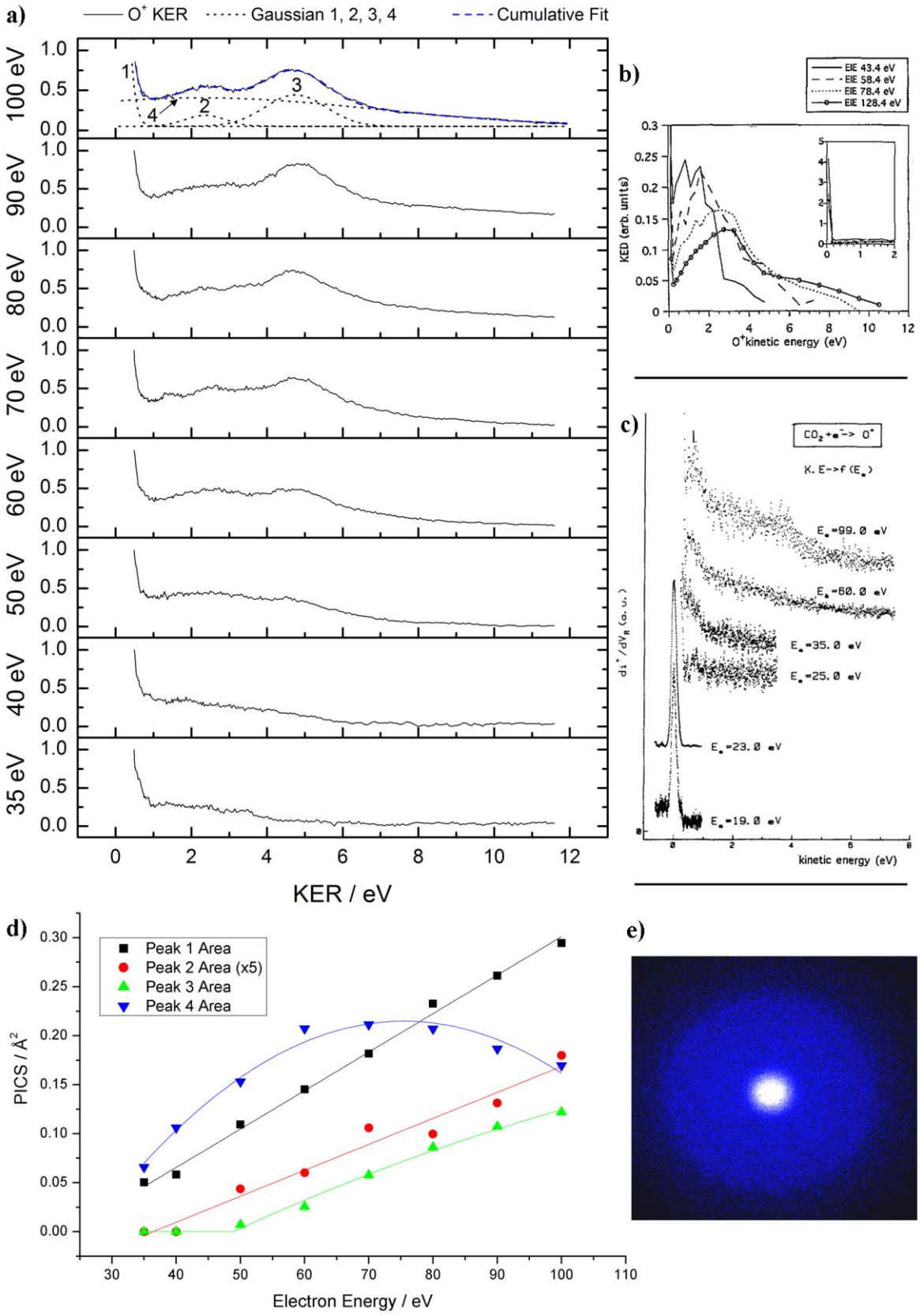

Figure 35 – The KER distributions measured for O^+ at different electron energies by: a) this work; b) Velotta *et al*[64]; c) Locht *et al*[65]; d) The energy dependence of the features labelled in a). e) The O^+ ion image recorded at an electron energy of 100 eV.

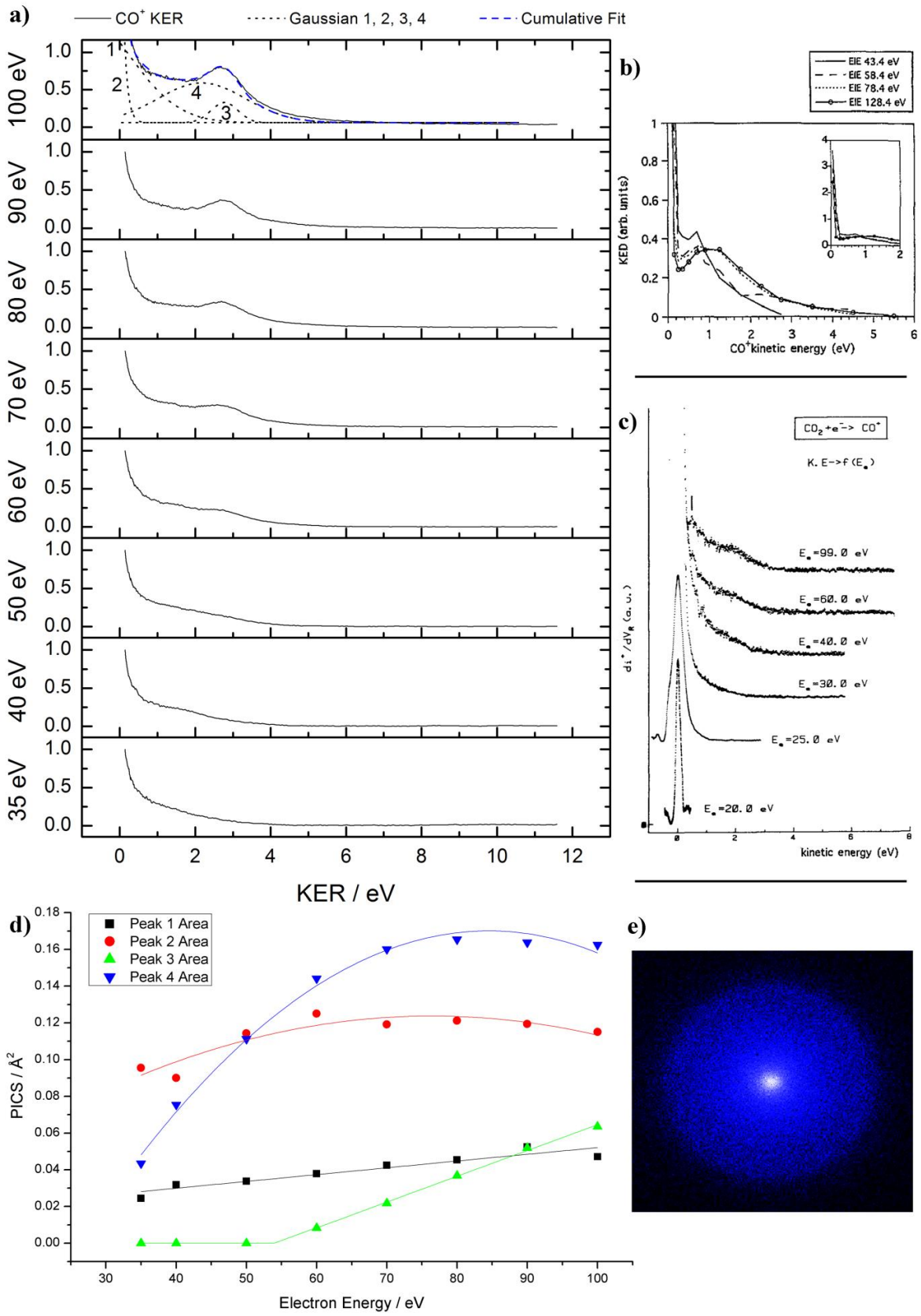

Figure 36 – The KER distributions measured for CO^+ at different electron energies by: a) this work; b) Velotta *et al*[64]; c) Locht *et al*[65]; d) The energy dependence of the features labelled in a). e) The CO^+ ion image recorded at an electron energy of 100 eV.

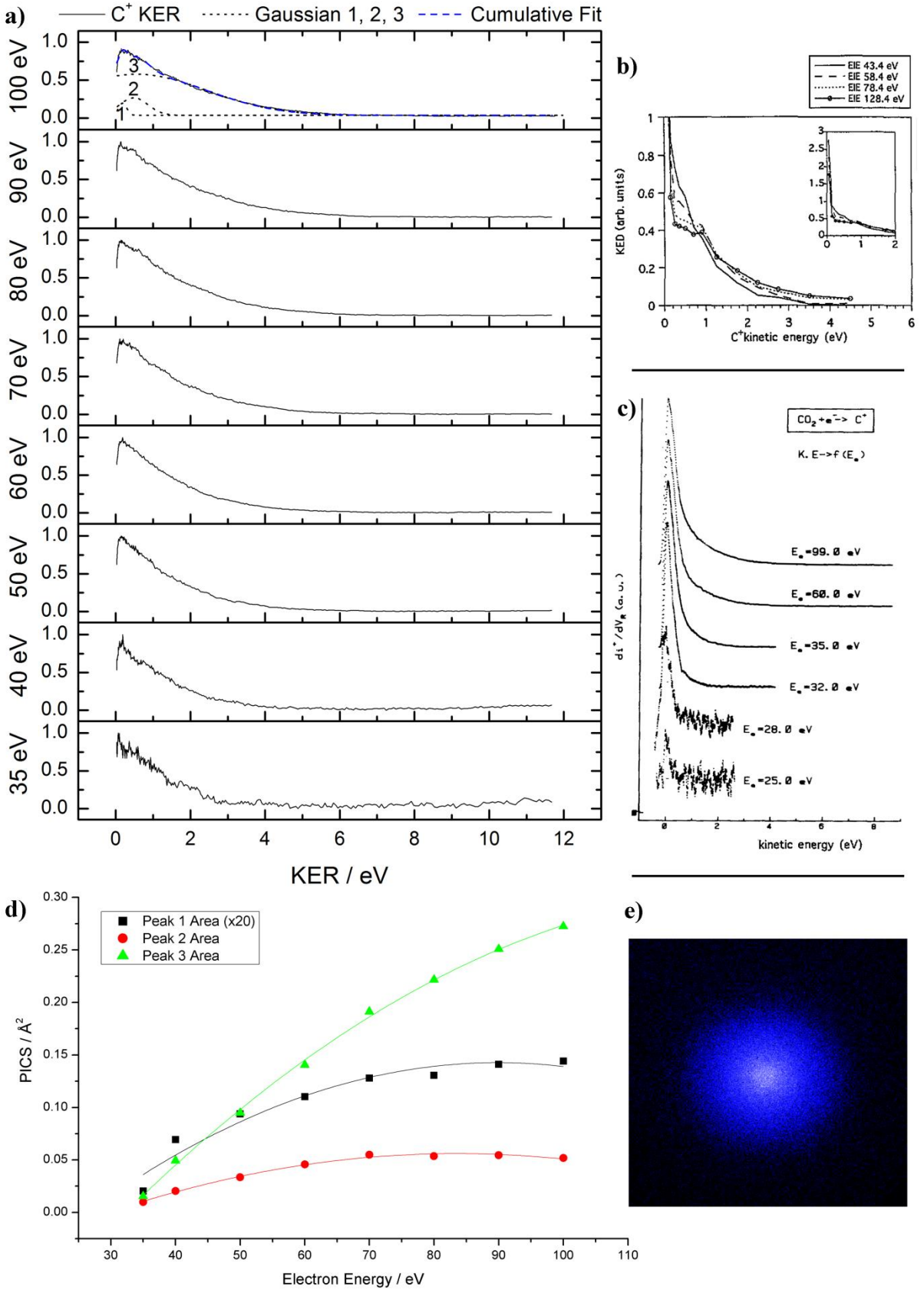

Figure 37 – The KER distributions measured for C^+ at different electron energies by: a) this work; b) Velotta *et al*[64]; c) Locht *et al*[65]; d) The energy dependence of the features labelled in a). e) The C^+ ion image recorded at an electron energy of 100 eV.

The predicted appearance energies of the O^+, CO^+ and C^+ ions have been calculated using the Hess cycles shown in Figure 38 and are compared to the values determined experimentally by Tian and Vidal[73] in Table 3. Ions are assumed to be formed in their electronic ground state. The various energies required to form products in their lowest lying excited states are tabulated in the Appendix (Section 16.4).

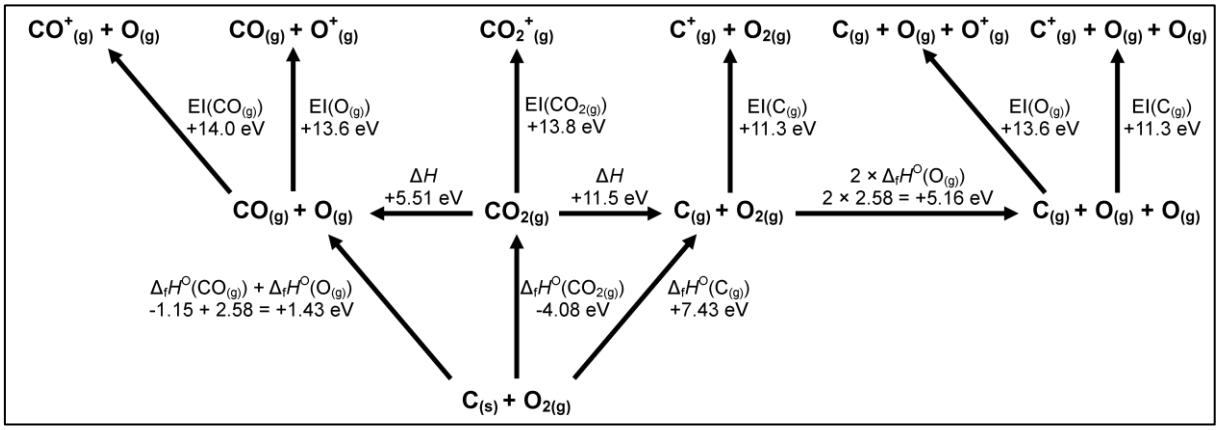

Figure 38 – The energetic pathways for the formation of the ground state products for ionisation and dissociative ionisation of CO_2. All values taken from the NIST database[74].

Table 3 – Appearance energies of the ions resulting from electron impact of CO_2, from Tian and Vidal[73].

Ion	Appearance Energy / eV	Ionisation Products	Formation Energy / eV
CO_2^+	13.8	CO_2^+	13.8
CO^+	19.5	$CO^+ + O$	19.5
O^+	19.1	$CO + O^+$, $C + O + O^+$	19.1, 30.3
C^+	27.8	$C^+ + O_2$, $C^+ + O + O$	22.8, 28.0

O^+ can be formed through either a two-body or a three-body dissociation, involving cleavage of one or two C=O bonds, respectively. The reaction $CO_2 \rightarrow O^+ + CO$ would require 19.1 eV, whereas $CO_2 \rightarrow O^+ + C + O$ would require 30.3 eV. Formation of CO^+ requires only one C=O bond to be broken and the simplest production method, $CO_2 \rightarrow O + CO^+$, is predicted to require 19.5 eV. Formation of C^+ requires two C=O bonds to be broken and would be expected to require 28.0 eV if two oxygen atoms were produced, i.e. $CO_2 \rightarrow C^+ + O + O$. A rearrangement producing O_2, i.e. $CO_2 \rightarrow C^+ + O_2$ would only require 22 eV, but as this is below the appearance energy of C^+, there is no evidence for this pathway.

A significant proportion of O^+ ions are formed with very little kinetic energy, resulting in the large signal intensity near 0 eV, which is characteristic of statistical decay. This might be expected from the high population of CO_2^+, indicating that there are bound states in the vertical excitation region,

which, if formed in non-equilibrium geometries with internal excitation (vibrational or electronic), can redistribute energy and statistically fragment. The O^+ KER distribution also shows three additional features: two narrow peaks centred at approximately 2.5 eV and 4.5 eV; and one peak centred at 2.5 eV with a much broader distribution. The amplitudes of the four fitted Gaussians are plotted at different electron energies in Figure 35b), showing that three of the features exhibit a reasonably linear dependence on electron energy, while the fourth exhibits a broad peak with a maximum at approximately 70 eV. Curves 3 and 4 have extrapolated appearance thresholds of around 35 eV and 50 eV respectively, whereas curves 1 and 2 are closer to the ion appearance energy of O^+ at 19.1 eV.

The KER distribution of CO^+ also shows that a large proportion of ions are formed with low kinetic energy (< 1 eV), and the maximum ion energy recorded is approximately 6 eV. The CO^+ KER distributions are fitted well by a sum of four Gaussians and the relative contributions of these components are plotted as a function of electron energy in Figure 36b). A pronounced feature at approximately 2.75 eV has an appearance energy in the region of 50-60 eV, and increases in intensity at higher electron energies.

The KER distributions recorded for C^+ are simpler than those recorded for O^+ and CO^+, exhibiting a weak dependence on the incident electron energy. The results from the EIVMIMS instrument show a peak very close to 0 eV with an exponential-like decay. A sum of three Gaussians is required to account for the changes seen across the different spectra recorded and their dependence on electron energy is plotted in Figure 37d). Curves 1 and 2 exhibit a broad maximum at 85 eV and 80 eV, respectively. The ion appearance energy of C^+ is 27.8 eV, which matches the approximate appearance energy of all three curves reasonably well.

One point of interest is a feature that appears in both the O^+ and the CO^+ KER distribution at around 50 eV. One explanation is that these ions could result from double ionisation of CO_2, namely:

$$CO_2 \rightarrow CO_2^{2+} \rightarrow CO^+ + O^+ \qquad \text{(vii)}$$

The double ionisation potential of CO_2 reported as 37.2 eV by Märk and Hille[75]. A Hess cycle, shown in Figure 39, predicts that the energy required for the dissociation forming both ions in their ground states would be 33.1 eV.

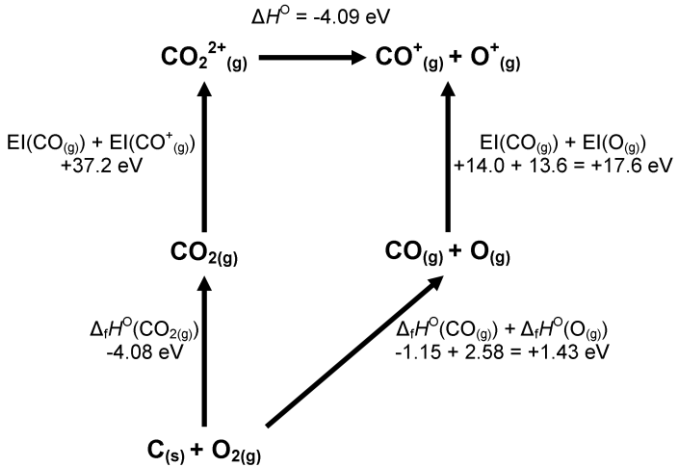

Figure 39 – The energetic pathways for the reaction $CO_2 \rightarrow CO_2^{2+} \rightarrow CO^+ + O^+$ with all ions formed in their electronic ground state. Values taken from Märk and Hille[75] and the NIST database[74].

Both features have appreciable kinetic energy, 4.5 eV and 2.75 eV for O^+ and CO^+ respectively, which matches the expected ratio due to conservation of momentum in the unimolecular decay step. The total kinetic energy is 7.25 eV, which is slightly higher than the predicted value of 4.1 eV if both ions were formed in the ground state. This indicates that the fragmentation results from an excited state of CO_2^{2+}.

It is also noted that the cross section for O^+ formation is generally a factor of two higher than for CO^+. If the ions are indeed resulting from the decay of CO_2^{2+}, it may be that CO^+ is formed with a significant degree of internal energy and further fragments to form either $C^+ + O$ or $C + O^+$. The cross sections for the resulting C^+ and O^+ would be too small to be seen in the current measurements of the KER distributions.

The measured KER distributions for all ions show reasonable qualitative agreement with those measured by Velotta *et al* and Locht *et al*, with similar features emerging in the KER distribution at around the same electron energies. The EIVMIMS instrument has a significantly better ion kinetic energy resolution, allowing the features to be seen more clearly. This is evidenced by the improved signal-to-noise ratio in the KER distributions shown for these ions. A rigorous theoretical study of the fragmentation of CO_2 would allow a detailed interpretation of the various features that have been highlighted in the KER distributions.

Part II: The Pixel Imaging Mass Spectrometry (PImMS) Sensor

Publications

- PImMS: A self-triggered, 25ns resolution CMOS Sensor for Time-of-Flight and Imaging Mass Spectrometry
  A. T. Clark, J. P. Crooks, I. Sedgwick, R. Turchetta, J. W. L. Lee, J. J. John, E. S. Wilman, L. Hill, R. Pisarczyk, E. Halford, C. S. Slater, B. Winter, W. H. Yuen, S.H. Gardiner, M. L. Lipciuc, M. Brouard, A. Nomerotski, and C. Vallance
  NEWCAS 2012 (Conference Proceedings)

- PImMS, a fast event-triggered monolithic pixel detector with storage of multiple timestamps
  J. J. John, M. Brouard, A. Clark, J. Crooks, E. Halford, L. Hill, J. W. L. Lee, A. Nomerotski, R. Pisarczyk, I. Sedgwick, C. S. Slater, R. Turchetta, C. Vallance, E. Wilman, B. Winter and W. H. Yuen
  JINST 7, C08001, (2012).

- Multimass Velocity-Map Imaging with the Pixel Imaging Mass Spectrometry (PImMS) Sensor: An Ultra-Fast Event-Triggered Camera for Particle Imaging
  A. T. Clark, J. P. Crooks, I. Sedgwick, R. Turchetta, J. W. L. Lee, J. J. John, E. S. Wilman, L. Hill, E. Halford, C. S. Slater, B. Winter, W.H. Yuen, S. H. Gardiner, M. L. Lipciuc, M. Brouard, A. Nomerotski, and C. Vallance
  J. Phys. Chem. A 116, 10897, (2012).

- The application of the fast, multi-hit, pixel imaging mass spectrometry sensor to spatial imaging mass spectrometry
  M. Brouard, E. Halford, A. Lauer, C. S. Slater, B. Winter, W. H. Yuen, J. J. John, L. Hill, A. Nomerotski, A. Clark, J. Crooks, I. Sedgwick, R. Turchetta, J. W. L. Lee, C. Vallance, and E. Wilman
  Rev. Sci. Instrum. 83, 114101, (2012).

- Exploring surface photoreaction dynamics using pixel imaging mass spectrometry (PImMS)
  M. D. Kershis, D. P. Wilson, M. G. White, J. J. John, A. Nomerotski, M. Brouard, J. W. L. Lee, C. Vallance, and R. Turchetta
  J. Chem. Phys. 139, 084202, (2013).

5 The Need for an Ultra-Fast Multi-Mass Detector

In time-of-flight ion-imaging experiments, such as those described in Part I, the ion flight time, t, is dependent on the mass-to-charge ratio, according to the relationship: $t \propto \sqrt{m/q}$, where m is the ion mass and q is the ion charge. The achievable time-of-flight resolution therefore determines the mass resolution, and the study of large molecules which undergo extensive fragmentation, often generating a number of fragments with similar mass, therefore requires a suitably fast detector. The experimental requirements typically consist of a detector time resolution on the order of 10 ns or better over a time window of interest (i.e. a difference in flight time between the earliest and latest arriving ions) spanning 20-100 µs.

Ions are typically imaged using an MCP/phosphor detector that converts and amplifies the incident ions to yield pulses of light. The resulting spatial image can be captured by a camera. Typically, a Charge-Coupled Device (CCD) sensor is used, which consists of a two-dimensional array of pixels that convert the incident light to charge during an experimental cycle. Two methods can be employed to record the image associated with a narrow ion flight time range, which is a process known as *gating*.

The first method relies on the fact that the signal amplification of an MCP is dependent on the voltage applied to it. During the experimental period, the CCD sensor is continuously exposed and one of the MCPs in the MCP/phosphor detector is maintained at a sufficiently low voltage that the phosphor screen produces no light or a negligibly low level of light. For the period of interest, an increased voltage is applied to the MCP, increasing the signal amplification, allowing the detector to become “active” for the period of the voltage pulse. The CCD therefore only records the image associated ions incident on the detector within the duration of the voltage pulse. Electronic pulsing units typically allow a period of 10 ns or longer to be recorded.

The second method is to use an Intensified Charge-Coupled Device (ICCD) sensor, which consists of a CCD imaging sensor coupled with an image intensifier. The intensifier has two functions; to increase the sensitivity of the detector by amplifying the incident signal; and to provide a short exposure time, as the detector is sensitive to signal only when the intensifier is active. The MCP/phosphor detector is active throughout the experimental period and the intensifier is activated for the period of interest. The achievable time resolution therefore is limited by how quickly the intensifier can be

activated and deactivated, i.e. the period of time-gating. The 4 Picos ICCD camera from Stanford Computer Optics, for example, is capable of achieving a gating time as low as 200 picoseconds.[76]

For an ion-imaging experiment, the spatial distribution associated with a particular value of *m/z* can be recorded by setting the gated exposure time to coincide with the ion arrival time. In experiments with multiple ion masses (and therefore multiple flight times), this method requires the experiment to be repeated for each ion of interest and the total experimental time is given by $\tau \times n$ if τ is the time taken to acquire an ion image, and n is the number of different ions. Large molecules that fragment to form many daughter ions therefore have a significantly increased overall acquisition time. An imaging detector capable of simultaneously recording the spatial and temporal distribution of ions would reduce the experimental acquisition time to τ, regardless of the number of ions formed, as long as the range of ion flight times lay within the acquisition time window of the detector.

Such a detector would also confer a number of additional benefits. For example, in spatial-map imaging experiments, sample damage caused by ablation and ionisation would be lowered due to the reduced number of laser pulses required; a faster experimental time would reduce the ex-vivo degradation of biomolecules that occurs at room temperature[77]; and recording multiple ions in a single acquisition cycle opens the possibility of coincidence experiments. This section outlines several detectors with the potential to be used in multi-mass imaging experiments.

5.1 Fast CCD Sensors

A conventional CCD-based camera reads out the data contained in each pixel after each frame. The data transfer step requires the charge in each pixel to be transferred to the end of the sensor where it is digitised. However, the transfer of the charge is a slow process, typically operating at rates of 10-50 Hz, whereas ions arriving within 100 ns of each other would require an operating frequency of at least 10 MHz to be resolved.

One method of overcoming this limitation is to substitute part of the light sensitive region, which is known as the *photoactive region* or *active area*, of each pixel with a number of memory registers. This allows the charge collected in an exposure period to be transferred to a memory register instead of the end of the sensor, which can be performed significantly faster as the charge does not have to be moved as far. Using multiple memory registers allows an equivalent number of images to be stored on the sensor before the data is read out. For example, the 300-kpixel Ultrahigh-Speed CCD V6,[78] developed by Goji Etoh, has 144 memory registers per pixel and is capable of operating at 2MHz, storing images continuously. These specifications correspond to a time resolution of 500 ns and a total experimental period of 72 μs, which, although not meeting the requirements for ion

imaging experiments, nonetheless provides a good example of the increase in throughput achievable through incorporating onboard memory and logic.

The DALSA Zenith camera is another example of a CCD detector with memory registers in each pixel.[79] The sensor has a resolution of 64 × 64 pixels, with each pixel containing 16 memory registers. The camera can be programmed with sixteen consecutive exposure times between 10 ns and 1.275 μs,[80] with the image corresponding to each exposure stored in one of the memory registers. The ability to program short exposure times allows ion-imaging experiments to be performed by synchronising short exposure periods with the known arrival times of ions within the time-of-flight distribution. As images are acquired continuously with no time gap between them, every second exposure must in many cases be used to fill in the intervals between ion arrival times, limiting the number of memory registers available for ion images to eight. The Zenith camera was used for initial proof-of-concept velocity-map and spatial-map imaging mass spectrometry experiments to show that the acquisition of images associated with multiple ion masses on each TOF cycle was possible. These experiments are described below in Sections 5.1.1 and 5.1.2.

Another approach is to incorporate an optical beam splitter into a camera to illuminate multiple ICCD sensors with the same image. These detectors are known as multi-channel ICCD cameras. The images associated with different times can be captured by different CCD sensors by programming the exposure of individual intensifiers and, like ordinary CCDs, the time resolution is limited by the intensifier gate period. The XXRapidFrame (Stanford Computer Optics) is a recent example with eight separately controlled 1.4 Mpixel ICCD sensors and an intensifier gating time as low as 200 ps. The drawbacks associated with multi-channel detectors are that the beam-splitter reduces the intensity of light incident on each of the ICCD sensors and that multiple ICCD sensors increase the cost and size of the device. As with the DALSA Zenith camera, the exposure times can be chosen to coincide with the ion arrival times in a TOF experiment with a different ICCD sensor being exposed for each ion. Up to eight ion images can be recorded by the detector in a single experimental cycle, which would lead to an eight-fold increase in the experimental throughput.

5.1.1 Proof-of-Concept Multi-Mass Velocity-Map Imaging Experiments

Proof-of-concept multi-mass VMI experiments using the DALSA Zenith camera were performed in 2008 by Brouard *et al*[80] with a conventional VMI apparatus. Two products, $CS(^1\Sigma^+)$ and $S(^1D_2)$, from the one photon 193 nm dissociation of CS_2 were imaged in the same experimental cycle using the Zenith camera and also imaged separately under the same conditions using a conventional CCD camera (576 × 768 pixels). In the latter case, the two fragment images were recorded in separate experiments. A comparison of the images, velocity distributions and calculated β parameters for the

CS fragment, shown in Figure 40, reveals excellent agreement between the two sets of data. The data recorded for the S fragment using the two cameras also showed good agreement, but discrepancies were apparent at low fragment velocities due to the low pixel density of the fast-framing camera. Experiments were also carried out in which four photofragments were imaged from a mixture of dimethyldisulfide and CS_2, further demonstrating the viability of multi-mass VMI experiments.

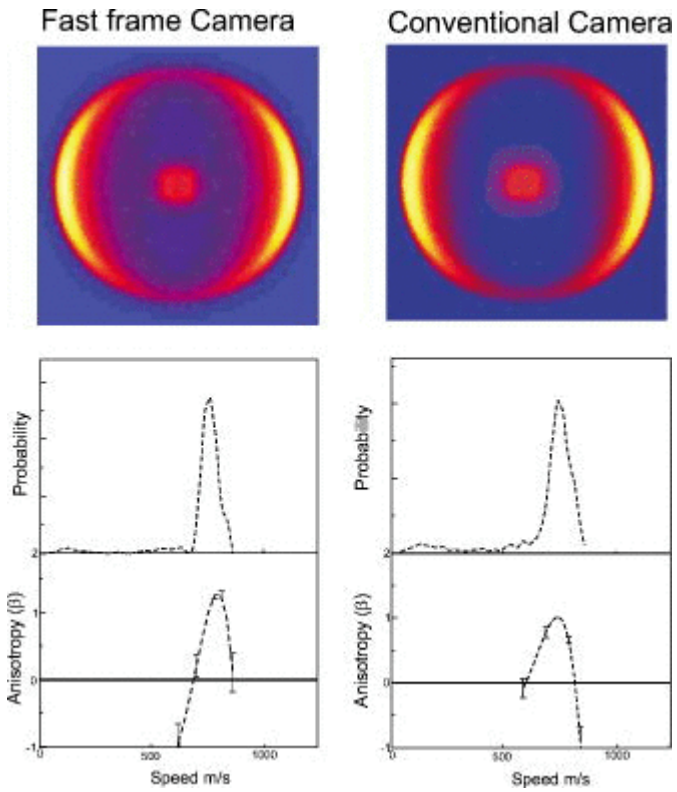

Figure 40 – Top panels: a comparison of CS fragment images from the 193 nm dissociation of CS_2, obtained with the DALSA fast-framing camera and a conventional CCD camera. Velocity distributions and *β* parameters derived from the images for both cameras are shown in the middle and bottom panels, respectively. Reproduced from Brouard *et al*.[80]

5.1.2 Proof-of-Concept Multi-Mass Spatial-Map Imaging Experiments

Proof-of-concept spatial-map imaging experiments using the DALSA Zenith camera were carried out in 2010 by Brouard *et al*[81] using an adaption of the velocity-map ion imaging instrument used in the previously described experiment[80]. A sample consisting of red and blue dyes covered by a nickel mesh was imaged. A photograph of the sample is shown in Figure 41. The red and blue dyes have different chemical constituents, and yield characteristic distributions of ions upon irradiation with UV laser light. Using TOF-MS to separate ions of different masses and setting the framing camera exposure times to the appropriate values for the masses of interest allowed the spatial distribution of fragment masses from each dye to be determined on each experimental cycle.

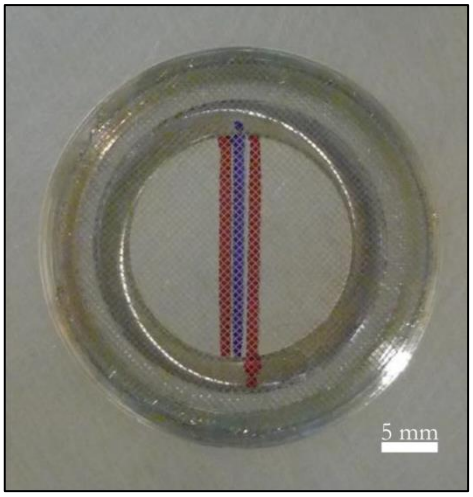

Figure 41 – The sample used for the proof-of-concept spatial imaging experiments. Reproduced from Brouard *et al*[81].

The result of the imaging experiment, summed over 200 acquisition cycles, is shown in Figure 42. At different flight times, separated out by the camera exposure times, the spatial distributions of the two dyes are clearly resolved. The camera is also able to resolve some features of the nickel mesh, although a higher pixel resolution would provide more definition in the images.

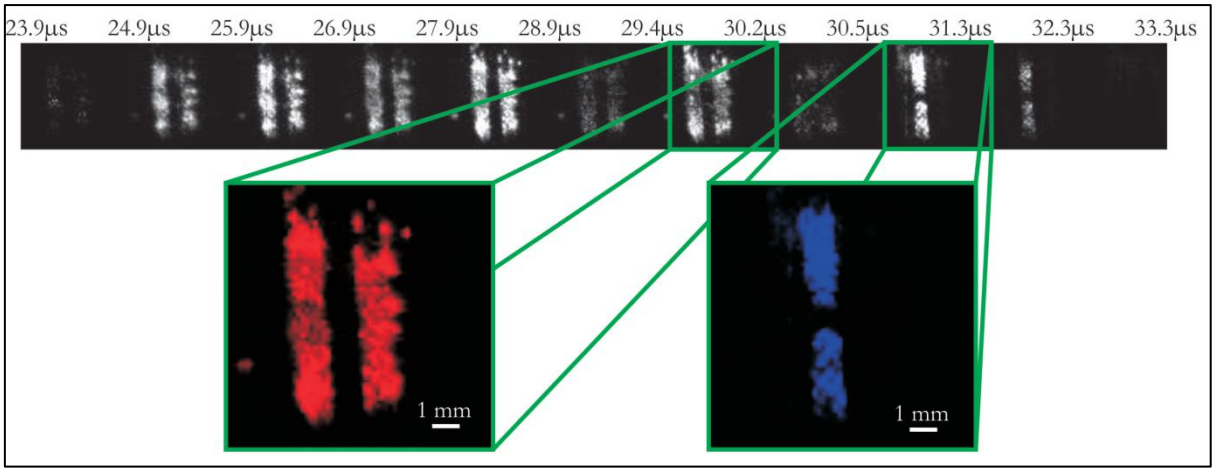

Figure 42 – The images obtained by setting the exposures of the fast-framing camera to detect selected ions generated from the two dyes. As the two expanded images show, the different dyes can be clearly resolved in time and space. Reproduced from Brouard *et al*[81].

5.1.3 The Suitability of Fast CCD Cameras for Multi-Mass Imaging

Whilst the experiments described above were successful in demonstrating a new approach to imaging mass spectrometry, there are a number of limitations when using CCD based cameras. Firstly, the arrival times of the ions of interest must be known in advance in order to program the camera exposure windows to coincide with the masses of interest. Secondly, with sensors that record consecutive images with no time gap between them, the images used to pad the intervals

between ion arrival times of interest generally consume half of the available memory registers. Increasing the number of memory registers, achieved in several recently developed cameras[82], can alleviate this problem; however increasing the number of memory registers generally decreases the photoactive fraction of the pixel, which decreases the sensitivity. CCD-based cameras provide a viable option for imaging mass spectrometry experiments on small to medium-sized molecules with a limited number of daughter ions, but do not provide a general route to imaging mass spectrometry of more complex systems due to the limited number of images that can be recorded per experimental cycle.

5.2 CMOS Sensors

The optical pulses from an MCP/phosphor detector can be recorded by a complementary metal–oxide–semiconductor (CMOS) sensor. In common with CCD sensors, incident light is converted to charge during an experimental cycle. However, the way in which the signal is processed is radically different. In the case of a CCD camera, the charge generated during an exposure is integrated over the exposure time and read out at the end of the exposure. In contrast, a CMOS sensor possesses circuitry in each pixel which allows the signal to be analysed and processed on the sensor before readout occurs. In the sensors typically employed in imaging experiments, the circuitry allow the positions and arrival times of light pulses arriving at the CMOS sensor to be recorded. As the incident pulses of light cause data to be recorded, the detectors are therefore referred to as *event-triggered sensors* or *event-triggered cameras*.

In general, each pixel in an event-triggered sensor contains one or more memory units. When the rising edge of the incident signal crosses a predefined threshold, as illustrated in Figure 43, the pixel circuitry references a timing counter on the sensor, allocating an arrival time or "timestamp" to the signal. The timestamp is stored in the memory of the pixel and the time resolution of the sensor is therefore determined by how well the rising edge can be resolved. These timestamps are read out from the sensor at the end of the experimental cycle with the *x* and *y* coordinates of the pixel giving the location of the signal.

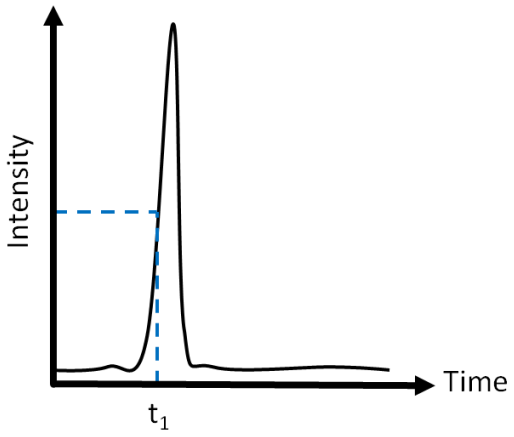

Figure 43 – The basis of recording the arrival time of signal with an event-triggered camera. The dashed line represents the digital threshold and the time that the signal crosses the threshold is recorded as t_1.

Event-triggered cameras offer a number of advantages over framing CCD cameras for TOF particle imaging applications. The ion arrival times do not need to be known in advance and a large number of different ions can be recorded in a single experiment. Additionally, the data handling and data transfer requirements for multiple arrival times tend to be significantly more efficient compared to reading out multiple frames that are sparsely populated.

An example of an event-triggered detector is the TimePix sensor developed at CERN, originally designed for applications in particle physics. The spatial resolution of the TimePix sensor is 256 x 256 pixels, and the external clock can be set to frequencies as high as 100 MHz, giving a time resolution of 10 ns.[83] One of the disadvantages of the TimePix sensor for experiments requiring the detection of many particles per cycle is that each pixel can only store a single timestamp each experimental cycle. While this is not problematic in many applications, in imaging mass spectrometry experiments with relatively high signal levels, the arrival of a high *m/z* ion striking the detector at the same position as an earlier, low *m/z* ion is not recorded due to the fact that the pixel memory is already filled. Nonetheless, TimePix has been successfully employed in a number of multi-mass imaging applications, recording the images associated with ion masses produced in a range up to 80 kDa.[84] For experiments requiring a detector with a larger area or increased spatial resolution, four Timepix sensors can be "tiled" to produce an overall pixel resolution of 512 x 512.

5.3 MCP/Delay-Line Anode Detectors

Multi-mass imaging of ions can also be achieved using MCPs to convert incident ions to electron bursts that are then detected by a delay-line anode. A schematic of the operation of a delay-line anode in one dimension is shown in Figure 44. The electron bunch from the MCPs strikes a wire that has been arranged to span one dimension, in this case, the *x* dimension. This induces an electrical

pulse that propagates to the end of the wire, where time-to-digital conversion (TDC) units record the arrival time of the pulse. The difference in the arrival time recorded at each end of the wire allows the *x* position to be determined. The ion flight time can be calculated through comparing the centre of the recorded times to a fixed reference (i.e. a bunch marker) in the time spectrum, such as the original photon source that causes ion formation or an external trigger. A second delay-line rotated azimuthally by 90° can yield the same information for the *y* dimension, allowing the three dimensions of *x*, *y* and *t* of an incoming ion to be recorded. The resolution of the position and arrival time are dependent on the accuracy of the TDCs employed in the delay-line anode, with a timing precision better than 1 ns and 1 Mpixel resolution commonly achievable.[85] Delay-line anodes are capable of operating at repetition rates in the kHz range.

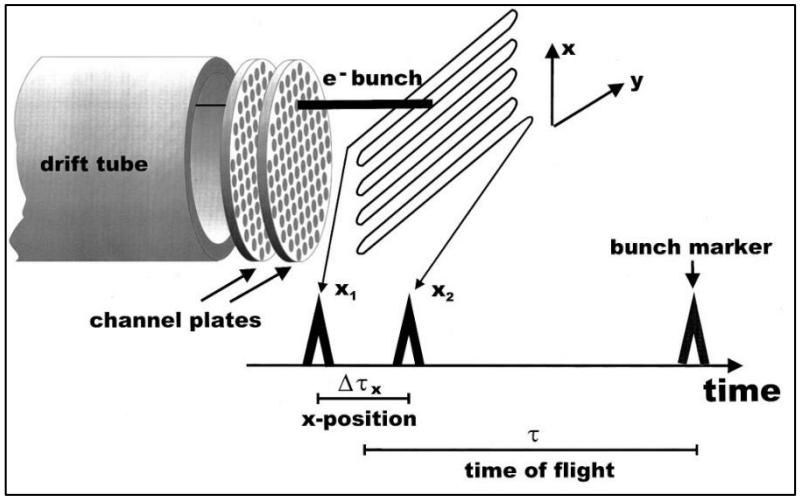

Figure 44 – The operating principle of a delay-line detector, shown for one dimension. The *x* position can be calculated from the time delay $\Delta\tau_x$ of the arrival time at the two ends x_1 and x_2 of the delay line. The TOF can be derived from the MCP pulse or the arrival time of the centre of x_1 and x_2 with respect to the bunch marker. Adapted from Oelsner *et al*[86].

The signal throughput for delay line anodes can be restricted due to the time required to reset the electronics for each measurement. A delay line measurement requires approximately 100 ns, and therefore can limit the detection rate to one signal per 100 ns. This can be mitigated somewhat by the use of three delay lines, referred to as hexanode detectors.[87] Hexanodes record seven signals per ion (one from the external bunch marker and two propagation times for each delay line) and the redundancy in measurements allows multiple signals incident on the detector within the electronics dead time to be discerned using a reconstruction algorithm. A hexanode detector has been successfully employed by Klerk *et al*[88] to perform multi-mass ion imaging, although the authors note that, along with the difficulty in image reconstruction and tuning of the ion optics, the limit in signal throughput makes the detector unsuitable for high count rate experiments.[89]

6 The PImMS Sensor Project

The development of the Pixel Imaging Mass Spectrometry (PImMS) sensor began as a collaborative effort between the research groups of Claire Vallance and Mark Brouard in the Department of Chemistry, University of Oxford; Andrei Nomerotski in the Department of Physics, University of Oxford; and the CMOS Sensor Design Group at the Rutherford Appleton Laboratory (RAL), led by Renato Turchetta. In 2013, upon Nomerotski's departure from the University of Oxford, Richard Nickerson replaced Andrei Nomerotski as the Oxford Physics representative within the collaboration.

The aim of the project was to create a CMOS sensor that was tailored for imaging mass spectrometry applications. The ideal sensor combines spatial imaging with a high time resolution and the ability to record multiple ion events per experimental cycle. The sensor devised operates in the same way as the event-triggered detectors described in Section 5.2. An important consideration was to ensure that ions with different arrival times would be detected even when incident on the same location of the detector. The signal from these 'superimposed' ions can be recorded by implementing multiple memory registers per pixel. Detailed computer simulations were performed to determine the optimum number of registers, as described in Section 6.1.

The components of the PImMS detector can be described under three headings: hardware; firmware; and software. The hardware has three major components – the PImMS sensor, the sensor board and the camera. The sensor is wire-bonded onto a sensor board, which is then mounted in a camera supplied by aSpect Systems.[90] The camera has connections that supply power to the sensor and sensor board and allow readout to a computer via a USB2 interface. Six SMB connections allow for trigger control of the camera. Two of these connections are currently in use, one allows the user to provide a trigger input to begin a data acquisition cycle (when the detector is operating in triggered mode), and one provides a trigger out at the beginning of each acquisition cycle, in both triggered and free-running mode, which can be used to trigger other experimental equipment.

Each PImMS detector has three field-programmable gate arrays (FPGAs), which are manufactured by Xilinx.[91] FPGAs are circuits that can be reprogrammed to perform desired function after manufacturing. This is in contrast to application-specific integrated circuits (ASICs), which are manufactured for a single specific function. The flexibility of FPGAs means that changes to the logic controlling the detector can be made by changing the FPGA firmware instead of remanufacturing ASICs. The firmware consists of the code which controls, configures and reads out the sensor, and is

responsible for the low-level operation of the detector. The three FPGAs execute independent firmwares, and their respective functions can be summarised as follows:

- The Pattern FPGA and firmware control the operation of the sensor;
- The Video FPGA and firmware provide readout of the sensor;
- The USB FPGA and firmware provide conversion of the raw readout to USB2 format and provide control of the camera via the USB2 interface.

The camera has a connection to allow the firmware of the FPGAs to be reprogrammed using a software package called iMPACT and a programming module to interface the camera with a computer. Both of these are also supplied by Xilinx.

The software consists of the code running on the computer which allows the user to control the camera, acquire images from the sensor and to record, process and visualise the data. Basic software provided by aSpect System, written in LabVIEW, provides a user interface with basic read operations and the ability to change certain camera parameters such as the detector sensitivity. The software and modifications made are described in more detail in Section 7 as part of the work carried out for this thesis.

6.1 Detection Efficiency Simulation

Prior to the commissioning of the PImMS sensor, simulations were performed in order to determine the optimum number of memory registers to include within each pixel. The simulations were designed to determine the effect of the number of registers on the detection efficiency of ions in an imaging mass spectrometry experiment run under typical operating conditions. Trajectories through the VMI instrument were simulated for fragment ions with a range of masses and velocity distributions. Figure 45 shows the two extreme cases of: a) the 'best case' in which each ion has its maximum possible velocity within the energetic constraints of the dissociation process that led to its formation (yielding a velocity-map image consisting of a single ring or Newton sphere); and b) the 'worst case' in which each ion has a random uniform distribution of velocities up to the maximum energetically accessible velocity. In the best case, ions only have spatial overlap when they have similar velocities, and the degree of overlap is dependent on the radius of the Newton sphere. In the worst case, ions can overlap even if their maximum velocities are different, as all ions are able to impact the central region of the detector.

In both simulations, the angular distribution of the ions was isotropic. The detection efficiency of a 72 × 72 pixel PImMS sensor with n timestamp registers was simulated by assuming that an ion would be detected if fewer than n ions had already been detected by the relevant pixel. Most ion distributions

are likely to be intermediate between the two extreme cases considered, so the simulations are expected to give upper and lower bounds on the required number of timing registers. As expected, once the total number of ions increases to the point at which multiple ions strike a single pixel during an acquisition cycle, the detection probability becomes strongly dependent on the number of available memory registers. From the plots in Figure 45, it can be seen that when a single memory register is available, the detection efficiency falls off sharply as the total number of ions increases, due to the shadowing effect for heavier ions noted in Section 5.2. Adding a second timestamp improves the situation considerably, and while incorporating additional timestamp registers improves the situation further, the relative improvement is less with each additional timestamp. Since increasing the number of timestamp registers above four yields relatively little improvement in detection efficiency, but adds considerably to the cost and complexity of the sensor chip, as well as decreasing the active area, four timestamps were chosen for the PImMS sensor as a compromise between optimum ion detection efficiency, particularly for heavier ions, and available real estate on the chip. An ion-imaging experiment might be expected to generate up to 1000 ions per experimental cycle, with four memory registers improving the efficiency from below 70% to above 90% in the simulated worst case scenario.

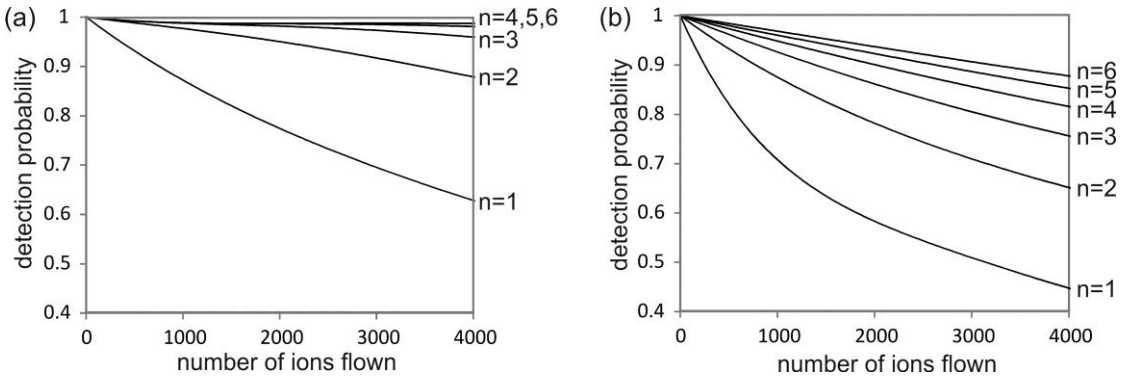

Figure 45 – Simulations showing the effect on ion detection efficiency of including between one and six memory registers (denoted n = 1 to n = 6) within each pixel: (a) best case and (b) worst case scenarios, as described in the text.

6.2 The PImMS Sensor Design

The PImMS sensor is based on a 180 nm CMOS technology[92] on a 200 mm silicon wafer. There currently exist two generations of the sensor, referred to as the PImMS1 and PImMS2 sensors. The project was carried out in two stages with the intention that the PImMS1 sensor would act as a prototype. This allowed the PImMS1 sensor to be tested in different applications and any necessary modifications to be made to the design of the second-generation PImMS2 sensor before the final manufacturing process. The resolution of the PImMS1 sensor is 72 × 72 pixels, compared to 324 × 324 for the PImMS2 sensor. The pixels on the PImMS1 and PImMS2 sensors measure 70 µm × 70 µm.

The pixel operation for each experimental cycle will be discussed below. The PImMS2 sensor has a small modification to the pixel architecture to allow an improved calibration process, which will be discussed in more detail in Section 8.4. Additionally, the PImMS2 sensor has a reduced pin count on the sensor to allow it to be operated more easily in a vacuum, as well as extra digital outputs on the sensor allowing an increase in the output data rate. These changes are elaborated on in more detail by Sedgwick *et al*[93]. Each pixel is equipped with four memory registers, allowing four signal arrival times to be recorded per experimental cycle.

In total, each PImMS sensor pixel contains over 600 transistors. The technology that made it possible to include this amount of processing circuitry in each pixel is the Isolated N-Well Monolithic Active Pixel Sensor (INMAPS) process, developed at the Rutherford Appleton Laboratory[92]. The Pattern FGPA, which controls the timing of the pixels, operates at 160 MHz i.e. a time period of 6.25 ns. The sensor was originally designed at 20 MHz, i.e. a time period of 50 ns, corresponding to eight FPGA clock cycles. Firmware modifications have enabled successive improvements to 25 ns and 12.5 ns (4 and 2 clock cycles respectively) without loss of performance by the sensor. The ultimate achievable time resolution in the present design is limited to 6.25 ns due to the FPGA clock frequency; with a redesign in the clocking and rate interworking of the FPGA, an improved time resolution should be feasible.

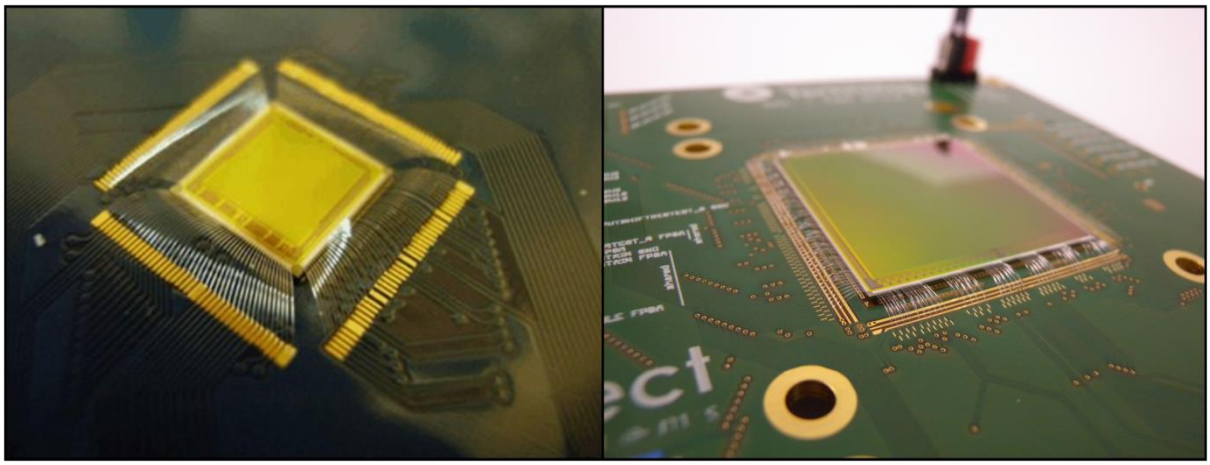

Figure 46 – The PImMS1 and PImMS2 sensors, left and right, respectively. Both are shown bonded to a sensor board.

6.3 Operation of the PImMS Sensor

At the beginning of an experimental cycle, a clock counter is reset and begins to increment with the chosen time step (e.g. 50, 25 or 12 ns). The clock counter provides a digitised time value, referred to as a *timecode* when signal is recorded in a pixel, and the rate at which the counter increments determines the duration of each timecode in the experiment. The clock counter is 12 bits wide, so when a time step of 12.5 ns is used, the total experimental period is 51.2 µs. The experimental period

can be lengthened by setting the clock counter to increment in higher multiples of 12.5 ns i.e. four cycles of 12.5 ns would correspond to the counter incrementing every 50 ns and an experimental period of 204.8 μs. This is necessary for experiments that take place on a long timescale, such as those described in Part I.

The process of signal being recorded, from signal input to digital output, is shown schematically in Figure 47. Particles or photons incident on the 5 μm thick boron-doped silicon layer of the sensor cause electron-hole pairs to be formed. Sufficiently high charge can be generated by several thousand incident photons, as is the case when detecting light from an MCP/phosphor ion detector, or by a single high energy particle, such as an alpha particle or an electron. In the latter case, the charged particle leaves an ionising track as the silicon layer is traversed; this process is described in more detail in Section 9.4. The electrons generated by the incoming photons or particles diffuse to four charge-collecting diodes in each pixel. Each diode is centred in a 14.5 μm × 14.25 μm area which is free of any other circuitry, covering 16.9% of the pixel area in total. Initial optical characterisation[94] indicates a quantum efficiency (i.e. the ratio of incident photons to converted electrons in the silicon layer) of approximately 9% at 470 nm, and a diode full well capacity of 24,000 electrons. When the charge generated by incident particles arrives at one of the detection diodes, it causes a step reduction in the diode voltage (see the signal denoted (A) in Figure 47). This is the same process by which a conventional (non-event-triggered) CMOS image sensor detects an incoming signal. In the PImMS sensor, the charge from the four detection diodes is summed and then amplified and inverted by the preamplifier (signal (B)). This converts the weak current signal reaching the diode into a voltage step. The output of the preamplifier is connected to an analogue readout circuit. Following the acquisition cycle, the voltage of a pixel preamplifier may be digitised to 16 bits and read out from the camera, representing the total “analogue” signal collected during the experimental period. The analogue and digital circuitry are carefully partitioned to minimise any noise in the sensitive analogue components generated from signals within the high speed digital circuitry. The analogue image is useful during experimental setup, allowing the image from a phosphor screen to be focussed easily onto the sensor.

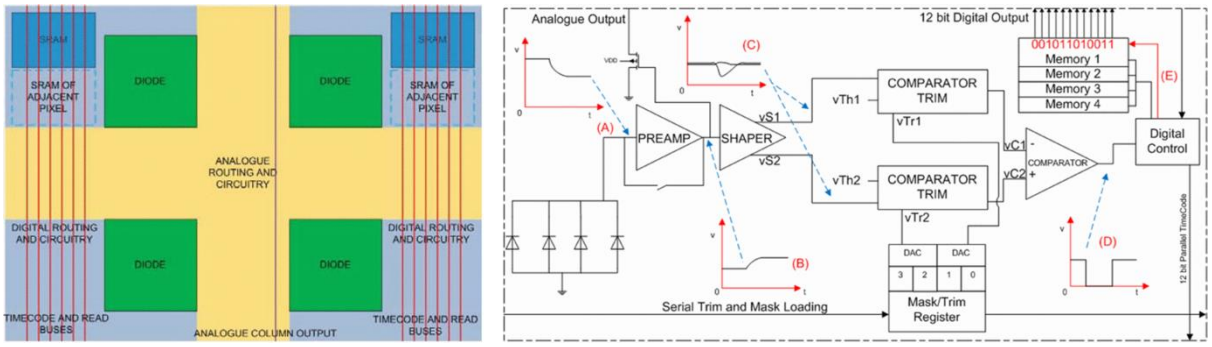

Figure 47 – Left: layout of a PImMS sensor pixel, showing the positions of the charge-collection diodes and the circuitry. Right: schematics of the circuitry of a PImMS sensor pixel. Adapted from Sedgwick *et al*[93].

Following the preamplifier, the signal enters shaper circuitry to create a differential output pulse (signal (C)) which enters comparator circuitry to perform a thresholding function. If the signal exceeds the pixel threshold, the comparator will generate a digital pulse (signal (D)). Setting the threshold of the pixels is described in detail in Section 8.1. The digital pulse triggers the digital controller to store the current timecode from the previously mentioned digital clock counter into the first available 12 bit memory register (signal (E)). Once the timecode is stored, the digital circuitry updates a memory pointer to indicate that the memory register is full, and that the next hit should be written to the following memory register. Four memory registers on each pixel allow the recording of four timecodes. The thresholding process and storage of multiple timecodes is represented in Figure 48.

If the signal crosses over the threshold (which causes a timecode to be recorded), the signal must fall back below the threshold value before another timecode can be recorded. This is because the generation of the digital pulse by the comparator is performed on the rising edge, as shown in Figure 48. This recovery period is known as the "dead-time", as the camera cannot record an ion hit during this interval. The dead time for an individual pixel is typically on the order of several hundred nanoseconds, with higher intensity signals expected to have a longer recovery time than lower intensity signals. It is worth noting that incident particles or photons arriving during the recovery period will have the effect of increasing the magnitude and width of the shaped signal, further extending the dead-time. It is also worth emphasising that only the pixel that has just registered a signal experiences the dead time; nearby pixels can still record incident particles.

Each PImMS sensor contains a single “test pixel” in the top left corner of the array. This gives direct access to the two shaper output voltages, the two comparator inputs and the comparator output. These outputs are used for debugging and characterisation.

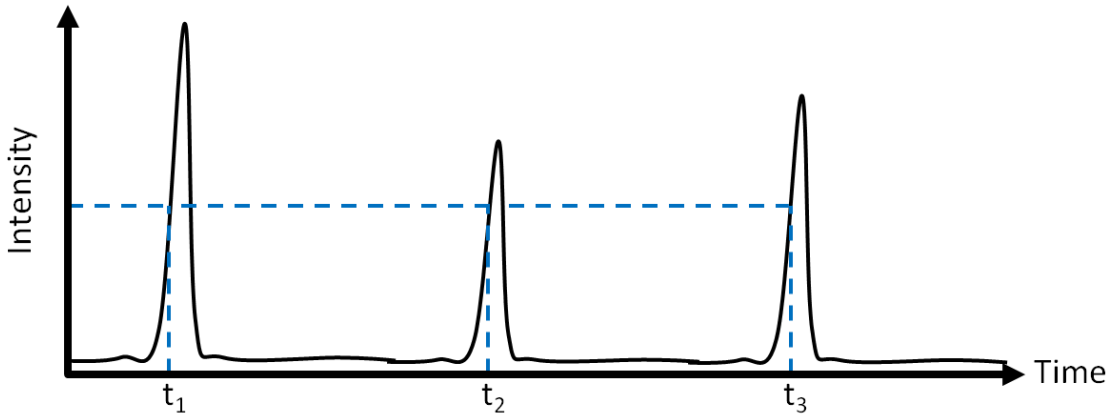

Figure 48 – The basis of detecting signal at multiple points during the same experimental cycle using the PImMS sensor pixels. In this example, the three peaks due to signal cross the digital threshold, shown as a dashed line, and three timecodes, t_1, t_2, and t_3, are stored to the pixel memory registers.

6.4 Readout from the PImMS Sensor

The PImMS sensor can operate in two readout modes: "analogue and digital output"; or "digital output only". In the "analogue and digital output" mode, the digitised signal representing the total charge during the experimental period (signal (B) in Figure 47) is read out as a 16-bit two-dimensional array, along with the four 12-bit two-dimensional arrays containing the population of the pixel memory registers. The array sizes match the dimensions of the sensor, with each array element corresponding to a particular pixel. The "digital output only" mode provides the digital signal without the analogue data. Readout for both sensors is currently performed using a USB2 interface. The PImMS1 sensor operates at readout rates of up to 550 Hz with digital and analogue output and 660 Hz for just digital output, although the readout rate is limited to ~300 Hz by the USB2 interface. The much larger PImMS2 sensor currently operates at a maximum readout rate of ~15 Hz for digital output. The readout rates of both sensors should increase significantly with the planned implementation of a CameraLink interface, as the protocol allows a higher rate of data transfer.

The readout is performed by the Video FPGA firmware provided by aSpect, which for PImMS1 in "analogue and digital output" mode, reads data out from the sensor as five 72 × 72 arrays. The first four arrays contain the arrival times stored in each timestamp memory and the fifth contains the analogue image. In "digital output only" mode, the first four arrays, corresponding to the digital data, are read out. LabVIEW software has been developed in-house to process and store the incoming data; this is described in more detail in Section 7.1. The data is stored in the format (*x*, *y*, *t*, *m*, *n*), where *x* and *y* denote the pixel coordinates, *t* is the timecode, *m* the acquisition cycle, and *n* the memory register that the signal was stored in. During the readout phase, the sensor is not active, and

the sensor requires approximately 250 µs after readout to reset before the next acquisition cycle commences.

Each pixel can also have the comparator disabled, which allows an analogue signal to be read from the pixel but prevents any digital signal from being written to the memory registers. Disabled pixels are known as *masked pixels* and the pattern of disabled pixels is referred to as the *mask*. Masking pixels is beneficial as it can be used to circumvent an issue in CMOS technology known as *power droop*. Writing a timecode value to a pixel memory register requires current to be supplied to the pixel location, and attempting to simultaneously write to the memory register of many pixels in the same area may demand too much current in a local area of the sensor. This produces errors in the values stored in the memory registers. For the PImMS1 sensor, this becomes apparent when an area larger than approximately 30 × 30 adjacent pixels is illuminated during the same acquisition cycle. For typical uses of the PImMS sensor, the signal does not approach this limit and power droop should therefore not be an issue during normal operation. However, during calibration, settings are accessed which would be expected to illuminate all pixels at the same time, and without the appropriate application of masking, calibration of the sensor would not be possible. The sensor calibration procedure is elaborated on in Section 7.

7 The PImMS Sensor Software

The software used in the PImMS project consists of two packages: software used for acquisition of data from the sensor; and software used to process the data once it has been recorded. This section describes the advances made in both areas. Software development has formed a major part of the research within this D.Phil. One of the most important developments was a calibration routine for the sensor, which is described in detail in Section 8.

The term “online processing” refers to any data processing that is performed in real time as the data is read from the detector to the computer. This includes visualising the images acquired from the sensor in real time or filtering noise from the data before it is saved to disk. Conversely, “offline processing” involves performing analysis algorithms on data that has already been stored to disk after the experiment. This could apply to visualising the image associated with a particular timebin accumulated over the course of the entire experiment or to operations too computationally demanding to be performed in real time. To store each revision of the software, a Subversion server[95], also known as an SVN, was established. This allowed any unsuccessful software modifications to be reversed easily, as well as providing a constant backup and centralised distribution server hosting the latest software version for users.

7.1 The PImMS Sensor Acquisition Software

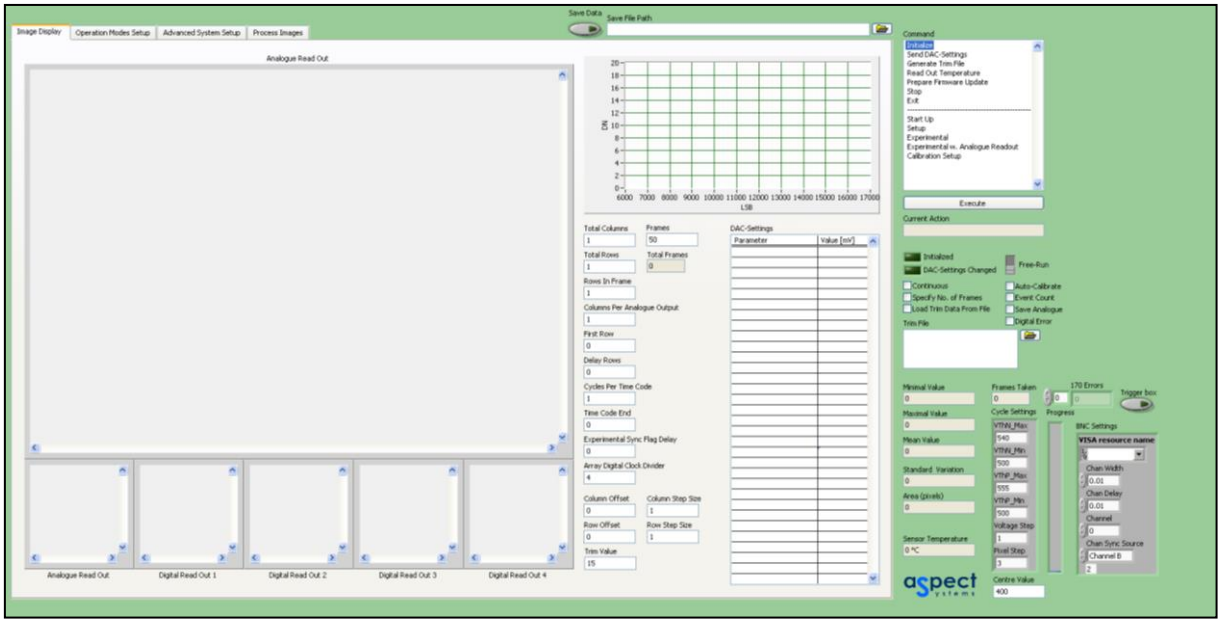

Figure 49 – A screenshot (before data acquisition) of the main PImMS acquisition program with numerous front-end modifications visible, including data saving, calibration settings and online digital error analysis.

Basic software was provided with the camera by aSpect that allowed data to be read from the sensor and displayed on a user interface. The software allowed a number of operating parameters to be controlled, such as the sensitivity of the sensor and the width of each timebin. The base software has been modified multiple times to increase the functionality, user friendliness and the suitability of the software for acquiring data from a variety of experiments. Although a full description of the changes made is beyond the scope of this document, the following sections give examples of some of the notable features that have been implemented. The front end of the acquisition software is shown in Figure 49.

7.1.1 Saving Data

The aSpect base software provided no method of saving the data. This was one of the first modifications made, providing a foundation for data analysis to be performed on the saved files. When the camera is used to acquire the digitised analogue[a] and digital data, as is the case for the majority of experiments, each acquisition cycle returns a two-dimensional array, consisting of five subarrays matching the size of the sensor (72 x 72 and 324 x 324 for the PImMS1 and PImMS2 sensor, respectively) appended consecutively. The five subarrays contain the analogue image and the timecodes stored in each pixel for each of the four timing registers. Under normal operating conditions, the signal level is relatively low, with only a few pixels storing digital signal on each experimental cycle. The digital data can therefore be reduced in size, without any data loss, by converting any signal to *x, y, t, acquisition cycle, register* format before being saved. This is a more efficient storage format, provided that fewer than 20% of the memory registers across the sensor are populated in a given acquisition cycle (as each signal data point is now represented by five integer values instead of one integer being stored in the case of both signal and absence of signal). To put this in perspective, this corresponds to 4,147 incident ions per acquisition cycle for the PImMS1 sensor and 83,980 for the PImMS2 sensor. The digital data is saved as a tab-delimited ASCII text file, with each data point being written to a new line. The main reason for this choice of file format was to allow end users of the sensor to analyse the data in the programming language of their choice, as opposed to other file formats that may have been language specific.

The analogue data can be extracted from the native two-dimensional array relatively easily. An option was added to the acquisition software to allow the complete analogue frame to be continuously appended to a file for offline analysis, such as correlating high intensity signal in the analogue display to data points in the digital data files.

[a] For convenience, the digitised analogue image will be referred to as the analogue image in this section.

Another method of saving data was developed for the calibration process, in which the previously-mentioned data format contains significant amounts of redundant data. The event-counted data option records the number of digital signals recorded by each pixel accumulated over multiple frames. The motivation and details behind this choice of data storage protocol during calibration are elaborated on further in Section 8.2.4.

7.1.2 Data Visualisation

The base software from aSpect provided the facility to display the population of each memory register acquired for each acquisition cycle as a two-dimensional image representing the incident signal for that particular cycle. A number of new visualisation tools have been integrated into the main acquisition program for online display during experiments. Most of these tools can be set to display the data acquired from the most recent (user-specified) number of frames to allow a statistically more reliable representation of the data. For example, a histogram of timecodes recorded by the pixels can be plotted to yield the TOF spectrum of the detected particles. This provides a simple and reliable way of identifying mass peaks during an ion imaging experiment, and the signal can quickly be compared with the signal from a photomultiplier trace to verify that the PImMS sensor is being triggered correctly.

One of the most useful tools that has been developed is a two-dimensional image display that only shows the signal associated with a user-specified time range. The routine works well when combined with the previously mentioned TOF spectrum plot, which allows the location and width of peaks of interest (and therefore the time range of interest) to be identified easily. A scale bar above the TOF spectrum allows users to specify a timebin range for which the images should be displayed. An example of the use of both the TOF spectrum and the image display is shown in Figure 50.

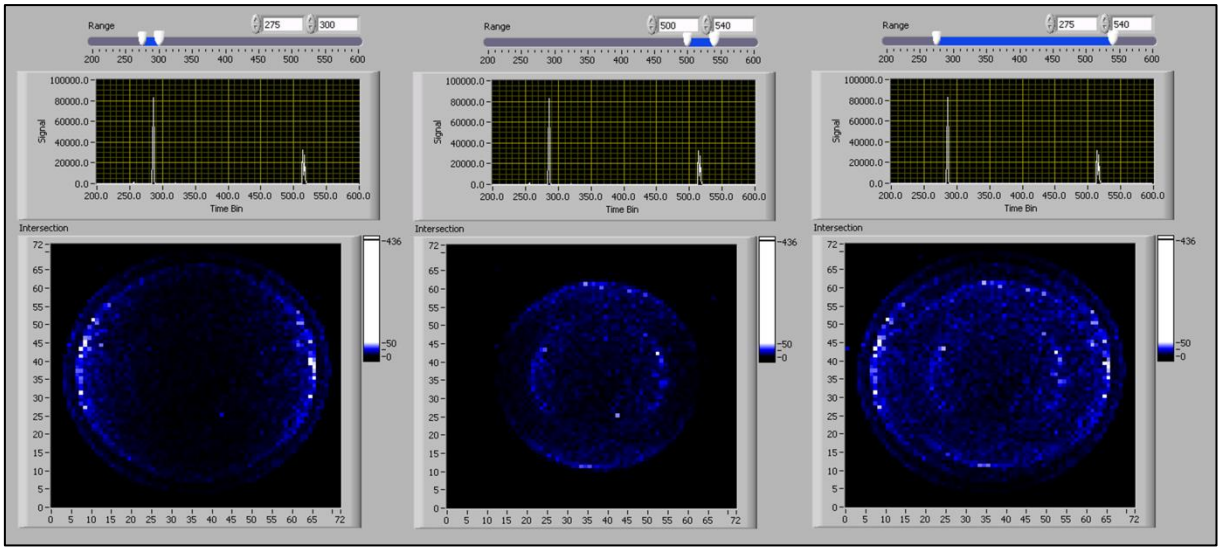

Figure 50 – An example of the use of the two-dimensional image display. The data shown is from the experiment described in Section 9.3, in which the first and second peaks in the TOF spectrum are due to electrons and Br^+ ions respectively. The slide bar shown at the top of the figure is used to specify the range of timebins for which the 2D image is plotted. Left to right: the TOF spectrum and the image obtained by integrating between timebins 275-300, 500-540 and 275-540, showing the image associated with the electrons, the Br^+ ions, and the combination of the two images, respectively.

7.1.3 Online Digital Error Analysis

An analysis of digital data files revealed a number of erroneous data points with a very low occurrence rate. For example, the same pixel in the same frame could show later registers having timecode values lower than time values recorded in earlier registers. Due to the way that the pixel architecture was designed to operate, this was likely due to a bug within the detector firmware. Similarly, it was also seen that pixel memory registers were occasionally omitted i.e. registers 1, 2, and 4 recording timecodes but not register 3.

The underlying cause of these errors was often firmware bugs that could be corrected once characterised properly. The nature of the errors sometimes made it difficult to identify erroneous data points – for example, one of the major firmware flaws caused timecode values to be corrupted by occasionally changing a random bit in the binary representation. However, this bug could not be isolated when a single timecode was recorded by a pixel, as no distinction could be made between corrupted and uncorrupted signal.

A program was written that could analyse the data online and assess whether the data contained an identifiable digital error according to a set of pre-specified parameters. When erroneous data was detected, a line was written to a digital error file with the following values:

x-pixel, y-pixel, register 1 timecode, register 2 timecode, register 3 timecode, register 4 timecode, digital error type

The *digital error type* was a parameter that represented the type of digital error detected. As the occurrence of identifiable digital errors was very low, these files became extremely valuable during debugging for analysing the identity of timecodes generating errors, and the frequency with which the errors occurred.

7.1.4 Acquisition Mode

The PImMS camera can be set to acquire data in two different modes: free-running mode, in which the camera acquires as rapidly as the acquisition and readout cycle will allow; or triggered mode, in which the acquisition cycle begins once an external trigger is received. Experimental procedure often involves first using the camera in free-run mode to focus the image, and then switching to triggered mode so that the sensor acquisition cycle is synchronised with other timing parameters of the experiment, e.g. a laser pulse that marks the beginning of the ion time-of-flight sequence. Additionally, development and debugging the sensor often involved switching between the two modes.

In the original version of the software provided by aSpect, it was only possible to switch acquisition modes by altering a section of source code within the acquisition program. Changing the acquisition mode therefore involved shutting down both the camera and the acquisition program, manually altering the code and restarting the software and camera. Restarting would reset all of the camera parameters, making the reproduction of an experimental setup difficult. The software was modified to allow the mode to be changed via the user interface whilst the camera was running. This is not only much more convenient and significantly faster than the previous procedure, but also allows the detector to be used by end users who do not have extensive knowledge of the program structure and programming language.

7.1.5 Pixel Memory Population Analysis

During the development of the software, concerns were raised regarding saturation of the capacity of the four memory slots on each pixel due to experimental conditions outside those modelled by the simulations described in Section 6.4. For example, this might be possible during a VMI experiment in which parent ions of a number of different species, and therefore different masses, are formed. The loss of a single electron in the formation of a parent ion has a negligible effect on the ion velocity due to the difference in mass and the parent ions are hence expected to all strike the central pixel. A modification was written to perform an online analysis of the pixel memory population. The resulting algorithm can either plot a simple histogram showing how often a pixel or pixels have recorded a

digital signal or can display a two-dimensional image of the sensor with colour representing how many memory registers have been used. Any pixels that have all four memory registers consistently filled are easily identified.

7.2 Post-Processing of the PImMS Sensor Data

Several post-processing techniques have been developed in order to improve the quality of the "raw" images acquired from the PImMS sensors. These, along with many of the visualisation tools described above, were amalgamated into the PImMS Post-Processing Suite, a user interface that allows the user to quickly and easily select operations to perform on the data set and to visualise the result. The intention of this was to provide a compiled program that delivers the full range of post-processing options to users. The program also generates a detailed log of each operation performed, and allows the data to be stored and recalled from memory. The front-end of the Post-Processing Suite is shown in Figure 51.

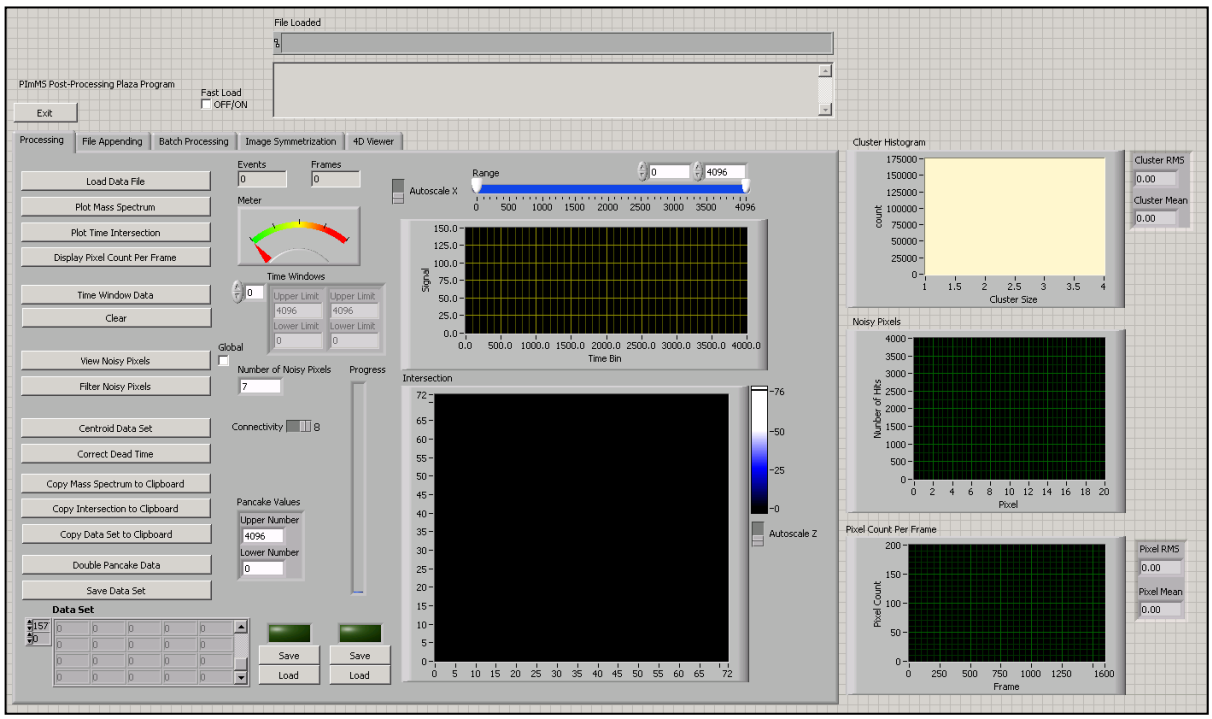

Figure 51 – The user interface of the PImMS Post-Processing Suite. All image processing techniques and visualisation methods are easily accessible.

The PImMS Post-Processing Suite was designed with an event-driven architecture, meaning that it responds to user commands as opposed to constantly polling the data. This significantly reduces the computational demands and makes the program more responsive. An entire data file can be loaded into memory for processing, or a quick-load option can be selected. In the latter case, a small portion of the data is loaded in order to allow data to be quickly manipulated, generally to investigate

whether analysis of the full larger data set is warranted. Each analysis operation can be performed independently and in any order. The program also allows multiple files to be loaded as a single data set (for experiments that consisted of several data files) as well as offering a number of new image processing features such as symmetrisation, anti-aliasing and background subtraction.

A meter on the front panel of the user interface indicates the size of the data set; since some operations are computationally intensive, the meter provides a rough indication of how long the various algorithms are likely to take to complete. Large data sets can quickly be decimated by noise filtration and time-windowing, both of which are described below.

7.2.1 Time-Windowing

The program supports decimation of the data for user-specified time windows. Multiple windows can be specified, allowing many peaks in the time dimension to be isolated. Time-windowing provides an efficient way of reducing the size of the data set, either by removing time regions in which noise is the dominant source of "data", or by focussing on the signal due to a single peak.

7.2.2 Viewing and Filtering of Noisy Pixels

The behaviour of pixels with respect to the threshold settings is described in more detail in Section 8. One of the important characteristics of the PImMS sensor is that pixels have a very sharp noise response with respect to lowering the threshold. As shown in Figure 54, a relatively small change of 3 mV in the threshold can cause a pixel to go from a completely noiseless state to a state that is dominated by noise, with all memory registers filled[b]. Experiments were generally performed under conditions that would maximise the sensitivity of the entire sensor, at the expense of a small percentage of pixels being saturated by digital noise. In post-processing, it was therefore essential to identify and filter these noisy pixels.

Taking advantage of the sharp noise response, noisy pixels can be identified by looking at the total digital count for each pixel. As noisy pixels typically fill all memory registers in each frame, the total digital signal is usually at least an order of magnitude higher than non-noisy pixels. Figure 52 shows an example of a data set with six noisy pixels, and clearly demonstrates how much higher the summed count rate in these pixels is compared with pixels experiencing normal signal. Noise can be filtered from the data set once the noisy pixel locations have been successfully identified. Due to the high frequency of noise, noise filtering can significantly reduce the size of a data set without removing signal.

[b] For reference, *VThN* and *VThP* values (defined in Section 8.1) are usually around 400 mV during an experiment.

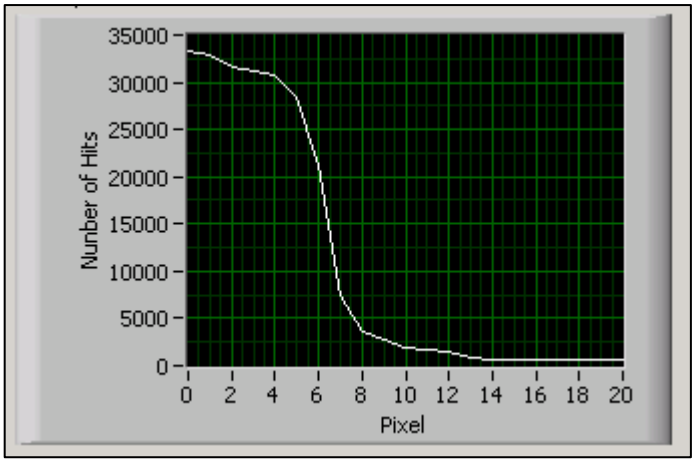

Figure 52 – An example of the display from the noise identification algorithm. The noisy pixels are easily discerned from those recording signal by the significantly higher count rate. The graph indicates six noisy pixels in this data set which can be easily filtered.

7.2.3 Spatial Centroiding

The improvements in spatial resolution achievable through centroiding in ion-imaging experiments are discussed in Section 3.4. One of the difficulties in implementing this for the PImMS sensor data sets is the fact that the data must be centroided in three dimensions (*x*, *y*, *t*) rather than simply in two (*x*, *y*) dimensions as in conventional single mass imaging measurements. An additional complication is that an ion stimulating several pixels may have data saved in different memory registers in the different pixels.

The algorithm developed to centroid the data works as follows:

1. The data set (in *x, y, t, acquisition cycle, register* format) is divided up into separate acquisition cycles.
2. For each cycle, the 3D (*x*, y, *t*) data set of detected signals is constructed. In a single cycle, the recorded signal at a particular value of *x, y, t* is binary, with an intensity of either 0 or 1.
3. Each time slice in the *t* dimension is indexed as a 2D image (*x* and *y*). If the 2D array contains signal, it is centroided using the routine described in Section 3.4.
4. The 3D data set is reassembled from the centroided 2D images and the data converted back to *x, y, t* format. The register value is necessarily removed in this step.
5. The process is repeated for each frame in the data set.

The resulting data set is stored in memory and can be further processed or visualised using the routines described previously. The algorithm also outputs statistics from the centroiding process, including a histogram of the cluster sizes, the mean cluster size, and the percentage reduction in the size of the data set.

7.2.4 4D Data Display

This visualisation tool provides a four-dimensional display in which the accumulated signal intensity is plotted as a function of *x*, *y*, and *t*. The algorithm is too computationally intensive to be performed online in order to view the entire data set during data acquisition, but is extremely useful during post-processing. The coordinates *x, y* and *t* are plotted as the *x, y, z* dimensions in 3D space, with the colour of the data point representing the intensity of the signal summed over multiple acquisition cycles. This display mode provides a visual representation of the data set across the time window of interest. User options include intensity thresholding (removing low intensity noise recorded in the experiment), control of the range of all three axes, and display options include control over the size and shape of each data point and the colour scale used to indicate signal intensity. The 4D display module was used to create many of the figures showing experimental data for the experiments described in Section 9 and an example is shown in Figure 53.

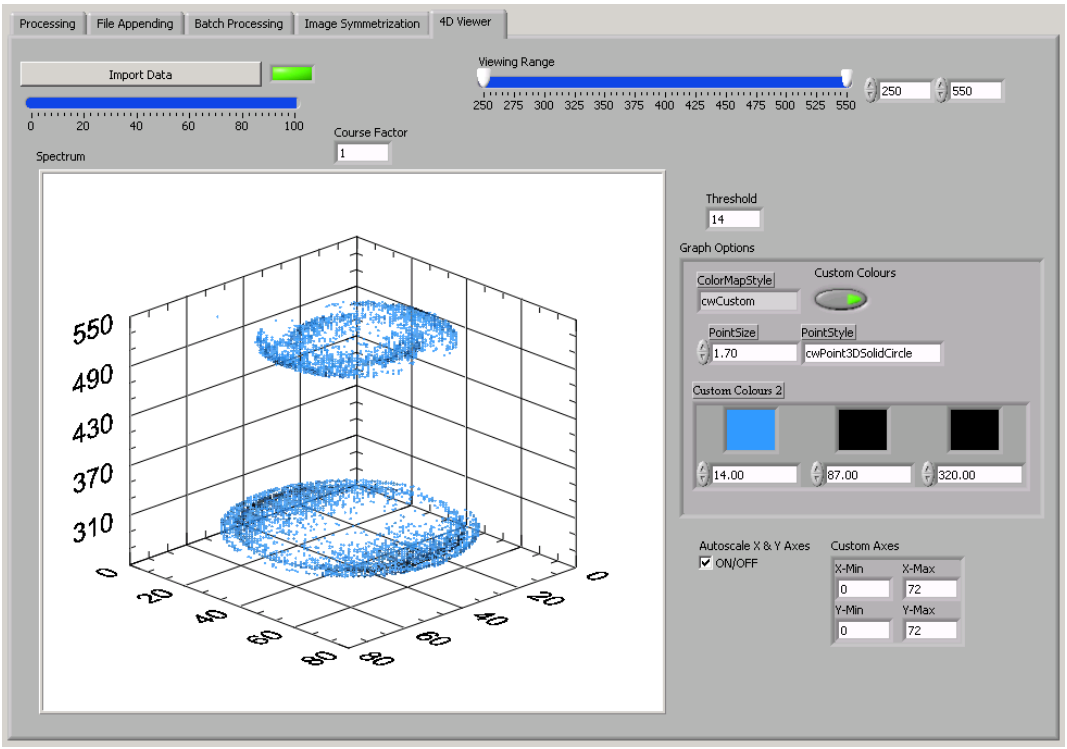

Figure 53 – An example of the 4D Data Display in the PImMS Post-Processing Suite. The display options are shown on the right, and include the axis range in all three dimensions, point size and shape and custom colours.

7.2.5 Digital Error Viewer

The digital errors from the camera are described in Section 7.1.3. Code was written to analyse an error file and display the temporal and spatial data to help discern the nature of the errors. This was helpful in identifying timecodes within which errors frequently occurred, as well as any characteristic spatial distribution of the errors across the sensor.

8 The PImMS Sensor Calibration Procedure

The physical attributes (length, width, and oxide thickness) of transistors, resistors and capacitors fabricated in a CMOS process are subject to a certain degree of variation, known as "process variation". The effects of this variation become more pronounced when the components become smaller, as the variation becomes a larger percentage of the full width or length of the device. The use of over 600 transistors per pixel in the PImMS sensor, and the inherent process variation, leads to a difference in detection sensitivity from pixel to pixel. This means that for pixels with identical settings, a different minimum intensity of light is required for a digital hit to be registered. In order to correct this discrepancy between pixels, a calibration routine was devised and implemented. The calibration routine must be performed for each individual sensor, as each sensor has a different level and pattern of variation between the pixels.

8.1 The Calibration Routine

The digital signal threshold, which determines the sensitivity of each pixel, is controlled by three variables: Voltage Threshold Negative (*VThN*), Voltage Threshold Positive (*VThP*), and *Trim*. These three variables are used in the comparator circuitry, as shown in Figure 47. *Trim* is a 4-bit integer, taking values between 0 and 15. Each pixel can be assigned a *Trim* value independently of the other pixels, which determine the digital threshold of the pixel. The effect of different *Trim* values is described below. *VThN* and *VThP* take values between 0 and 1000 mV and affect all pixels across the sensor uniformly. An increase in the value of (*VThP – VThN)* causes a decrease in the digital threshold across the sensor. Because the difference between the values of *VThP* and *VThN* is the determining factor, it is useful to define the difference (*VThP – VThN*) as *Voltage Threshold* (*VThres*). Overall, *Trim* can be used to equalise the sensitivity of all pixels, and *VThP* and *VThN* can be used to control the global sensitivity of the sensor.

The first step in the calibration procedure is to determine the sensitivity of each pixel relative to the rest of the pixels in the sensor. The sensitivity of a pixel can be determined by scanning across a large range of thresholds and monitoring the signal recorded by the pixel under dark conditions. In dark conditions, when the threshold is set to a low value, noise in the pixel circuitry can cause signal to be recorded. The optimum threshold for a pixel should be as low as possible without noise being recorded, thereby maximising the sensitivity to signal. The initial pixel sensitivity is determined by setting the *Trim* value to 15 across all pixels and changing the values of *VThN* and *VThP* such that *VThres* ranges from -100 mV to +200 mV. The reasoning behind setting *Trim* to 15 will be elaborated on below. At low values of *VThres* (high threshold), the pixel is insensitive and no signal (i.e. noise) is

detected under dark conditions. As *VThres* is increased (and the threshold is therefore decreased), the pixel begins to record digital signal arising from noise. Figure 54a) shows the ideal threshold response function of a single pixel to the value of *VThres* over 50 acquisition cycles. As each pixel has four memory registers to store digital hits, the maximum number of noise events that can be detected is 4 × 50 = 200. Once *VThres* is sufficiently high, noise saturates the pixel circuitry in such a way that the comparator only records the first noise event. This is because the comparator records digital signal when the signal from the diodes crosses above the digital threshold (see Section 6.1); under low threshold conditions, noise causes the threshold to be exceeded immediately without coming below threshold again during the experimental cycle, preventing a second digital signal from being detected. Hence, one event is recorded per acquisition cycle and is stored in the earliest available timecode of 1.

The threshold response function for each pixel on the sensor will have a characteristic peak width and value of the voltage threshold at which noise begins to appear. The threshold value at the rising edge of the response function can be used to quantify the pixel sensitivity, as it represents the lowest threshold that can be used before the pixel becomes noisy. Plotting a histogram of the rising edge values of pixels across the sensor shows the distribution of pixel sensitivities across the sensor. The distribution (shown in Figure 54) is approximately Gaussian, and can be fitted to a Gaussian function in order to quantify the sensitivity. A perfectly uniform sensor would have identical pixel responses for each pixel in threshold scans, and would therefore display an infinitely narrow Gaussian curve, essentially a delta function. In contrast, uncalibrated PImMS1 sensors have approximately Gaussian distributions with standard deviations of approximately 13 mV. Calibration of the sensor consists of modifying the individual pixel threshold response functions (Figure 14a)) in order to achieve the narrowest Gaussian distribution of pixel sensitivities. This is achieved by adjusting the *Trim* values for each pixel.

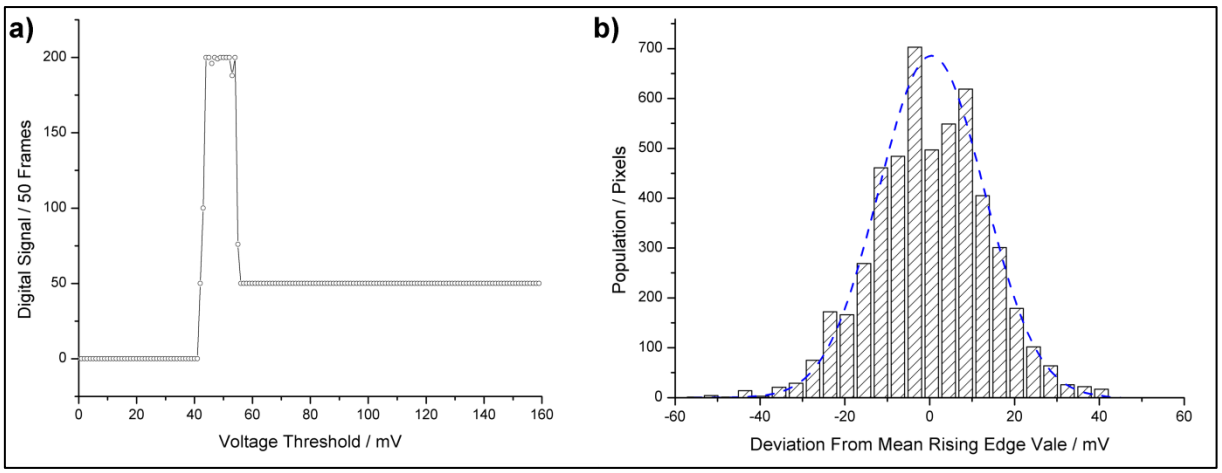

Figure 54 – a) The idealised pixel response to voltage threshold as noise recorded over 50 frames. Pixel sensitivity as Voltage Threshold increases (from left to right). b) A histogram showing the distribution of pixel rising edges before calibration. The standard deviation of the fitted Gaussian curve is 12.5 mV.

Changing the *Trim* value of a pixel alters the sensitivity, and corresponds to a horizontal translation of the peak in the pixel threshold response function shown in Figure 54a). Calibration of the sensor is achieved by selecting the *Trim* value for each pixel that results in the least deviation of the rising edge value from the mean rising edge value determined from the initial threshold scans, in which the *Trim* value for all pixels is set to 15. A *Trim* value of 15 is used for the scan across *VThres*, as it corresponds to a medium pixel threshold, thus allowing pixels to be raised or lowered in sensitivity by selecting other values of *Trim*. (N.B – *Trim* takes values between 0 and 15, but the threshold does not change monotonically with increasing *Trim*; thus although a value of 15 is at the limit of the range, the value represents a medium pixel threshold).

To determine the optimum values of *Trim* for individual pixels, the *VThres* scan is repeated for all possible values of *Trim.* This requires 15 more scans to cover the remaining *Trim* values of 0 to 14. Performing this process allows the noise profile to be determined for each pixel for each *Trim* value, which in turn allows the rising edge at each *Trim* value to be determined. Hence, calibration is achieved by choosing the optimum value of *Trim,* as defined previously, and the calibration file for a sensor consists of an array containing the optimum *Trim* value for each pixel in the sensor.

To test how well the calibration has worked, the pixels can be set to their calibrated *Trim* values and the *VThres* scan repeated in order to construct a 'calibrated' distribution of pixel sensitivities. As before, the rising edge values of the pixels are plotted as a histogram and fitted to a Gaussian to quantify the standard deviation in sensitivity in the calibrated state. A comparison of the resulting pixel sensitivity distribution for a PImMS1 sensor before and after performing the calibration procedure is shown in Figure 55.

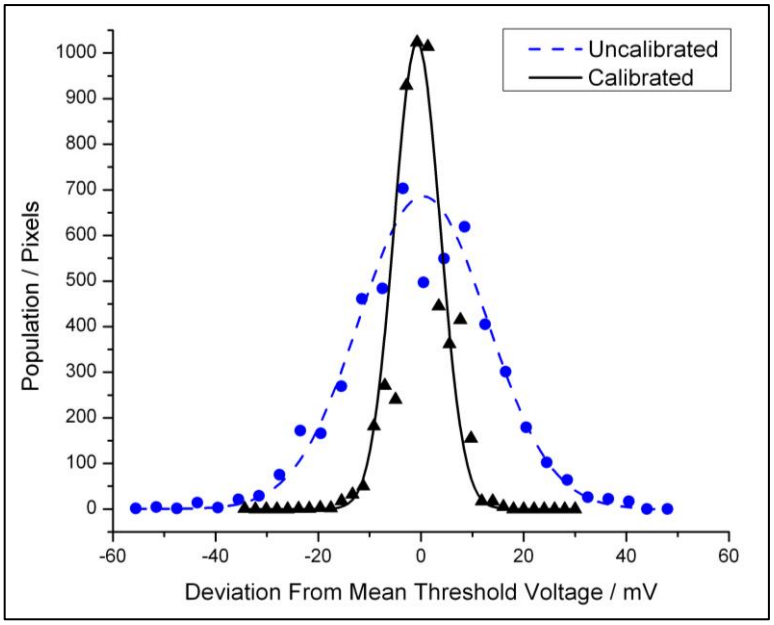

Figure 55 – A comparison of the spread of rising edge value from the global mean rising edge at a *Trim* value of 15, before and after calibration for a typical sensor. The standard deviation of the fitted Gaussian improves from 12.5 mV to 4.5 mV.

8.2 Development of the Calibration Routine

The discussion above presents an idealised version of the calibration routine. In practice, a number of additional steps were found to be necessary in order to establish a reliable calibration process. Several of these are described in the following sections.

8.2.1 Power Droop and Pixel Masking

As noted in Section 6.1, a problem known as power droop appears when attempting to write to the memory registers of a large area of adjacent pixels simultaneously. This is particularly problematic during calibration, since at particularly high *VThres* values, all pixels across the sensor are expected to experience digital signal due to noise within the pixel. Attempting to write this "noise signal" across the entire sensor would result in power droop skewing the initial pixel sensitivity characterisation. Masking is therefore used during the calibration process in order to disable eight out of nine pixels, as shown in Figure 56, which is the highest density of enabled pixels that avoids the issue of power droop. Instead of recording the threshold sensitivity functions across all pixels simultaneously, these scans are instead run for this subset of pixels, and the mask is then cycled to record functions for the next set of pixels. This necessary modification increases the time required for calibration by a factor of nine.

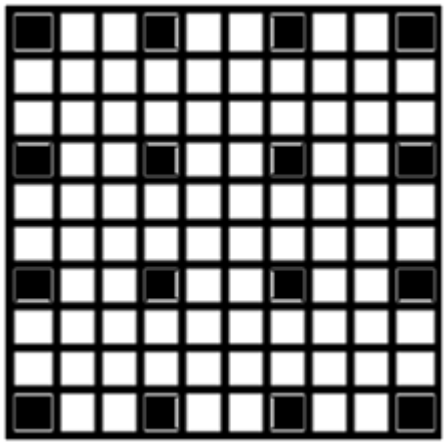

Figure 56 – A representation of the pixel masking pattern used during calibration. Black represents pixels that have the comparator enabled and are therefore able to record digital signal.

8.2.2 Masks Not Transferring Properly

There were occasions when the mask would not transfer from the computer to the camera properly, and a random distribution of pixels was powered instead of the expected uniform grid of pixels. This was due to a hardware communication bug with an occurrence rate of this error of approximately 0.1%. A subroutine was written that compared the data received from the camera to the mask that was last uploaded to the camera. If any pixels that should have been masked recorded digital signal, upload of the mask was repeated and the signal compared again. This filtering process occurred automatically, and, when implemented, eliminated the false data recorded when the mask was not transferred properly.

8.2.3 Pixel Response to Trim

The dependence of pixel sensitivity on *Trim* was initially determined for one pixel which was originally assumed to be representative of all pixels across the sensor (Figure 57a)). This would have allowed calibration to be performed by taking an initial *VThres* scan across the sensor and charactering only a single pixel. The ideal *Trim* value for each pixel could then be chosen based upon the properties of the characterised pixel. However, after some investigation, it was found that each pixel had a markedly different response to *Trim*, which arises due to process variation in the resistors used in the *Trim* circuitry. The difference in response to *Trim* values can be demonstrated by performing two *VThres* scans with a different *Trim* value across the sensor. Two rising edge values could then be extracted for each pixel, one associated with each *Trim* value. If all pixels responded to a change in *Trim* value equally, the difference between the two rising edge values should be equal throughout the sensor and correspond to a single value. However, a wide distribution for all different *Trim* values is seen. An example of this is shown in Figure 57b). The different responses to *Trim* necessitated characterising each pixel at each value of *Trim*.

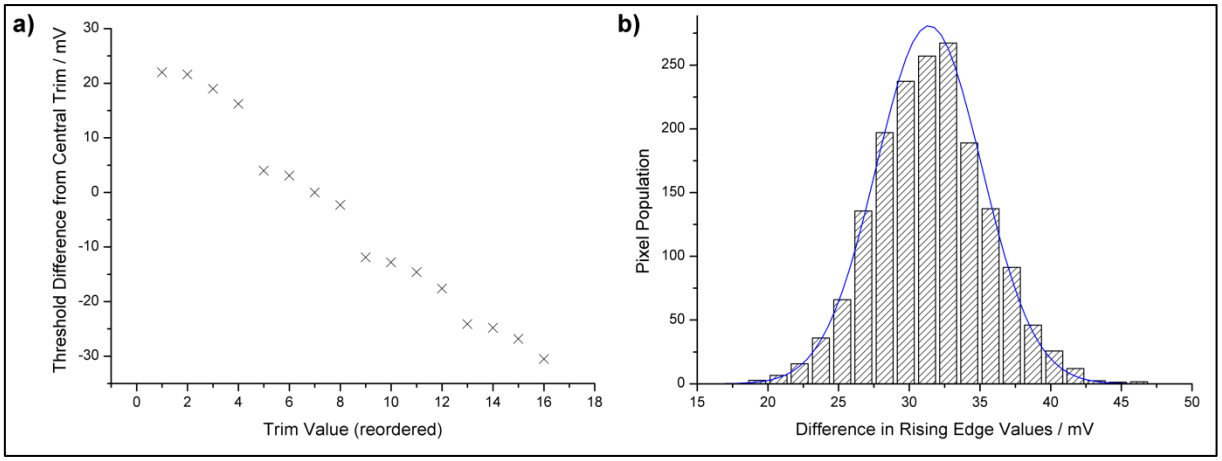

Figure 57 – a) The dependence of the rising edge (sensitivity) as a function of *Trim* value for a single pixel. The shape of the curve is discussed in Section 8.4. b) The difference in rising edge values pixel-by-pixel when changing *Trim* across the sensor. The change in *Trim* is equivalent to changing the value from 8 to 16 using the reordered *Trim* values in a). If all pixels responded uniformly to a change in *Trim*, the difference would be a single value. The fitted Gaussian has a standard deviation of 9.09 mV.

8.2.4 Event-Counted Files

During the calibration routine, low threshold values are accessed repeatedly and all pixels are expected to experience noise. The details of each noise signal (position, time, register and frame) were originally recorded during the calibration process, as it used the same code that was originally written to record signal. Saving the details of each noise event resulted in files approximately 700 MB in size for each calibration that was performed. In actuality, the only data parameter required at each *Trim* and *VThres* value is the number of noise hits that have occurred over the 50 recorded acquisition cycles. An online subroutine was written to analyse the data from the 450 cycles required for calibration (50 cycles each with the pixel mask in nine different positions). The routine outputs a 2D array with the same dimensions as the sensor, containing the number of noise signals generated by each pixel. The resulting array contains all of the necessary calibration data, and is saved for each acquisition during the calibration routine as an event-counted file. The size of the files resulting from a calibration using event-counted files is approximately two orders of magnitude smaller than when using the previous format. This reduces the disk space required to store calibration files, and also significantly reduces the processing time required, which was previously limited by the hard disk read speed.

8.2.5 Processing the Data Set

Processing the calibration data to produce a calibration file involves determining the optimum *Trim* value for each pixel. Achieving this using the files that were created by scanning *VThres* at each *Trim* value requires accessing the full data set for each pixel individually. Even with the use of event-

counting to reduce the volume of data stored (noted in Section 8.2.4), limitations on the maximum array size permissible in LabVIEW means that the complete data set cannot not be stored in memory as a single array. Reading in the data set for each pixel for the PImMS1 sensor would have taken over 72 hours due to the inefficiency of reading thousands of small files from a hard disk. Instead, a workaround was created that allows the full data set to be stored in memory through the use of memory queues, which only require the data to be read from disk once. This reduces the processing time to a matter of seconds instead of hours.

8.2.6 Determining the Rising Edge

Developing a robust algorithm for determining the threshold voltage corresponding to the rising edge in the pixel threshold response function required some thought. The pixel response to changing *VThres*, shown in Figure 54a), is idealised; in reality, the noise experienced by a pixel is subject to statistical variation and the response is not completely predictable. Figure 58 depicts a more representative case, in which outlying data points may arise from noise experienced at high thresholds and a lack of noise experienced at a low threshold. In order to detect the rising edge accurately, a combination of point-to-point comparison, data smoothing, and thresholding was first used to remove erroneous data points. The rising edge value was then determined by interpolating between the first occurrence of the global maximum (when the four memory slots were full on all 50 cycles) and the first global minimum that preceded it (i.e. between the beginning and the end of the rising edge). This process was found to identify the rising edge value accurately and consistently, even for pixels experiencing significant deviation from ideal behaviour.

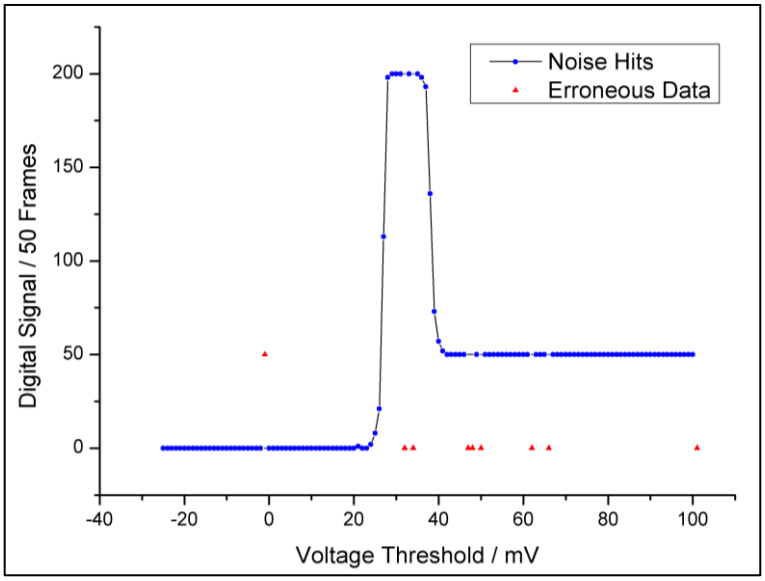

Figure 58 – An example of measured pixel response to changes in Voltage Threshold with an ideal response shown. Erroneous data points are highlighted in red.

8.2.7 Automated Calibration

During the development of the calibration routine, the *VThres* scans, stepping through the *Trim* values, saving of the data, and the subsequent processing and analysis were performed separately by the user. Once the routine was finalised, each of these tasks was combined into a single automated routine that performed the full calibration. Automation conferred a number of benefits:

- Simplicity of use – calibration completed with a single button click, resulting in a calibration file that could be used without further processing;
- Automatic meta-data tagging, noting the time that a calibration took place, the camera parameters that each measurement was taken with and which camera and sensor combination the calibration was performed with;
- Systematic creation of files and folders – this allowed analysis of the calibration procedure itself to be performed much more easily as the files were in a consistent location;
- "Hard-restarts" – a feature was added that automatically logged the progress of the calibration. At times when a calibration was interrupted (e.g. power failure, system crash, repurposing of a computer), the calibration routine could be resumed, even if the computer and the camera were both depowered.

The automated calibration routine takes approximately 20 hours to complete for a PImMS1 sensor.

8.3 Testing of the Stability of Calibration

To test the stability of the calibrated sensor, two *VThres* scans were performed using the same calibration file. This allowed the calibrated rising edge values of each pixel to be determined twice. It was found that, across the sensor, only six pixels (~0.1%) showed deviations of 4 mV or greater in their rising edge values between the two *VThres* scans.

Another test compared the results of two calibration routines on the same camera and sensor. The rising edges of the pixels were again compared. A perfectly reproducible calibration would return the exact same values for calibrated rising edge values. In practice, over 98.5% of pixels had no more than a 10 mV difference in the values. 10 mV is the approximate difference in sensitivity between consecutive *Trim* values, which governs the resolution of calibration.

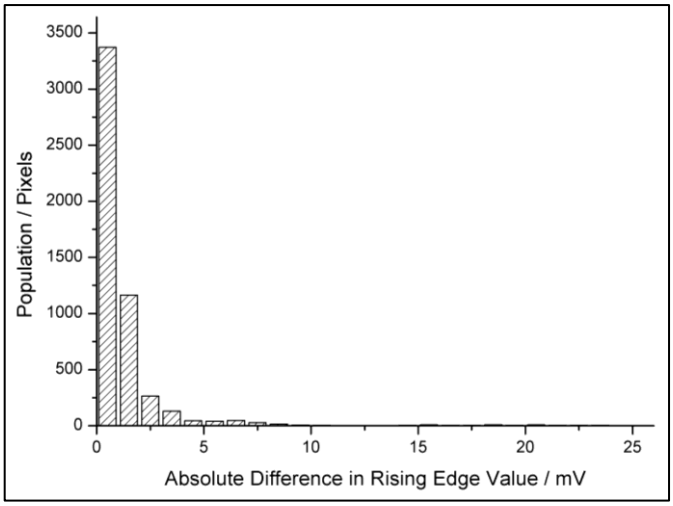

Figure 59 – The distribution of differences in rising edge values between two independent calibrations carried out on the same camera and sensor.

8.4 Design Considerations for the PImMS2 Sensor

Analysis of the data from calibration of a number of PImMS1 sensors showed some interesting features, which led to a change in the pixel design during the design phase for the second-generation (PImMS2) sensors. A plot of the mean pixel rising edge values as a function of *Trim* value is shown in Figure 60. The number of pixels assigned each *Trim* value after calibration is noted by the size of the circles associated with the points on the graph. The data is also tabulated in Table 4. The first four *Trim* values are only used by two pixels (a negligibly small number) indicating that the total range of thresholds provided by the 16 *Trim* values is too large. Spreading the available number of *Trim* values across a smaller range of thresholds would improve the resolution of the *Trim* feature, allowing more precise control of pixel sensitivity during calibration. Similarly, the non-linear response to *Trim* that was found for the test pixel (shown in Figure 57a) was found to occur across the sensor. The non-linearity reduces the ability to tune the pixel sensitivity optimally. Both of these issues lead to a reduction in the uniformity achievable in pixel sensitivity during calibration. Based on these observations, the PImMS2 sensor design was modified to enable the *Trim* range to be adjusted and to allow the shape of the *Trim* response curve to be modified. This should allow improved uniformity of pixel response to be achieved in the PImMS2 sensor relative to the PImMS1 prototype.

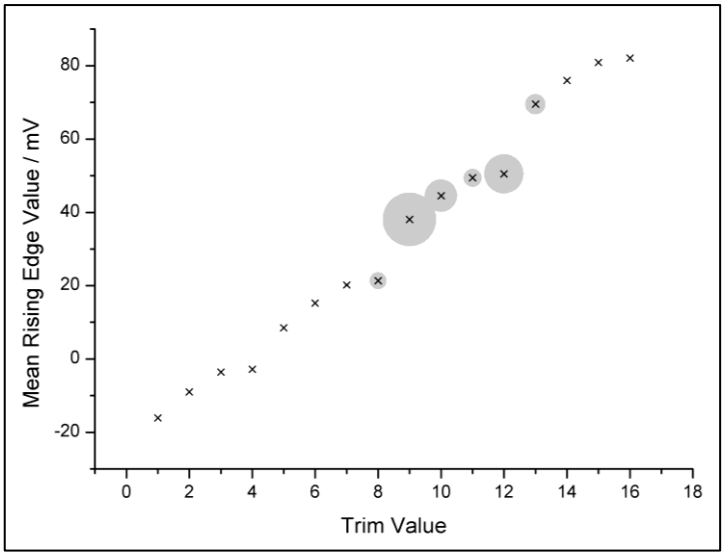

Figure 60 – A representation of the mean rising edge of pixels across a sensor at different reordered *Trim* values. The extent of the circles associated with each point represents the number of pixels assigned that particular *Trim* value after sensor calibration.

Table 4 – The number of pixels that have been assigned a particular *Trim* value after calibration. Certain *Trim* values are under populated, which decreases the achievable resolution in pixel sensitivity.

Trim	Mean Rising Edge / mV	Pixel Population
1	-16.1	0
2	-9.0	0
3	-3.6	0
4	-2.8	2
5	8.5	17
6	15.2	38
7	20.2	116
8	21.3	453
9	38.1	1444
10	44.5	871
11	49.4	490
12	50.5	1063
13	69.5	550
14	76.0	91
15	80.9	16
16	82.1	3

9 Applications of the PImMS Sensor

The versatility of the time and position-resolved detection offered by the PImMS sensor allows it to be deployed in a variety of experiments, including a number that had not been envisaged at the time of design. The types of experiments in which the PImMS sensor has been utilised to date include:

- Velocity-Map Imaging (VMI);
- Coincidence Imaging;
- Spatial-map Imaging;
- Slice Imaging;
- Investigation of Molecular Motion;
- Investigation of Surface Photoreaction Dynamics;
- Detection of High Energy Alpha and Beta Particles;
- Neutron Imaging.

The advances in neutron imaging are described in detail in Part III. A selection of other applications is described in the present chapter.

9.1 Bench Testing of the PImMS Sensor using a Pulsed Laser

The fastest and easiest method of testing the operation of a new PImMS sensor is to use a pulsed diode laser to generate a known input signal for the detector and to compare the recorded data with the expected result. A pulse generator can be used to modulate the laser at a known frequency, and also to synchronise the laser pulses with the beginning of a PImMS acquisition cycle, ensuring that the value of recorded timecodes remains consistent over multiple frames taken. Pulsed laser irradiation has remained the best method of verifying that a PImMS sensor responds properly to external optical signals. The experimental setup can also be used to investigate the effect of lower intensity signal by regulating the intensity of the incident laser beam, either by changing the current through the laser diode or through the use of one or more neutral density filters. If the laser intensity is high, the sensors can be tested in an uncalibrated state, as high signal thresholds can be used to eliminate noise whilst still allowing signal to be registered. In the experiments described in this section, the same pixels are illuminated on each laser pulse. This is in contrast to the situation in VMI or spatial-map imaging experiments, in which ion signals illuminate different pixels on each experimental cycle. The consequence is that in the pulse laser experiments, each laser pulse is expected to populate one memory register, allowing up to four laser pulses to be recorded per experimental cycle.

The first experiment of this kind utilised a 405 nm laser emitting 25 ns pulses every 40 µs and an opaque piece of plastic with holes created by a pin to form an optical mask. Laser light was passed through the holes on the mask, illuminating a selected region of the PImMS1 sensor. The timing resolution of the sensor was set to 50 ns per timebin, meaning that each laser shot was expected to be separated by 800 timebins. Data from a single acquisition cycle was recorded and analysed, and was found to match the expected result perfectly. The 3D representation of the data set and histograms of each of the memory registers summed across the sensor are shown in Figure 61.

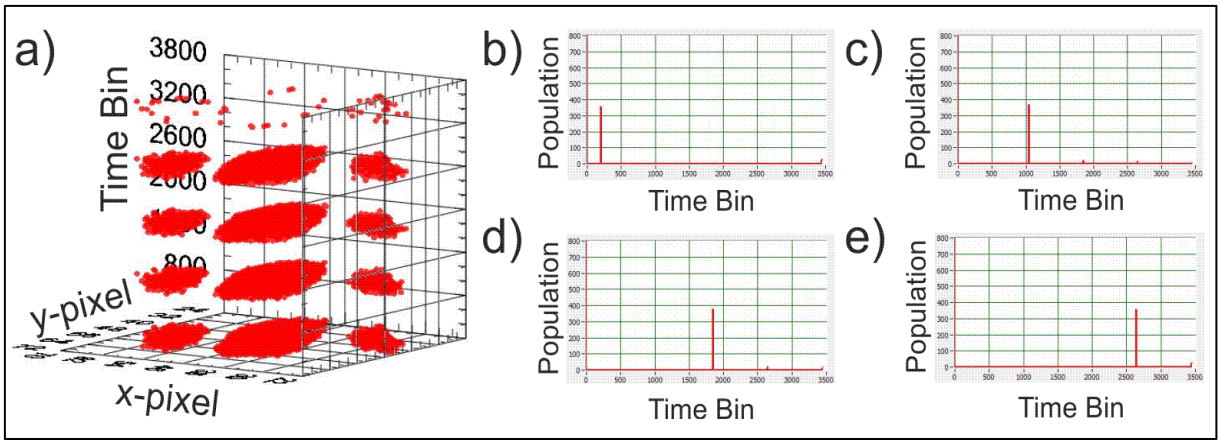

Figure 61 – a) A single frame of several laser pulses shone through a plastic mask. The ability of registering multiple events on the same pixel is clearly displayed. b)-e) show the population of memory registers 1-4 across the sensor. Each peak corresponds to a different laser shot.

The experiment was then repeated with the laser beam passing through a 2D diffraction grating, creating a pattern over a large area of the sensor. The width of the timebins was again set to 50 ns, giving a total exposure time of 204.8 µs. The laser pulse length was kept to 25 ns and the time between each laser pulse was set to 30 µs. This meant that a total of six laser pulses were incident on the sensor on each acquisition cycle. A neutral density filter was used to reduce the incident laser intensity so that the input signal was approximately at the level of the digital threshold of the sensor, and a pulse generator was again used to synchronise the laser pulses and the acquisition cycle of the PImMS sensor. Data was accumulated over 3,194 frames and the resulting image is shown in Figure 62. The first four laser pulses on each acquisition cycle are almost always detected, giving a high count when summed over all frames. However, occasionally one of the first four laser pulses would not exceed the pixel threshold and would therefore not populate a pixel memory register with a timecode. This meant that when the fifth laser pulse was incident on the sensor, the timecode could be recorded. By recording thousands of frames, the fifth and sixth pulse can therefore be seen relatively weakly in the data set.

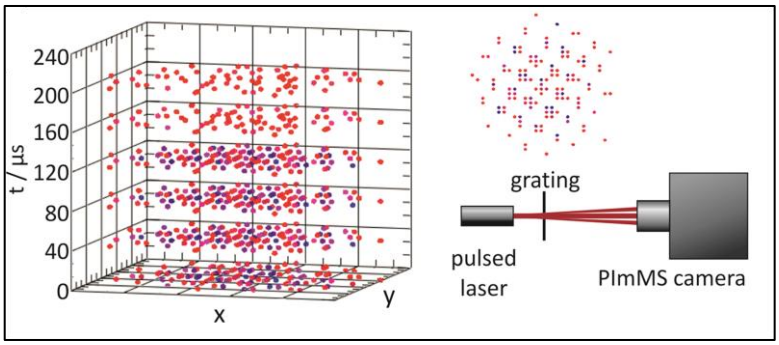

Figure 62 – A plot showing images from successive laser pulses acquired over 3194 frames. The colour of each data point indicates the total signal count; red to blue represents low to high intensity respectively. The fifth and sixth pulses have a lower intensity as the memory registers for most pixels have already been filled by the four prior laser pulses.

Once the ability to run the PImMS sensor at 40 MHz (25 ns per timebin) was established, a similar experiment was performed using two 650 nm pulsed lasers that illuminated different regions of the sensor. Each laser was operated at 250 kHz (4 µs spacing) with one laser offset from the other by 2 µs. The laser pulses were again synced to the PImMS sensor acquisition and 1,000 frames were accumulated. The results are shown in Figure 63.

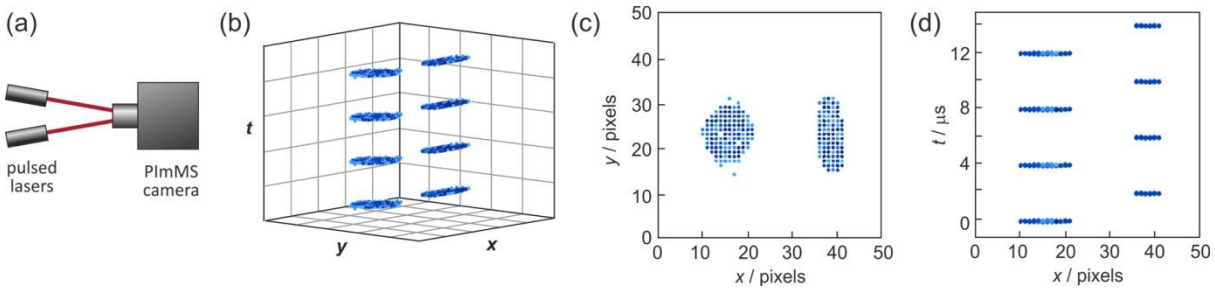

Figure 63 – Bench testing data from the PImMS sensor, consisting of images acquired by illuminating the sensor with a pair of pulsed diode lasers. a) Schematic of experiment; b) 3D plot of the signal acquired from eight laser pulses, four from each laser (pixel numbers have been omitted from the axes for clarity; see c) and d) for scales); c) top-down view of data set, showing spatial pattern of laser pulses on the PImMS sensor surface; d) (*x,t*) plot showing the acquisition of signal into the four available timestamp memories in the two illuminated regions of the sensor.

Following the manufacture of the PImMS2 sensor, verification of the temporal and spatial capabilities was performed using a 405 nm laser with 25 ns pulses separated by 30 µs. The PImMS sensor was operated at 40 MHz (25 ns per timebin), allowing four pulses during the acquisition cycle. 1,000 frames were recorded and the resulting time data and spatial data matched the expected result perfectly, as shown in Figure 64. Although calibration of the PImMS2 sensor had not yet been achieved, this test was still possible through a combination of high signal levels and high thresholding to improve the signal-to-noise ratio.

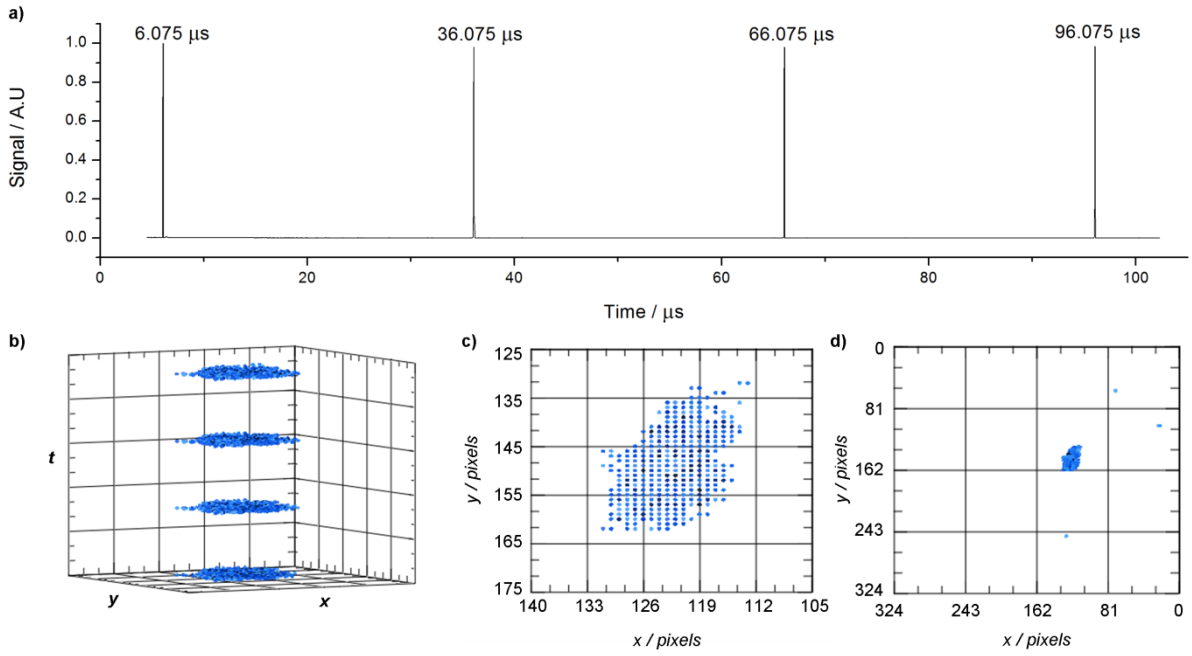

Figure 64 – a) The time data extracted from the data set showing the laser pulses of uniform height and spaced by exactly 30 µs; b) 3D plot of the signal acquired from four laser pulses, see a), c) and d) for axis scales); c) zoomed-in top-down view of data set, showing spatial pattern of laser pulses on the PImMS2 sensor surface; d) top-down view of data set showing the laser signal size compared to the size of the entire PImMS2 sensor.

9.2 CS_2 and DMF VMI Experiments

Following the initial tests described in the previous sections, a PImMS1 camera was installed on a velocity-map imaging apparatus designed to study molecular photodissociation processes, to perform the first multimass velocity-map imaging experiments. Photolysis of CS_2 and N,N-dimethylformamide (DMF) were chosen as suitable test molecules as they produce fragments with different masses and spatial distributions upon interaction with 193 nm laser light.

The experimental apparatus used in the VMI experiments has been described in detail by Hopkins *et al*[96]. The custom-built VMI spectrometer consists of three vacuum chambers: source, imaging, and detection. Within the source chamber, the CS_2 or DMF gas sample is introduced into high vacuum via a pulsed solenoid valve operating at 10 Hz, generating a molecular beam which travels along the time-of-flight axis. The molecular beam is skimmed prior to entering the imaging chamber, which contains the three-element velocity mapping ion lens. The ion lens consists of repeller, extractor, and ground electrodes, with the ratio of potentials applied to the extractor and repeller electrodes maintained at ~0.71 to achieve velocity mapping conditions. Between the repeller and extractor electrodes, the molecular beam is crossed orthogonally by a 193 nm pulsed laser beam from a Neweks PSX-100 ArF excimer laser. For the experiments on CS_2, the 193 nm laser performed both the ionisation and the fragmentation steps. For the DMF experiments, the molecules were photolysed by the 193 nm pulses and the resulting neutral fragments were subsequently ionised after a delay of 10 ns by a 118 nm laser pulse generated from the ninth harmonic of a Continuum Surelite I Nd:YAG laser. For both molecules, the resulting Newton spheres of ionized photofragments were accelerated by the velocity mapping field and passed through the apertures in the extractor and ground electrodes into the field free flight tube, traversing a 0.48 m flight tube before striking a 2D position-sensitive ion detector. The detector assembly consists of a pair of 40 mm-diameter chevron MCPs coupled to a P47 phosphor screen. The time-of-flight spectrum of the ions was monitored via the optical signal on the phosphor screen using a photomultiplier tube coupled to a digital oscilloscope.

For the PImMS measurements on CS_2 and DMF photolysis, the PImMS camera was mounted behind the ion detector to capture the ion images formed on the phosphor screen. The timebin width was set to 50 ns, and the sensor threshold was set so that in dark conditions no noise was seen across the sensor. An F-mount optical lens was used to focus the image from the phosphor screen onto the PImMS sensor in the CS_2 experiments, and a C-mount lens with a larger aperture was used in the DMF experiment. The reasons for the change in lens are elaborated on in the following section.

CS_2 interacts with 193 nm photons to produce C^+, S^+, CS^+ and CS_2^+ ions, with the most predominant ions under the conditions employed being CS^+ and CS_2^+. The difference in the ion masses causes a

significant difference in ion flight time, allowing them to be resolved temporally with relative ease. The parent ion CS_2^+ is formed through the loss of an electron from neutral CS_2. This has a minimal effect on the velocity of the molecule due to the very small mass of the departing electron relative to that of the CS_2 molecule. The parent ion velocity is therefore essentially identical to that of the neutral CS_2 in the collimated molecular beam, and since the ion detector is located on-axis with the molecular beam, the signal from this ion is expected to take the form of a single well-defined spot in the centre of the detector. Conversely, fragmentation of CS_2 or CS_2^+ to form daughter ions and neutrals leads to considerable release of kinetic energy into relative translation of the fragments, and daughter ions should therefore be characterised by a much broader velocity distribution.

N,N-dimethylformamide (DMF) was already under investigation within the research group as a prototype for studying fragmentation of the peptide bond. DMF exhibits numerous competing fragmentation pathways following absorption of a UV photon, generating multiple different daughter ions. DMF therefore represented an excellent test molecule for the PImMS sensor due to the multiple ion arrival times, each with a different spatial distribution.

9.2.1 Results and Discussion

The data set for CS_2 is shown in Figure 65, demonstrating that the PImMS sensor was able to detect CS^+ and CS_2^+, the two most abundant ions. As expected, the parent ion (CS_2^+) signal was recorded by a single pixel in the centre of the detector, reflecting the narrow velocity distribution within the molecular beam, whereas the CS^+ ion showed a distinct circular distribution, reflecting the kinetic energy release associated with the fragmentation process. The TOF spectrum obtained from the data set was also consistent with that expected for the two ion masses. The C^+ and S^+ ions were not detected by the PImMS sensor; their expected arrival times are indicated on the TOF spectrum in Figure 25. It is thought that under the conditions of this early experiment, the signal from the phosphor screen for a single ion striking the detector was not of sufficient intensity to register a hit within a PImMS1 sensor pixel. Two or more ions striking the detector in close proximity at the same time, known as a double ion event, generate a more intense signal from the phosphor screen that is more easily detected by a single pixel. It is believed that the ion distributions of CS^+ and CS_2^+ are more likely to result in a double ion event, especially for CS_2^+ since the narrow velocity distribution within the molecular beam means that any ions formed must strike the MCP in essentially the same position. Conversely, C^+ and S^+ ions have comparatively diffuse spatial distributions, decreasing the probability of a double ion event. Without the intense signal resulting from a double ion event, the PImMS sensor was unable to detect signal at those arrival times.

The results of this experiment prompted an investigation into ways of maximising the level of light emitted from the phosphor screen that would be incident on the PImMS sensor. Optimising the lens used to focus the image from the phosphor screen onto the surface of the PImMS sensor was one of the first considerations. This requires choosing the largest possible lens aperture consistent with focusing the 40 mm image from the phosphor screen onto the active area of the PImMS sensor. The CS_2 experiment was performed using an F-mount lens, whereas the optimum lens was determined to be a C-mount lens, which would allow for a larger aperture and approximately a five-fold increase in the total intensity of light focussed onto the sensor. A number of C-mount lenses with large apertures were purchased, and the housing of the PImMS cameras was modified to allow the new lenses to be mounted.

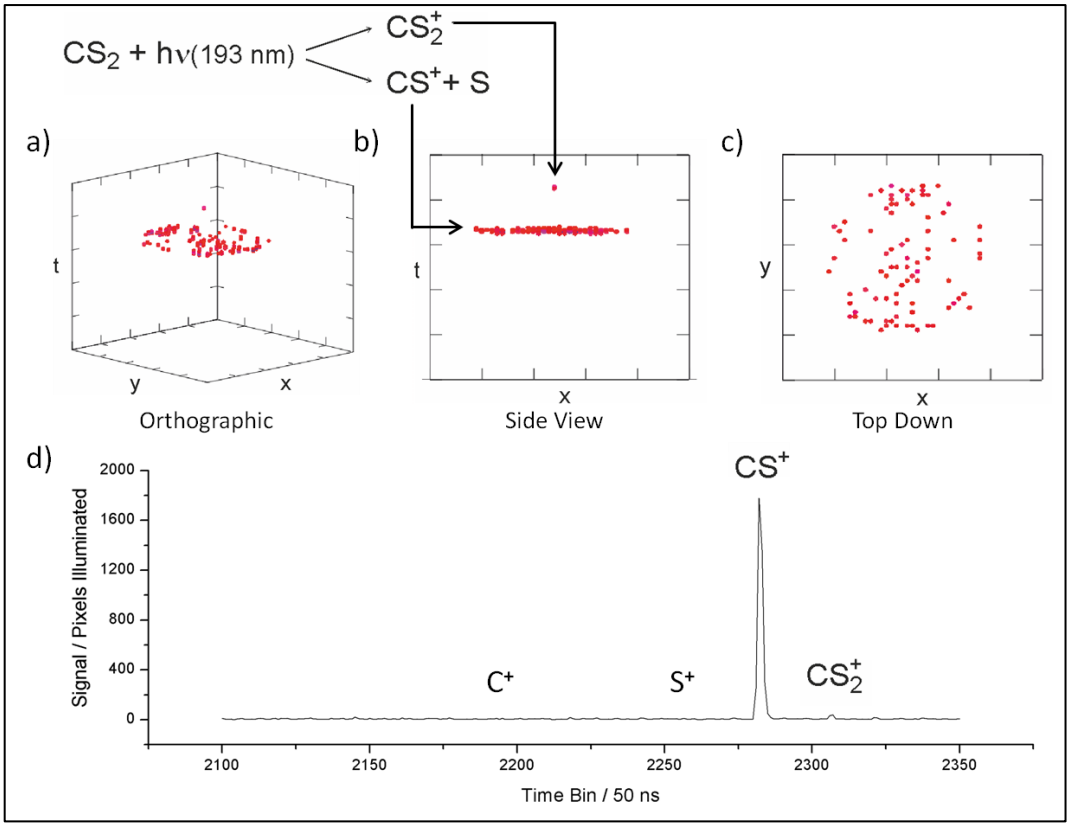

Figure 65 – a)-c) the orthographic, side and top down view of the data obtained for the photolysis of CS_2 respectively. The parent is detected by a single pixel as expected due to the fact that the loss of one electron has a negligible effect on the kinetic energy of the ion. d) The TOF spectrum obtained for CS_2. The peaks for all expected ions are marked; C^+ and S^+ are not seen in the data set recorded by the PImMS sensor.

The *x,y,t* data set for N,N-dimethylformamide, acquired over 4,000 acquisition cycles, is shown in Figure 66. The TOF spectrum from the data is also shown alongside the full data set, representing the total signal intensity recorded in each timebin. A time-gate was applied to turn off the MCP detector at the arrival time of the parent ion peak at *m/z* = 73; this was a precaution to prevent saturation or

potential damage to the MCP detector due to the high signal intensity. Peaks recorded at timebins later than the parent ion arrival time are due to the formation of clusters, such as dimers and trimers, within the molecular beam, which can also be photolysed and ionised.

A key process in the fragmention of DMF is the fission of the N-C "peptide" bond, yielding CHO and $N(CH_3)_2$ fragments, with respective masses of 29 and 44 amu. Following the ionisation step, the $N(CH_3)_2$ fragment usually loses a proton to produce an ion with *m/z* = 43. The images for the *m/z* = 29 and 43 fragments show significant anisotropy in the fragment angular distribution, with β parameters of 1.6 and 1.2, respectively. Another fragmentation channel of interest is loss of a methyl group to form fragments at *m/z* = 15 and 58 following ionisation. However, only the CH_3 signal at *m/z* = 15 is seen in the data set, indicating that the majority of the *m/z* = 58 product dissociates further to produce lower mass fragments. The images for these fragments do not show significant anisotropy, indicating a slower, more statistical dissociation mechanism.

The DMF experiment provided an excellent example of the benefits of multi-mass imaging using the PImMS sensor; a significantly longer experimental time would be required to image all fragments individually due to the high number of fragments formed. Furthermore, with the traditional method of gating a CCD camera, the images are generally recorded at the arrival times as seen by a photomultiplier displaying the signal from the phosphor screen. In this case, the signal from higher order clusters was too weak to be resolved by the photomultiplier but was recorded by the PImMS sensor as their arrival time was within the experimental exposure time.

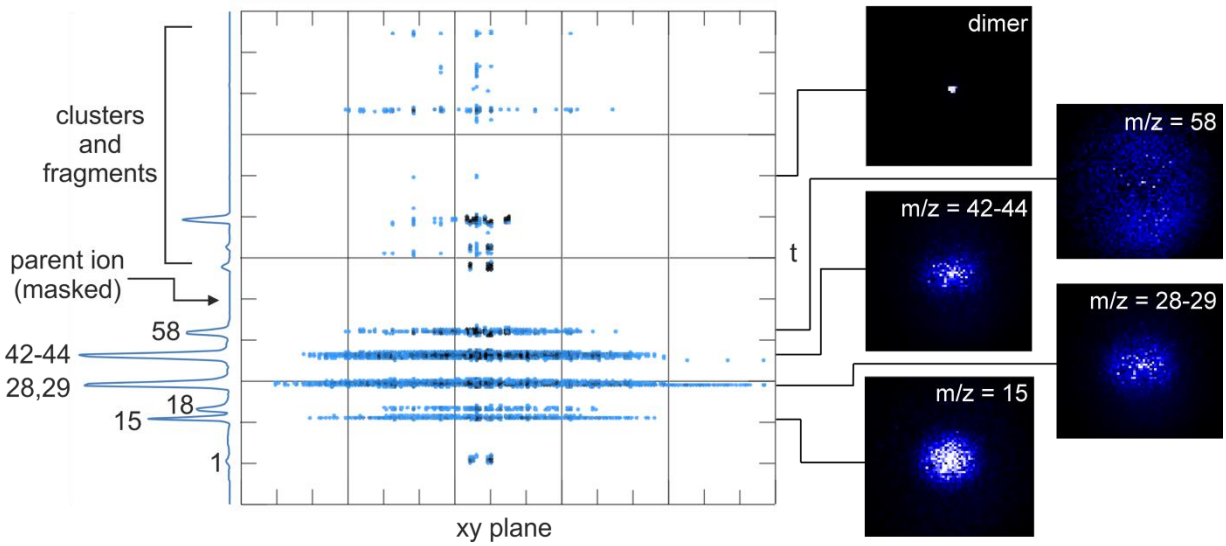

Figure 66 – A 3D view of the spectrum obtained for DMF. Increasing darkness of the data points represents a higher ion count rate when summed over the 4,000 frames. The images from a number of prominent ions are shown on the right. The origin of each ion is described in the discussions.

9.3 Coincidence Experiments: Photolysis of Br_2

In the simplest example of a photoionisation process, a photon interacts with a molecule to produce a singly-charged positive ion and an electron. Both energy and momentum are conserved in the interaction, and detecting the ion and electron produced from the same ionisation event may provide an insight into the dissociation dynamics. As the ion and electron must be detected in the same experimental cycle, these measurements are known as *coincidence* experiments.[97,98] It is possible to detect the ion and electron on the same detector through appropriate manipulation of the electric fields, described below. As the electrons and ions have different arrival times, a multi-mass imaging detector must be employed in the experiments; recording the spatial distribution of the electrons and the spatial distribution of the ions in separate experiments using an ordinary CCD sensor (without time resolution) would not allow coincidence events to be assigned, since the detected electrons and ions would necessarily arise from different photoionisation events.

The ability of the PImMS sensor to record the position and arrival time of incident particles on each experimental cycle allows it to be used to perform coincidence experiments of the type described above. Additionally, in ionisation events that create two or more charged particles, the PImMS sensor is able to detect all ions; this could allow further levels of analysis to be performed, for example, using conservation of momentum to assign coincidence events under high signal regimes.

In the following, the first experimental demonstration of photoelectron-photoion coincidence detection is described, using a single ion detector with switched extraction fields combined with a PImMS sensor. The data analysis procedures required to extract the coincidence information from these data have been developed recently by Craig Slater and described in his D.Phil. thesis.

The photolysis of Br_2 was used to demonstrate the use of the PImMS sensor as a photoelectron-photoion coincidence detector. The photodissociation of Br_2 produces Br atoms in both the ground and the first electronically excited state. Ground-state Br products can be ionized state-selectively via a (3+2)REMPI process at 446.32nm to produce Br^+ ions and an electron. Both charged particles can be detected by first biasing the ion optics for detection of the negatively-charged electron, and then switching the polarity of the field in order to extract the positively charged Br^+ ion. This procedure relies on the fact that the electrons are much lighter than the Br^+ ions, so that the Br^+ ions remain essentially stationary while the electrons are extracted to the detector and their measured velocity distribution is relatively unperturbed by switching the fields. Using the PImMS sensor, the electrons and ions can be imaged simultaneously on each experimental cycle, allowing their correlated velocity distributions to be determined. Such correlations cannot be determined in an experiment in which the electron and the ion are imaged in separate experiments.

These experiments were performed on a velocity-map imaging apparatus similar to the apparatus described previously that was used for the CS_2 and DMF experiments. The experimental setup for the Br_2 experiments was prepared by Craig Slater, working in the Brouard research group. Briefly, the ion optics assembly consists of four electrodes: a repeller, extractor, and two ground plates. Home-built pulsed high voltage power supplies supply respective voltages of -6.000 kV and -4.420 kV to the repeller and extractor lenses for imaging electrons, which are switched to +2.000 kV and +1.485 kV for imaging of the ions. The charged particles traverse a flight tube of length 0.68 m before impinging on a 75 mm position sensitive detector (Photonis) consisting of a pair of chevron microchannel plates and a P47 phosphor screen.

The molecular beam consisted of 1% Br_2 in He gas with a stagnation pressure of 2 bar, and was admitted into the apparatus through a Jordan pulsed valve operating at 10 Hz. The molecular bromine was photolysed at 446.32 nm and the ground state Br atoms formed in the photolysis step were ionised by the same laser pulse via (3+2)REMPI. The laser source was a Lambda Physik LPD 3000 dye laser. As noted above, the electrons were imaged first, before the voltages of the ion optics were switched to extract the ions. The PImMS camera was set to 50 ns per timebin and the pixel thresholds set such that the sensitivity of the sensor was as high as possible without noise becoming problematic.

9.3.1 Results and Discussion

Figure 67 shows the TOF spectrum obtained from the experiment and displays the images obtained by integrating the signal over a small window of timebins around each mass peak. The electrons can be seen to possess a bimodal velocity distribution, with two clear velocity components (seen as two concentric rings in the image), and the two isotopes of bromine, ^{79}Br and ^{81}Br, are resolved. As the bromine isotopes are chemically identical, the same images are expected for both peaks.

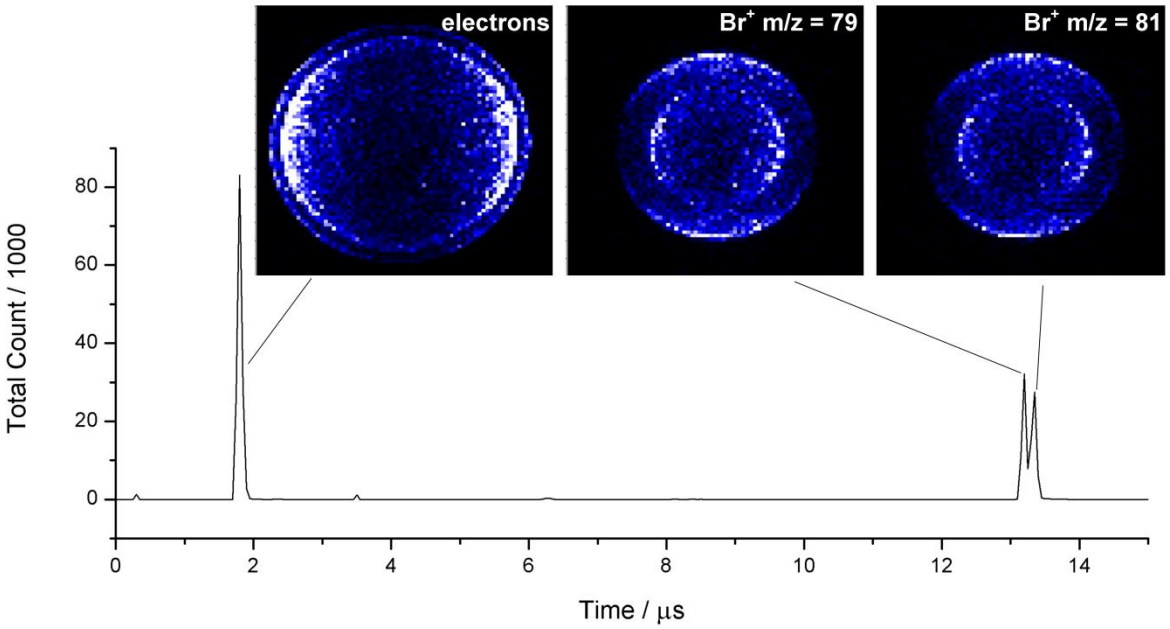

Figure 67 – The mass spectrum obtained for the photolysis of Br_2. The first peak is due to electrons, and the second is due to Br^+ ions with the isotopes resolved. The small peaks seen either side of the electrons are due to the cross talk bug that at the time of the experiment had not been resolved (Section 7.1.3). The two bromine isotopes are chemically identical and therefore display the same image resolved at different arrival times. Note that the time shown is relative to the beginning of the PImMS sensor exposure time, as opposed to the absolute flight time of the electrons and ions.

The two rings in the ion images, shown in Figure 67, correspond to the formation of atomic bromine in two energetic states. Excitation of ground state molecular bromine by 446.32 nm laser light populates the $A^2\pi_u(1_u)$ and the $B^3\pi_u(0_u^+)$ states, which dissociate to give Br + Br and Br + Br* respectively, where Br and Br* denote atomic bromine in the $^2P_{3/2}$ electronic ground state and $^2P_{1/2}$ first spin-orbit excited state, respectively. These dissociation processes can be summarised in the molecular equations:

$$Br_2 \xrightarrow{446\ nm} Br_2(A^2\pi_u(1_u)) \rightarrow Br(^2P_{3/2}) + Br(^2P_{3/2}) \quad \text{(viii)}$$

$$Br_2 \xrightarrow{446\ nm} Br_2(B^3\pi_u(0_u^+)) \rightarrow Br(^2P_{3/2}) + Br(^2P_{1/2}) \quad \text{(ix)}$$

Because formation of Br* requires more energy than formation of Br, conservation of energy dictates that, for a fixed photon energy, the atoms formed via the Br + Br* reaction must have a lower kinetic energy than those formed via the Br + Br pathway. Hence, after ionisation of the ground state Br atom, the Br^+ ion formed via the Br + Br* pathway is lower in translational energy and appears as a ring closer to the centre of the image. The outer ring corresponds to the Br + Br pathway, in which both Br atoms are formed in their electronic ground state with a higher translational kinetic energy. The anisotropy in the images shows that excitation of molecular bromine from the electronic ground

state to the $A^2\pi_u(1_u)$ and $B^3\pi_u(0_u^+)$ states are perpendicular and parallel, respectively (β = -1 and β = 2). Note that the laser beam is polarised horizontally relative to the images in Figure 67.

When electrons are liberated from the ground state Br atoms, the (3+2)REMPI process provides enough energy to form ions in either the ^3P_J electronic ground state (with J = 0, 1, 2) or the $^1D_2$ electronically excited state. Whilst this has no effect on the velocity distribution of the Br^+ ions, due to the negligible momentum transfer from the departing electron, the final electronic state of the ion has a marked effect on the kinetic energy distribution of the electrons. Conservation of energy means that the formation of more excited ions is partnered by lower energy electrons, yielding a distinct ring in the electron image for each electronic state. However, the acquired electron image, shown in Figure 68b), exhibits two rings instead of the expected four, which correspond to the formation of the $^3P_0/^3P_1$ states and the $^3P_2$ state. The ring associated with formation of the $^1D_2$ state is not seen due to the weakness of the transition and the experiment does not have sufficient resolution to separate the rings from the $^3P_0$ and $^3P_1$ states. The anisotropy of the rings reflects the relative symmetries of the electronic states involved in the ionisation process.

A 3-dimensional representation of the full experimental data is shown in Figure 68a), with the electron and ion signals shown with an expanded time axis in Figure 68b) and Figure 68c), respectively. It can be seen that the signal for each mass arrives over 3-4 timebins, even for the electrons which should have a very short range of arrival times. This anomaly is due to a combination of the effects of the ~120 ns 95% decay lifetime of the P47 screen and the temporal response of the circuitry in the PImMS pixels. Although not shown here, the data recorded in this experiment allows a coincidence analysis to be performed, for example, correlating the Br^+ ion velocity distribution with the electron velocity distribution.

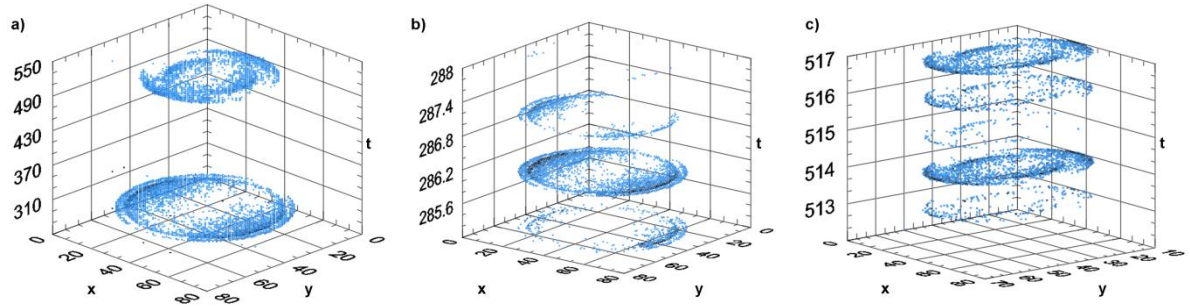

Figure 68 – a) The 3D representation of the signal obtained from photolysis of Br_2, showing both the spatial distribution of the electrons at earlier timebins and the Br^+ ions at later timebins. b) and c) The spatial distributions of the electrons and Br^+ ions respectively, expanded in the time axis. Each timebin corresponds to 50 ns.

9.4 Detection of High Energy Alpha and Beta Particles

As mentioned in Section 6.1, the PImMS sensor is capable of detecting single high energy particles that leave an ionising track through the silicon layer. This forms the basis of the neutron detection work that will be elaborated on in Part III, by the detection of high energy conversion electrons. These experiments, performed at the Rutherford Appleton Laboratory (RAL), were devised to investigate the sensitivity of the PImMS sensor for high energy alpha and beta particles. A compressed pellet of radium-226, with a decay energy of 4.8 MeV and half-life of 1601 years, and a rod of strontium-90, with a decay energy of 0.546 MeV and half-life of 28.6 years, were used as the alpha and beta sources respectively. Strontium-90 beta decay produces yttrium-90, with a half-life of 64.1 hours, which in turn undergoes beta decay, with 2.279 MeV of decay energy and a 0.02% chance of producing 1.7 MeV gamma photons. The decay pathways are summarised in Figure 69.

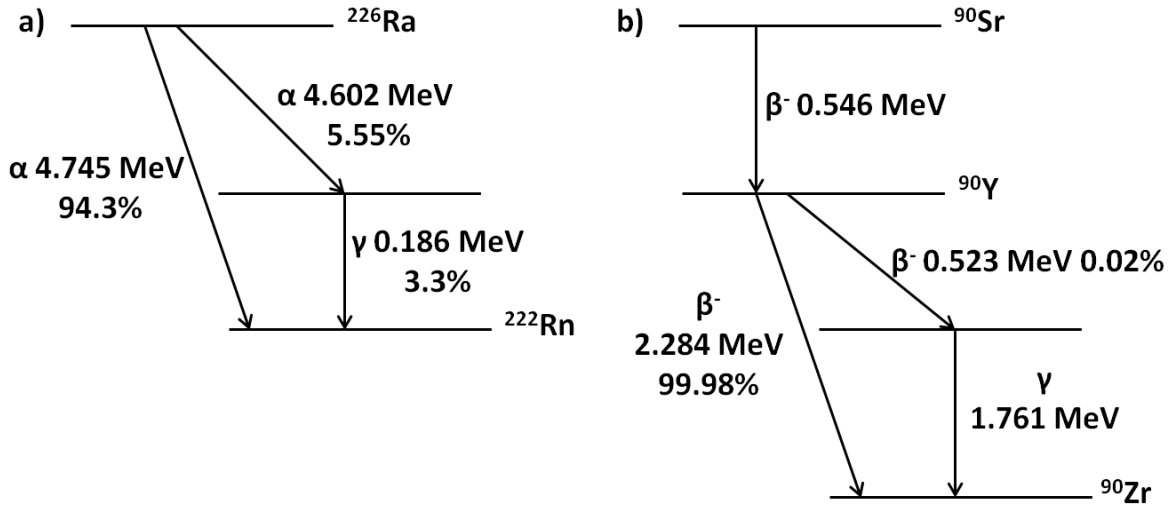

Figure 69 – The decay pathways, decay products and particle energy in the alpha and beta decay of ^{226}Ra and ^{90}Sr. Data taken from Modern Physics A – Z[99].

The emission from the pellet of ^{226}Ra was recorded at distances of approximately 12 mm from the sensor and 2 mm from the sensor. The beta particles from ^{90}Sr were collimated using wood and the signal count was recorded at a distance of approximately 0.7 mm from the sensor. The ^{90}Sr emissions were retested using a piece of 5 mm aluminium between the source and the sensor to shield beta radiation but permitting any gamma radiation to reach the sensor. The beta particle emission from the ^{90}Sr source was also measured using a 10 mm thick BC400 circular scintillator disk, with a diameter of 30 mm, connected to a photomultiplier at a series of distances from 0 – 5 cm in 1 cm increments.

The PImMS sensor was calibrated and the threshold set such that no digital signal was recorded under dark conditions. As the detector did not need to be synchronised with an external source, it

was operated in a free-running mode with the longest exposure time possible with the firmware at the time. This corresponded to a timebin length of 200 ns and therefore a total experimental period of 819.2 µs.

9.4.1 Results and Discussion

The results of the experiments are shown in Table 5. The PImMS sensor showed a marked response to both sources indicating sensitivity to both alpha and beta particles. Whilst neither source acted as a point source, it was clear that decreasing the distance between the PImMS sensor and the ^{226}Ra source had the expected effect of increasing the count rate dramatically. The count rate recorded with the ^{90}Sr source and aluminium shielding is negligibly small and within experimental error, indicating that the contribution of gamma radiation to the measurements performed is low.

Table 5 – A summary of the recorded counts for each source in the different experimental setups.

Radiation Source	Acquisition Cycles Recorded	Counts / Acquisition Cycle	Counts / s
^{226}Ra (12 mm distance)	5000	1.16	1412
^{226}Ra (2 mm distance)	5000	8.53	10412
^{90}Sr (0.7 mm distance)	5000	10.36	12643
^{90}Sr (Al shielding)	5000	0.029	35

Each pixel in the PImMS sensor spans 70 µm × 70 µm and the resolution of the PImMS1 sensor used in these experiments is 72 pixels × 72 pixels. The area of the sensor is 0.254 cm^2 and the beta particle flux recorded at a distance of 7mm from the ^{90}Sr source can therefore be calculated as 49,770 s^{-1}cm^{-2}. The flux recorded by the BC400 scintillator and PMT at the same distance was found to be 24490 s^{-1}cm^{-2}. The difference in measurement indicates that the PImMS sensor is significantly more sensitive than the BC400 scintillator and PMT for low energy beta particles. The difference in sensitivity is shown schematically as a function of the incident beta particle energy in Figure 70.

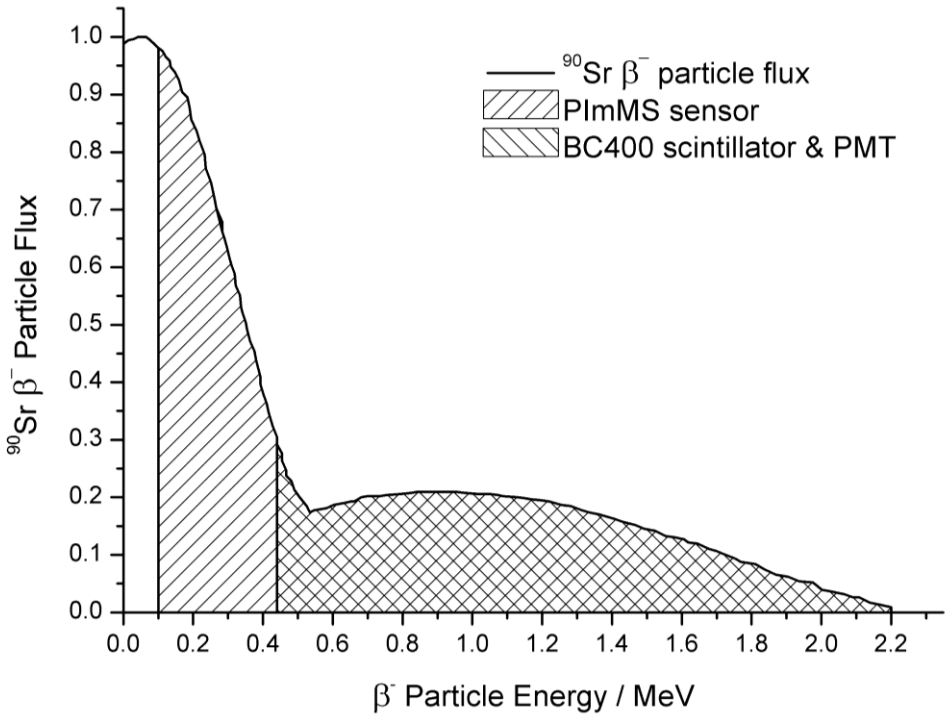

Figure 70 – The beta particle flux from the ^{90}Sr source as a function of incident energy. The energy is reduced as ^{90}Sr does not act as a point source and the beta particles are moderated down in energy as they traverse the material from their initial position. The beta particles detected by the PImMS sensor and the BC400 scintillator and PMT are demonstrated by the shaded area as indicated by the legend. Emission spectrum adapted from Carmona *et al*[100].

Part III: The GadMOS Project

Publications

- Fast sensors for time-of-flight imaging applications
  C. Vallance, M. Brouard, A. Lauer, C. S. Slater, E Halford, B. Winter, S. J. King, J. W. L. Lee, D. E. Pooley, I. Sedgwick, R. Turchetta, A. Nomerotski, J. J. John, and L. Hill
  Phys. Chem. Chem. Phys. 16, 383, (2014).

- GP2: a new detector for time-resolved neutron imaging
  J. W. L. Lee, D. E. Pooley, *et al*
  In preparation

10 Introduction to Neutron Imaging

Neutron beam transmission measurements provide a unique non-destructive approach to imaging of materials. The penetrative nature of the particles makes them suitable for imaging most substances, and, in contrast to X-rays, they interact strongly with many materials containing light or low atomic-number elements. Whereas X-ray imaging relies on scattering of the X-rays from electrons within the material and increases in attenuation with electron density, and therefore atomic number, neutrons interact with the nucleus of the atom, with no such systematic correlation across the periodic table. The difference between the attenuation of X-rays and neutrons is shown in Figure 71. This allows neutrons to give contrast between elements close to each other on the periodic table and even enable the distinction between different isotopes. ^{1}H and ^{2}H, for example, are notoriously difficult to detect with X-ray diffraction methods but show a high contrast with neutron imaging.

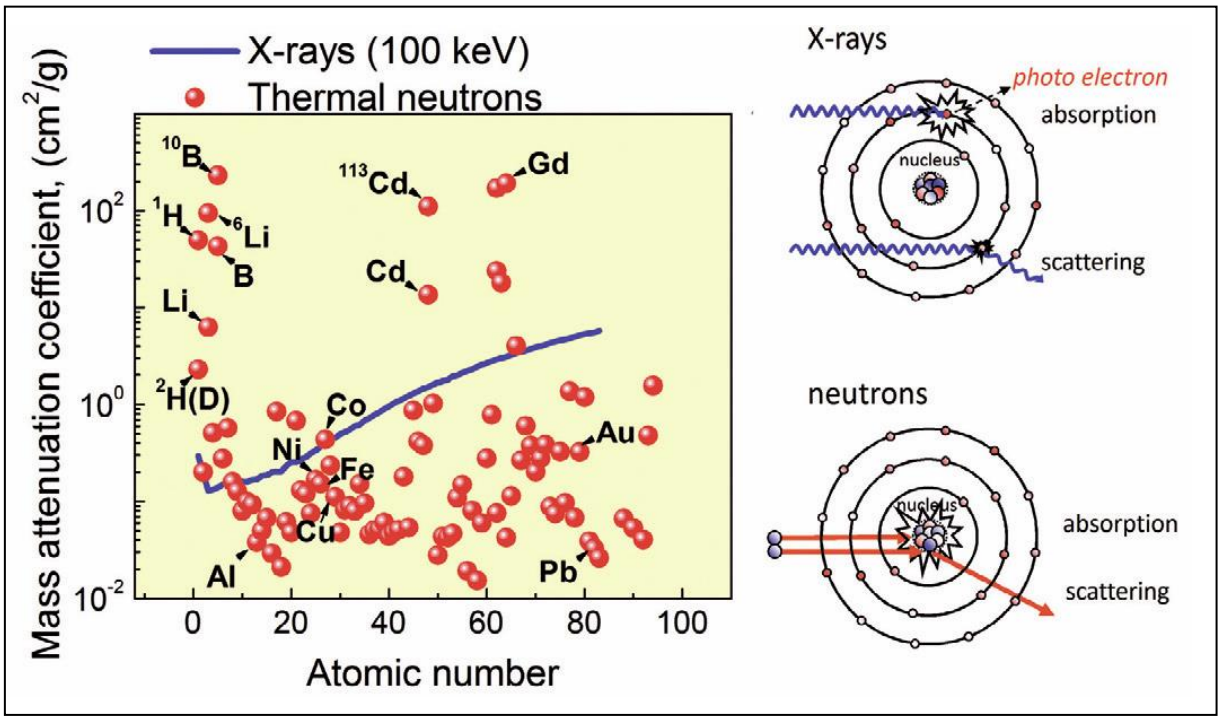

Figure 71 – Left: the comparison of the dependence of the mass attenuation coefficient on atomic number for X-rays and thermal neutrons. Right: schematic illustrations showing X-rays interacting with the electrons of an atom contrasted with and neutrons interacting with the nucleus. Adapted from Hartnig *et al*[101].

To perform neutron imaging, neutrons must initially be created by a suitable neutron source. Neutron sources generally produce neutrons with a range of energies and therefore require an energy selection procedure to select neutrons appropriate for a particular experiment. These neutrons are then exposed to the sample and after the interaction has taken place, the resulting

neutrons must be detected. A background measurement without the sample present may be taken which can be used to enhance the signal contrast. The four steps of: neutron creation; energy selection; interaction with sample; and detection are considered in more detail in the following sections.

10.1 Neutron Creation

Conventional neutron imaging experiments typically employ a nuclear reactor or dedicated spallation source beamline as the neutron source. Both of these generators are considered as high flux sources with approximately 10^{15} neutrons cm^{-2} s^{-1} produced for reactor-based sources and a peak flux of 10^{17} neutrons cm^{-2} s^{-1} for spallation sources. Smaller neutron sources, producing much lower fluxes, can employ radioisotopes that undergo spontaneous fission on an appropriate experimental time-scale (e.g. ^{252}Cf, $t_{1/2}$ 2.6 years). Alternatively, neutrons can be produced from a radioisotope that undergoes alpha decay combined with a low atomic mass element; a ^{241}Am-Be alloy, for example, generates neutrons and gamma radiation when alpha particles emitted from Am nuclei interact with Be, as shown in the following reaction sequence:

$$^{241}Am \rightarrow {}^{236}Np + {}^{4}He + \gamma \quad \text{(x)}$$

$$^{9}Be + {}^{4}He \rightarrow {}^{12}C + {}^{1}n + \gamma \quad \text{(xi)}$$

The typical total neutron emission rate for the radioisotope sources of this type ranges from 10^{6} to 10^{9} neutrons s^{-1}, emitted in all directions.

The experiments described in this thesis took place at the ISIS spallation source which provides pulses of neutrons with a flux of 10^{12} neutrons cm^{-2} s^{-1}. The facility is described in more detail in Section 11.2.

10.2 Energy Selection

Neutron imaging typically uses neutrons of thermal energy (~0.025 eV; see Table 6) requiring the nascent high-energy neutrons from the source to be moderated down in energy. This is achieved by passing the neutron beam through a suitable moderating medium, such as water, liquid deuterium, polyethylene or graphite, which results in a beam of neutrons with a distribution of energies. In continuous neutron sources, e.g. nuclear reactors, selection of a specific energy can be achieved by Bragg-reflection from a crystal, the same process that is detailed in Section 10.3. Alternatively, with a pulsed neutron source, a time-of-flight tube and mechanical chopper can be used to isolate a particular energy. Neutrons with different kinetic energies travel at different speeds along the flight tube, and therefore have a different time at the chopper. This allows the desired energy range to be selected by synchronising the chopper with the initial neutron pulse. Unfortunately, both of these

energy selection methods drastically reduce the neutron flux, and thus significantly increase the experimental time.

Table 6 – The classification of neutrons according to their energy.[102]

Neutron Energy	Classification
0 – 0.025 eV	Cold
0.025 eV	Thermal
0.025 – 0.4 eV	Epithermal
0.4 – 0.6 eV	Cadmium
0.6 – 1 eV	EpiCadmium
1 – 10 eV	Slow
10 – 300 eV	Resonance
300 eV – 1MeV	Intermediate
1 – 20 MeV	Fast
> 20 MeV	Relativistic

10.3 Interaction with Sample

Once the neutron energy range has been selected, the object to be imaged must be exposed to the neutron beam. To produce the sharpest image, the neutron beam should be as well collimated as possible and the sample should be as close to the detector as possible. Improved collimation can be achieved using pinhole apertures, at the cost of reducing neutron flux.

Neutrons incident on a sample have four possible fates: elastic coherent or Bragg-scattering (undergone by a fraction, *B*, of incident neutrons); absorption (*A*); incoherent/small angle/inelastic thermal scattering (*S*); or transmission (*T*), such that, taking *B*, *A*, *S* and *T* to also represent the fraction of neutrons undergoing their respective process, $B + A + S + T = 1$. The scattering and absorption processes remove neutrons from the incident beam, yielding a transmitted flux fraction as: $T = 1 - (B + A + S)$. The overall reduction in the transmitted fraction is dominated by scattering at short neutron wavelengths (i.e. high energies) and nuclear absorption at long neutron wavelengths as shown by the example spectrum in Figure 72a). Absorption, with few exceptions, is linearly dependent on wavelength, and the absorption cross section can generally be expressed as $\sigma_{\mathrm{abs}}(\lambda) = \beta\lambda$ where β is a material-dependent constant. Certain elements, such as boron and cadmium, have particularly high absorptions, allowing them to be used as contrast agents in neutron imaging. Contrary to the broad wavelength dependence observed for absorption, Bragg-scattering occurs at precise wavelengths determined by Bragg's law:

$$\lambda_{hkl} = 2d_{hkl}\sin\theta_{hkl} \tag{17}$$

where d_{hkl} is the interplanar distance for the atomic planes with Miller indices *hkl*,[103] and θ_{hkl} is the angle between the neutron beam and the *hkl* crystal planes. As a result of this relationship, by measuring the intensity of Bragg scattering at particular characteristic wavelengths λ_{hkl}, the quantity of crystallites with a specific orientation within an ideal sample can be determined. In the limiting case of a single crystal, for which an example of the wavelength-dependent Bragg scattering is shown in Figure 72a), the Bragg peaks are sharp due to the presence of well-defined crystal planes. In contrast, a powder sample contains a large number of randomly oriented crystallites with an essentially continuous distribution of Bragg angles, such that the Bragg condition is satisfied for all wavelengths smaller than $2d_{hkl}$. At wavelengths greater than $2d_{hkl}$, Bragg scattering ceases, causing a sharp increase in the transmitted signal, as shown for copper powder in Figure 72b). These Bragg edges occur at $\lambda = 2d_{hkl}$ for each (*hkl*) plane, allowing multiphase materials to be analysed using the transmitted spectrum.

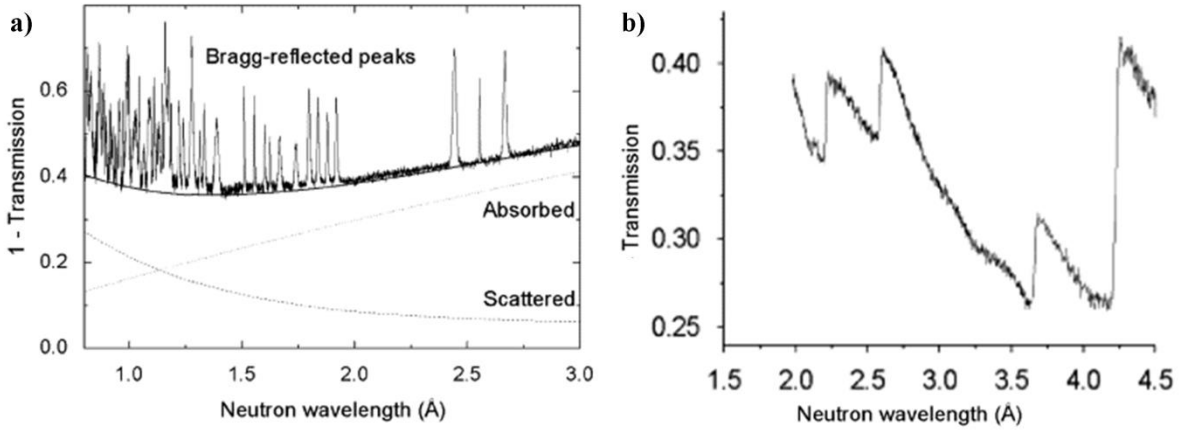

Figure 72 – a) The neutron transmission spectrum of a Cu single crystal. b) The neutron transmission spectrum of copper powder showing distinct Bragg edges. Both adapted from W. Kockelmann *et al*[104].

Other scattering processes are generally grouped together under the umbrella of *thermal diffuse scattering* (TDS). The efficiencies of these processes have a smooth and continuous dependence on wavelength.[105] When all neutron attenuation processes are accounted for, the overall transmitted intensity I_t can be written:

$$I_t(\lambda) = I_o(\lambda)\exp(-n\sigma_{\mathrm{tot}}(\lambda)z) \tag{18}$$

where $I_o(\lambda)$ is the initial beam intensity, n is the number of unit cells per unit volume, z is the sample thickness, and $\sigma_{\mathrm{tot}}(\lambda)$ is the total cross section for interaction with the medium of interest:

$$\sigma_{\mathrm{tot}}(\lambda) = \sigma_{\mathrm{abs}} + \sigma_{\mathrm{Bragg}} + \sigma_{\mathrm{TDS}} \tag{19}$$

10.4 Neutron Detection

As neutral particles, neutrons are difficult to detect directly, and are generally detected indirectly by interactions producing secondary charged particles or photons. Neutrons do not directly cause ionisation, but various conversion materials may be used to generate charged particles or photons. Converter materials for thermal neutrons include ^{3}He, ^{6}Li, ^{10}B, ^{155}Gd and ^{157}Gd. The neutron capture cross sections of these isotopes for neutrons with 25 meV of energy are listed in Table 7. The ideal neutron converter material should exhibit the following properties:

- A large neutron capture cross section to provide high sensitivity;
- Secondary particles that have a long mean-free path compared to the thickness of the converter material;
- A small cross section for neutron activation. Neutron activation refers to the effect that occurs when atomic nuclei capture free neutrons, increasing in mass and entering excited states. These excited states often decay radioactively producing protons, alpha particles and/or gamma rays which would cause a significant background contribution to the detector;
- Low sensitivity to gamma rays, which are simultaneously and necessarily generated with neutron production, as well as in neutron interaction with nuclei.

Table 7 – The thermal neutron capture cross section for some elements commonly used as neutron conversion materials.[106]

Isotope	Cross section for neutron capture (25 meV/1.8 Å) / barn / 10^{-28} m^2
^{3}He	5,330
^{6}Li	940
^{10}B	3,835
^{155}Gd	61,000
^{157}Gd	255,000

^{3}He is commonly used as a conversion material due to the reasonably high thermal neutron capture cross section and low gamma sensitivity. Collision of a ^{3}He nucleus with a neutron yields ^{3}H and ^{1}H nuclei and releases 764 keV of energy.

$$n + {}^{3}He \rightarrow {}^{3}H + {}^{1}H + 764\ keV \qquad \text{(xii)}$$

Passing the neutron beam through a 1 cm path length of ^{3}He at a pressure of 20 atm converts approximately 94% of incident neutrons via this process.[107] The resulting ^{3}H and ^{1}H particles can be detected through the use of a gas proportional detector (a gas-filled detector which is sensitive to particle energy through the ionization cascade initiated by an incident high-energy ionizing particle)

or a Geiger-Müller tube. One method of recording a large two-dimensional neutron image, such as the diffraction pattern from a crystalline sample, is to use a series of cylinders filled with ^{3}He, arranged in an array. Each tube provides spatial resolution in one dimension. As the production of the ^{3}H + ^{1}H from ^{3}He following capture of a neutron must conserve momentum, the two particles have 191 keV and 574 keV of kinetic energy respectively, and must travel in opposite directions, thus being detected at opposite ends of the same cylinder. By recording the arrival times and pulse heights associated with each particle, the incident neutron position in the dimension perpendicular to the cylinder array can be calculated. The procedure is similar to that employed in analysing data from the delay-line detectors commonly used in photoelectron-photoion coincidence measurements as described in Section 5.3.

For many years, ^{3}He was the conversion material of choice for neutron detection. However, ^{3}He has a natural abundance of only 0.00014%, and is produced either through the decay of tritium (half-life of 12.3 years) or irradiation of ^{6}Li in nuclear reactors. The increased demand for neutron detectors and restrictions on export has led to a critical shortage in ^{3}He over the last decade. Taken together with the necessity of using high pressures in neutron detectors in order to increase detection efficiency, this has made ^{3}He-based detectors increasingly unfeasible for the long term.

An alternative neutron converter material is ^{10}B, which is widely available and therefore significantly less expensive. ^{10}B has a natural abundance of 20%, and can be enriched to almost 100% for use as a neutron-capture material for fission control in nuclear reactors. Thermal neutrons are captured by the ^{10}B atoms to produce ^{11}B, which decays with a lifetime of $\sim 10^{-12}$ seconds to produce an α particle, a ^{7}Li nucleus, and, in 94% of the reactions, gamma rays. The reaction energy is 2.31 MeV.

$$n + {}^{10}B \rightarrow {}^{11}B \rightarrow {}^{4}He + {}^{7}Li + \gamma \qquad \text{(xiii)}$$

^{10}B may be used in a gas-filled proportional detector either by filling the detector with gaseous boron trifluoride or alternatively by coating the walls of the detector with solid ^{10}B. In the latter case, only one of the two particles escape into the proportional counter, as the reaction takes place on the inner surface of the detector. Solid state ^{10}B detectors have a detection efficiency of 3-4%.

Another alternative to ^{3}He is ^{6}Li, which can be used in solid-state scintillator-based neutron detectors by incorporating it into glass fibres along with Ce^{3+} ions. ^{6}Li interacts with a neutron to produce ^{4}He and ^{3}H, which interact with the glass matrix to produce ionisation and electronically excited Ce^{3+} ions. Ce^{3+} relaxation to the ground state is accompanied by photon emission at 390 – 600 nm.

$$n + {}^{6}Li + Ce^{3+} \rightarrow {}^{4}He + {}^{3}H + (Ce^{3+})^{*} \rightarrow {}^{4}He + {}^{3}H + Ce^{3+} + h\nu \qquad \text{(xiv)}$$

Each absorbed neutron yields several thousand photons, which can be detected using one or more photomultipliers. Pulse-height discrimination can be used to distinguish between incident neutrons and gamma rays, which also excite scintillation. Although the cross section of ^{6}Li is lower than that of ^{6}He, the atomic density of ^{6}Li in the fibre can be greater by a factor of 50. However, the overall efficiency of ^{6}Li based scintillators is rarely above 1%.

Table 8 – The abundance, neutron capture cross section, daughter isotopes and daughter isotope lifetime for the stable isotopes of Gd.[108]

Isotope	Abundance / %	Neutron Capture Cross section at 1.8 Å / barn	Daughter Isotope	Daughter Isotope $t_{1/2}$
^{nat}Gd	100	48,890	-	-
^{154}Gd	2.2	90	^{155}Gd	Stable
^{155}Gd	14.7	61,000	^{156}Gd	Stable
^{156}Gd	20.6	2	^{157}Gd	Stable
^{157}Gd	15.7	255,000	^{158}Gd	Stable
^{158}Gd	24.9	2	^{159}Gd	18.6 h
^{160}Gd	21.9	1	^{161}Gd	3.66 mins

Gadolinium has two isotopes with extraordinarily large thermal neutron capture cross sections (see Table 8); in fact, ^{157}Gd has the largest thermal neutron capture cross section of any stable nuclide. The large cross section allows gadolinium thin films to be used as high efficiency neutron converters, with the additional benefits of low activation and low gamma sensitivity. The reaction energy of 7,937 keV associated with ^{157}Gd neutron capture can be released through the emission of gamma rays or through ionisation. A total of 390 gamma ray lines have been observed in the energy range 79.5 – 7857 keV.[109] Ionization begins with a radioactive decay process known as *internal conversion* (IC). Internal conversion requires the wavefunction of an inner-shell s electron to penetrate the nucleus. The resulting coupling interaction allows direct energy transfer from the excited nucleus to the electron, leading to ejection of the electron from the atom without the necessity for an intermediate gamma ray. The majority of conversion electrons originate from the 1s subshell, though electrons in the 2s, 3s and 4s subshells can also be emitted. These are referred to as K, L, M and N electrons respectively. The emission of a core electron through IC leaves a vacancy that can be filled by an electron from a higher shell. This releases energy which can either be emitted as a photon or cause the emission of another electron. These secondary electrons are known as *Auger electrons*, and their energies and emission cross sections have been documented by Larkins.[110] The high cross section for thermal neutron capture is the reason that gadolinium was selected as the conversion material in this project.

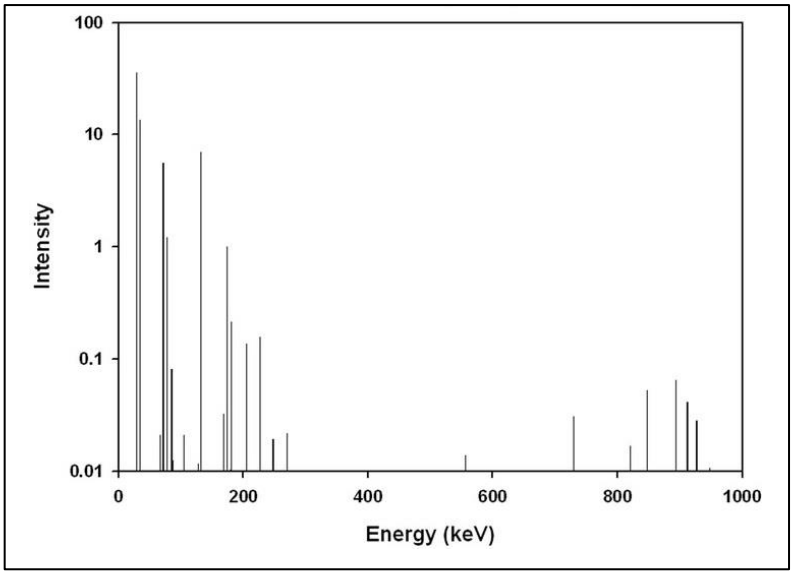

Figure 73 – The intensity of emitted IC electrons in ^{157}Gd neutron capture, per 100 neutrons.[108]

10.5 Applications of Neutron Imaging

The properties of neutrons and their interaction with materials allow imaging of samples that would be difficult or impossible to study using other methods such as X-ray imaging. Examples include the detection of hydrogen-containing materials, such as water, lubricants or plastics, especially in samples contained within metals which are impenetrable by X-rays. As the technique is relatively young, new applications of neutron imaging are constantly emerging. A description of all potential applications is beyond the scope of this work, but the following sections aim to demonstrate the advantages of using neutron imaging in a variety of scenarios.

10.5.1 Strain Mapping and Visualisation of Crystalline Phases

As discussed in Section 10.3, neutrons incident on a sample containing crystallites undergo diffraction at characteristic energies satisfying Bragg's law. Polycrystalline materials have an essentially continuous distribution of Bragg angles, meaning that the Bragg condition is satisfied for all wavelengths smaller than $2d_{hkl}$. When the neutron wavelengths increase to values greater than $2d_{hkl}$, the neutron attenuation coefficient decreases suddenly as neutrons are no longer being diffracted. These wavelengths are referred to as Bragg cut-off wavelengths, or Bragg edges, and for typical atomic spacings occur for neutrons in the thermal energy region. The wavelength of the Bragg cut-off can be measured accurately, and the corresponding d_{hkl} spacings of the crystalline lattice can be calculated. Applying stress and strain to a crystal can cause a measurable change to the Bragg cut-off wavelengths, allowing the strain to be quantified. Additionally, the measurement of Bragg edges can be used to identify and distinguish between different crystalline phases.

Strain imaging has been demonstrated by Santisteban *et al*[111] using a 12 mm thick ferritic steel plate with a cold-expanded hole, shown in Figure 74. Cold-expansion is a common technique used for extending the lifetime of metallic components which involves pulling an oversized tapered mandrel through a hole to expand the width. This process produces a compressive stress zone around the hole.[112] The experiment was performed using a 10 × 10 array of 2 mm × 2 mm scintillator detectors with a 2.5 mm pitch. Each scintillator recorded a thermal neutron TOF spectrum corresponding to a particular position of the sample, and through measuring the wavelengths of the Bragg edges, the strain values could be calculated.

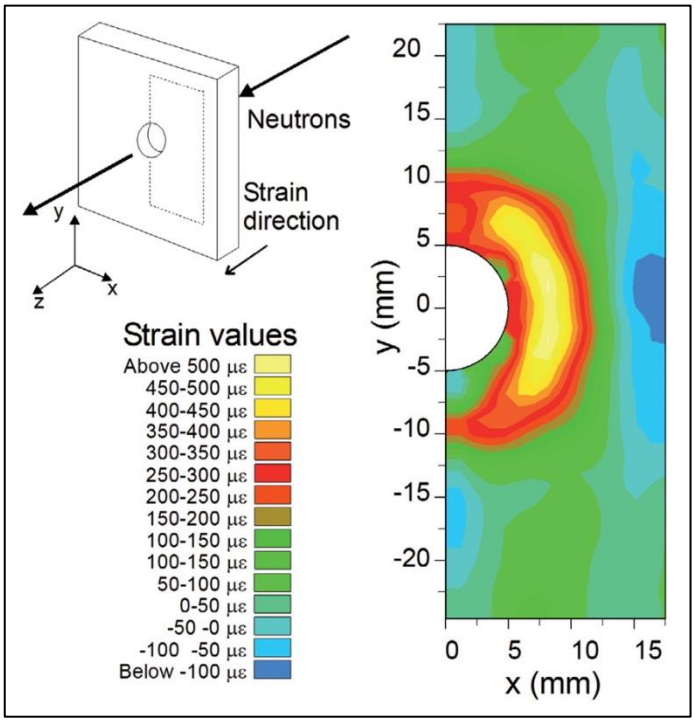

Figure 74 – A schematic of the 12 mm thick steel plate and the variation in strain around the cold-expanded hole. Adapted from Santisteban *et al*[111].

10.5.2 Neutron Radiography in Plant Science

The powerful interaction of thermal or cold neutrons with hydrogen, specifically ^{1}H, allows relatively small amounts of water to be imaged. In plant sciences, neutron radiography has been used for a variety of applications, ranging from the non-destructive observation of plant roots[113], possible due to the high neutron transparency of soil, to the water absorption process of timber.[114] These experiments relied on dehydrating the plant specimen and observing the uptake of water over time. More recently, steady-state flows in plants have been investigated through neutron imaging of D_2O.[115] The physical and chemical properties of D_2O are very similar to H_2O, but as the neutron attenuation coefficient of ^{2}H is significantly lower than for ^{1}H (see Figure 71), D_2O provides contrast and can act as a tracer. Using a tomato seedling and an automated H_2O/D_2O injector, neutron

radiographs were taken every 15 seconds after changing the water supply from H_2O to D_2O. The water flow from the root system to the stem was visible in the radiographs, shown in Figure 75, showcasing the viability of neutron imaging in the spatial and temporal dynamics of water movement.

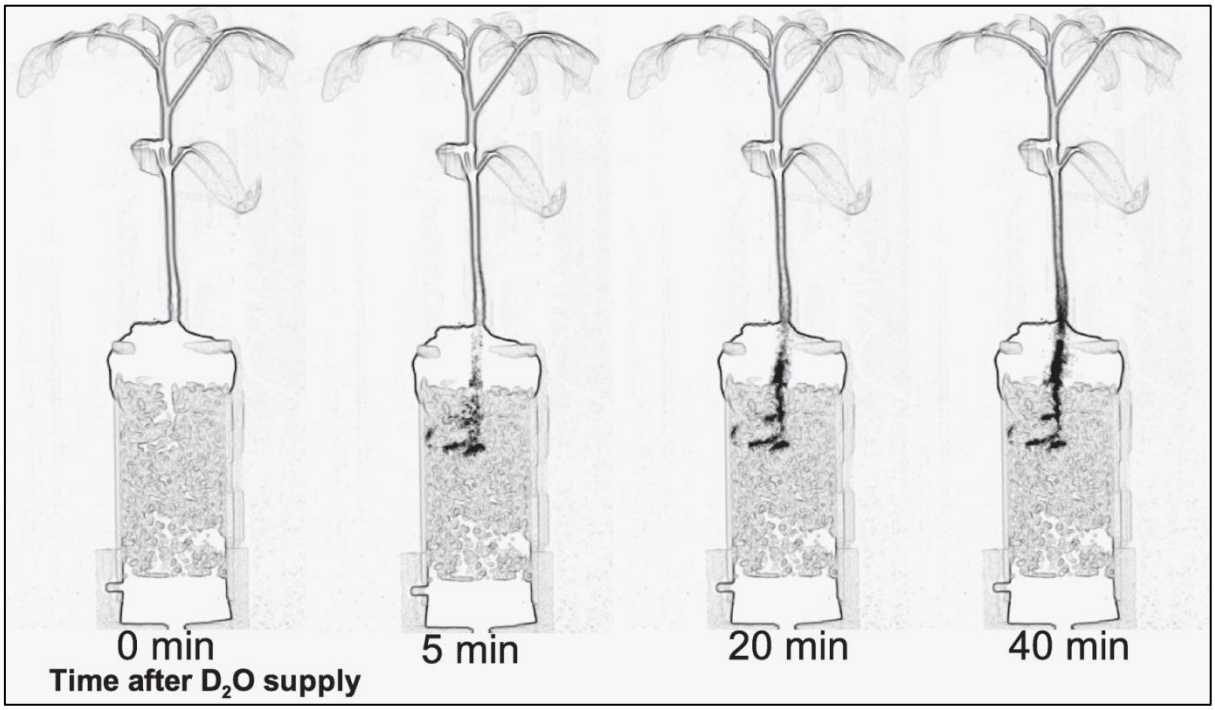

Figure 75 – The flow of water into the stem of a tomato seedling over time using D_2O as a tracer. Dark areas correspond to indicate regions of higher D_2O concentration. Adapted from U. Matsushima *et al*[115].

10.5.3 Internal Imaging of Fuel Cells

One of the recent developments in fuel cell technology has been the creation of a polymer electrolyte membrane fuel cell (PEMFC).[116, 117] The electrolytic process consists of supplying H_2 and O_2 to the cathodic and anodic side of the cell, respectively, and reacting them to create water. The water produced in the reaction is required to wetten the membrane for cell performance purposes, although excess water agglomerations must be removed to maintain a steady gas input rate. Water also causes corrosion of a number of the internal components, including the electrodes and membrane. Hence, appropriate water management in the fuel cell is important for both the efficiency and lifetime of the cell.

As noted above, neutron imaging has a high sensitivity for water due to the high mass attenuation constant for hydrogen. The water distribution of the inside of a fuel cell at four different current densities was imaged using neutrons by Hickner *et al*[118]. The resulting radiographs are shown in Figure 76. At current densities of 0.1 A cm^{-2} and 0.75 A cm^{-2}, significant levels of water can be seen on

the anode. However, the amount of water decreases at a current density of 1.25 A cm^{-2} due to the resulting temperature rise of the cell increasing the rate of evaporation.

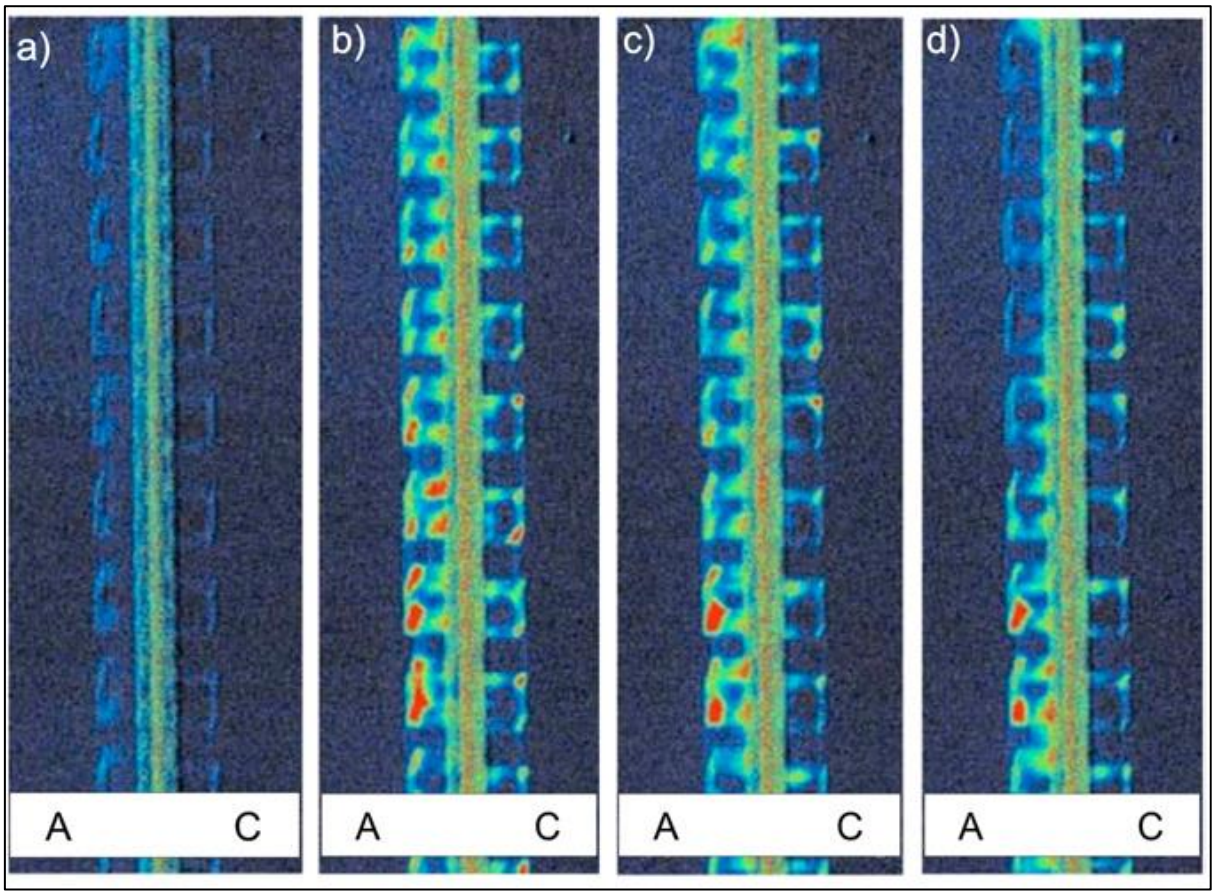

Figure 76 – Radiographs of an operating fuel cell at four different current densities. Left to right, 0 A cm^{-2}, 0.1 A cm^{-2}, 0.75 A cm^{-2}, 1.25 A cm^{-2}. The anode and cathode sides are marked A and C respectively. Adapted from Hickner *et al*[118].

11 The GadMOS Project

By taking advantage of the conversion processes outlined in Section 10.4, coupling a gadolinium thin film with a suitable electron detector allows detection of thermal-energy neutrons with high efficiency. This approach forms the basis of the GadMOS project, also known as the GdMOS, GadMos and GP (gadolinium-PImMS) project. The PImMS sensor has already been described in depth in Part II and was originally developed as an imaging sensor for detecting pulses of light generated by ion impact on an MCP/phosphor detector. Detection usually occurs when incident photons generate electron-hole pairs within the silicon layer of the sensor. Electron liberation requires 3.6 eV and the resulting electrons are then detected at charge-collecting diodes located within each pixel. In contrast to photon detection, high-energy electrons incident on the silicon layer can result in an ionising track, with a single high-energy electron causing many electrons to be liberated. In the case of neutron-capture by Gd, a 71.7 keV conversion electron could theoretically liberate (ionise) up to 20,000 electrons. When combined with a pulsed neutron source, the GadMOS sensor allows spatial imaging to be achieved in tandem with recording the neutron kinetic energy spectrum. This provides a vast increase in the data throughput when compared with the traditional method of stepping a time-gate through the neutron energy distribution and recording the images at each energy individually, as the entire position and energy-resolved data set can be recorded in a single measurement.

11.1 GadMOS Sensor Configurations

The first experiments employed a PImMS1 sensor with a 300 µm thick foil of gadolinium mounted in front of the sensor at the shortest achievable distance without risking damage to the sensor bond wires (approximately 1 mm). The thickness of the gadolinium foil necessitated the experiments to be carried out in “reverse geometry”, as opposed to “forward geometry”, both of which will be described below.

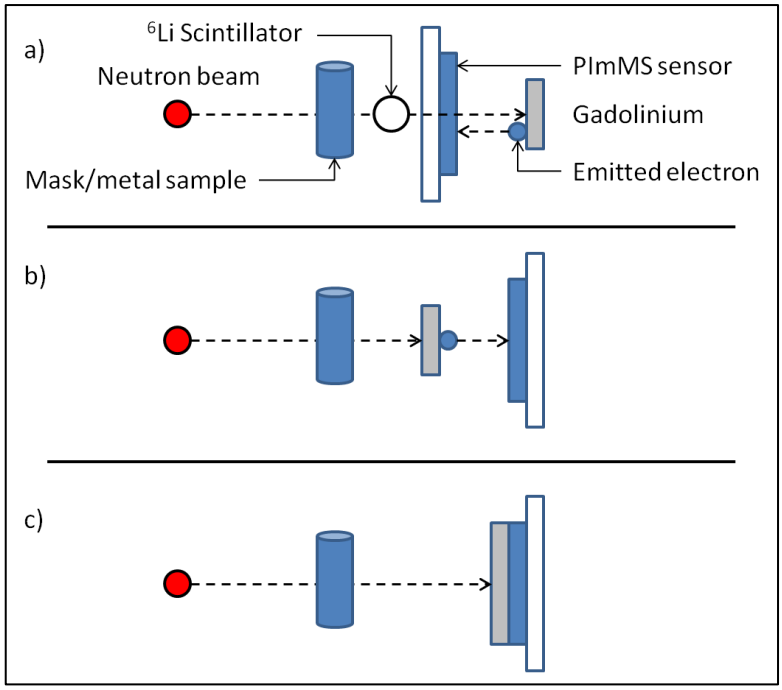

Figure 77 – a) The experimental geometry for reverse illumination with sample and ^{6}Li scintillator position noted (if present). b) The experimental geometry for front, or forward, illumination – this arrangement no longer requires passing the neutron beam through the PImMS sensor and sensor board which would cause attenuation of the beam. c) A PImMS sensor with gadolinium sputtered directly onto the surface, significantly improving the spatial resolution of the detector. In all setups, the distances between the gadolinium sheet and the PImMS sensor and the thicknesses of all components have been exaggerated for clarity.

The detection of neutrons by the PImMS sensor can be considered in terms of four physical processes:

1. Thermal neutron capture by the nucleus of the converter, which is dependent on the gadolinium thickness and the neutron capture cross section. The cross section is dependent on the isotopic composition and the incident neutron energy;
2. Secondary charged particle creation, i.e. IC and Auger electrons;
3. Escape of the secondary electrons from the converter. This is dependent on the energy of the electrons (and thus the electron mean free path) and the thickness of the material;
4. Detection of the electrons by the PImMS sensor. The IC and Auger electrons must have sufficient energy to ionise the silicon layer of a PImMS sensor extensively enough for the signal threshold to be exceeded and a digital hit to be registered.

In the reverse geometry arrangement, the neutron beam passes through the sample and the transmitted beam then passes through the sensor board and the sensor itself before impinging on the gadolinium conversion layer (Figure 77a). The sensor then detects the electrons that are emitted toward the sensor, i.e. from the same side of the gadolinium on which neutrons are incident.

However, this geometry necessitates the neutron beam to pass through the PImMS sensor and the sensor board, which causes significant attenuation of the beam due to gold and copper present in these components, both of which interact strongly with neutrons. Increasing the thickness improves the probability of neutron capture but electrons that are liberated from deeper within the gadolinium are less likely to escape the layer. The overall effect of increasing the thickness of the gadolinium is to asymptotically increase the efficiency of a conversion electron being emitted (and therefore a signal being detected by the PImMS sensor), achieving over 95% of the maximum efficiency at a thickness of 10 µm (see Figure 78). Based on these arguments, gadolinium films or foils of any thickness can be used as a neutron conversion material in this geometry.

In the front, or forward, geometry, the gadolinium conversion layer is placed after the sample but before the sensor (Figure 77b). This orientation avoids the previously mentioned problem of beam attenuation, but requires the thickness of the gadolinium layer to be carefully selected; neutron conversion efficiency is maximised with a gadolinium thickness for which the combination of neutron capture and electron transmission (escape) is maximised. However, in forward geometry, the efficiency is predicted to peak at approximately 4 µm, decreasing exponentially with increasing gadolinium thickness at greater thicknesses. This renders the 300 µm foil unsuitable for forward geometry experiments.

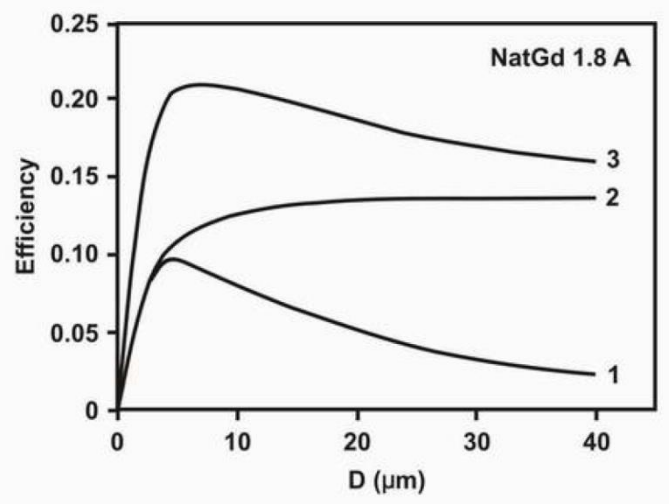

Figure 78 – The calculated efficiency of electron-emission from a gadolinium thin film as a function of thickness performed by D. A. Abdushukurov *et al*[106]. The three lines correspond: 1 - forward geometry; 2 - reverse geometry; 3 - forward & backward geometry summed.

Once the proof-of-concept experiments had been carried out with the 300 µm thick gadolinium foil, a second set of experiments were performed in which the neutron signal was recorded in both forward and reverse geometry using gadolinium films of different thicknesses. Gadolinium films

sputtered onto silicon supports were supplied by Kelvin Nanotechnology Ltd (University of Glasgow) with thicknesses of 1 µm, 2 µm, 3 µm, 4 µm, 5 µm and 7 µm. Experiments were also performed using gadolinium foils of 5 µm and 10 µm thicknesses (stated tolerances of 20%), purchased from Goodfellow. The 5 µm and 7 µm sputtered thin films were initially found to be unstable, and delaminated from their silicon substrate over the period of several weeks. This was resolved by using a support layer of titanium between the Si and Gd layer.

Following determination of the optimum gadolinium thickness, gadolinium was then sputtered directly onto the PImMS sensor. This gave two benefits: firstly the composite detector was more robust than the predecessor, and the performance was not dependent on manually optimising the distance between the gadolinium foil and the sensor for each experiment; and secondly, due to the isotropic emission of electrons following a gadolinium-neutron interaction, by coating the conversion material directly onto the sensor surface and thereby eliminating the gap between the point of electron generation and electron detection within the PImMS sensor, the spatial resolution was improved from approximately 1 mm to better than 0.1 mm. A schematic of the PImMS sensor with gadolinium directly sputtered on the surface is shown in Figure 77c) and photographs show a PImMS2 sensor before and after the sputtering process has been applied are shown in Figure 79.The early experiments described in Sections 12.1 - 12.2 were carried out using the PImMS1 sensor, while the later experiments described in Section 12.3 - 12.4 employed the larger PImMS2 sensor. The increased sensor size of PImMS2 compared to PImMS1 allows for an increased region of the neutron beam to be imaged, and therefore facilitates imaging of significantly larger objects than was possible using the PImMS1 sensor.

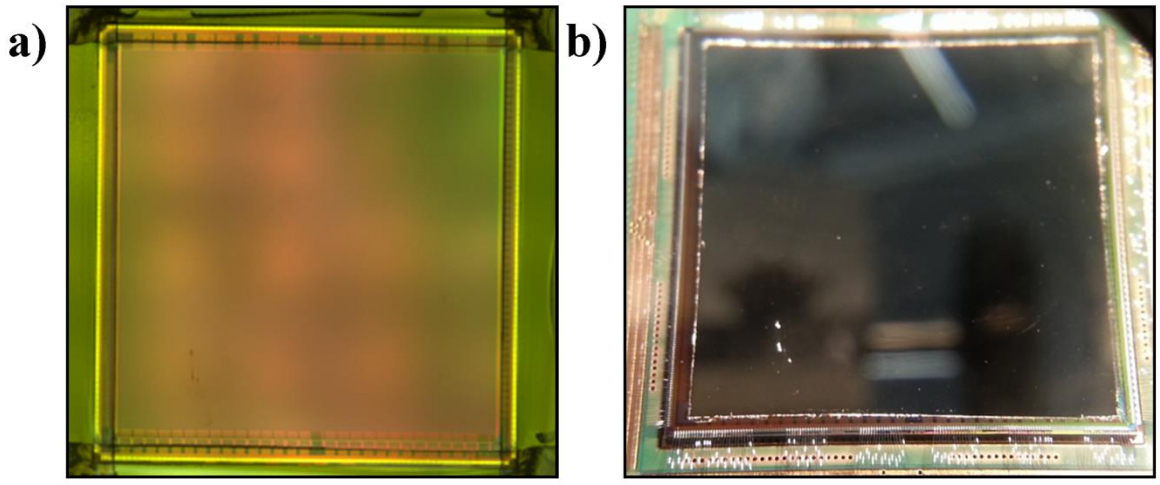

Figure 79 – a) a bare PImMS2 sensor, prior to wire bonding onto the sensor board; b) a PImMS2 sensor wire bonded onto the sensor board, with gadolinium directly sputtered onto the sensor surface.

The use of the PImMS sensor for neutron detection required a number of modifications to the normal operation of the sensor. In the initial proof-of-concept experiments, the sensor board, PImMS1 sensor and gadolinium foil were placed directly in the neutron beam path. The sensor board was removed from the camera and was connected remotely using a series of 50 cm ribbon cables. This allowed the camera, which constituted a large proportion of the cost of the detector, to be placed out of the beam path, thereby minimising the risk of equipment damage due to neutron exposure. However, the cables introduced a significant level of noise which required new algorithms to be developed in order to reduce the noise through a combination of screening the signal as it was being recorded, as well as identifying and removing noise in the recorded data set. Following the initial experiments, all subsequent studies were performed with a layer of cadmium shielding placed between the sensor board and camera, allowing the entire detector to be placed in the neutron beam path without the risk of camera damage and removing the effect of noise due to the cables.

The PImMS sensor is usually cooled using a copper cooling finger and Peltier cooler. However, as neutrons incident on the copper finger could potentially be scattered or reflected onto the PImMS sensor, there existed a possibility of the detector recording false data or artefacts due to the copper finger. Tests were performed with and without the copper finger present and no appreciable difference was seen without the copper finger present. All experiments thereafter were performed without the copper finger present (i.e. uncooled).

An additional consideration is the fact that the arrival time distribution of neutrons from pulsed spallation sources span a significantly longer time scale (~10-100 ms) than those of ions detected in an imaging mass spectrometry experiment (~100 μs). In order to perform these experiments, custom firmware was coded for the PImMS sensors to allow longer time periods to be assigned to each timebin, thus increasing the maximum data acquisition time per experimental cycle. For experiments performed on the Rotax beamline, an experimental period of 20 ms allows the entire neutron arrival time distribution to be recorded. Given the 160 MHz clock frequency of the PImMS timing electronics, this corresponds to assigning 800 clock cycles for each timecode, much longer than would typically be employed in an imaging mass spectrometry measurement, where values of 2-10 clock cycles per timecode are typically used. The increased experimental period caused a previously unseen source of noise to be observed, namely that the build up of leakage or 'parasitic' charge in each pixel over a long period of time could cause the charge to exceed threshold and register as a digital hit. This manifests as a late timecode occurring with a broad Gaussian distribution over time, compared to the normal thermal pixel noise, which generally occurs at very early timecodes and exhibits an exponential decay with time. The effect of parasitic charge can be suppressed by

increasing the signal threshold, though at the cost of reducing the sensitivity of the pixel, since a higher charge is then required for a signal to be recorded. Alternatively, as the noise consistently occurred within the same pixels at a rate of 1 digital hit per frame, it could be removed with a similar discrimination to that used for thermally noisy pixels (Section 7.2.2). This source of noise has been termed “dark-current noise” or “dark noise”. Figure 80 shows an example data set recorded by the PImMS sensor with a 300 µm thick gadolinium foil when placed in the neutron beam. The raw TOF spectrum (including dark noise) integrated over the sensor is plotted in black and the TOF spectrum after the dark noise has been filtered is plotted in red. The difference between the spectra, plotted in blue, represents the isolated dark current noise and shows the characteristic occurrence occurring at late timebins. The figure also shows how effectively the noise can be removed, giving the broad curve matching the gadolinium neutron capture cross section. The accuracy of the TOF spectrum will be compared in more detail in the following sections.

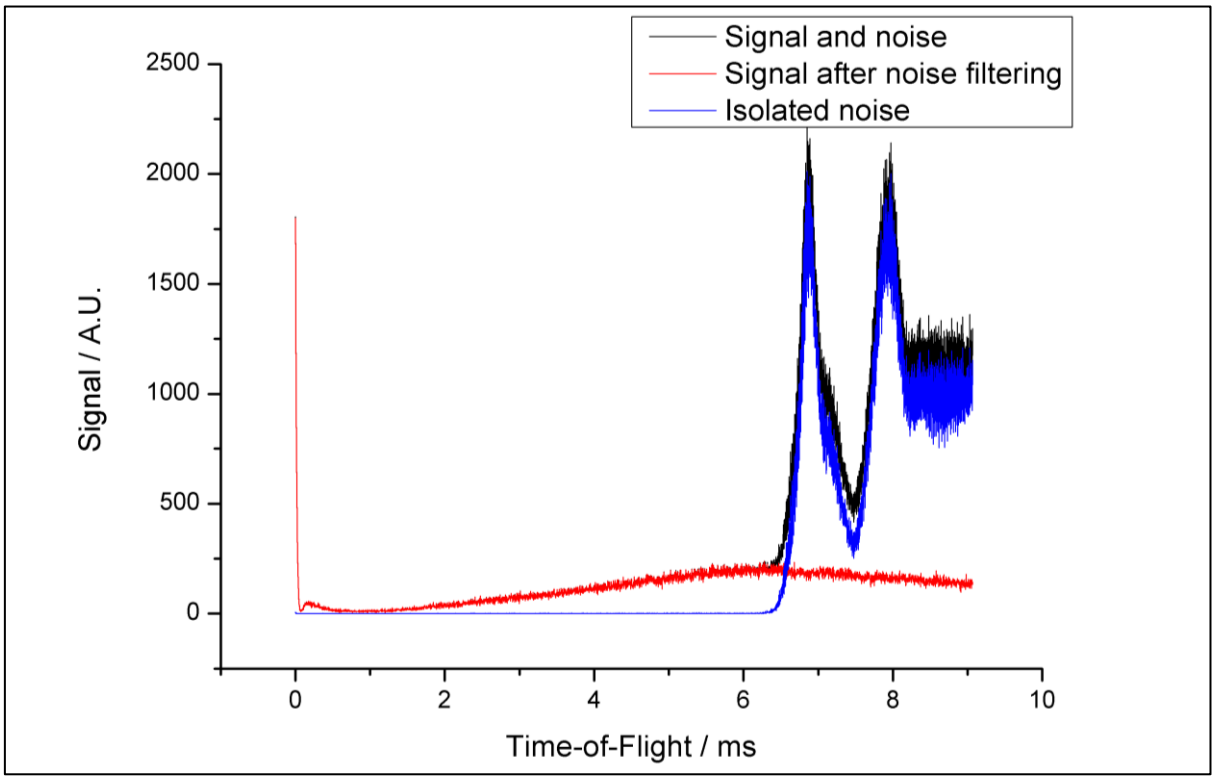

Figure 80 – An example of a TOF spectrum before and after dark noise has been filtered. Although dark noise can contribute significantly towards a data set, it can be filtered out very effectively to leave the signal due to the sample.

11.2 The ISIS Neutron Spallation Source

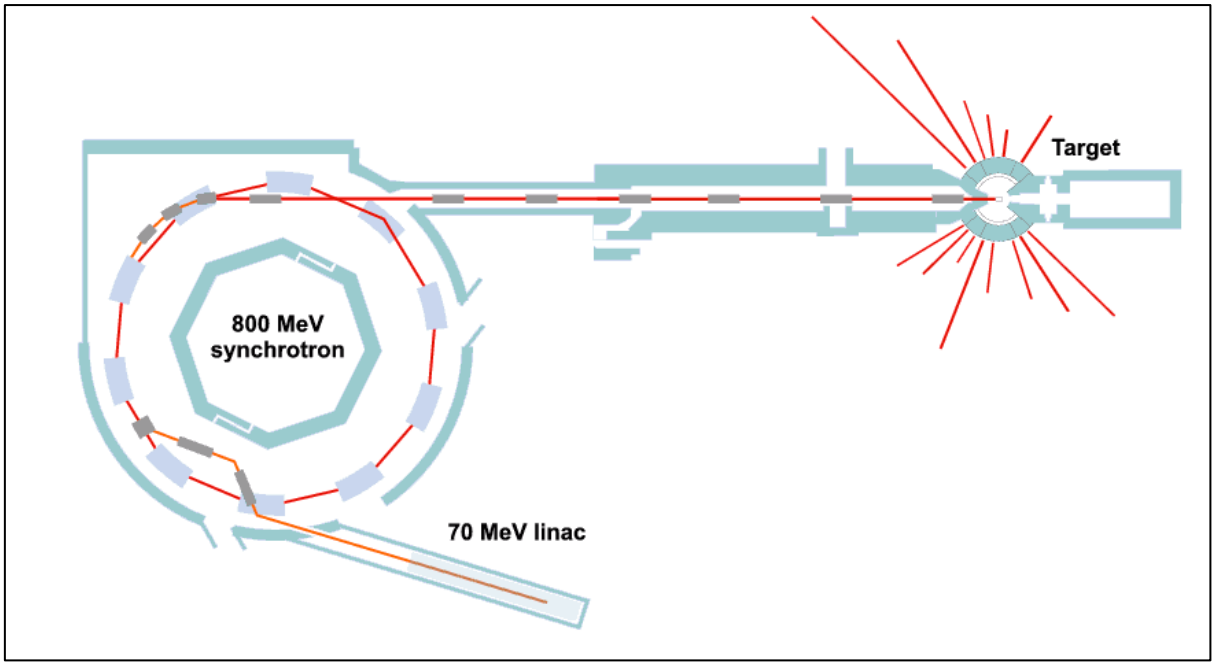

Figure 81 – A schematic representation of the ISIS Neutron Spallation Source, showing the linear accelerator (linac) used to accelerate H^- ions, the synchrotron that accelerates H^+ ions and the spallation target consisting of the tungsten block. Spallation produces neutrons with an isotropic distribution. The red lines emerging from the target show the path of neutrons to different beamline instruments.

The ISIS neutron spallation source is an STFC-funded research facility based at the Rutherford Appleton Laboratory in Harwell in the United Kingdom. A schematic of the neutron source is shown in Figure 81. ISIS uses spallation (impact-induced emission) to produce pulses of neutron and muon beams. The process begins with an ion source fed with hydrogen gas and caesium vapour to create H^- ions during an electric discharge. The H^- ions are extracted in 200 µs pulses to form a beam which is passed through a 90° bending magnet to remove any electrons. The negative hydride ions are accelerated through a uniform electric field to a kinetic energy of 34 keV. The beam then passes into a Radio Frequency Quadrupole (RFQ) accelerator that uses electric fields to focus, bunch and accelerate the beam. The resulting ion bunches are further accelerated to 37% of the speed of light in a linear accelerator consisting of four 10 m long copper electrodes.

The H^- ions are passed through a 3 µm thick aluminium oxide stripping foil that strips the electrons, leaving a beam of H^+ ions (protons) for injection into a synchrotron. By synchronising the pulsed ion source with the orbital period of the synchrotron, approximately 2.8×10^{13} protons are accumulated and accelerated over 130 revolutions. Once the injection period is complete, the protons are separated into two bunches that are accelerated over a further 10,000 revolutions to 84% of the speed of light. The extracted proton beam delivers 4 µC of protons in two 100 ns pulses separated by

300 ns, to the neutron target consisting of a tungsten block approximately the size of a house brick. The high energy protons drive neutrons from the tungsten nuclei in a process known as spallation, producing an intense neutron pulse and only moderate heat. The neutrons are slowed to energies between 0.1 meV and 800 meV using moderators of water, liquid methane (100 K) and liquid hydrogen (20 K), and travel to target stations surrounding the tungsten source. Choppers are used to remove gamma rays and fast neutrons produced in the spallation event from the beam. The repetition rate of the neutron pulses is 50 Hz, with every fifth pulse of protons from the synchrotron used for a different experiment, producing no neutrons on the GadMOS detector beamline for 20% of the triggered events.

All experiments described here took place in the Rotax test facility, located in Target Station 1 at the ISIS neutron spallation source. The flight distance of the neutrons from the tungsten source to the detector was 15.5 meters and the neutron beam was collimated by the flight tube and further collimated using solid blocks of boron carbide (B_4C), a highly effective neutron absorber, before being exposed to the experimental sample and GadMOS detector.

11.3 Comparative TOF Measurements

In the initial stages of the project, it was important to compare the performance of the GadMOS detector with that of a traditional ^{6}Li neutron detector. One of these ^{6}Li detectors is shown in Figure 82. The detector consists of GS20 (alumina-silicate doped with lithium-6 oxide) scintillator material with a maximum active area of 30 × 80 mm^2, housed in aluminium. The quoted detector efficiency is 10^{-4} at incident neutron energies of 1 Å. The high neutron transparency of both the scintillator material and the aluminium housing of the ^{6}Li detector meant that the neutron beam intensity was not appreciably altered by its presence in the beam. This allowed the ^{6}Li detector to be placed in the beamline ahead of the GadMOS sensor without perturbing the neutrons incident on the GadMOS sensor (as shown in Figure 77a). In this way, both detectors were exposed to essentially the same neutron signal allowing a direct comparison in performance. Differences in the TOF spectra recorded by the two detectors are expected due to the different energy dependences of the neutron capture cross sections for ^{6}Li and $^{155/157}$Gd. However, useful comparisons can still be made between the general shapes of the distributions recorded with each detector, and in particular with respect to their response to sample-dependent features of the distribution, for example the positions of Bragg edges.

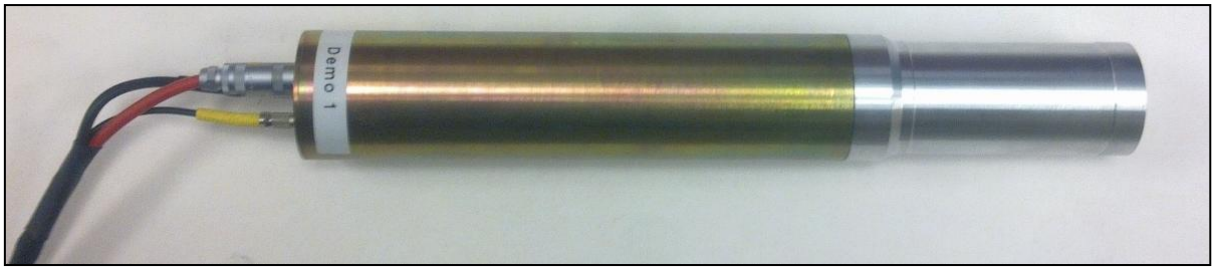

Figure 82 – The Neutron Beam Monitors used at ISIS. The aluminium housing at the end contains the scintillator material.

12 GadMOS Experiments

12.1 Proof-of-Concept Experiments

The principle objective of the first experiments was to show that the GadMOS sensor was sufficiently sensitive as a neutron detector in comparison with existing detectors, and also to show that the time resolving capabilities of the PImMS sensor allowed the neutron TOF distribution and images to be recorded simultaneously. The initial experimental setup consisted of the 300 μm gadolinium foil cut to a 3 × 3 mm^2 square and placed in reverse geometry (see Figure 77). The GadMOS data was taken in four sets of TOF windows, each 6.66 ms in duration, using an analogue delay generator to scan over the 20 ms TOF window. The processed data was then concatenated to produce a data set representative of the entire window of interest. The shortened TOF window was necessary to mitigate the effects of the dark-current noise mentioned in Section 11.1.

The TOF spectrum recorded by the experiment is the result of the kinetic energy distribution of the neutron beam convoluted with the energy dependent neutron-capture cross section of gadolinium. The expected image integrated over all timebins for the same data set was predicted to reproduce the 3 × 3 mm^2 square of gadolinium from which the detected electrons were emitted. Once experiments had been performed, further TOF spectra and images were obtained by placing different samples in the neutron beam path.

12.1.1 Gadolinium TOF Spectrum and Image

Four data sets, each summed over 40,000 neutron pulses, were taken at incremental delays of 5 ms relative to the neutron pulse. The TOF spectra recorded using the GadMOS detector and the ^{6}Li scintillator showed significant deviations from each other at early flight times due to the different neutron capture cross sections of ^{6}Li and $^{155/157}Gd$ for high energy neutrons. At later arrival times, corresponding to thermal neutrons, the cross sections have a similar dependence on energy, and the neutron beam arrival time profiles recorded by the two detectors are very similar, with characteristic features seen in both spectra (see Figure 83).

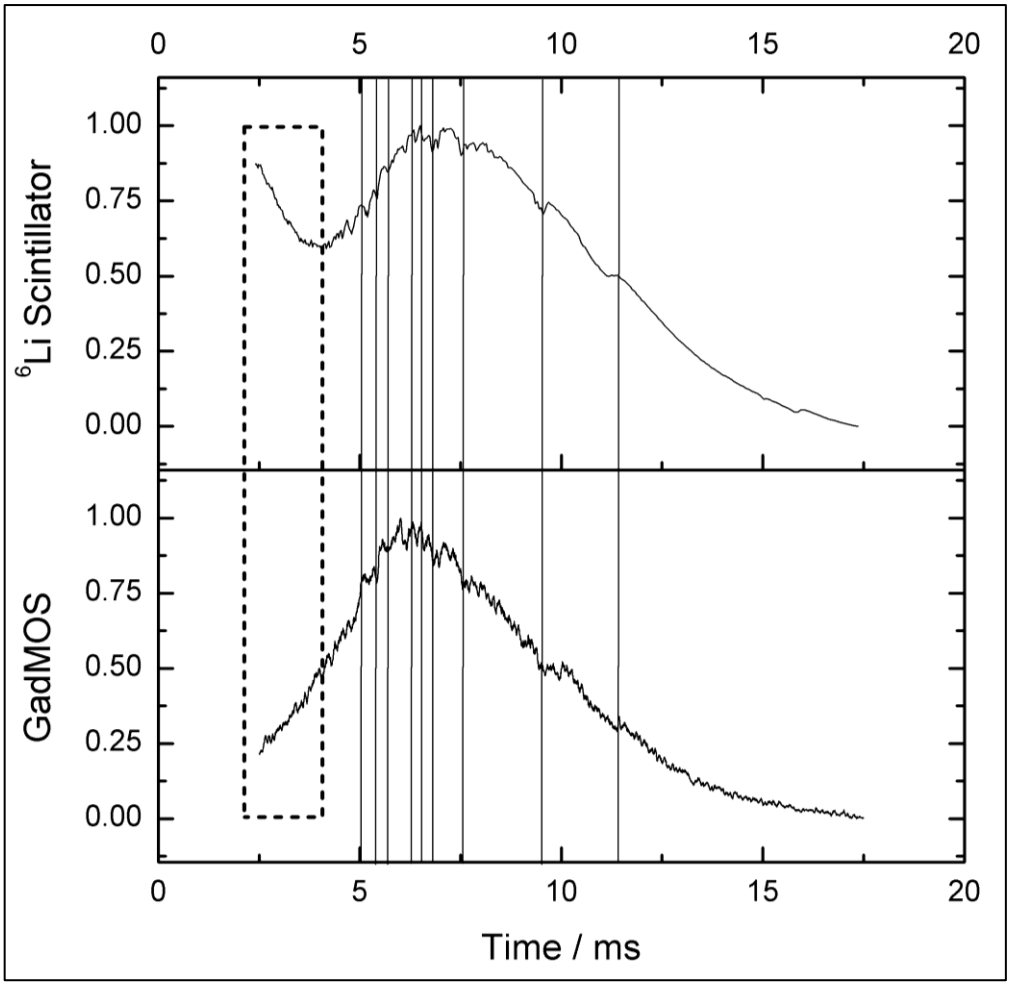

Figure 83 – A comparison between the TOF spectra recorded with the GadMOS sensor and the ^{6}Li scintillator. Known features in the neutron kinetic energy distribution are highlighted by vertical lines. Significant deviation at high neutron energies (early TOF) is highlighted by the dashed region and is attributed to the difference in neutron capture cross section between ^{6}Li and $^{155/157}$Gd. The number of recorded events by the GadMOS sensor and ISIS scintillator were 1,781,157 and 527,973 respectively.

The spatial distribution of neutrons, recorded in tandem with the TOF spectra described above, is shown in Figure 84a). The image of the 3 x 3 mm^2 300 µm thick gadolinium foil is poorly resolved due to the relatively large spacing of 4 mm between the foil and the PImMS sensor surface. As shown in Figure 84b), moving the foil closer to the PImMS sensor, from approximately 4 mm to 0.5 mm, yielded both a drastic improvement in the spatial resolution and an overall increase in the detection efficiency. An intensity profile through the centre of the resulting square is shown in Figure 84c), and demonstrates the expected steep rising edge and uniform signal in the region where neutrons are being generated, i.e. where the gadolinium foil overlaps the PImMS sensor.

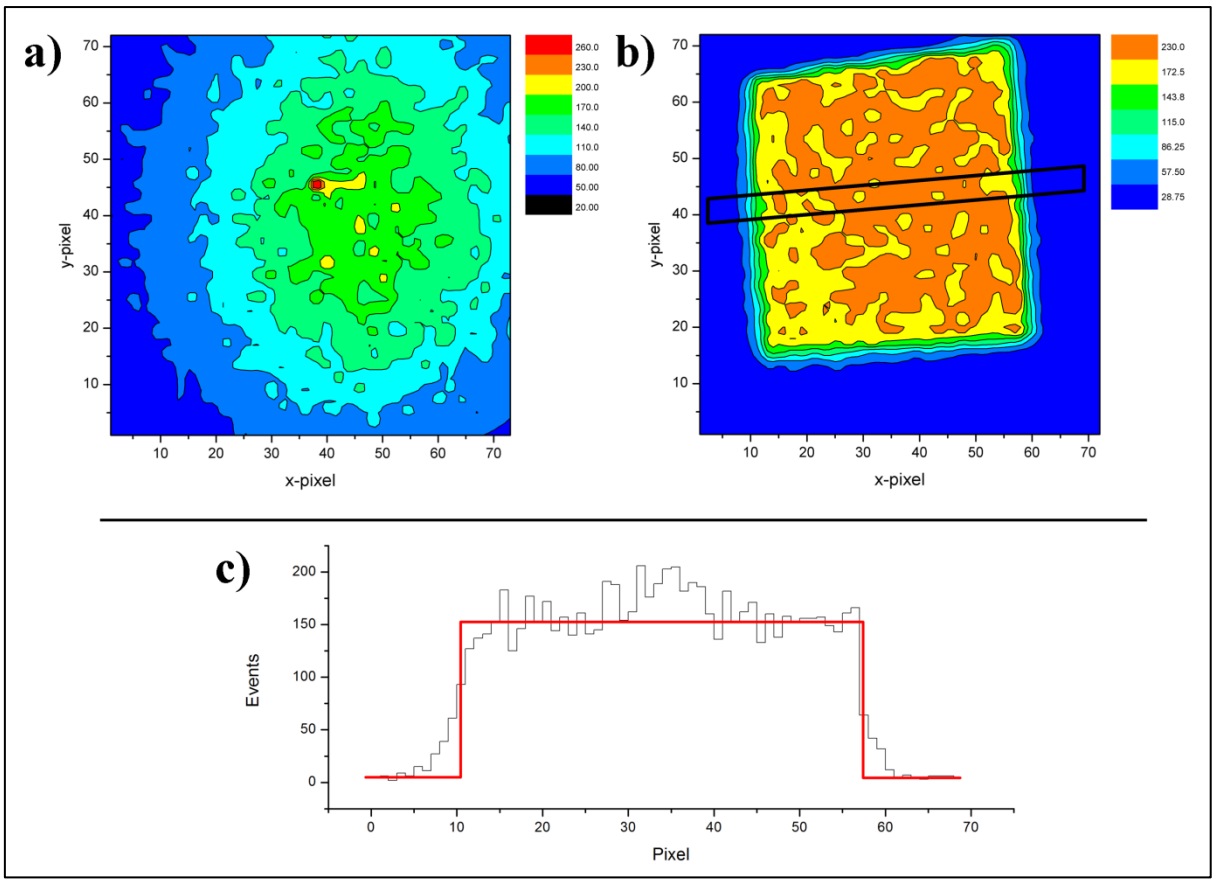

Figure 84 – a) The spatial distribution recorded from the data set in Section 12.1.1, accumulated over 40,000 frames. The poor resolution can be attributed to the large distance between the 3 x 3 mm^2 square gadolinium foil and the PImMS sensor, leading to significant electron divergence. b) The spatial distribution obtained by minimising the distance between the gadolinium foil and the PImMS sensor. The square can clearly be seen in a data set of 10,000 frames. c) The profile obtained by vertically integrating the black square marked in b). The red line (arbitrary height) shows the expected result based on the known dimensions of the gadolinium foil.

12.1.2 Iron and Copper TOF Spectra

Having demonstrated the viability of the GadMOS detector as a neutron detector, the assembly was used to record the thermal neutron TOF spectra for two metal samples. The samples consisted of cylindrical blocks of solid ferrite, i.e. pure iron in a body-centred cubic structure and solid copper with a face-centered cubic crystal structure. Comparative measurements were taken with the ISIS ^{6}Li scintillator monitor with deviation in the measurements at high neutron energies expected due to the difference in neutron capture cross section of the two conversion materials as in the previous experiment. Each of the metal samples studied was large enough to cover the area of the PImMS sensor. For the ferrite sample, two energy windows of interest were observed, one containing a single Bragg edge for an initial comparison and the other with many Bragg edges and further fine structure. The normalised TOF spectra are shown in Figure 85, and show clear agreement between

the two detectors. The number of neutron pulses and detected neutrons for each detector are shown in Table 9.

Table 9 – The number of neutron pulses and number of total neutrons recorded by each detector in the TOF experiments.

Sample	Neutron Pulses	GadMOS Detected Neutrons	^{6}Li Scintillator Detected Neutrons
Ferrite (13 – 19 ms)	65,535	170,776	24,658
Ferrite (6 – 12.5 ms)	193,583	961,522	206,182
Copper (6 – 12.5 ms)	177,057	13,780,300	316,363

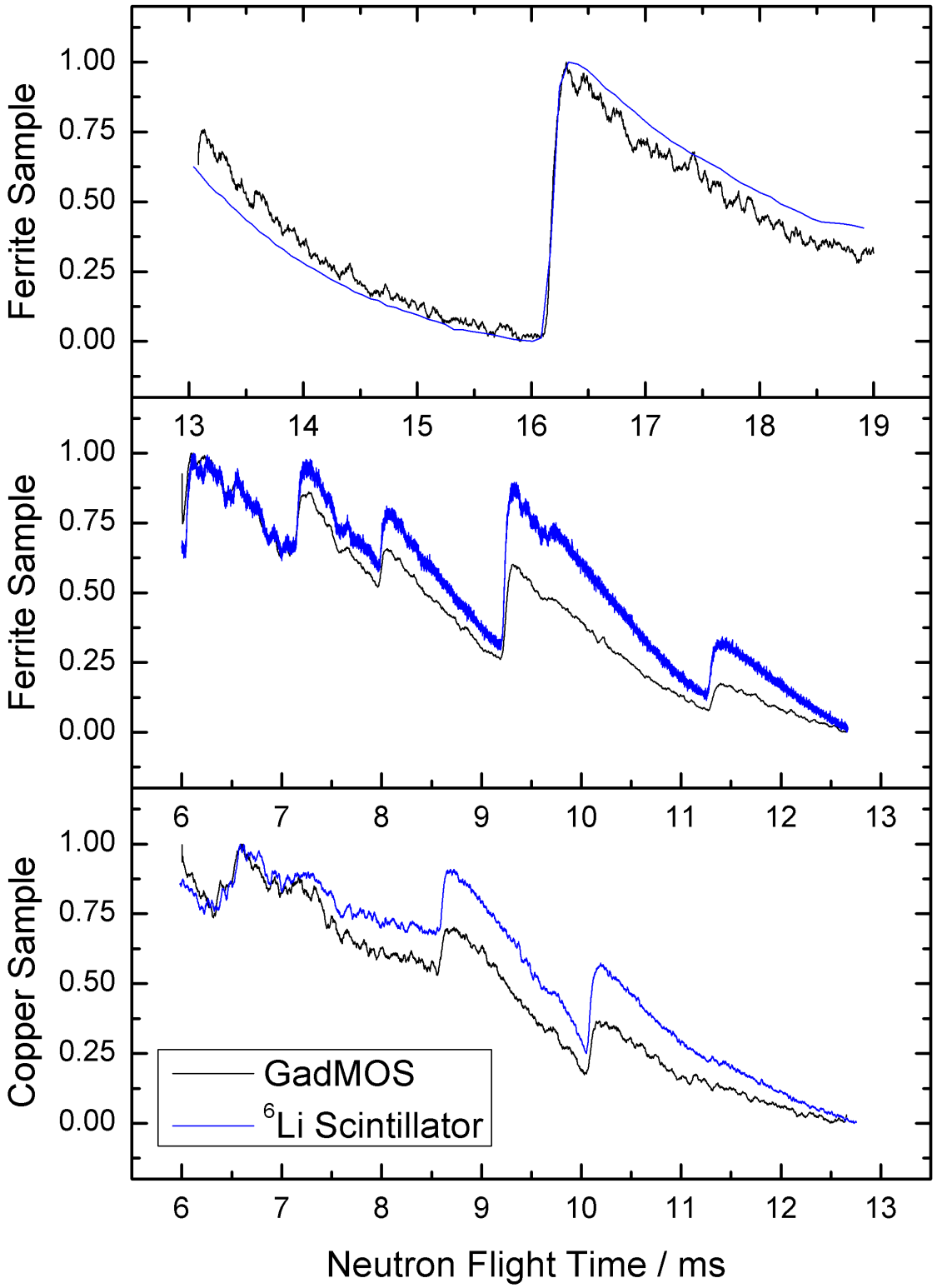

Figure 85 – The normalised TOF spectra recorded for copper and ferrite samples by the GadMOS and the ^{6}Li scintillator showing excellent agreement in the general features. The higher time resolution of the GadMOS detector allows finer features to be seen in the spectrum.

12.1.3 Cadmium Aperture Imaging

With the time-resolving and imaging abilities of the GadMOS detector established, an experiment was designed to show different images at different neutron energies. In this experiment, a sheet of cadmium placed in front of the gadolinium foil was used to create intensity contrast as a function of neutron energy: cadmium exhibits a sharp change in neutron transmission as a function of incident neutron energy (see Figure 86). Neutrons with an energy higher than approximately 0.5 eV pass through the cadmium, whereas lower energy neutrons are absorbed, causing cadmium to act as an energy-selective neutron mask. The sheet of cadmium employed in these measurements covered the area of the PImMS1 sensor and had a 1 mm diameter hole drilled in the centre. Time-resolved images were acquired over 40,000 neutron pulses, and the TOF spectrum was extracted from the data set. Extracting the image associated with early timecodes (i.e. the image of high energy neutrons that are expected to be transmitted through the cadmium) revealed the gadolinium square as expected. At later timecodes, low energy neutrons can only pass through the aperture in the cadmium, projecting a smaller circular beam onto the gadolinium foil. Integrating over the late TOF timebins reproduces the circle as expected. These images and the regions that they were created from are shown in Figure 87.

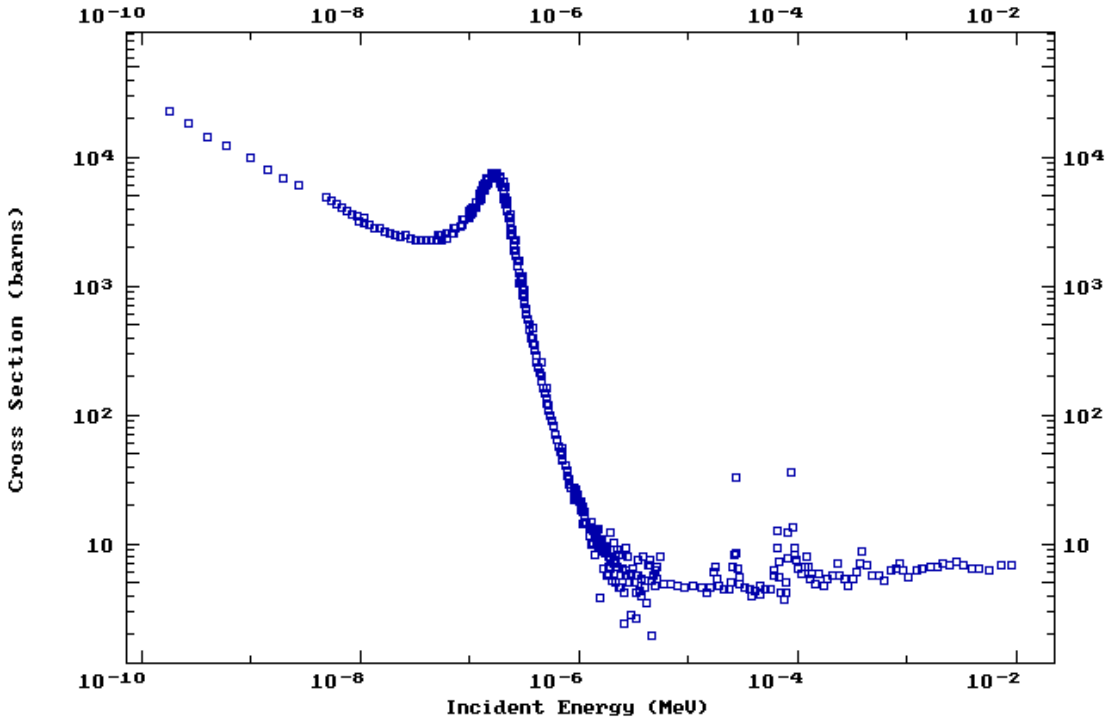

Figure 86 – The neutron absorption cross section of cadmium as a function of incident neutron energy. At energies below 0.5 eV, the cross section increases dramatically, preventing the transmission of low energy neutrons. Taken from the Nuclear Data Services database[119].

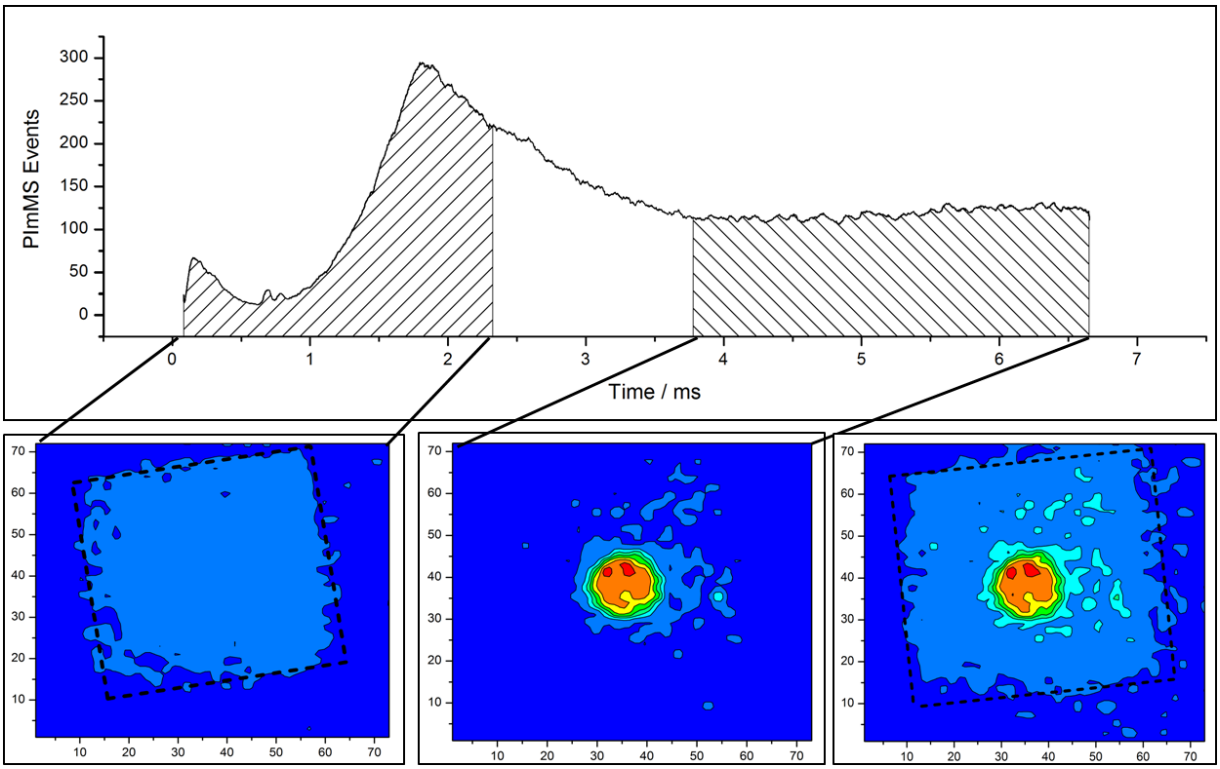

Figure 87 – Anticlockwise from top: the TOF spectrum obtained from the data set with a much earlier (higher energy) maximum due to the low transmission of cadmium; the spatial image obtained for early TOF neutrons showing the gadolinium square; the spatial image obtained for late TOF showing the aperture in the cadmium sheet; the spatial image obtained by integrating over the entire TOF spectrum.

The experiment was later repeated by taking a 19.6 × 19.6 mm square of cadmium with seven 1 mm diameter holes drilled in it. A 4 µm gadolinium thin film was mounted against the cadmium square and the assembly mounted as close to the PImMS sensor as possible. Again, the holes were faithfully reproduced in the images generated by integrating the PImMS sensor signal acquired over late timecodes, shown in Figure 88. The image also showed that a spatial resolution better than 1mm was achievable when using Gd foils separated from the PImMS sensor.

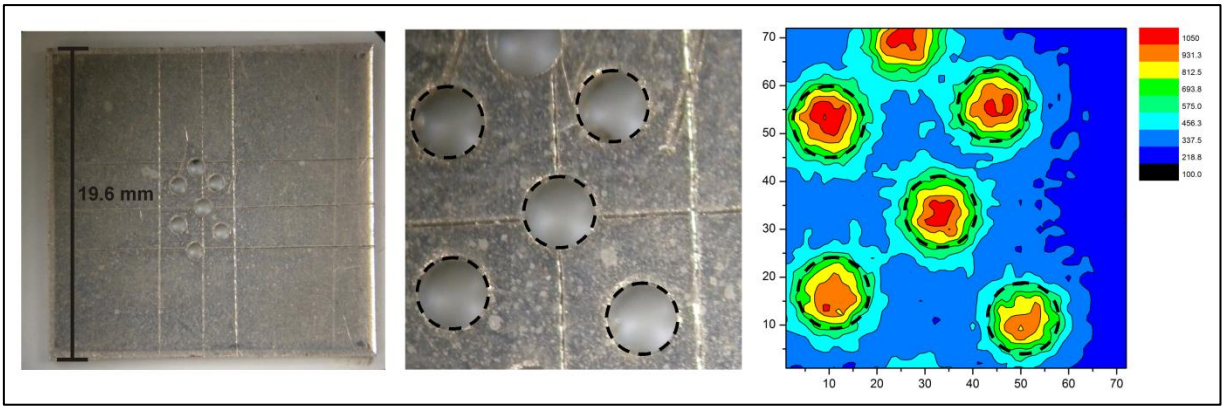

Figure 88 – From left: an optical image of the cadmium mask used, measuring 19.6 mm in height; zoomed-in optical images of the cadmium mask with 1 mm apertures highlighted; the spatial image recorded by PImMS with the aperture positions and sizes marked identically to the optical image.

12.2 Optimising the Gadolinium Thickness

The optimum gadolinium thickness for the GadMOS sensor was defined to be the thickness that gave the highest overall secondary electron count per neutron pulse counted over the complete arrival time distribution of the neutron beam. This was determined experimentally by recording the neutron count obtained using the various foils and thin films available (described in Section 11.1) over 40,000 frames. The experiments were repeated in both forward and reverse geometries. The gadolinium foils and films were fixed on aluminium mounts, and a set of digital callipers was used to ensure that the sensor and gadolinium distance remained constant at 0.2 ± 0.1 mm. As the size and shape of the gadolinium sample varied slightly for each thickness, a 25 × 25 pixel subarea of the data set was taken from the centre of the gadolinium image and used to perform the analysis.

During the experiments, the neutron signal with no gadolinium present was also recorded to determine the inherent sensitivity of the PImMS sensor to neutrons. The silicon on the sensor is doped with natural abundance boron, 19.9% of which is boron-10, a neutron-sensitive material (as previously discussed in Section 10.4). The PImMS sensor therefore exhibited a very small sensitivity to thermal neutrons, which was found to be 0.15 recorded counts per neutron pulse. This is negligible compared to the sensitivity when paired with gadolinium, generally two orders of magnitude greater, but was nonetheless appropriately subtracted from the GadMOS experimental data when studying the effect of gadolinium layer thickness.

Due to the time required to set up and measure the neutron flux for each thickness of gadolinium and the restricted availability of beam time, the measurements were carried over three separate allocations of beam time. The positioning of the sensor within the beam on different visits meant that the absolute signal recorded for an identical experimental setup was not entirely reproducible

between visits. To ensure that the data from various experimental runs could be compared reliably, detection efficiency measurements were taken with a standard thickness gadolinium film on each visit, allowing data acquired on different visits to be linearly scaled for comparison.

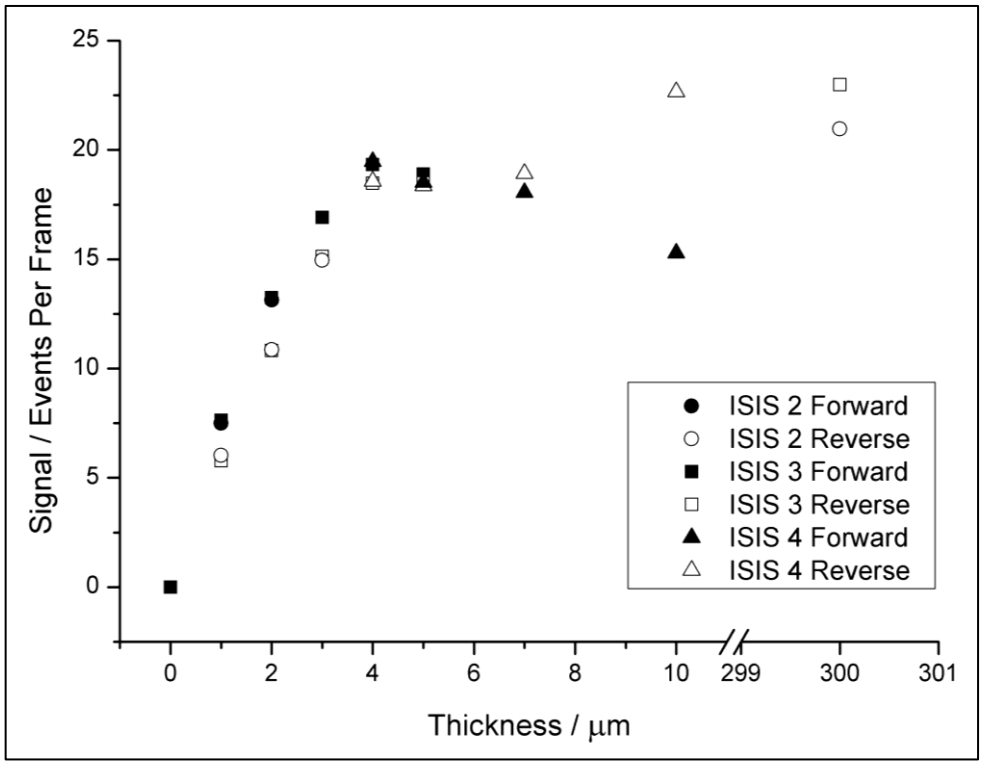

Figure 89 – The measured neutron events per frame for different gadolinium thicknesses and geometries, averaged over 40,000 frames. Symbol shapes denote the visit on which the experiments were performed and the fill denotes the experimental geometry. On each beam time allocation, at least two measurements that had been performed previously were repeated in order to ensure that the data acquired on different allocations could be compared. ISIS 2, ISIS 3 and ISIS 4 refer to the second, third and fourth beamline visit respectively.

The signals recorded for the various different Gd foil thicknesses are shown in Figure 89. The experimental data reproduce the curves expected from the theory presented by Abdushukurov *et al* (Figure 78). The curves for front-side illumination show a broad peak at a foil thickness of 4 μm, which represents the optimum balance between path length over which electrons can be generated, and path length over which electrons can escape the foil to be detected. In the reverse geometry the latter parameter is effectively fixed, and the signal reaches a maximum, after which it remains constant. The theory predicts equal detection efficiency in both experimental geometries up to a Gd foil thickness of approximately 4 μm, after which the decreased signal seen for the forward geometry is due to conversion electrons being unable to escape from the foil for detection.

12.3 Experiments with the Directly Coated PImMS Sensor

With the optimum gadolinium thickness experimentally determined, a number of PImMS1 and PImMS2 sensors had gadolinium sputtered directly onto the surface of the sensor. An increase in spatial resolution was expected, due to the decrease in electron dispersion. The same resolution limit was expected for the PImMS1 and PImMS2 sensors due to the common pixel size of 70 µm × 70 µm. The spatial and temporal resolution of the new GadMOS sensors were tested in a series of experiments that are described in the following sections.

12.3.1 Copper Powder TOF Spectrum (Temporal Resolution Test)

Newly commissioned PImMS sensors are usually tested using a signal generated by a pulsed diode laser incident on the sensor, allowing a direct comparison between the input signal and the signal recorded by the sensor. This is not possible for a PImMS sensor coated with gadolinium as no light is transmitted through the layer of metal. The GadMOS sensors were therefore tested directly in the neutron beam by observing structure in the TOF spectra caused by Bragg edges from materials placed in the neutron beam in front of the sensor.

A PImMS2 sensor with a 4 µm gadolinium coating was used for these experiments. Each timebin was set to 1.125 µs, giving a 4.608 ms exposure time. The sample was copper powder contained within an aluminium box. The edges of the box were sealed using aluminium tape to prevent copper powder from escaping. This was important for safety reasons due to the risk of inhalation of neutron-activated radioactive copper powder. The internal depth of the box was measured to be 10 mm. A background measurement was taken for the empty box before filling it with Cu powder and recording a second data set. The high neutron transparency of aluminium meant that the presence of the box had a negligible effect on the TOF spectra recorded. In both cases, the data set was acquired over 32,688 neutron pulses.

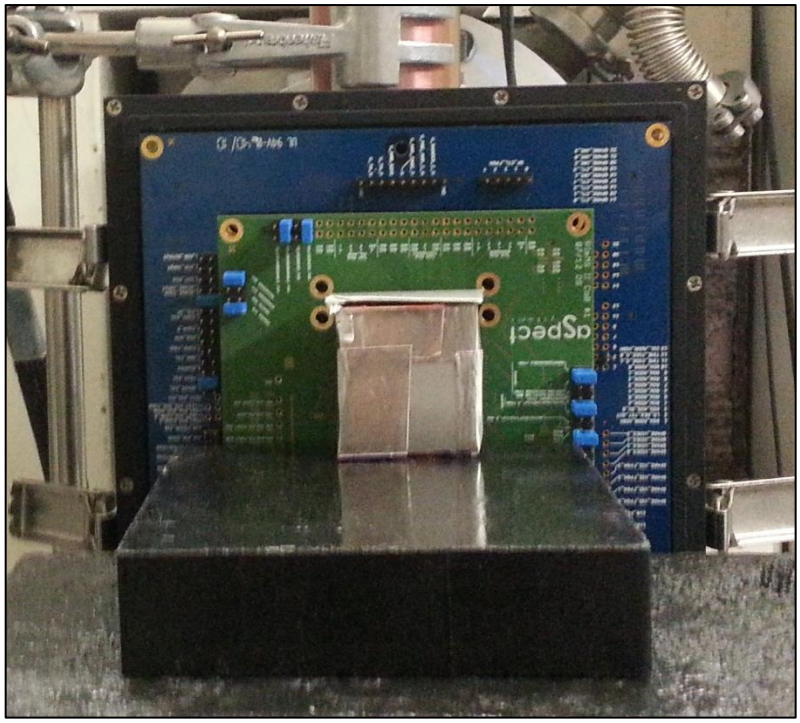

Figure 90 – The experimental setup of the copper powder contained within the aluminium sample holder. The sample holder was stood on a block of B_4C and spatial covered the majority of the PImMS2 sensor.

The resulting image had the expected uniform appearance over the area that the sample covered. The TOF spectrum was extracted from the same region of interest of 70,000 pixels from the sample and background measurements. Dividing the normalised signal spectrum by the normalised background signal removed any features due to the aluminium box or the neutron profile, allowing the Bragg edges due to the copper powder to be resolved. The results of the measurements, shown in Figure 91, indicated that the gadolinium-coated PImMS sensor retained the time resolution required to resolve Bragg edges.

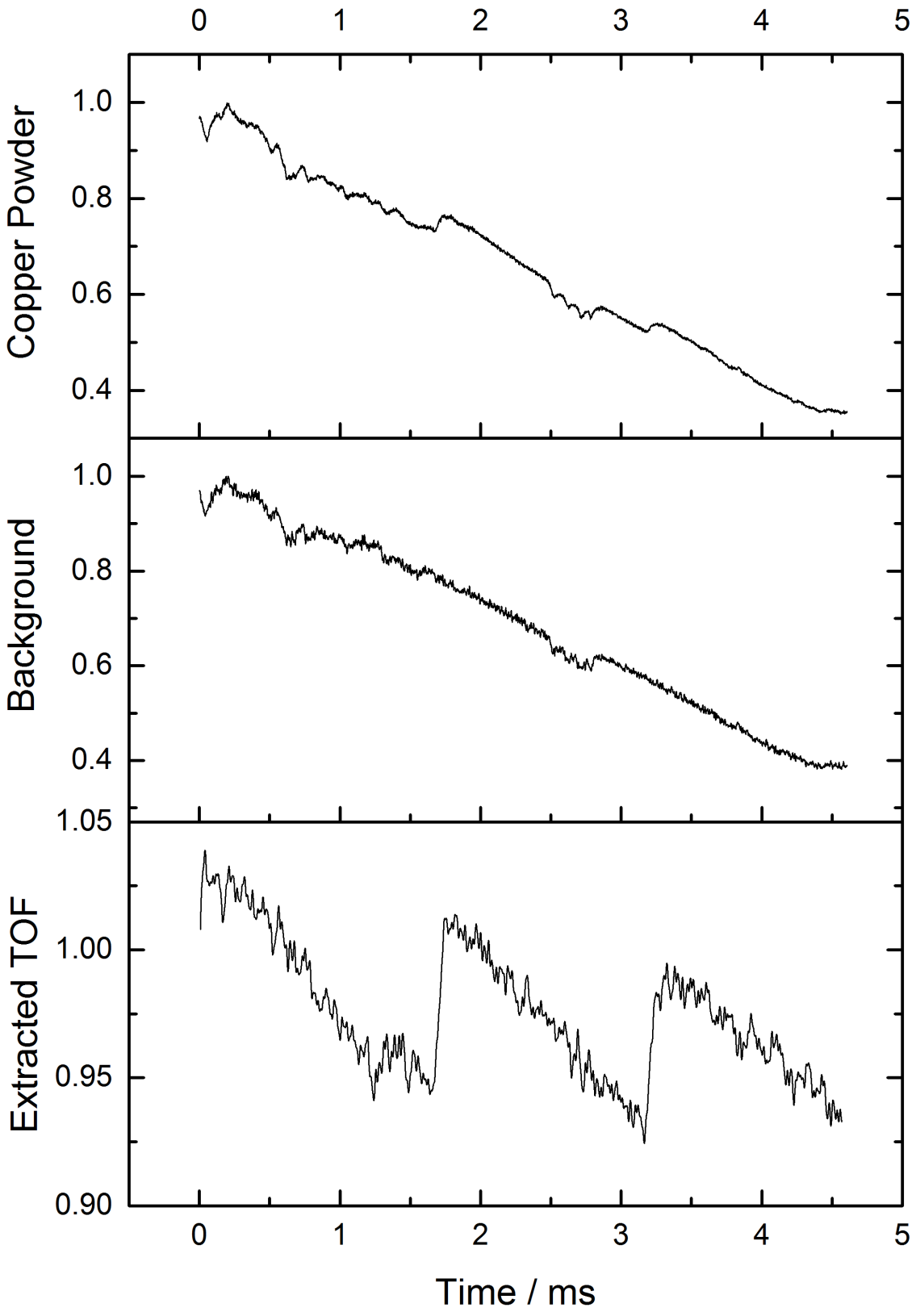

Figure 91 – Upper: the normalised sample TOF spectrum; middle: the normalised background TOF spectrum; lower: the resulting TOF spectrum after the sample spectrum has been divided by the background spectrum and a low pass FFT with a frequency of 2 has been applied.

12.3.2 Siemens Star Imaging (Spatial Resolution Test)

The spatial imaging tests were carried out with both a PImMS1 and PImMS2 sensor, both of which had a 4 µm layer of gadolinium sputtered onto the surface. The sample imaged was a *Siemens star* – a test structure commonly used in characterising the spatial resolution of an imaging detector – which was laser cut from a 4 µm gadolinium thin film coated onto a layer of silicon for support. The star included additional radial lines measuring 200 µm in thickness, as shown in Figure 92a). The portion of the neutron beam incident on the gadolinium layer is absorbed, producing conversion electrons which are absorbed by the silicon layer and therefore blocked from reaching the GadMOS sensor. In contrast, neutrons incident on regions in which the gadolinium layer has been ablated are transmitted through the silicon and strike the gadolinium-coating on the GadMOS detector. The increasingly convergent lines of the Siemens star provide a convenient means of characterising the spatial resolution of the detector. The neutron beam was well collimated and the mask was placed as close to the sensor surface as possible. As the 4 µm gadolinium mask was not thick enough to absorb all incident neutrons, a data set was recorded with and without the mask to allow a background corrected to be performed.

The images recorded by the PImMS1 sensor and PImMS2 sensor were acquired over 60,000 and 77,150 neutron pulses respectively with the Siemens star in the neutron beam. Background images of 40,000 pulses and 45,913 pulses respectively were scaled and subtracted from the data set. Analysis of isotropic regions of the images indicated that the lowest standard deviation in pixel intensity was consistently obtained by dividing the sample image by the background, whereas subtracting, then dividing gave an improved contrast, as shown in Figure 92. The radial lines of 100 µm can clearly be seen with both the PImMS1 and PImMS2 sensors, indicating that the spatial resolution is limited only by the pixel size of the sensors of 70 µm × 70 µm.

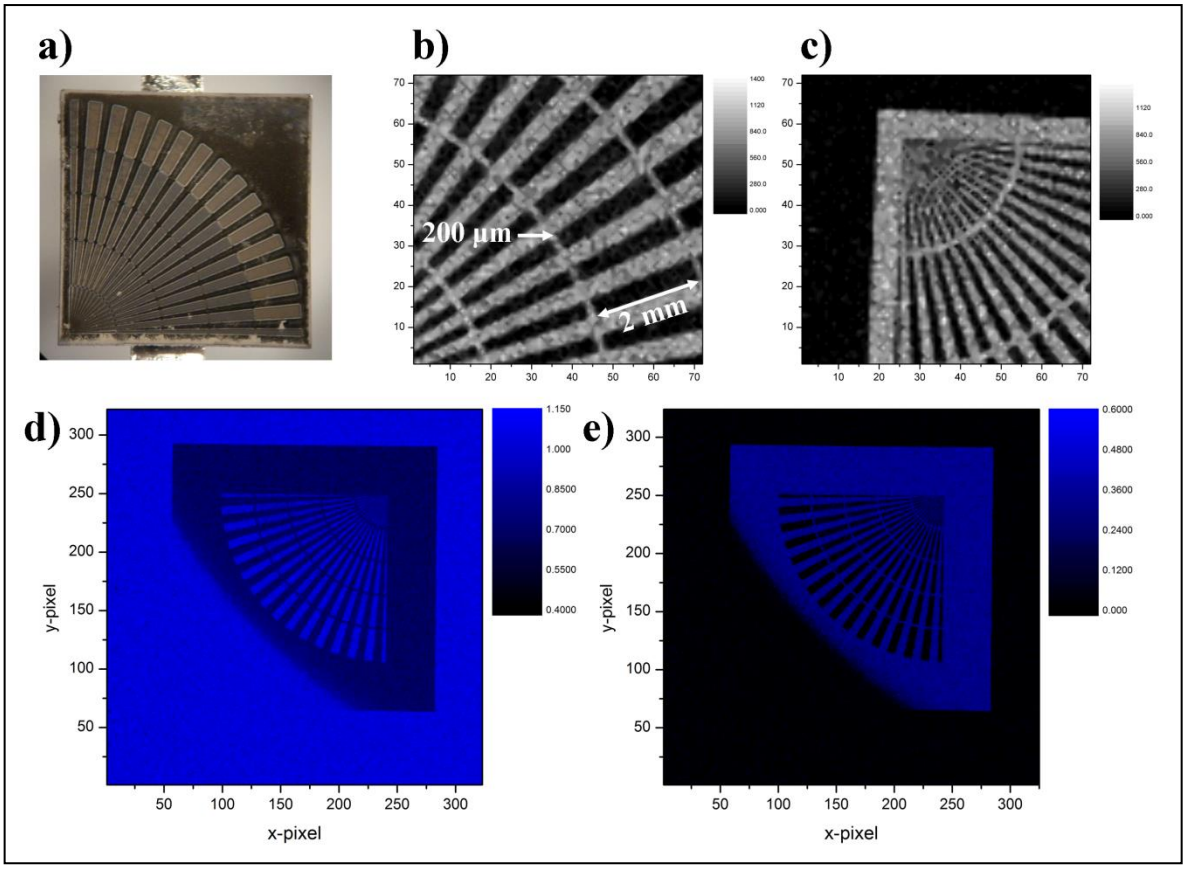

Figure 92 – a) An optical image of one of the masks used for the imaging experiments consisting of 4 µm gadolinium backed on silicon. b) An image of a region of large mask spacing recorded using a PImMS1 sensor. The radial lines are marked as 200 µm in thickness and each radial section spans 2 mm. c) An image of a region of small mask spacing recorded using a PImMS1 sensor. d & e) The entire mask imaged using a PImMS2 sensor. d) has been divided by the background whereas e) has been subtracted and divided. Note that the spatial resolution is identical to the images recorded using PImMS1 due to the identical pixel size. All PImMS sensors used had a 4 µm layer of gadolinium directly sputtered onto the surface of the sensor.

12.4 Applications

The gadolinium-coated sensor represents the best performance for neutron detection achievable with the existing PImMS hardware. Potential future improvements requiring modifications to one or more aspects of the PImMS hardware are discussed in Section 1. Having optimised the experimental parameters, a PImMS2 sensor coated with a gadolinium layer of thickness 4 µm was used for all experiments described in this section. As calibration of the PImMS2 sensor had not yet been achieved (2013 - 2014) due to outstanding firmware problems, the sensor was operated in an uncalibrated state. The high signal strength of the neutron beam meant that reliable data could still be obtained from the GadMOS sensor under these conditions. Calibration of the sensor in the future will provide an improvement in the signal-to-noise ratio achievable in neutron imaging experiments.

In the following, data is showcased from imaging a diverse range of samples with the newly optimised GadMOS sensor.

12.4.1 Shrink-Fitted Cylinder TOF Imaging

The aim of this experiment was to showcase how effectively the GadMOS detector could be used to acquire the TOF spectra for different samples in the same image in contrast to previous experiments that had used a single environment, such as pure copper or pure iron. To facilitate this, a shrink-fitted cylinder consisting of a copper centre surrounded by ferritic iron was imaged. At room temperature, the copper dimensions exceed the inner diameter of the iron; the cylinder was created by heating the iron, causing it to expand, and placing the copper rod, cooled by liquid nitrogen, inside it. Upon cooling back to room temperature, the metals experience increased strain which alters the position of the Bragg edges.

A mount fabricated from B_4C was used to support the cylinder in the desired position in the neutron beam. The aim of the experiment was to demonstrate the possibility of imaging four different environments simultaneously with the GadMOS sensor and to extract the TOF spectrum for each environment. Neutrons travelled either through air, through B_4C (neutrons almost completely blocked), through copper, or through iron before reaching the sensor.

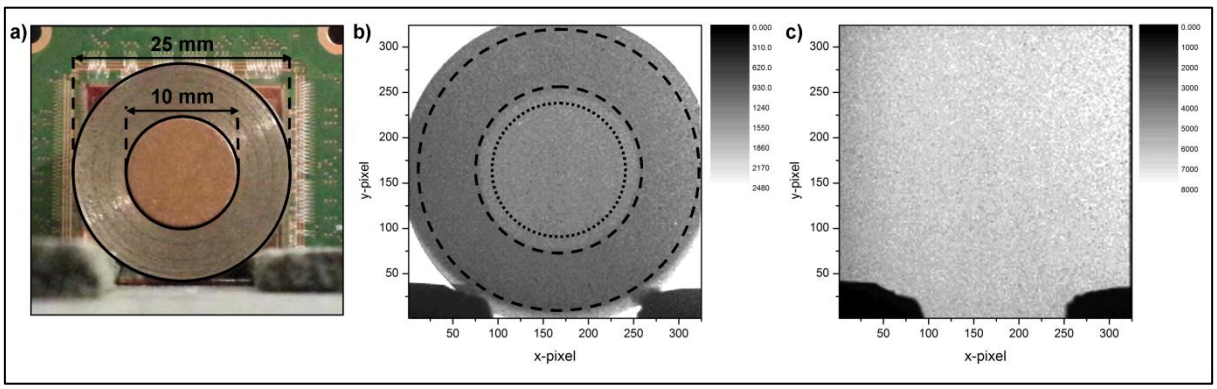

Figure 93 – a) The shrink-fitted cylinder with dimensions marked and the experimental setup with the PImMS2 sensor behind the cylinder. B_4C blocks holding the cylinder in place are visible. b) the image recorded with the cylinder present. The interior of the dotted circle and the dashed annulus denotes the areas for the copper and iron analysis respectively. c) the image recorded without the cylinder present, used for background correction.

945,660 neutron pulses with the cylinder in the neutron path were recorded with the GadMOS detector. The cylinder axis was aligned parallel to the direction of the neutron beam as shown in Figure 93a). A background image acquired over 747,342 neutron pulses was measured with the cylinder absent but the B_4C present. The width of the PImMS timebins was set to 1.125 µs, leading to a total experimental time of 4.608 ms. The beginning of the acquisition was offset from the beginning

of the neutron pulse by 5.2 ms so that 4.608 ms exposure was in the thermal neutron region. This maximised the recorded signal due to the overlap with the gadolinium neutron capture-section, and was also the region that Bragg edges were present.

The images acquired from integrating over all timebins with the cylinder present and absent are shown in Figure 93b) and Figure 93c). To extract the Bragg edges, the sample run, (signal intensity $I(x,y,t)$), was divided by the measurement with no sample present, (signal intensity $I_0(x,y,t)$). This corrected any features present in the time-of-flight structure in the neutron beam itself. The extracted TOF spectra for the copper and iron regions denoted in Figure 93b) are shown in Figure 94 and Figure 95.

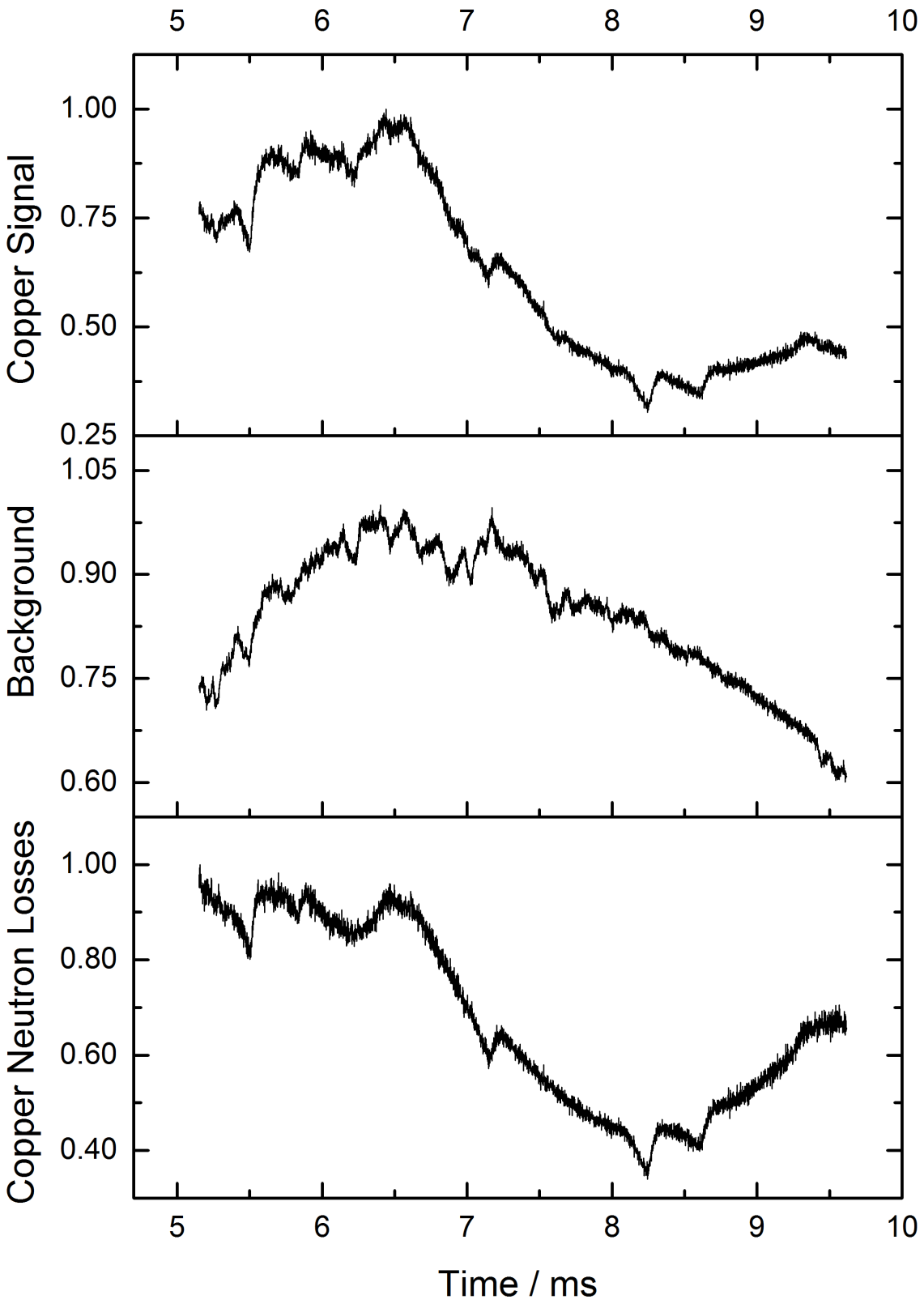

Figure 94 – The TOF spectra recorded for the region of copper, the same region without the sample present, and the result of dividing the spectra. The division allows Bragg edges to be extracted from the neutron beam profile more easily.

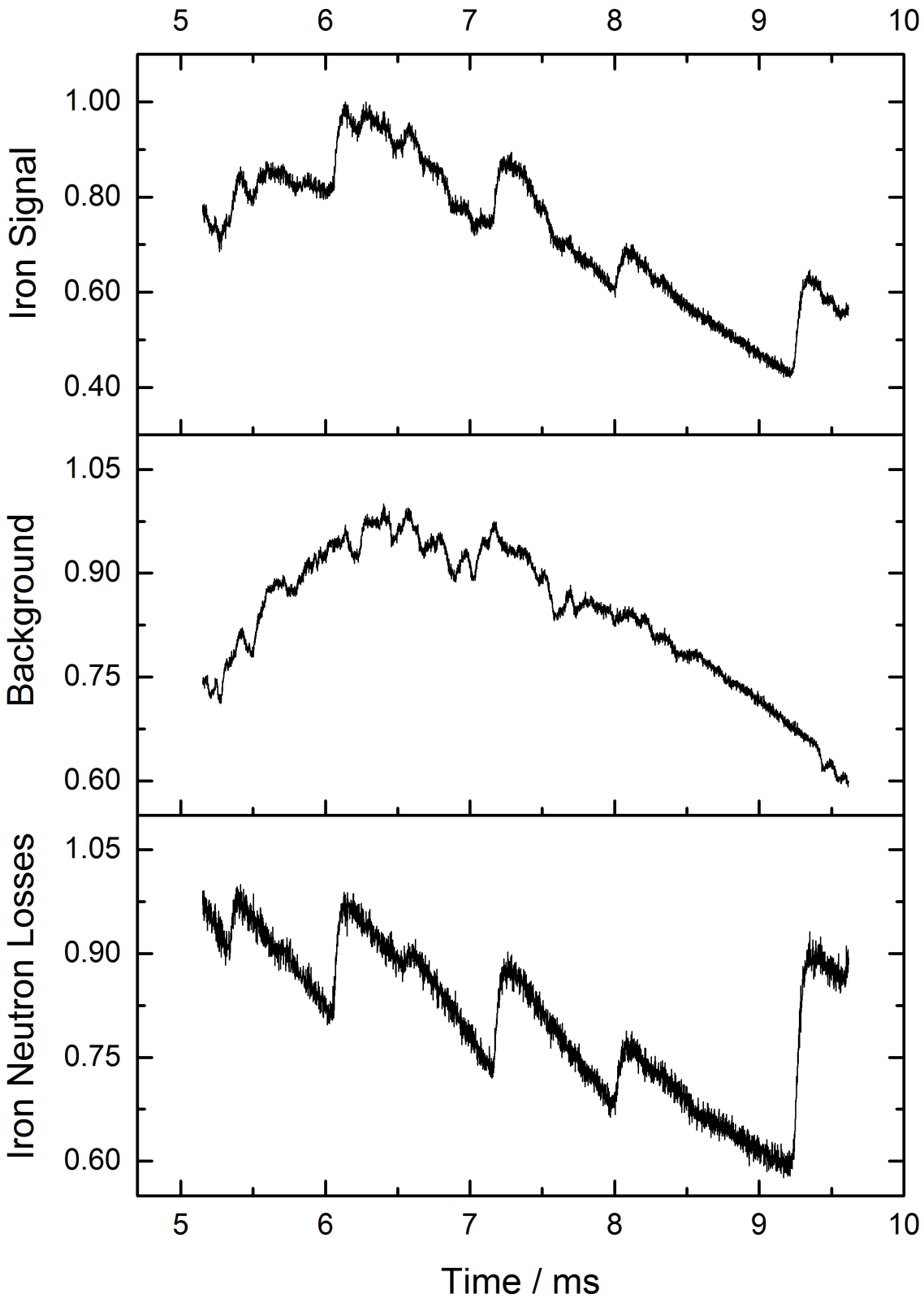

Figure 95 – The TOF spectra recorded for the region of iron, the same region without the sample present, and the result of dividing the spectra. The division allows Bragg edges to be extracted from the neutron beam profile more easily.

The positions of the Bragg edges show excellent agreement with measurements performed by Steuwer *et al*[120] on the same sample but with a ^{6}Li, which had the same background correction procedure, as shown in Figure 96.

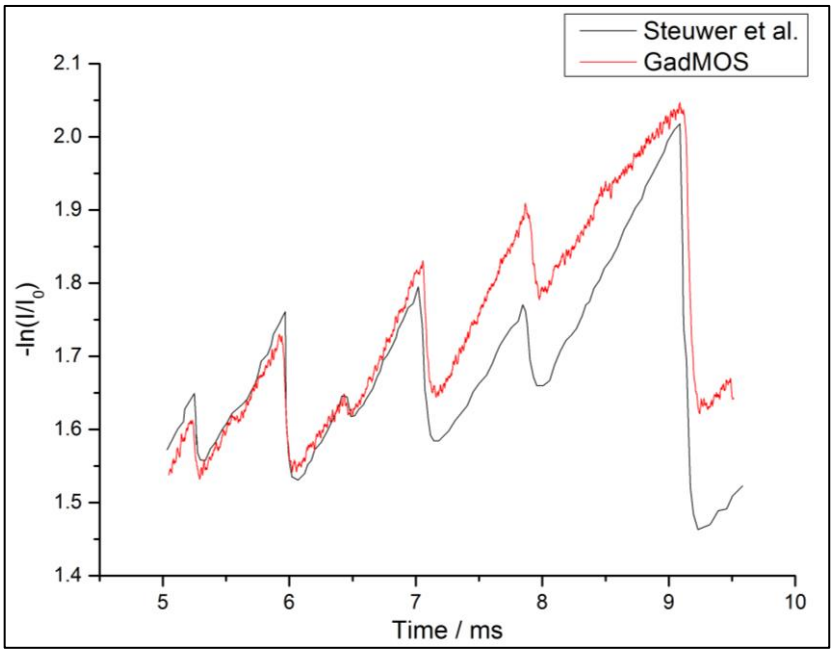

Figure 96 – The TOF spectra for the iron Bragg edges recorded by the GadMOS sensor and a ^{6}Li detector after the same background correction procedure has been applied.

12.4.2 Fossil Radiography

In a GadMOS data set, each timebin corresponds to a particular neutron energy. Extracting the image acquired for neutrons within a narrow energy range corresponding to a Bragg edge for a selected material provides enhanced contrast in the image. This allows the material to be identified in the neutron image in the presence of other materials whose neutron transmission characteristics are different at the energy of interest. To attempt to demonstrate this feature of time-resolved neutron imaging, a trilobite fossil embedded in rock was imaged using the GadMOS detector, with the aim being to demonstrate that the minerals constituting the fossil would be visible at certain neutron energies. This would allow non-destructive imaging of the fossil through the rock.

A data set was acquired over 559,141 neutron pulses with the trilobite sample placed in the beam path as shown in Figure 97. Unfortunately, whilst an image could be obtained when integrating over all timebins, it was not possible to extract meaningful images for different arrival time windows, most probably due to the levels of characteristic materials within the fossil being too low to be isolated against the background scattering from the encasing rock.

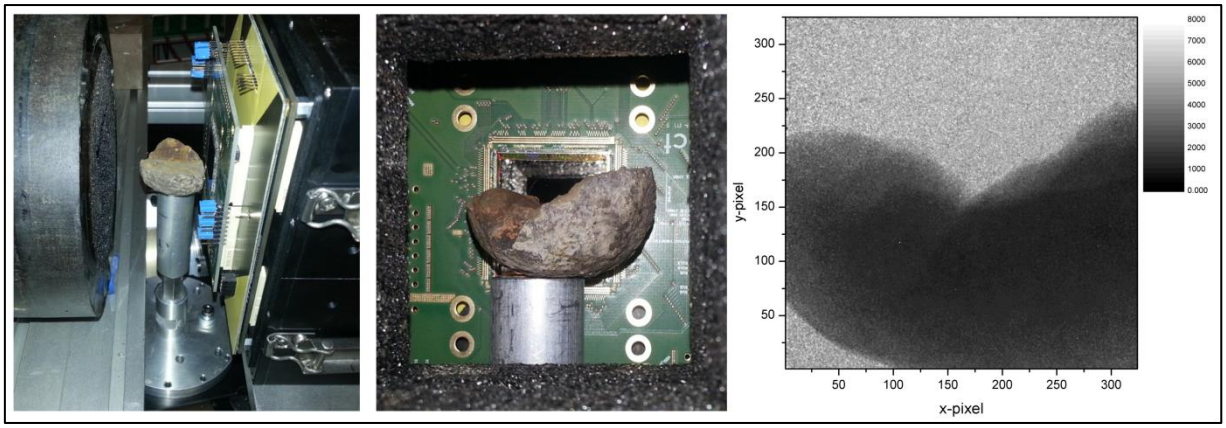

Figure 97 – From left; the experimental setup of the fossil radiography experiment, with the B_4C collimator and PImMS sensor and camera visible; the profile view of the fossil with the PImMS2 sensor behind it; the image recorded by the PImMS sensor after background correction showing the outline of the rock.

12.4.3 Neutron Tomography

Three-dimensional imaging can be achieved through a process known as tomography. This involves using a penetrating imaging technique, such as neutron imaging, and acquiring multiple projections of the sample by recording images at multiple angles. The images can then be reconstructed computationally, yielding a three-dimensional tomogram. Reconstruction algorithms require the object to stay within the field-of-view while it is rotated through all the angles sampled, and acquiring more projections will reduce the uncertainty in the tomogram. As a rough guide, tomography requires πx different projections to be recorded, where x is the number of x-pixels in the imaging detector. In the case of the PImMS2 sensor with 324 x-pixels, this corresponds to approximately 1000 angles.

Neutron tomography can be performed using a continuous neutron source and a non-time-resolved imaging detector. In this regime, the high neutron flux allows images to be collected quickly, albeit without any data about the energy of the neutrons. This is equivalent to the image obtained from integrating over all timebins in the PImMS data sets. As different materials attenuate the neutron beam to various extents, following 3D reconstruction, it may be possible to identify the material contained in each voxel (volume element) by examining the level of attenuation. However, any materials with the same total attenuation across the energy range of the neutron beam cannot be distinguished.

The advantage of using the GadMOS detector with a pulsed neutron source is that the arrival time distribution is also available for analysis. This allows normal tomography to be performed by reconstruction using a series of images integrated over all timebins at different angles. Alternatively,

by creating images from timebins specific to materials that increase their contrast, 3D reconstruction can selectively take place for a specific substance, for example, only iron or only copper.

Performing these measurements added several layers of experimental complexity. The Rotax beamline, where the experiments were performed, houses a computer-controlled rotation and translation stage that could be used to automatically rotate the sample. It was important to ensure that at any angle, enough data was collected to provide reliable statistics and therefore the stage was programmed to rotate only after a certain total flux from the neutron beam had been recorded. However, the neutron flux provided by the ISIS neutron source could be interrupted by external factors, which meant that the number of neutron pulses incident on the sample and detector was not necessarily dependent on the length of time that was recorded. To circumvent this issue, extra software was written to periodically timestamp the frame that was being recorded by the PImMS sensor as well as to record the timestamp of each rotation. By combining these data files, the images associated with each angle could be extracted unambiguously.

Another experimental consideration was planning which set of angles would be employed, and the order in which the images would be taken. If the total experimental time and the time required to image a single projection are both known, the number of images can be calculated by dividing the former by the latter. The images could then be acquired sequentially and at an isotropic distribution of angles. However, due to the unpredictability of the neutron beam, the total experimental time was not known, and thus taking sequential angles may produce a data set that was too undersampled at particular angles for a tomographic reconstruction to be achieved. To prevent this from happening, the golden section rule can be applied. The premise of the golden section rule is that at any time, the next considered projection angle should maximise the amount of information about the object that is independent of previous recorded projections. This can be achieved by maximising the angular distance of each subsequent projection. Over 180°, each subsequent angle is calculated by taking the largest angular gap and dividing it by the golden ratio: $g = \frac{\sqrt{5}-1}{2} \approx 0.618$ as demonstrated in Figure 98. This guarantees a maximum of new information and further ensures that the sampling pattern is non-periodic as the golden ratio is irrational.

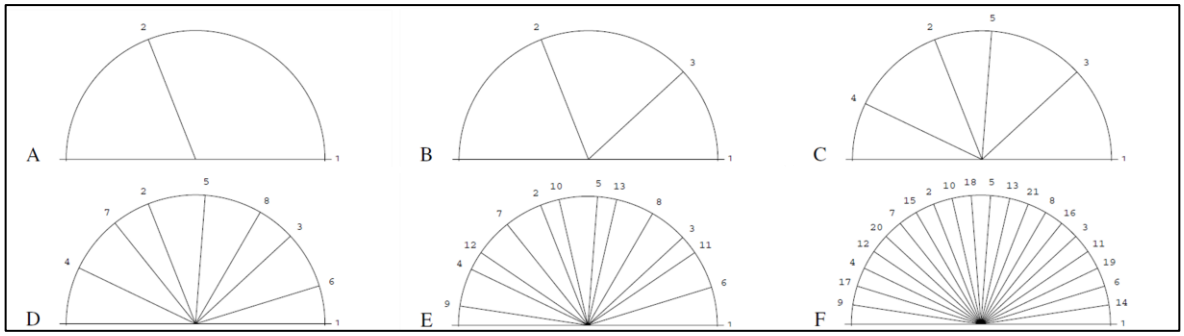

Figure 98 – The sequence for recording projections for 21 angles over a 180 degree sample rotation. At each stage (A-F), the largest section is divided into two smaller sections. Adapted from Kohler *et al*[121].

As noted earlier, one of the requirements for computational reconstruction is that all of the body of the sample must stay within the field-of-view for all recorded projections. To ensure that this was the case, a sample holder, shown in Figure 99a), was machined from a ¾ inch diameter rod of aluminium, bored out to create a cup with walls of approximately 0.5 mm thickness. Aluminium was chosen due to its high transparency for neutron transmission. To ensure that the interior of the cup remained in the field-of-view of the GadMOS sensor at all angles, a cadmium spring pressing against the inside of the cup was imaged at four perpendicular angles. The top of the cadmium spring was bent over the top of the aluminium sample holder. The spring is shown in Figure 99b) and the resulting images are shown in Figure 100.

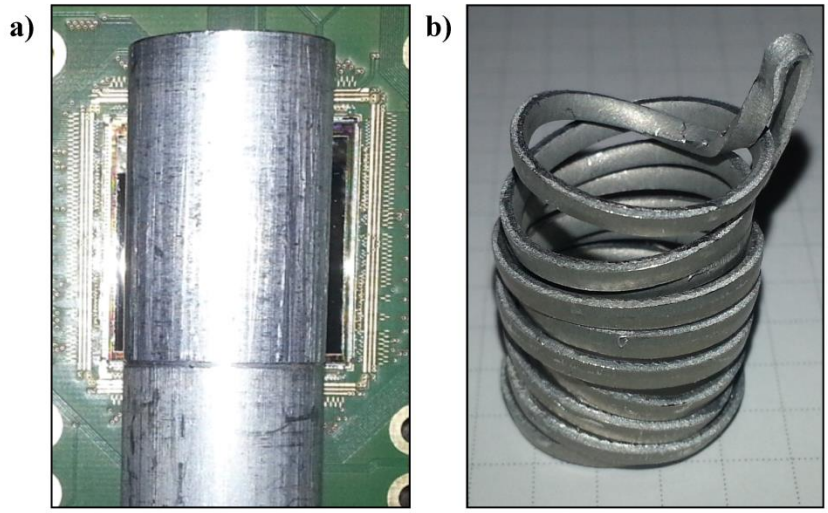

Figure 99 – a) The aluminium sample holder with the PImMS sensor visible behind it. b) The cadmium spring imaged in Figure 100 to show the internal dimensions of the sample holder.

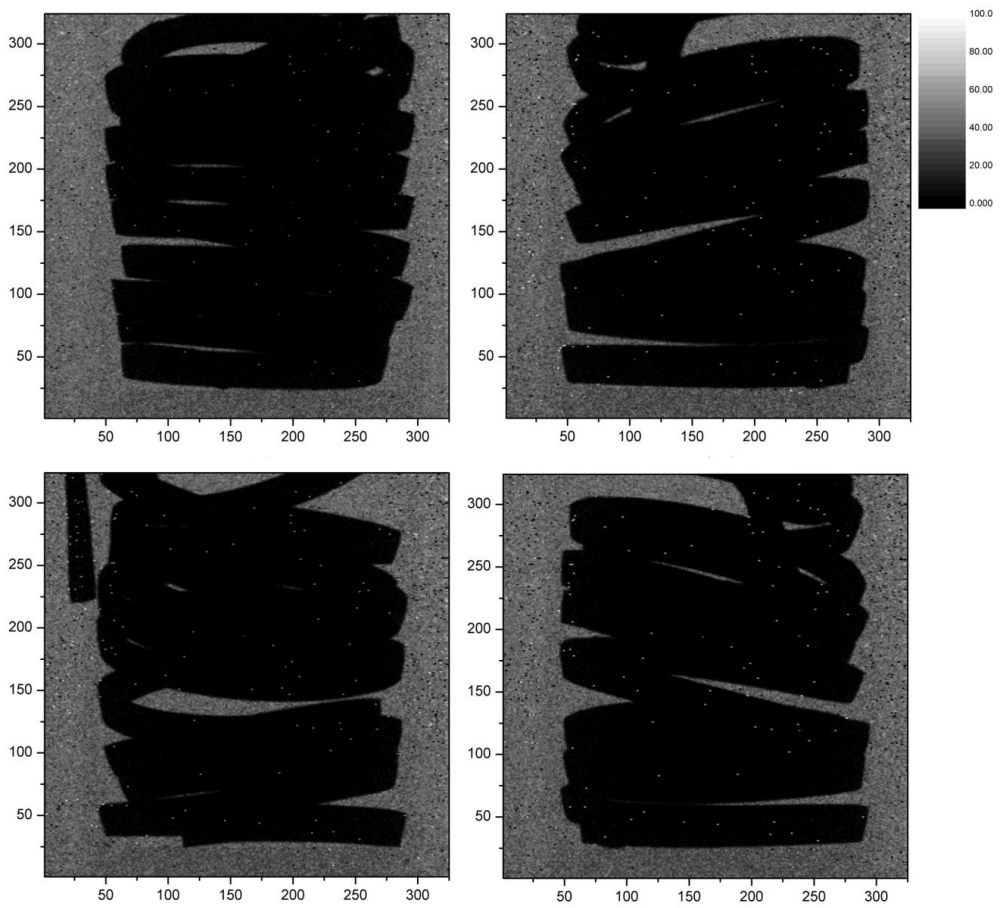

Figure 100 – The four images obtained from imaging the cadmium spring pressed against the interior of the sample holder. No background correction was required as the images were only needed to show the interior dimensions of the sample holder.

From the images obtained, shown in Figure 100, it was clear that the sample holder was both sufficiently narrow and sufficiently well centred around the rotation axis for the experiment to be performed.

The sample used for the main experiment consisted of a series of ball bearings, washers, nails and screws pressed into aluminium foil to hold the objects in place. The objects were composed of different materials including iron and copper. Images acquired over 40,000 neutron pulses were collected at each angle over the course of 5 days. In total, 137 projections at different angles were taken. In post-processing, the files were split according to the projection angle and corrected for noise and background-subtracted using a background data set acquired over 105,000 neutron pulses without the sample or sample holder present.

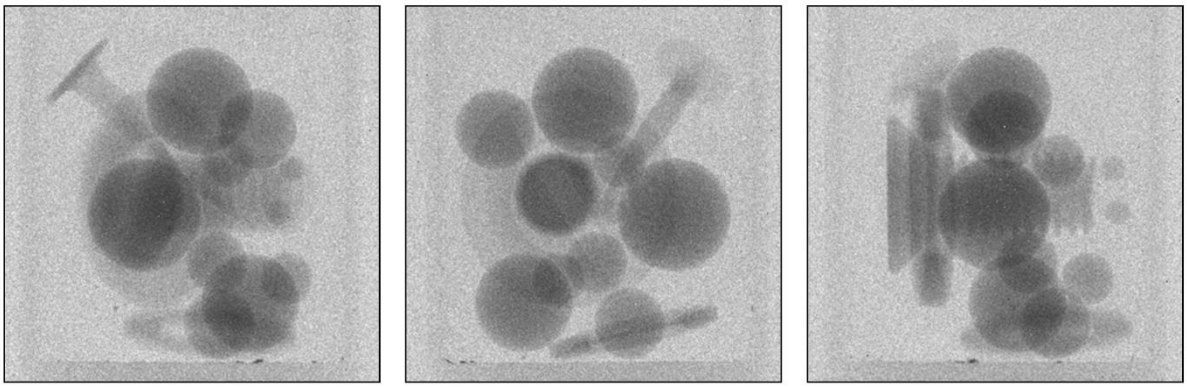

Figure 101 – Three projections recorded at different angles. At particular angles, features in the sample become evident such as the nail head and screw threading.

Each of the images obtained constitutes a radiograph, or single projection, in which all of the objects are superimposed. It was clear that at particular angles, features such as the head of the nail or the threading on the screw could be resolved. By placing the images in angle order, the rotating sample could be shown. The images were processed by Dr Daniel Pooley using a piece of software called Octopus[122] to perform a tomographic reconstruction. The algorithms for reconstruction are detailed by Kak *et al*[123]. The resulting tomogram allowed a surface render to be created and horizontal slices through the sample to be extracted, shown in Figure 102 and Figure 103.

The experiment was successful in proving that tomography with the GadMOS detector was feasible with excellent spatial resolution. As the data was acquired with the detector uncalibrated, the detector thresholds were set significantly higher than at the optimum level, decreasing the acquired signal. A tomographic reconstruction was possible by integrating over all timebins, but the low signal levels prevented the creation of a tomogram using the data as specific timebins, which would have contrasted different materials. Calibration and other future developments (see Section 13.2) will increase the sensitivity of the detector which may allow material specific tomograms to be recorded in the future.

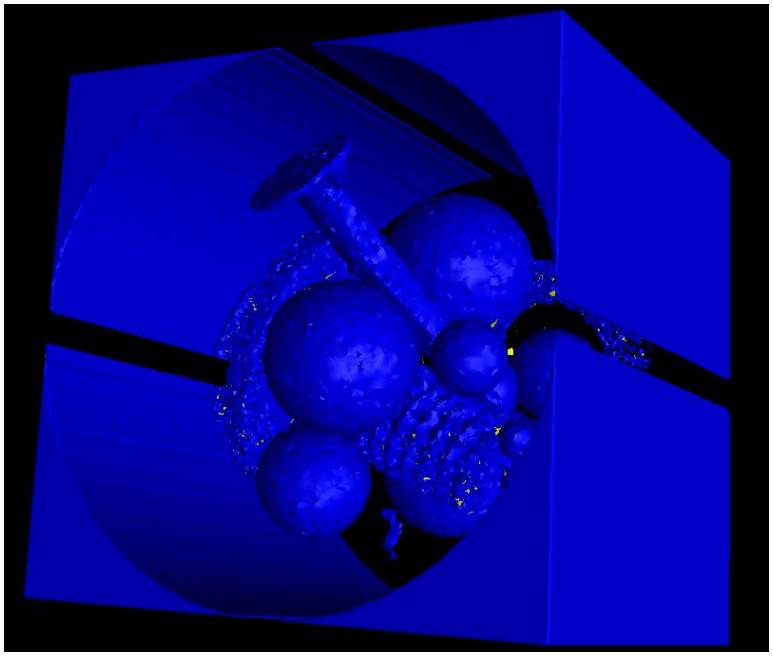

Figure 102 – A surface render of the contents of the sample holder. The nail head, ball bearings and screw thread are resolved.

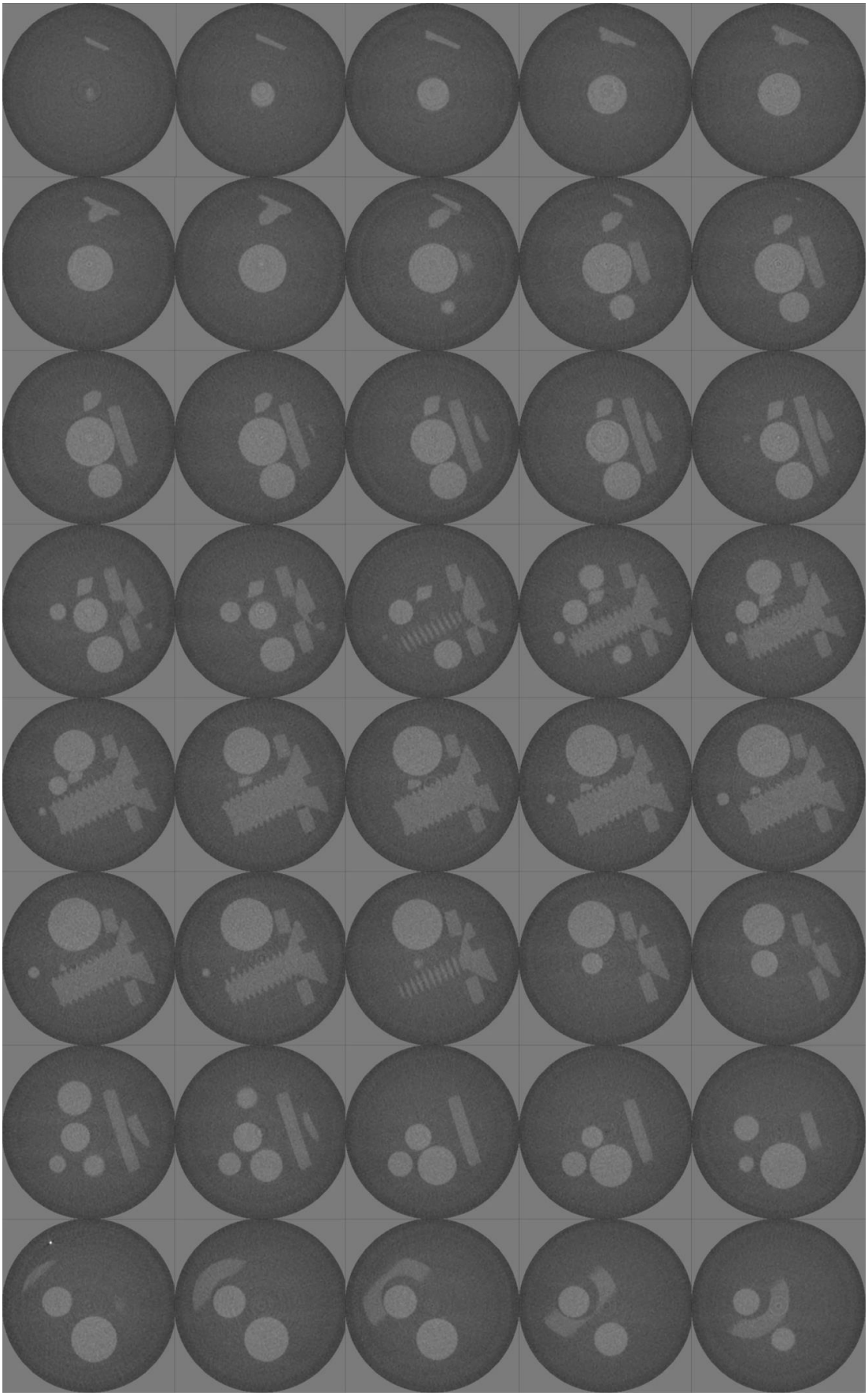

Figure 103 – Left to right and downward; horizontal slices from the tomograph, from top to bottom of the sample.

13 Future Work

13.1 Gamma Sensitivity Characterisation

As explained previously, neutron capture can cause indirect ionisation through excitation of the nucleus, the energy of which is then passed to the electrons, causing the emission of conversion and Auger electrons. The excited nucleus can also emit gamma radiation directly. Thus, neutrons incident on a sample, in addition to those being transmitted, absorbed, reflected or scattered (see Section 10.3), can also cause the emission of gamma photons. It is therefore important to characterise the gamma sensitivity of any new neutron detector as accurately as possible.

In principle, this is relatively simple to achieve; the signal count of the GadMOS sensor must be measured with and without the presence of a known flux of gamma radiation. The count rate can then be background corrected to give the count due to the gamma radiation, which is then compared to the calculated number of incident gamma rays. Accuracy in the measurement can be improved by recording count rates for longer periods or time or by increasing the gamma radiation flux.

Unfortunately, access to a reliable gamma source to perform these experiments has not yet been possible. However, these experiments are scheduled to be carried at RAL in the near future using a cobalt-60 gamma source over the period of several weeks.

13.2 GadMOS Hardware and Firmware Improvements

13.2.1 Increased Repetition Rate

As the repetition rate of the ISIS neutron source is 50 Hz (see Section 11.2), and the current maximum readout frequency of the PImMS2 sensor is 15 Hz, the overall acquisition rate falls to 12.5 Hz. This results in a fourfold increase in experimental acquisition time compared to the optimum for the ISIS neutron source. The PImMS2 sensor was designed with hardware to allow a faster readout (and thus an increased acquisition rate), but requires a different sensor board to allow for the increased data throughput, as well as firmware changes for the running of the camera. Additionally, the cameras that house the PImMS sensors are planned for an upgrade from USB2 to CameraLink which would provide an increase in the readout speed to the computer. These upgrades should allow the detector to be operated at 50 Hz, matching the neutron source.

13.2.2 New Sensor Boards

The PImMS circuit boards contain large quantities of copper and gold, which are susceptible to neutron activation upon neutron capture. These excited nuclei quickly decay radioactively, emitting gamma radiation. Whilst the majority of the circuit boards are contained within the camera, which is shielded with cadmium, the PImMS sensor board is exposed directly to the neutron beam. B_4C shielding can be used to prevent the neutron beam from penetrating most of the circuit board, but the centre of the board, containing the PImMS sensor itself, must necessarily be exposed to neutron flux. To remove the hazard of neutron activation, new sensor boards were commissioned with the section behind the PImMS sensor removed. A schematic of the PImMS sensor on the new sensor board is shown in Figure 104. At the time of writing (March 2014), the new sensor boards have been manufactured and delivered and will be used for all future neutron experiments.

13.2.3 Increased GadMOS Neutron Sensitivity Through the Use of Enriched ^{157}Gd

The thermal neutron capture cross section of ^{157}Gd is significantly higher than that of the other isotopes, but ^{157}Gd is only 15.7% abundant, as shown in Table 8. Using enriched ^{157}Gd would yield two benefits for the GadMOS sensor: firstly, there would be a significant increase in the likelihood of neutron capture compared to natural Gd of the same thickness and secondly, the optimum thickness for neutron detection in the forward geometry would be reduced (Abdushukurov *et al*). This latter effect increases the probability that conversion electrons are able to escape the gadolinium layer and be detected by the GadMOS sensor, improving the neutron sensitivity. It has so far proven difficult or prohibitively expensive to source pure ^{157}Gd. 100 g of pure ^{157}Gd, which is the amount required to create a sputter target for deposition on a PImMS sensor is currently valued at $1.2 million. Investigations are currently underway into the viability of purifying $^{157}Gd_2O_3$, which is available at a significantly lower cost.

13.2.4 Increased GadMOS Neutron Sensitivity by Implementing Dual Gd Layers

In neutron detection by the GadMOS sensor, IC and Auger electrons ionise the silicon layer of the PImMS sensor causing the emission of many electrons. The resulting electron burst is detected by the charge collecting diodes that are present in each pixel of PImMS sensor. The sensor has silicon present on the front and the back of the sensor. By reducing the thickness of the back layer of silicon, through a process known as back-grinding, and laying down another gadolinium thin film, neutron detection can occur in both forward and reverse geometry. This significantly increases the efficiency of neutron detection. The layers of gadolinium and silicon are shown schematically in Figure 104.

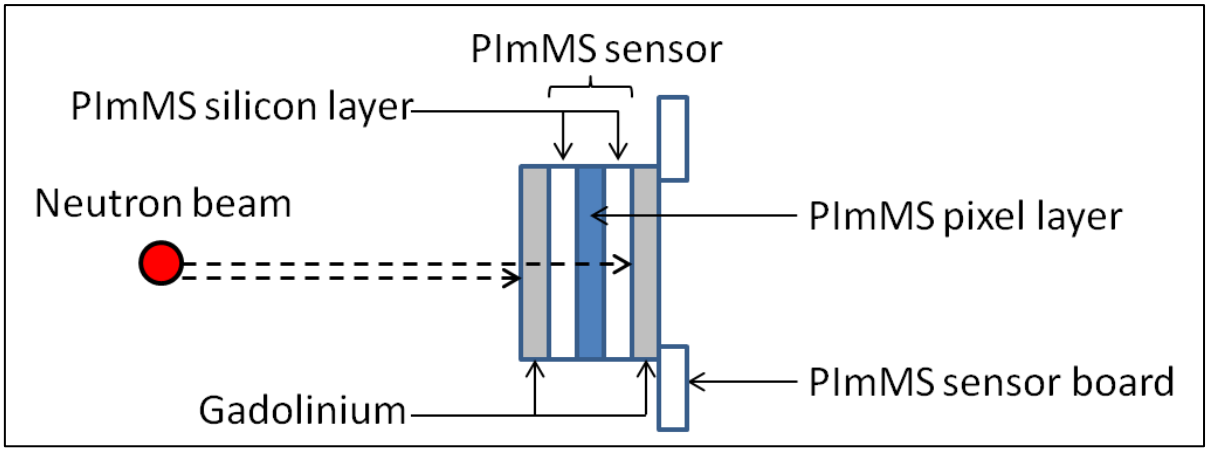

Figure 104 – A schematic representation of the dual gadolinium layer GadMOS sensor. The layer thicknesses have been exaggerated for illustration purposes.

The second layer of gadolinium functions similarly to the reverse geometry of early experiments, and consequently, the detection efficiency increases with gadolinium thickness to an asymptote (see Figure 78). However, the problem of unstable gadolinium thin films has already been noted, so in practice the achievable film thickness is limited. The back-grinding process significantly reduces the structural integrity of the sensor, causing the sensor to bend due to the internal stress. This means that the sensor must remain adhered to on a support substrate for the gadolinium deposition process.

At the time of writing (March 2014), the first prototype dual layer GadMOS sensor has been created. The back layer of silicon has been back-ground to match the thickness of the front layer and gadolinium has been sputtered on to front and back of the sensor with thicknesses of 2 µm and 7 µm respectively. The project is currently awaiting the delivery of the new sensor boards, after which the sensors will be wire-bonded and the efficiency of the detector measured.

14 Conclusions

The GadMOS neutron detector project has progressed from the initial proof-of-concept experiments, through to a well-characterised detector that has been demonstrated in a range of experiments. The detector is capable of simultaneous spatial and temporal data acquisition and has been developed at a significantly lower cost than typical neutron detectors.

At the time of writing, there exists only one neutron detector with comparable attributes to the GadMOS sensor i.e. sufficiently fast time-resolved imaging with sub-1 mm spatial resolution. The operating principle is similar to that of the GadMOS detector, with microchannel plates (MCPs) used in place of a thin film of Gd to convert incident neutrons into localised electron bursts and Timepix sensors in place of the PImMS sensor to record the position and arrival time of the electron burst. Conversion efficiency can be increased by doping the glass used to fabricate the MCPs with boron or gadolinium and also by increasing the number of stacked MCPs. A Z-stack (triple) MCP detector in which the front MCP was doped with ^{10}B was measured to have ~70% conversion efficiency for a cold neutron beam (Table 6), with a similar efficiency predicted for thermal neutrons. The first-order spatial resolution (with no post-processing) is determined by the physical dimensions of the pixels in the Timepix sensor. At 55 × 55 μm, the pixel size is significantly larger than the ~10 μm pore dimensions of the MCPs. The entire assembly must be housed within a vacuum chamber, since a pressure lower than 10^{-5} Torr is required for MCP operation. The detector is shown in Figure 105. A comparison of the TimePix-based and GadMOS detectors is provided in Table 10. The MCP/Timepix detector has been noted with the highest possible specifications – it should be noted that four Timepix sensors and a triple MCP stack adds a significant production cost to the detector.

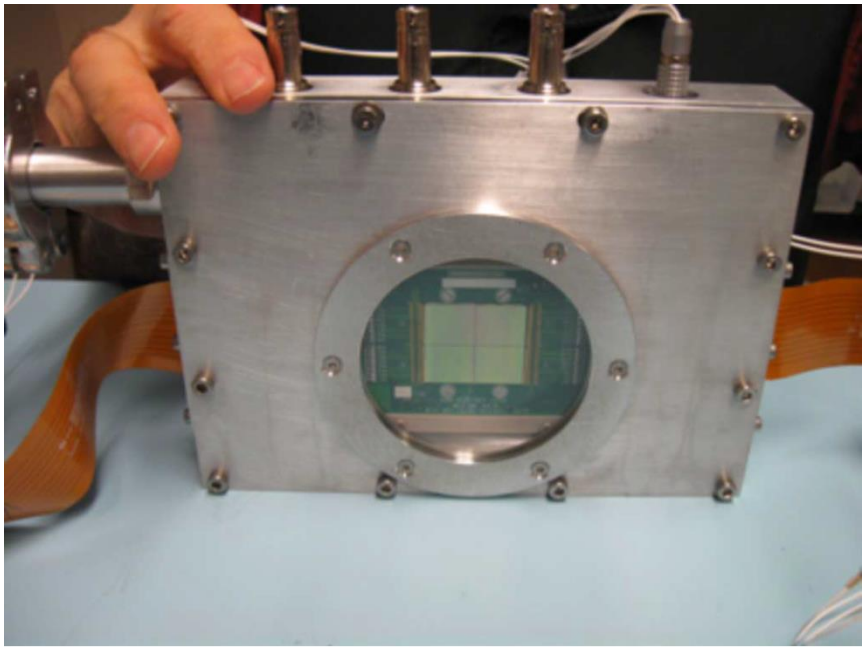

Figure 105 – A photograph of the detector vacuum housing with the quad Timepix readout board installed behind the window (MCP assembly not present).

Table 10 – A comparison of the specifications between the time-resolved spatial neutron detectors.[124, 125,126,127]

Detector	GadMOS PImMS 1	GadMOS PImMS2	MCPs / 2 × 2 Timepix
Time Resolved	✓	✓	✓
Pixel Size	70 µm × 70 µm	70 µm × 70 µm	55 µm × 55 µm
Spatial Resolution	72 × 72	324 × 324	512 × 512
Active Area	5 mm × 5 mm	22.7 mm × 22.7 mm	28 mm × 28 mm
Production Cost	$	$	$$$
Timing Registers Per Pixel	4	4	1
Readout Rate	550 Hz	15 Hz	1200 Hz

Both sensors are easily capable of resolving the Bragg edge positions of different materials within the neutron kinetic energy distribution. As noted earlier, each timebin is often assigned a time period that is several orders of magnitude longer than the sensor is capable of in order to record a longer total experimental period. If a higher time resolution is required by the experiment, the whole experimental period can still be recorded by measuring one or more separate data sets that have been delayed such that they span the period of interest.

The active area of the different sensors is a very important characteristic for neutron imaging. This is because the area of the neutron beam that can be imaged, and therefore the maximum sample size, is determined entirely by the size of the sensor due to the fact that the neutron beam cannot be focussed, unlike an optical image. This is obviously not the case when the PImMS sensor is used to image photons, since a lens can be used to map the region of interest (e.g. the phosphor screen of an

ion imaging detector) onto the sensor. The spatial resolution is mainly determined by the size of the pixels, with increased resolution achievable through post-processing techniques such as centroiding. The active area and pixel size are comparable between the PImMS2 sensor and the 2 × 2 Timepix sensor, therefore leading to a similar maximum sample size and spatial resolution.

The achievable repetition rate of the Timepix based sensor is significantly higher than that of PImMS2. However, it should be noted that at a pulsed neutron source (which is required to take advantage of the time-resolving ability of both sensors), the experimental repetition rate is likely to be limited by the frequency of the neutron pulses. With the development described in Section 13.2.1, the PImMS2 sensor should be able to operate at 50 Hz, matching the neutron pulse frequency of the ISIS spallation source.

The multiple memory registers of PImMS allow multiple neutrons to be detected by each pixel within each neutron pulse. In experiments with a sufficiently high neutron flux, the single memory registry of Timepix can cause a lower detection efficiency for low energy neutrons with later arrival times – analysis of a preliminary data set acquired with the neutron beam incident on a 300 µm gadolinium foil that covered the area of a PImMS1 sensor showed that 3% of the signal was recorded in memory registers 2-4. This data would be lost without the presence of multiple registers and the memory loss will become significantly higher with the planned sensors with dual layers of gadolinium, which should approximately double the neutron detection efficiency, or at a facility with a higher neutron flux.

15 References

1. Dempster, A., A new method of positive ray analysis. *Physical Review* **1918,** *11* (4), 316-325.

2. Davis, R.; Frearson, M., ACOL: Mass Spectrometry. Wiley: 1987.

3. Mark, T., Ionization by electron impact. *Plasma Physics and Controlled Fusion* **1992,** *34* (13), 2083.

4. Müller, A., Electron-impact ionization of ions: a brief review with emphasis on data for metallic impurities in fusion plasmas. *Physica Scripta* **1991,** *1991* (T37), 14.

5. Jung, Y.-D., Double ionization of H− ions by electron impact in the solar atmosphere. *The Astrophysical Journal* **2008,** *674* (2), 1207.

6. Baccarelli, I.; Bald, I.; Gianturco, F. A.; Illenberger, E.; Kopyra, J., Electron-induced damage of DNA and its components: experiments and theoretical models. *Physics Reports* **2011,** *508* (1), 1-44.

7. Zheng, Y.; Wagner, J. R.; Sanche, L., DNA damage induced by low-energy electrons: electron transfer and diffraction. *Physical Review Letters* **2006,** *96* (20), 208101.

8. McCulloh, K.; Rosenstock, H., Experimental Test of the Franck-Condon Principle: Double Ionization of Molecular Hydrogen. *The Journal of chemical physics* **2003,** *48* (5), 2084-2089.

9. Quayle, A.; West, A. R.; Daly, N. R., *Advances in Mass Spectrometry*. Institute of Petroleum: 1959.

10. Futrell, J. H., *Gaseous Ion Chemistry And Mass Spectrometry*. John Wiley & Sons: 1986.

11. McLafferty, F., *Mass spectrometry of organic Ions*. Elsevier Science: 2012.

12. Brodbelt, J. S.; Wilson, J. J., Infrared multiphoton dissociation in quadrupole ion traps. *Mass spectrometry reviews* **2009,** *28* (3), 390-424.

13. Beynon, J.; Gilbert, J., *Energetics and Mechanisms of Unimolecular Reactions of Positive Ions: Mass Spectrometric Methods*. Academic Press: New York: 1979; Vol. 2.

14. Itikawa, Y., *Photon and electron interactions with atoms, molecules and ions*. Springer: 2000.

15. Van Brunt, R.; Kieffer, L., Electron energy dependence of the energy and angular distributions of O− from dissociative ion pair formation in O2. *The Journal of chemical physics* **2003,** *60* (8), 3057-3063.

16. Straub, H.; Renault, P.; Lindsay, B.; Smith, K.; Stebbings, R., Absolute partial cross sections for electron-impact ionization of H 2, N 2, and O 2 from threshold to 1000 eV. *Physical Review A* **1996,** *54* (3), 2146.

17. Harrison, A. G., *Chemical Ionization Mass Spectrometry, Second Edition*. Taylor & Francis: 1992.

18. Robinson, J. W., *Undergraduate Instrumental Analysis, Fifth Edition*. Taylor & Francis: 1994.

19. Eppink, A. T. J. B.; Parker, D. H., Velocity map imaging of ions and electrons using electrostatic lenses: Application in photoelectron and photofragment ion imaging of molecular oxygen. *Review of Scientific Instruments* **1997,** *68* (9), 3477-3484.

20. Chandler, D. W.; Houston, P. L., Two-Dimensional Imaging of State-Selected Photodissociation Products Detected by Multiphoton Ionization. *Journal of Chemical Physics* **1987,** *87* (2), 1445-1447.

21. Montgomery Smith, L.; Keefer, D. R.; Sudharsanan, S., Abel inversion using transform techniques. *Journal of Quantitative Spectroscopy and Radiative Transfer* **1988,** *39* (5), 367-373.

22. Rakitzis, T. P.; Samartzis, P. C.; Toomes, R. L.; Tsigaridas, L.; Coriou, M.; Chestakov, D.; Eppink, A. T. J. B.; Parker, D. H.; Kitsopoulos, T. N., Photofragment alignment from the photodissociation of HCl and HBr. *Chemical Physics Letters* **2002,** *364* (1-2), 115-120.

23. Bull, J.; Lee, J.; Gardiner, S.; Vallance, C., An Introduction to Velocity-Map Imaging Mass Spectrometry (VMImMS). *European Journal of Mass Spectrometry* **2014,** *20*, 0-0.

24. Lockyer, N. P.; Vickerman, J. C., Single photon ionisation mass spectrometry using laser-generated vacuum ultraviolet photons. *Laser Chemistry* **1997,** *17*, 139-160.

25. Burlingame, A.; Boyd, R. K.; Gaskell, S. J., Mass spectrometry. *Analytical chemistry* **1996,** *68* (12), 599-652.

26. Dunn, G. H., Anisotropies in angular distributions of molecular dissociation products. *Physical Review Letters* **1962,** *8* (2), 62.

27. Goddard III, W.; Huestis, D.; Cartwright, D.; Trajmar, S., Group theoretical selection rules for electron-impact spectroscopy. *Chemical Physics Letters* **1971,** *11* (3), 329-333.

28. Stevenson, D.; Schissler, D., Reactions of gaseous molecule ions with gaseous molecules. IV. Experimental method and results. *The Journal of chemical physics* **2004,** *29* (2), 282-294.

29. Rapp, D.; Englander-Golden, P.; Briglia, D. D., Cross sections for dissociative ionization of molecules by electron impact. *The Journal of chemical physics* **2004,** *42* (12), 4081-4085.

30. Berry, C. E., Effects of initial energies on mass spectra. *Physical Review* **1950,** *78* (5), 597.

31. Coggeshall, N. D., Initial Kinetic Energy Discrimination Effects in Crossed-Field Ion Sources. *The Journal of chemical physics* **2004,** *36* (6), 1640-1647.

32. Stebbings, R.; Lindsay, B., Comment on the accuracy of absolute electron-impact ionization cross sections for molecules. *The Journal of chemical physics* **2001,** *114* (10), 4741-4743.

33. Feil, S.; Bacher, A.; Zangerl, M.; Schustereder, W.; Gluch, K.; Scheier, P., Discrimination effects for ions with initial kinetic energy produced by electron ionization of C2 H2 in a Nier-type ion source. *International Journal of Mass Spectrometry* **2004,** *233* (1), 325-333.

34. Märk, T.; Egger, F., Cross-section for single ionization of H2O and D2O by electron impact from threshold up to 170 eV. *International Journal of Mass Spectrometry and Ion Physics* **1976,** *20* (1), 89-99.

35. Märk, T., Cross section for single and double ionization of N2 and O2 molecules by electron impact from threshold up to 170 eV. *The Journal of chemical physics* **2008,** *63* (9), 3731-3736.

36. Brehm, B.; Grosser, J.; Ruscheinski, T.; Zimmer, M., Absolute detection efficiencies of a microchannel plate detector for ions. *Measurement science and Technology* **1995,** *6* (7), 953.

37. Oberheide, J.; Wilhelms, P.; Zimmer, M., New results on the absolute ion detection efficiencies of a microchannel plate. *Measurement science and Technology* **1997,** *8* (4), 351.

38. Straub, H.; Mangan, M.; Lindsay, B.; Smith, K.; Stebbings, R., Absolute detection efficiency of a microchannel plate detector for kilo-electron volt energy ions. *Review of Scientific Instruments* **1999,** *70* (11), 4238-4240.

39. Müller, M.; Mikoviny, T.; Wisthaler, A., Detector aging induced mass discrimination and non-linearity effects in PTR-ToF-MS. *International Journal of Mass Spectrometry* **2013**.

40. Yagi, S.; Nagata, T.; Koide, M.; Itoh, Y.; Koizumi, T.; Azuma, Y., Relative counting efficiencies of ion charge-states by microchannel plate. *Nuclear Instruments and Methods in Physics Research Section B: Beam Interactions with Materials and Atoms* **2001,** *183* (3), 476-486.

41. Franco, A.; Geissbühler, J.; Wyrsch, N.; Ballif, C., Fabrication and characterization of monolithically integrated microchannel plates based on amorphous silicon. *Scientific reports* **2014,** *4*.

42. Richardson, O. W., *Thermionic Emission from Hot Bodies*. Lightning Source Incorporated: 2003.

43. Wolf, B., *Handbook of ion sources*. CRC press: 1995.

44. Gale, W. F.; Totemeier, T. C., *Smithells metals reference book*. Butterworth-Heinemann: 2003.

45. Dahl, D. A., SIMION for the personal computer in reflection. *International Journal of Mass Spectrometry* **2000,** *200* (1), 3-25.

46. Bull, J. N.; Lee, J. W.; Vallance, C., Absolute electron total ionization cross-sections: molecular analogues of DNA and RNA nucleobase and sugar constituents. *Physical Chemistry Chemical Physics* **2014**.

47. Straub, H.; Lindsay, B.; Smith, K.; Stebbings, R., Absolute partial cross sections for electron-impact ionization of H2O and D2O from threshold to 1000 eV. *Journal of Chemical Physics* **1998,** *108* (1), 109-116.

48. Kim, Y.-K.; Rudd, M. E., Binary-encounter-dipole model for electron-impact ionization. *Physical Review A* **1994,** *50* (5), 3954.

49. Hwang, W.; Kim, Y. K.; Rudd, M. E., New model for electron-impact ionization cross sections of molecules. *The Journal of chemical physics* **1996,** *104* (8), 2956-2966.

50. Bull, J. N.; Harland, P. W.; Vallance, C., Absolute total electron impact ionization cross-sections for many-atom organic and halocarbon species. *The Journal of Physical Chemistry A* **2011,** *116* (1), 767-777.

51. Harland, P. W.; Vallance, C., Ionization cross-sections and ionization efficiency curves from polarizability volumes and ionization potentials. *International journal of mass spectrometry and ion processes* **1997,** *171* (1), 173-181.

52. Lampe, F.; Franklin, J.; Field, F., Cross sections for ionization by electrons. *Journal of the American Chemical Society* **1957,** *79* (23), 6129-6132.

53. Pelletier, J.; Pomot, C., Work function of sintered lanthanum hexaboride. *Applied Physics Letters* **2008,** *34* (4), 249-251.

54. Chang, B.-Y.; Hoetzlein, R. C.; Mueller, J. A.; Geiser, J. D.; Houston, P. L., Improved two-dimensional product imaging: The real-time ion-counting method. *Review of Scientific Instruments* **1998,** *69* (4), 1665-1670.

55. Li, W.; Chambreau, S. D.; Lahankar, S. A.; Suits, A. G., Megapixel ion imaging with standard video. *Review of Scientific Instruments* **2005,** *76* (6), 063106.

56. Roberts, G.; Nixon, J.; Lecointre, J.; Wrede, E.; Verlet, J., Toward real-time charged-particle image reconstruction using polar onion-peeling. *Review of Scientific Instruments* **2009,** *80* (5), 053104.

57. Kahn, R., The evolution of CO2 on Mars. *Icarus* **1985,** *62* (2), 175-190.

58. Gornitz, V., *Encyclopedia of Paleoclimatology and Ancient Environments*. Springer: 2009.

59. Albritton, D. L.; Allen, M.; Baede, A.; Church, J.; Cubasch, U.; Xiaosu, D.; Yihui, D.; Ehhalt, D.; Folland, C.; Giorgi, F., Summary for policymakers: a report of Working Group I of the Intergovernmental Panel on Climate Change. *IPCC Third Assessment Report–Climate Change* **2001**.

60. Itikawa, Y., Cross sections for electron collisions with carbon dioxide. *Journal of Physical and Chemical Reference Data* **2002,** *31* (3), 749-768.

61. Raju, G. G., *Gaseous Electronics: Tables, Atoms, and Molecules*. Taylor & Francis: 2011.

62. Straub, H.; Lindsay, B.; Smith, K.; Stebbings, R., Absolute partial cross sections for electron-impact ionization of CO2 from threshold to 1000 eV. *The Journal of chemical physics* **1996,** *105* (10), 4015-4022.

63. Hudson, J. E.; Vallance, C.; Harland, P. W., Absolute electron impact ionization cross-sections for CO, CO2, OCS and CS2. *Journal of Physics B: Atomic, Molecular and Optical Physics* **2004,** *37* (2), 445.

64. Velotta, R.; Di Girolamo, P.; Berardi, V.; Spinelli, N.; Armenante, M., Kinetic-energy distributions of charged fragments from CO2 dissociative ionization. *Journal of Physics B: Atomic, Molecular and Optical Physics* **1994,** *27* (10), 2051.

65. Locht, R.; Davister, M., The dissociative electroionization of carbon dioxide by low-energy electron impact. The C+, O+ and CO+ dissociation channels. *International journal of mass spectrometry and ion processes* **1995,** *144* (1), 105-129.

66. Esposito, F.; Spinelli, N.; Velotta, R.; Berardi, V., Dead time correction of time distribution measurements. *Review of Scientific Instruments* **1991,** *62* (11), 2822-2827.

67. Locht, R.; Schopman, J., The dissociative ionization in oxygen. *International Journal of Mass Spectrometry and Ion Physics* **1974,** *15* (4), 361-378.

68. McCallion, P.; Shah, M.; Gilbody, H., A crossed beam study of the multiple ionization of argon by electron impact. *Journal of Physics B: Atomic, Molecular and Optical Physics* **1992,** *25* (5), 1061.

69. Knoll, G. F., *Radiation Detection and Measurement*. John Wiley & Sons: 2010.

70. King, S. J.; Price, S. D., Electron ionization of CO2. *International Journal of Mass Spectrometry* **2008,** *272* (2), 154-164.

71. Hagstrum, H. D.; Tate, J. T., Ionization and dissociation of diatomic molecules by electron impact. *Physical Review* **1941,** *59* (4), 354.

72. Lee, S. Y.; Brown, R. C.; Heller, E. J., Multidimensional reflection approximation: Application to the photodissociation of polyatomics. *The Journal of Physical Chemistry* **1983,** *87* (12), 2045-2053.

73. Tian, C.; Vidal, C., Electron impact dissociative ionization of CO2: Measurements with a focusing time-of-flight mass spectrometer. *The Journal of chemical physics* **1998,** *108* (3), 927-936.

74. Database, N., http://www.nist.gov/pml/data/.

75. Märk, T.; Hille, E., Cross section for single and double ionization of carbon dioxide by electron impact from threshold up to 180 eV. *The Journal of chemical physics* **2008,** *69* (6), 2492-2496.

76. Hoess, P.; Fleder, K. In *Subnanosecond optical gating and irising properties of different types of microchannel plate image intensifiers (MCPII)*, SPIE's International Symposium on Optical Science, Engineering, and Instrumentation, International Society for Optics and Photonics: 1999; pp 194-200.

77. Goodwin, R. J. A.; Pennington, S. R.; Pitt, A. R., Protein and peptides in pictures: Imaging with MALDI mass spectrometry. *Proteomics* **2008,** *8* (18), 3785-3800.

78. Arai, T.; Kitamura, K.; Yonai, J.; Ohtake, H.; Hayashida, T.; Maruyama, H.; KUIJK, H. V.; Etoh, T. G., A 300-kpixel ultrahigh-speed charge-coupled device with a dynamic range of 48.6 dB at 1 million frames per second. *IEEE transactions on electron devices* **2012,** *59* (4), 1107-1113.

79. Lazovsky, L.; Cismas, D.; Allan, G.; Given, D., CCD sensor and camera for 100 Mfps burst frame rate image capture. *Airborne Intelligence, Surveillance, Reconnaissance (ISR) Systems and Applications II* **2005,** *5787*, 184-190.

80. Brouard, M.; Campbell, E.; Johnsen, A.; Vallance, C.; Yuen, W.; Nomerotski, A., Velocity map imaging in time of flight mass spectrometry. *Review of Scientific Instruments* **2008,** *79* (12), 123115.

81. Brouard, M.; Johnsen, A. J.; Nomerotski, A.; Slater, C. S.; Vallance, C.; Yuen, W. H., Application of fast sensors to microscope mode spatial imaging mass spectrometry. *Journal of Instrumentation* **2011,** *6*.

82. Crooks, J.; Marsh, B.; Turchetta, R.; Taylor, K.; Chan, W.; Lahav, A.; Fenigstein, A. In *Kirana: A solid-state megapixel uCMOS image sensor for ultrahigh speed imaging*, IS&T/SPIE Electronic Imaging, International Society for Optics and Photonics: 2013; pp 865903-865903-14.

83. Holy, T.; Jakubek, J.; Pospisil, S.; Uher, J.; Vavrik, D.; Vykydal, Z., Data acquisition and processing software package for Medipix2. *Nuclear Instruments & Methods in Physics Research Section a-Accelerators Spectrometers Detectors and Associated Equipment* **2006,** *563* (1), 254-258.

84. Jungmann, J. H.; MacAleese, L.; Visser, J.; Vrakking, M. J.; Heeren, R. M., High dynamic range bio-molecular ion microscopy with the Timepix detector. *Analytical chemistry* **2011,** *83* (20), 7888-7894.

85. Schössler, S.; Bromberger, B.; Brandis, M.; Schmidt, L. P. H.; Tittelmeier, K.; Czasch, A.; Dangendorf, V.; Jagutzki, O., Time and position sensitive single photon detector for scintillator read-out. *Journal of Instrumentation* **2012,** *7* (02), C02048.

86. Oelsner, A.; Schmidt, O.; Schicketanz, M.; Klais, M.; Schönhense, G.; Mergel, V.; Jagutzki, O.; Schmidt-Böcking, H., Microspectroscopy and imaging using a delay line detector in time-of-flight photoemission microscopy. *Review of Scientific Instruments* **2001,** *72* (10), 3968-3974.

87. Jagutzki, O.; Cerezo, A.; Czasch, A.; Dorner, R.; Hattaß, M.; Huang, M.; Mergel, V.; Spillmann, U.; Ullmann-Pfleger, K.; Weber, T. In *Multiple hit read-out of a microchannel plate detector with a three-layer delay-line anode*, Nuclear Science Symposium Conference Record, 2001 IEEE, IEEE: 2001; pp 850-854.

88. Klerk, L. A.; Lockyer, N. P.; Kharchenko, A.; MacAleese, L.; Dankers, P. Y.; Vickerman, J. C.; Heeren, R. M., C60+ secondary ion microscopy using a delay line detector. *Analytical chemistry* **2009,** *82* (3), 801-807.

89. Jungmann, J. H.; Heeren, R., Emerging technologies in mass spectrometry imaging. *Journal of proteomics* **2012,** *75* (16), 5077-5092.

90. aSpect, http://www.aspect-sys.com/.

91. Xilinx, http://www.xilinx.com/about/index.htm.

92. Ballin, J. A.; Crooks, J. P.; Dauncey, P. D.; Magnan, A.-M.; Mikami, Y.; Miller, O. D.; Noy, M.; Rajovic, V.; Stanitzki, M.; Stefanov, K., Monolithic Active Pixel Sensors (MAPS) in a quadruple well technology for nearly 100% fill factor and full CMOS pixels. *Sensors* **2008,** *8* (9), 5336-5351.

93. Sedgwick, I.; Clark, A.; Crooks, J.; Turchetta, R.; Hill, L.; John, J.; Nomerotski, A.; Pisarczyk, R.; Brouard, M.; Gardiner, S. In *PImMS: A self-triggered, 25ns resolution monolithic CMOS sensor for Time-of-Flight and Imaging Mass Spectrometry*, New Circuits and Systems Conference (NEWCAS), 2012 IEEE 10th International, IEEE: 2012; pp 497-500.

94. Clark, A. In *PImMS – An event-triggered timestamping CMOS Image Sensor for Mass Spectrometry*, iWoRID, 2011.

95. Subversion, http://subversion.apache.org/.

96. Hopkins, W. S.; Lipciuc, M. L.; Gardiner, S. H.; Vallance, C., RG^+ formation following photolysis of NO-RG via the A - X transition: a velocity map imaging study. *Journal of Chemical Physics* **2011**.

97. Curtis, D.; Eland, J., Coincidence studies of doubly charged ions formed by 30.4 nm photoionization. *International journal of mass spectrometry and ion processes* **1985,** *63* (2), 241-264.

98. Dujardin, G.; Winkoun, D., State to state study of the dissociation of doubly charged carbon dioxide cations. *The Journal of chemical physics* **1985,** *83* (12), 6222-6228.

99. Rohlf, J. W., Modern Physics from A to Z. *James William Rohlf, Wiley* **1994**.

100. Heredia Carmona, J.; Díaz Rizo, O., Determinación experimental y por Monte Carlo de coeficientes de absorción másicos para partículas beta de en compuestos orgánicos. *Nucleus* **2009,** (45), 26-31.

101. Manke, I.; Hartnig, C.; Kardjilov, N.; Hilger, A.; Lange, A.; Kupsch, A.; Banhart, J., In-situ investigation of the water distribution in PEM fuel cells by neutron radiography and tomography. *Materials Testing* **2009,** *51* (4), 219-226.

102. Carron, N. J., *An introduction to the passage of energetic particles through matter*. Taylor & Francis: London, 2007.

103. Ashcroft, N. W.; Mermin, N. D., *Solid State Physics*. Harcourt Asia: 1976.

104. Kockelmann, W.; Frei, G.; Lehmann, E. H.; Vontobel, P.; Santisteban, J. R., Energy-selective neutron transmission imaging at a pulsed source. *Nuclear Instruments and Methods in Physics Research Section A: Accelerators, Spectrometers, Detectors and Associated Equipment* **2007,** *578* (2), 421-434.

105. Parks, D. E., *Slow neutron scattering and thermalization, with reactor applications*. W. A. Benjamin: 1970.

106. Abdushukurov, D.; Abduvokhidov, M.; Bondarenko, D.; Muminov, K. K.; Toshov, T.; Chistyakov, D. Y., Modeling the registration efficiency of thermal neutrons by gadolinium foils. *Journal of Instrumentation* **2007,** *2* (04), P04001.

107. Bolozdynya, A.; Bolotnikov, A.; Richards, J. *High-Pressure Helium-3 Scintillation Position-Sensitive Detector of Thermal Neutrons*; DTIC Document: 2002.

108. Abdushukurov, D. A., Mathematical Modeling of the Efficiency Gadolinium Based Neutron Converters. *Applied Mathematics* **2013,** *4*, 27.

109. Services, N. D., https://www-nds.iaea.org/capgam/byn/page182.html.

110. Larkins, F. P., Semiempirical Auger-electron energies for elements 10 ≤ Z ≤ 100. *Atomic Data and Nuclear Data Tables* **1977,** *20* (4), 311-387.

111. Santisteban, J.; Edwards, L.; Fizpatrick, M.; Steuwer, A.; Withers, P., Engineering applications of Bragg-edge neutron transmission. *Applied Physics A* **2002,** *74* (1), 1433-1436.

112. Özdemir, A.; Hermann, R., Effect of expansion technique and plate thickness on near-hole residual stresses and fatigue life of cold expanded holes. *Journal of materials science* **1999,** *34* (6), 1243-1252.

113. Nakanishi, T.; Matsumoto, S.; Kobayashi, H., Morphological change of plant root revealed by neutron radiography. *Radioisotopes* **1992,** *41*, 638-638.

114. Lehmann, E.; Hartmann, S.; Wyer, P., Neutron radiography as visualization and quantification method for conservation measures of wood firmness enhancement. *Nuclear Instruments and Methods in Physics Research Section A: Accelerators, Spectrometers, Detectors and Associated Equipment* **2005,** *542* (1), 87-94.

115. Matsushima, U.; Kardjilov, N.; Hilger, A.; Graf, W.; Herppich, W., Application potential of cold neutron radiography in plant science research. *Journal of Applied Botany and Food Quality* **2012,** *82* (1), 90-98.

116. Vielstich, W.; Lamm, A.; Gasteiger, H. A., *Handbook of Fuel Cells: Fundamentals, Technology, and Applications*. Wiley: 2003.

117. Carrette, L.; Friedrich, K.; Stimming, U., Fuel cells–fundamentals and applications. *Fuel Cells* **2001,** *1* (1), 5-39.

118. Hickner, M.; Siegel, N.; Chen, K.; Hussey, D.; Jacobson, D.; Arif, M., Understanding liquid water distribution and removal phenomena in an operating PEMFC via neutron radiography. *Journal of the Electrochemical Society* **2008,** *155* (3), 294-302.

119. Services, N. D., http://www-nds.iaea.org/exfor/exfor.htm.

120. Steuwer, A.; Withers, P.; Santisteban, J.; Edwards, L., Using pulsed neutron transmission for crystalline phase imaging and analysis. *Journal of applied physics* **2005,** *97* (7), 074903.

121. Kohler, T. In *A projection access scheme for iterative reconstruction based on the golden section*, Nuclear Science Symposium Conference Record, 2004 IEEE, IEEE: 2004; pp 3961-3965.

122. Vlassenbroeck, J.; Masschaele, B.; Cnudde, V.; Dierick, M.; Pieters, K.; Van Hoorebeke, L.; Jacobs, P., Octopus 8: A High Performance Tomographic Reconstruction Package for X-ray Tube and Synchrotron micro-CT. *Advances in X-ray Tomography for Geomaterials* **2006**, 167-173.

123. Kak, A. C.; Slaney, M., *Principles of computerized tomographic imaging*. Society for Industrial and Applied Mathematics: 2001.

124. Tremsin, A. S.; Vallerga, J. V.; McPhate, J. B.; Siegmund, O. H.; Raffanti, R., High Resolution Photon Counting With MCP-Timepix Quad Parallel Readout Operating at Frame Rates. *Nuclear Science, IEEE Transactions on* **2013,** *60* (2), 578-585.

125. Tremsin, A.; McPhate, J.; Steuwer, A.; Kockelmann, W.; M Paradowska, A.; Kelleher, J.; Vallerga, J.; Siegmund, O.; Feller, W., High-Resolution Strain Mapping Through Time-of-Flight Neutron Transmission Diffraction with a Microchannel Plate Neutron Counting Detector. *Strain* **2012,** *48* (4), 296-305.

126. Strobl, M.; Manke, I.; Kardjilov, N.; Hilger, A.; Dawson, M.; Banhart, J., Advances in neutron radiography and tomography. *Journal of Physics D: Applied Physics* **2009,** *42* (24), 243001.

127. Brenizer, J., A Review of Significant Advances in Neutron Imaging from Conception to the Present. *Physics Procedia* **2013,** *43*, 10-20.

128. Praet, M. T.; Lorquet, J.; Raşeev, G., Unimolecular reaction paths of electronically excited species. IV. The C̃ 2Σ+ g state of CO+ 2. *The Journal of chemical physics* **1982,** *77* (9), 4611-4618.

129. Moffitt, W., The electronic structures of carbon monoxide and carbon dioxide. *Proceedings of the Royal Society of London. Series A. Mathematical and Physical Sciences* **1949,** *196* (1047), 524-539.

130. O'Neil, S. V.; Schaefer III, H. F., Valence-Excited States of Carbon Monoxide. *The Journal of chemical physics* **2003,** *53* (10), 3994-4004.

131. Lee, A.; Leather, C.; Brenton, A., Excitation of CO+ and NO+ Electronic States Via Single-electron Capture by B2+ Ions. *Rapid communications in mass spectrometry* **1997,** *11* (6), 573-577.

16 Appendix

16.1 Electron Energy Resolution (TICS Instrument)

The energy resolution of the electron source described in Section 2.3 has been characterised using a variable retarding potential technique. Briefly, this procedure involves measuring the electron trap current at a fixed electron beam energy, whilst systematically increasing the potential applied to either the trap or some other element of appropriate geometry. Electrons with an energy high enough to overcome the potential on the trap contribute toward to the measured current; for a beam consisting of completely uniform energy electrons, the measured curve would resemble a Heaviside step function centred around the electron energy and differentiating the curve would yield a Dirac delta function. In reality, due to the spread in energy of the electrons, the recorded curve has a finite rise and differentiating the curve produces a Maxwell-Boltzmann-like distribution. The data shown in Figure 106 shows the energy distribution for an electron energy of 19 eV, with a FWHM of approximately 1 eV.

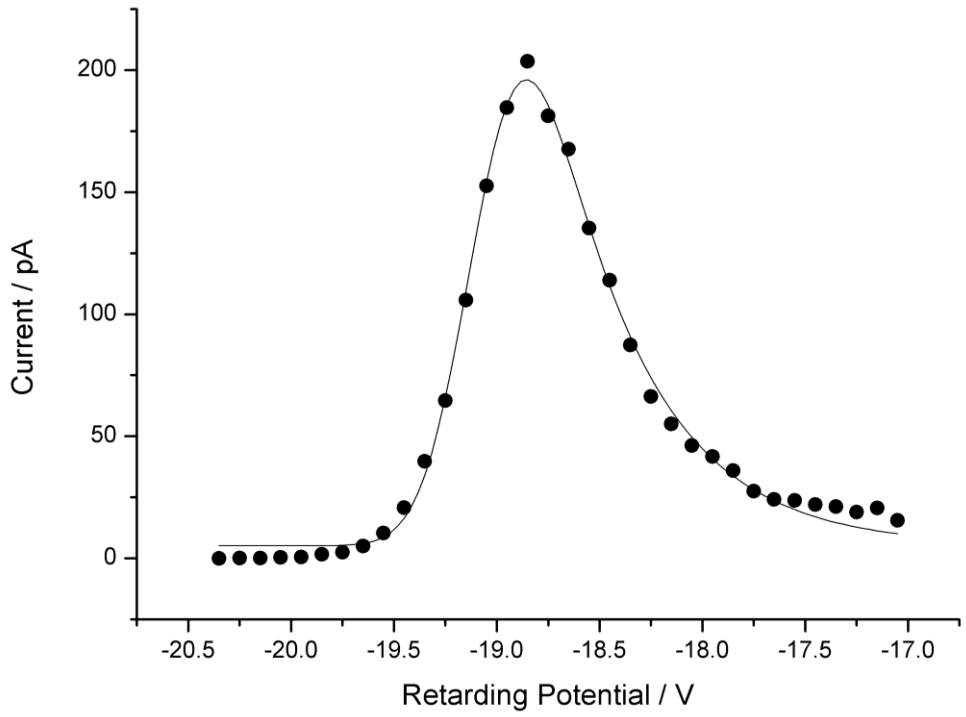

Figure 106 – The current curve, differentiated point-to-point, measured by the electron trap at a range of retarding potentials with the electron energy set to 19 eV. The curve has been fitted to a Maxwell-Boltzmann distribution.

Table 11 – The point-to-point differentiated current measurements recorded by the electron trap at an electron energy of 19 eV.

Retarding Potential / V	Current / pA
-20.35	0.04
-20.25	0.08
-20.15	0.13
-20.05	0.36
-19.95	0.57
-19.85	1.70
-19.75	2.44
-19.65	5.03
-19.55	10.32
-19.45	20.78
-19.35	39.80
-19.25	64.57
-19.15	105.77
-19.05	152.57
-18.95	184.67
-18.85	203.67
-18.75	181.33
-18.65	167.67
-18.55	135.33
-18.45	113.93
-18.35	87.47
-18.25	66.30
-18.15	55.10
-18.05	46.13
-17.95	41.67
-17.85	35.90
-17.75	27.50
-17.65	24.20
-17.55	23.73
-17.45	21.97
-17.35	21.13
-17.25	19.00
-17.15	20.57
-17.05	15.53

16.2 TICS Instrument Uncertainty

Section 2.4 notes that the TICS measurements made were all within the error of the TICS instrument. The uncertainty of each of the measurement devices used and their maximum uncertainties are shown in Table 12 with an overall error calculated to be 3.9%.

Table 12 – The errors of the measurement devices used in the construction of the TICS instrument.

Measurement	Component	Specification	Maximum Uncertainty
Ion Current (I^+)	Keithley 486	± 0.15% + 20 pA (at 200 nA)	0.2%
Electron Current (I^-)	Picoammeter	± 0.15% + 20 pA (at 200 nA)	0.2%
Pressure	MKS 690A	± 0.12%	0.1%
Temperature	Thermistor	320 ± 2 K	0.6%
Pathlength	N/A	35 ± 1 mm	2.8%
Total	-	-	3.9%

16.3 CO_2 TICS and PICS with a 5 keV Extraction Potential

The TICS and PICS measurements described in Section 4.2 were performed using an extraction potential of 7.5 kV. Shown in Figure 107 and Figure 108 are the TOF spectra and PICS from performing the same experiments using an extraction potential of 5 kV. The results are virtually identical, indicating ion kinetic energies were high enough that the MCPs did not suffer from mass discrimination effects.

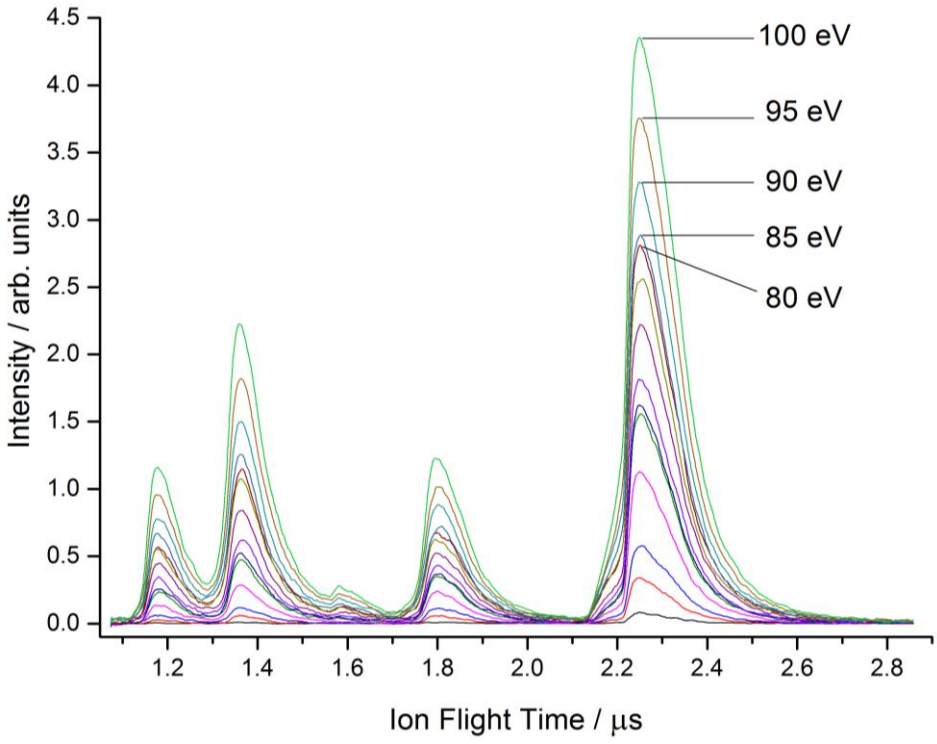

Figure 107 – The CO_2 ion spectra recorded with a repeller voltage of 5 kV.

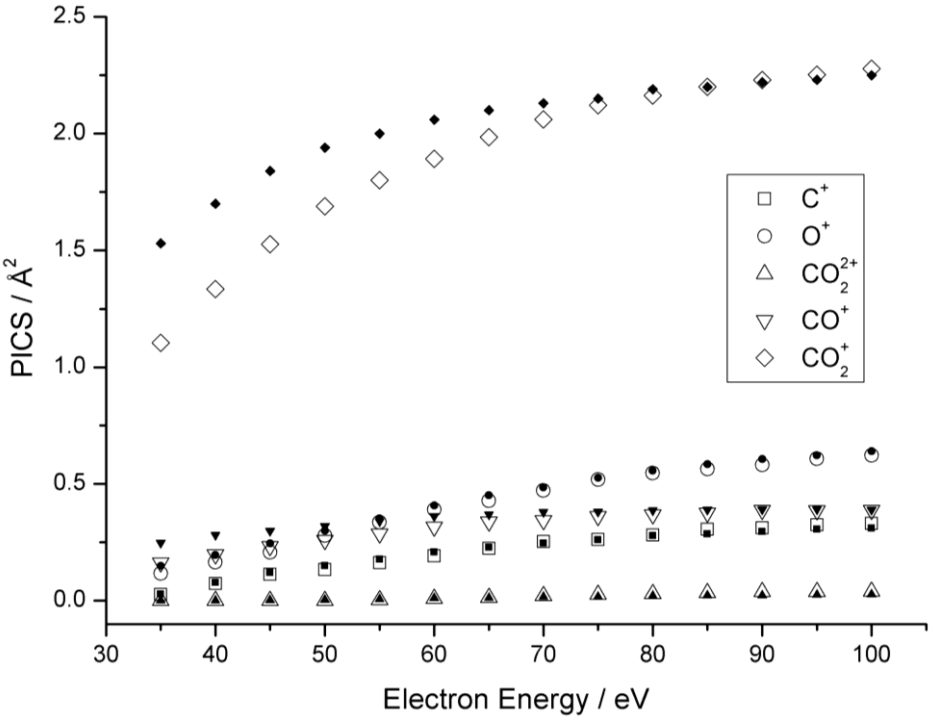

Figure 108 – PICS of ions formed in EI of CO_2, with a 5 kV extraction potential. Data from this work is shown with hollow symbols ○, measurements performed by Straub *et al* are shown with smaller filled symbols ●.

16.4 Low Lying Product Formation Energies

Listed here are the energies required to form the ions of O^+, CO^+ and C^+ with all products of ionisation formed in their ground electronic state, as well as the lowest lying excited electronic states. The energies are calculated using the data published by Praet *et al*[128], Moffitt[129], O'Neil and Schaefer[130], and Lee *et al*[131].

16.4.1 O^+ Formation

Table 13 – The predicted formation energy for products of the reaction $CO_2 \rightarrow O^+ + CO$.

Ionisation Products	Formation Energy / eV
$^4S\ O^+ + X^1\Sigma^+ CO$	19.1
$^2D\ O^+ + X^1\Sigma^+ CO$	19.1 + 3.32
$^2P\ O^+ + X^1\Sigma^+ CO$	19.1 + 5.02
$^4S\ O^+ + a^3\Sigma^+ CO$	19.1 + 5.06
$^4S\ O^+ + b^3\Pi\ CO$	19.1 + 5.22

Table 14 – The predicted formation energy for products of the reaction $CO_2 \rightarrow O^+ + C + O$.

Ionisation Products	Formation Energy / eV
$^4S\ O^+ + {}^3P\ C + {}^3P\ O$	30.3
$^4S\ O^+ + {}^1D\ C + {}^3P\ O$	30.3 + 1.26

^{4}S O$^+$ + ^{1}S C + ^{3}P O	30.3 + 2.68
^{4}S O$^+$ + ^{5}S C + ^{3}P O	30.3 + 4.18
^{4}S O$^+$ + ^{3}P C + ^{1}D O	30.3 + 1.97
^{4}S O$^+$ + ^{3}P C + ^{1}S O	30.3 + 4.19
^{4}S O$^+$ + ^{1}D C + ^{1}D O	30.3 + 3.23
^{4}S O$^+$ + ^{1}S C + ^{1}D O	30.3 + 4.65
^{2}D O$^+$ + ^{3}P C + ^{3}P O	30.3 + 3.32

16.4.2 CO^+ Formation

Table 15 – The predicted formation energy for products of the reaction $O_2 \rightarrow CO^+ + O$.

Ionisation Products	Formation Energy / eV
$X^2\Sigma^+CO^+ + {}^3$P O	19.5
$X^2\Sigma^+CO^+ + {}^1$D O	19.5 + 1.97
$X^2\Sigma^+CO^+ + {}^1$S O	19.5 + 4.19
$A^2\Pi$ $CO^+ + {}^3$P O	19.5 + 3.0
$B^2\Sigma^+CO^+ + {}^3$P O	19.5 + 5.7

16.4.3 C^+ Formation

Table 16 – The predicted formation energy for products of the reaction $O_2 \rightarrow C^+ + O_2$.

Ionisation Products	Formation Energy / eV
^{2}P C^+ + $X^3\Sigma_g^-$ O_2	22.8
^{2}P C^+ + $a^1\Delta_g$ O_2	22.8 + 0.98
^{2}P C^+ + $b^1\Sigma_g^+$ O_2	22.8 + 1.64
^{4}P C^+ + $X^3\Sigma_g^-$ O_2	22.8 + 5.33

Table 17 – The predicted formation energy for products of the reaction $O_2 \rightarrow C^+ + O + O$.

Ionisation Products	Formation Energy / eV
^{2}P C$^+$ + ^{3}P O + ^{3}P O	28.0
^{2}P C$^+$ + ^{1}D O + ^{3}P O	28.0 + 1.97
^{2}P C$^+$ + ^{1}D O + ^{1}D O	28.0 + 3.94
^{2}P C$^+$ + ^{1}S O + ^{3}P O	28.0 + 4.19

16.5 Future Improvements to the EIVMIMS Instrument

One of the primary drawbacks of the EIVMIMS instrument is that the low efficiency of ion formation means that a significant amount of experimental time is typically required to collect an ion image.

The experiment could be significantly improved by a number of design modifications to allow an increased repetition rate and/or faster data acquisition.

One of the simplest modifications is to replace the MCPs in the ion detector with MCPs possessing a higher open area ratio (OAR). A set of 90% OAR MCPs have recently been purchased and, once installed, will almost double the overall detection efficiency of the detector compared to the current MCPs which have approximately a 50% OAR.

A piezo electric pulsed valve would operate at a significantly higher repetition rate than the current solenoid valve, as well as providing the additional advantage of shorter molecular beam pulses. This would reduce the background gas contributing toward the ion image. Background gas could also be reduced by the implementation of differential pumping between the two vacuum chambers and replacing the LF-flanges with conflat flanges for a better vacuum seal.

The experiment is currently limited by the repetition rate of the CCD camera. The increase in demand in optics technology in recent years has led to a significant improvement in the data transfer and sensitivity of cameras. Megapixel cameras with a sensitivity similar to that of the intensified Photonic Science Mini FDI are available at the cost of a few hundred pounds and would allow a repetition rate of up to 50 Hz via an Ethernet connection. Other cameras, such as the PImMS sensor detailed in the following section, are capable of operating at over 100 Hz and if paired with the piezo valve described above, could lead to an order of magnitude increase in the currently achievable rate of acquisition.

More significant changes to the apparatus may include changing the ion optics. The spatial resolution of the images recorded may be improved by increasing the spacing between the plates and using higher extraction potentials, and the current lenses are the simplest form of VMI optics consisting of three equally sized electrodes. Simulations in SIMION may show that a better design is achievable, for example performing slice imaging by stretching out the Newton spheres.

Additionally, the experiment currently uses a neutral molecular beam combined with an electron beam. As an alternative, the experiment could form parent ions using a highly efficient process, such as electrospray ionisation, and focus them into an ion trap. The parent ions would then be pulsed out of the ion trap and focussed into the interaction region. This would allow non-volatile species to be studied with relative ease and the trap would allow the accumulation of sufficient ion intensity.

Finally, it is noted that EI allows a high number of molecular states to be occupied, which can make the study of molecules consisting of more than a few atoms very difficult. The characteristics of EI make it an effective universal ionisation source – it would therefore be possible to use the

instrument to carry out experiments whereby the molecular fragmentation step is performed by a laser and the resulting molecules are ionised by EI. A suitable combination of laser-only and electron only ion signal measurements would allow the respective contributions to be subtracted appropriately.